



Université  
de Toulouse

# THÈSE

En vue de l'obtention du

## DOCTORAT DE L'UNIVERSITÉ DE TOULOUSE

**Délivré par :**

Institut National Polytechnique de Toulouse (Toulouse INP)

**Discipline ou spécialité :**

Dynamique des fluides

---

**Présentée et soutenue par :**

M. OMER ATASI

le vendredi 28 septembre 2018

**Titre :**

Dynamics of bubbles in microchannels: theoretical, numerical and  
experimental analysis

---

**Ecole doctorale :**

Mécanique, Energétique, Génie civil, Procédés (MEGeP)

**Unité de recherche :**

Institut de Mécanique des Fluides de Toulouse (I.M.F.T.)

**Directeur(s) de Thèse :**

M. DOMINIQUE LEGENDRE

M. BENOIT HAUT

**Rapporteurs :**

Mme EMMANUELLE RIO, UNIVERSITE PARIS 11

M. STÉPHANE VINCENT, UNIVERSITE PARIS 12

**Membre(s) du jury :**

M. FRANK DUBOIS, UNIVERSITE LIBRE DE BRUXELLES, Président

M. BENJAMIN LALANNE, INP TOULOUSE, Membre

M. BENOIT HAUT, UNIVERSITE LIBRE DE BRUXELLES, Membre

M. DOMINIQUE LEGENDRE, INP TOULOUSE, Membre

## ACKNOWLEDGEMENTS

Je remercie Frank Dubois d'avoir accepté de présider mon jury de thèse, Anne De Wit et Benjamin Lalanne d'avoir accepté de faire parti de ce jury et tout particulièrement Emmanuelle Rio et Stéphane Vincent pour avoir accepté d'être les rapporteurs de ma thèse.

Je tiens a remercier Benoît Haut et Benoît Scheid, mes promoteurs de thèse, en particulier. Outre le financement de thèse FNRS que j'ai pu obtenir avec leur soutien, je leur suis reconnaissant de m'avoir soutenu pendant les périodes qui ont suivi les ruptures d'anévrisme que j'ai subies en 2013 et 2014. Concernant celà, je remercie également François Reniers, Laetitia Brone, et Anita Mathieu de l'Université libre de Bruxelles pour le soutien qu'ils m'ont apporté, tant financier que moral. De plus, je remercie tout particulièrement Benoît Haut d'avoir prolongé mon financement de thèse suite a l'année pendant laquelle je n'ai pas pu travailler.

Concernant mon apprentissage scientifique, je tiens à remercier mes promoteurs de thèse Benoît Haut, Benoît Scheid et Dominique Legendre, pour l'encadrement qu'ils m'ont fourni. En particulier, cette thèse a été l'occasion de m'initier à de nouveaux domaines et nouvelles techniques scientifiques, ce qui n'a été possible qu'avec leur patience et leur don à transmettre leurs connaissances. En particulier, je remercie Benoît Haut pour ses connaissances et la rigueur qu'il m'a transmises durant cette thèse. Je remercie Dominique Legendre de m'avoir introduit dans le monde de la "Computational Fluid Dynamics", domaine où j'ai pu apprendre et m'épanouir. Je remercie tout particulièrement mon co-promoteur de thèse Benoit Scheid qui m'a offert l'unique occasion de séjourner pendant 8 mois à la Princeton University afin de travailler dans l'équipe du Professeur Howard A. Stone. Je remercie aussi le Prof. Howard Stone. J'ai pu apprécier sa dévotion à la science et au bien être de ses collaborateurs et sa disponibilité malgré son planning très chargé. Cette expérience m'a beaucoup appris d'un point de vue scientifique et je lui en suis reconnaissant, ainsi qu'aux membres de son équipe, Sepideh Khodaparast, Estella Yu, Hyounghsoo Kim, Mirco Magnini et tous les autres.

Au sein de l'équipe du Laboratoire Transferts Interfaces et Procédés je tiens à remercier tout d'abord Sam Dehaeck, Adrien Dewandre et Alexei Rednikov pour leur contribution dans les aspects techniques de mon travail tant dans le domaine expérimental que théorique, et aussi Youen Vitry et Hervé Baudine de m'avoir assisté lors de problème technique au niveau des expériences conduites au laboratoire. Je remercie les membres et ex-membres du TIPs avec qui j'ai partagé de bons moments.

Parmi les membres de l'Institut de Mécanique des Fluides de Toulouse, je suis reconnaissant à Anaig Pedrono avec qui nous avons développé une partie de JADIM. Elle a toujours été disponible, même pour de longues séances de débogage. Je remercie également Mijail Febres Soria, avec qui nous avons eu de nombreuses discussions scientifiques, et les membres du service Interface : Mithlesh, Paul, Sébastien, Elena, Esli et Romain.

Un remerciement particulier à mon père, Samer Atassi, ingénieur et double docteur en automatique, qui a auparavant encadré de nombreux travaux de recherche et avec qui j'ai pu avoir des discussions scientifiques sur des sujets précis concernant des parties de ma thèse. Je remercie ma mère, Yasmine Atassi, pour sa bonne humeur et les soutiens qu'elle m'a apporté, et mon grand père Abdhul Karim Atassi, sans qui tout cela n'aurait pas été possible. Enfin, je remercie tout mes amis et proches qui ont contribué à rendre cette période de ma carrière inoubliable.

# ABSTRACT

Keywords: microfluidics, bubbly flow, Taylor flow, surfactants, lubrication film

This thesis aims at contributing to the characterization of the dynamics of bubbles in microfluidics through modeling and experiments. Two flow regimes encountered in microfluidics are studied, namely, the bubbly flow regime and the Taylor flow regime (or slug flow).

In particular, the first part of this thesis focuses on the dynamics of a bubbly flow inside a horizontal, cylindrical microchannel in the presence of surfactants using numerical simulations. A numerical method allowing to simulate the transport of surfactants along a moving and deforming interface and the Marangoni stresses created by an inhomogeneous distribution of these surfactants on this interface is implemented in the Level set module of the research code. The simulations performed with this code regarding the dynamics of a bubbly flow give insights into the complexity of the coupling of the different phenomena controlling the dynamics of the studied system. For example it shows that the confinement imposed by the microchannel walls results in a significantly different distribution of surfactants on the bubble surface, when compared to a bubble rising in a liquid of infinite extent. Indeed, surfactants accumulate on specific locations on the bubble surface, and create local Marangoni stresses, that drastically influence the dynamics of the bubble. In some cases, the presence of surfactants can even cause the bubble to burst, a mechanism that is rationalized through a normal stress balance at the back of the bubble. The numerical method implemented in this thesis is also used for a practical problem, regarding the artisanal production of Mezcal, an alcoholic beverage from Mexico.

The second part of the thesis deals with the dynamics of a Taylor flow regime, through experiments and analytical modeling. An experimental technique that allows to measure the thickness of the lubrication film forming between a pancake-like bubble and the microchannel wall is developed. The method requires only a single instantaneous bright-field image of a pancake-like bubble translating inside a microchannel. In addition to measuring the thickness of the lubrication film, the method also allows to measure the depth of a microchannel. Using the proposed method together with the measurement of the bubble velocity allows to infer the surface tension of the interface between the liquid and the gas. In the last chapter of this thesis, the effect of buoyancy on the dynamics of a Taylor flow is quantified. Though often neglected in microfluidics, it is shown that buoyancy effects can have a significant impact on the thickness of the lubrication film and consequently on the dynamics of the Taylor flow. These effects are quantified using experiments and analytical modeling. This work was performed at Princeton University with Professor Howard A. Stone during an eight month stay.

# CHAPTER 1

## Scientific Communications

### 1.1 Published articles

Atasi, O., Khodaparast, S., Scheid, B., Stone, H.A., 2017. Effect of buoyancy on the motion of long bubbles in horizontal tubes. *Physical Review Fluids* 2, 094304.

Khodaparast, S., Atasi, O., Deblais, A., Scheid, B., Stone, H.A., 2018. Dewetting of Thin Liquid Films Surrounding Air Bubbles in Microchannels. *Langmuir* 34, 1363-1370.

Atasi, O., Haut, B., Pedrono, A., Scheid, B., Legendre, D., 2018. Influence of soluble surfactants and deformation on the dynamics of centered bubbles in cylindrical microchannels. *Langmuir* 34, 10048-10062.

Atasi, O., Haut, B., Dehaeck, S., Dewandre, A., Legendre, D., Scheid, B., 2018. How to measure the thickness of a lubrication film in a pancake bubble with a single snapshot ? *Applied Physics Letter* (Editor's pick).

### 1.2 Submitted articles

G. Rage, Atasi, O., M. M. Wilhemus, J.F. Hernandez-Sanchez, Haut, B., Scheid, B., Legendre, D., Zenit, R., 2018. The pearls of mezcal: stability of surface bubbles as a traditional method to assess the ethanol content in distilled beverages . submitted to *Proceedings of the National Academy of Science*.

### 1.3 Scientific communications and conference papers

Atasi, O., Khodaparast, S., Scheid, B., Stone, H.A., 2016. Effect of gravity on the thin film surrounding a bubble translating in a tube. *American Physical Society, Division of Fluid Dynamics*, 19-21 November, Portland, Oregon.

Atasi, O., Khodaparast, S., Scheid, B., Stone, H.A., 2017. Effect of buoyancy on the motion of a long bubbles in horizontal tubes. *MicroMast annual meeting*, 13-14 September, Brussels, Belgium.

Atasi, O., Khodaparast, S., Scheid, B., Stone, H.A., 2017. Effect of buoyancy on the motion of long bubbles in horizontal tubes. *FLOW17 Conference*, 3-5 July, Paris, France.

Atasi, O., Haut, B., Scheid, B., Legendre, D., 2017. Effect of surfactants on the dynamics of a single bubble in a horizontal microchannel : A CFD study. *13th International Conference on Gas-Liquid and Gas-Liquid-Solid Reactor Engineering (GLS-13)*, 20-22 August, Brussels.

Atasi, O., Haut, B., Scheid, B., Legendre, D., Zenit, R., 2017. A numerical study of the lifetime of superficial



bubbles in water-alcohol mixtures with surfactants. American Physical Society, Division of Fluids Dynamics, 18-20 november, Denver, Colorado.

Atasi, O., Haut ,B., Scheid, B., Pedrono A., Legendre., D, Zenit., R., 2018. Numerical study of bubble bouncing and resting under a free surface in the presence of surfactants. Eurofoam, 9-12 July, Brussels, Belgium.

# TABLE OF CONTENTS

<b>ACKNOWLEDGEMENTS</b>	<b>1</b>
<b>ABSTRACT</b>	<b>2</b>
<b>1 Scientific Communications</b>	<b>3</b>
1.1 Published articles . . . . .	3
1.2 Submitted articles . . . . .	3
1.3 Scientific communications and conference papers . . . . .	3
<b>2 Introduction</b>	<b>1</b>
2.1 Bubbly flow and Taylor flow in microchannels . . . . .	1
2.2 Some important non dimensional numbers in microfluidics . . . . .	2
2.3 Use of surfactants in microfluidics . . . . .	3
2.4 Objectives of the thesis and structure of the manuscript . . . . .	3
<b>I Dynamics of bubbly flows in microchannels</b>	<b>5</b>
<b>3 Governing equations</b>	<b>6</b>
3.1 Introduction . . . . .	6
3.2 Mass conservation . . . . .	6
3.3 Momentum conservation . . . . .	7
3.4 Surfactant mass conservation on the bubble surface . . . . .	7
3.4.1 The general form . . . . .	7
3.4.2 The normal time derivative form . . . . .	8
3.4.3 The Eulerian form . . . . .	9
3.5 Surfactant transport in the liquid bulk . . . . .	12
3.6 Surface equation of state . . . . .	12
3.7 Conclusion . . . . .	12
<b>4 The numerical code JADIM-LS</b>	<b>13</b>
4.1 Numerical methods for multiphase flows . . . . .	13
4.2 The JADIM code . . . . .	15

4.2.1	One fluid formulation . . . . .	15
4.2.2	The projection method . . . . .	16
4.2.3	The Level-set method . . . . .	16
4.2.4	Spatial discretization . . . . .	17
4.2.5	Temporal discretization . . . . .	19
4.3	Numerical methodology to account for surfactants . . . . .	19
4.3.1	Transport of surfactants on the surface . . . . .	20
4.3.2	Transport of surfactants inside the bulk phase . . . . .	23
4.3.3	Marangoni stress . . . . .	23
4.4	Conclusion . . . . .	24
<b>5</b>	<b>Validation of the numerical procedure</b>	<b>26</b>
5.1	Validation of the numerical procedure used to transport surfactants on the bubble surface . . . . .	26
5.1.1	Expansion test . . . . .	26
5.1.2	Advection test . . . . .	27
5.1.3	Adsorption/desorption test . . . . .	30
5.1.4	Diffusion test . . . . .	31
5.1.5	Discussion . . . . .	32
5.2	Exchange term in the surfactant tranport equation inside the bulk phase . . . . .	34
5.3	Marangoni stress . . . . .	36
5.4	Bubble rising in an infinite stagnant liquid . . . . .	37
5.5	Conclusion . . . . .	41
<b>6</b>	<b>Influence of soluble surfactants and deformation on the dynamics of centered bubbles in cylindrical microchannels</b>	<b>42</b>
6.1	Introduction . . . . .	42
6.2	Problem statement . . . . .	44
6.2.1	Geometry . . . . .	44
6.2.2	Equations and modeling assumptions . . . . .	44
6.2.3	Dimensional analysis . . . . .	46
6.3	Results . . . . .	46
6.3.1	Spherical bubbles . . . . .	47
6.3.2	Deformable bubble without surfactants . . . . .	50
6.3.3	Deformable bubble with surfactants . . . . .	54
6.4	Conclusion . . . . .	58
<b>7</b>	<b>A numerical investigation of the lifetime of superficial bubbles inside Mezcal</b>	<b>60</b>

7.1	Introduction . . . . .	60
7.2	Experimental observations . . . . .	62
7.3	Problem statement . . . . .	63
7.4	Setup for the simulations . . . . .	64
7.4.1	Domain . . . . .	64
7.4.2	Mesh . . . . .	64
7.5	Results . . . . .	66
7.5.1	Determination of the lifetime . . . . .	66
7.5.2	Role of surfactants . . . . .	67
7.5.3	Lifetime of bubbles as a function of the alcohol volume fraction. . . . .	69
7.5.4	Scaling analysis . . . . .	70
7.6	Conclusion and perspective . . . . .	73
<b>II</b>	<b>Dynamics of Taylor flow in Microchannels</b>	<b>75</b>
<b>8</b>	<b>Introduction</b>	<b>76</b>
8.1	Lubrication approximation . . . . .	76
8.2	The analysis of Bretherton . . . . .	77
8.3	Extension of the Bretherton model . . . . .	79
8.4	Conclusion . . . . .	80
<b>9</b>	<b>How to measure the thickness of a lubrication film in a pancake bubble with a single snapshot?</b>	<b>81</b>
9.1	Introduction . . . . .	81
9.2	Methodology . . . . .	84
9.2.1	Experimental setup . . . . .	84
9.2.2	Raytracing . . . . .	87
9.2.3	Model of the bubble shape . . . . .	88
9.3	Results and discussion . . . . .	91
9.3.1	Establishment of an alternative equation for measuring the thickness of the lubrication film and the channel height . . . . .	91
9.3.2	Experimental measurements . . . . .	92
9.3.3	Effect of a finite numerical aperture . . . . .	94
9.4	Conclusion . . . . .	96
<b>10</b>	<b>Effect of buoyancy on the motion of a long bubble in a horizontal tube</b>	<b>97</b>
10.1	Introduction . . . . .	97
10.2	Experimental setup . . . . .	100

10.2.1	Refractive index matching . . . . .	100
10.2.2	Experiments . . . . .	100
10.2.3	Visualization and image processing . . . . .	101
10.2.4	First experimental observation . . . . .	102
10.3	Theoretical predictions . . . . .	102
10.3.1	Thickness of the liquid film at the front of the bubble . . . . .	102
10.3.2	Inclination angle in the thin film region . . . . .	108
10.4	Experimental results and discussions . . . . .	108
10.4.1	Thickness of the liquid film at the front of the bubble . . . . .	108
10.4.2	Inclination of the bubble . . . . .	110
10.4.3	Liquid film at the back of the bubble . . . . .	111
10.5	Conclusion . . . . .	112
<b>11</b>	<b>Conclusions and perspectives</b>	<b>114</b>
11.1	Conclusion . . . . .	114
11.2	Perspectives . . . . .	116
<b>12</b>	<b>Appendixes</b>	<b>118</b>
12.1	Appendix A . . . . .	118
12.2	Appendix B . . . . .	120

# CHAPTER 2

## Introduction

Microfluidics is a constantly evolving branch of technology, widely used in medicine, biology and biotechnology as an analytical tool, from cell culture to DNA extraction (Patel and Chandra (2016)). Apart from small scale analytic devices, microfluidics is becoming an important technology in process industry. In those industry, microfluidics contributes in reducing the hazards associated to highly exothermic reactions through the large surface area to volume ratio of the microfluidic devices. For example, three-phase hydrogenation reactions have been performed successfully using microfluidics (Kobayashi *et al.* (2004)). The high surface area to volume ratio of these devices also enhance the efficiency of unit operations such as gas-liquid absorption, heating or cooling and pervaporation (Hassanvand and Hashemabadi (2012); Han *et al.* (2012); Ziemecka *et al.* (2015)). These unit operations are performed through microfluidic devices in industry to some extent. However, there is a need to analyze and model the underlying physics for the optimal design and functioning of these microfluidic devices. This thesis aims at contributing to the understanding of the physics underlying the functioning of microfluidic gas-liquid absorption devices.

This research project is funded by the FNRS and is conducted in the frame of a collaboration between three laboratories:

1. Transfers, Interfaces and Processes (TIPs), Université libre de Bruxelles, 1050 Bruxelles, Belgium
2. Interfaces, Institut National Polytechnique de Toulouse (INPT), 31400 Toulouse, France
3. Complex Fluids group, Princeton University (PU), 08540 Princeton, New Jersey

## 2.1 Bubbly flow and Taylor flow in microchannels

In microfluidics, gas-liquid absorption is performed in bubble-microabsorbers. These devices consist in a microchannel of circular or rectangular cross section of hydraulic diameter,  $d_h$ , of the order of 0.1 – 2 mm. Gas bubbles dissolve inside a liquid while they translate along the microchannel axis. This translation is generated by an imposed pressure difference between the inlet and the outlet of the microchannel, or by injecting the gas and the liquid at constant flow rates,  $Q_g$  and  $Q_l$ , respectively. Two flow regimes are encountered in those devices:

1. The “bubbly flow” regime for which the bubble equivalent diameter,  $d = (6V/\pi)^{\frac{1}{3}}$ , where  $V$  is the bubble volume, is smaller than the microchannel hydraulic diameter (i.e.,  $d < d_h$ ).
2. The “Slug flow” or “Taylor flow” regime, where  $d > d_h$ . In this regime, a lubrication film is deposited on the microchannel wall as the bubble translate along the microchannel axis. The dynamics and the gas-liquid mass transfer capabilities of these flows rely, among other parameters, on this lubrication film.

A schematic of these flow regimes is presented in Fig. (2.1). The transition between the bubbly flow and the Taylor flow regimes was shown to depend on  $Q_l$  and  $Q_g$ . Several flow maps based on  $Q_l$  and  $Q_g$  were established (see for example Thulasidas *et al.* (1997); Triplett *et al.* (1999)), where the transition between those two regimes was determined. However, these flow maps depend upon the pair of fluids that is used. It was shown that the bubbly flow appears at high liquid and low gas flow rates. The Taylor flow, on the other hand, is obtained on a large range of low and intermediate gas and liquid phase flow rates.

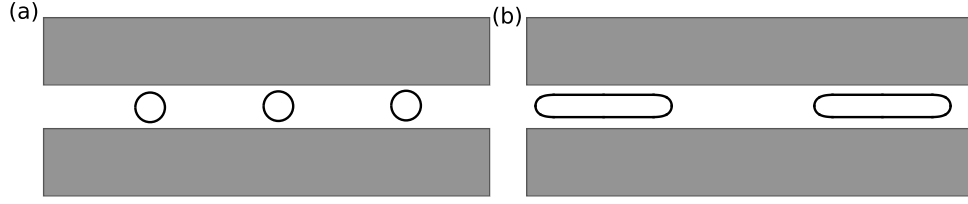


Figure 2.1: (a): Schematic of a bubbly flow inside a microchannel. (b): Schematic of a Taylor flow inside a microchannel.

In bubble microabsorbers, both the bubbly flow regimes and the Taylor flow are used to dissolve the gas inside the liquid. For example, Cubaud *et al.* (2012) studied the complete dissolution of small carbon dioxide bubbles inside pure methanol in microchannels. Shim *et al.* (2014) studied the dissolution of air bubbles inside aqueous solution in microchannels. Other work were also perform to study the dissolution of small bubbles inside microchannels (Mikaelian; Mikaelian *et al.* (2015)). In these studies, it was shown that, for  $d/d_h > 0.15$  the liquid recirculates in between bubbles, promoting mixing, thus enhancing the transfer of the gas towards the liquid. The Taylor flow regime has also received considerable attention. In addition to recirculation of the liquid in between air bubbles, Taylor bubbles have the advantage to exhibit a large surface area. Thus, the research on gas-liquid mass transfer using Taylor bubbles is an active area of research (van Baten and Krishna (2004); Irandoust *et al.* (2009); Liu and Wang (2011); Abadie *et al.* (2013); Abiev *et al.* (2017)).

In this thesis, we aim to analyze and model the dynamics of bubbles flowing in the bubbly flow regime and in the Taylor flow regime inside horizontal microchannels.

## 2.2 Some important non dimensional numbers in microfluidics

In microscale flows such as the ones encountered in bubble microabsorbers, inertial and buoyancy effects are often negligible while surface tension and viscous forces dominate the system. The relative importance of inertial to viscous forces is assessed by the means of the Reynolds number:

$$\text{Re} = \frac{\rho \mathcal{U} \mathcal{L}}{\mu} \quad (2.1)$$

where  $\rho$  and  $\mu$  are the density and viscosity of the liquid respectively, and  $\mathcal{U}$  and  $\mathcal{L}$  are the characteristic velocity and length of the studied system, respectively. The velocity scale,  $\mathcal{U}$ , can be set equal to the translating bubble velocity,  $U$ , or to the mean liquid velocity,  $J_l = Q_l/A$ , where  $A$  is the cross sectional surface area of the microchannel, depending on the studied system. The relative importance of buoyancy to surface tension effects is assessed by the means of the Bond number:

$$\text{Bo} = \frac{\rho g (\mathcal{L})^2}{\sigma} \quad (2.2)$$

where  $\sigma$  is the surface tension of the interface and  $g$  is the gravitational acceleration. The Bond number characterizing these microscale flows is often small when compared to unity. Finally, the relative importance of viscous forces to surface tension forces is assessed by the means of the capillary number:

$$\text{Ca} = \frac{\mathcal{U} \mu}{\sigma} \quad (2.3)$$

## 2.3 Use of surfactants in microfluidics

Surfactants are molecules formed of a polar group that preferentially dissolves in hydrophylic liquids, and an apolar group that is expelled from the polar phase towards a gas phase or a hydrophobic liquid phase. As a consequence, surfactants tend to adsorb at interfaces between a polar and an apolar medium such as air/liquid interfaces. As they adsorb on the air/liquid interface, they locally reduce the surface tension of the interface. Therefore, they can create a spatial imbalance in the surface tension, leading to stresses tangent to the interface called, Marangoni stresses. These stresses create a flow along the interface, from region of low surface tension to regions of high surface tension (Baroud *et al.* (2010); Anna (2016)). These properties make surfactants widely used in bubble/drop microfluidics to prevent bubble/drop coalescence (Mazutis and Griffiths (2012)) or maintain desired wetting conditions at the walls of the microchannel (Liu *et al.* (2017)).

In addition to Marangoni stresses, surfactants can create additional viscous stresses on interfaces, called surface viscosity stresses, which are due to non-covalent interactions between adsorbed molecules. These stresses may affect the fluid flow at the interface vicinity in systems characterized with a large surface to volume ratio. For small non charged surfactants molecules present in limited amounts, these stresses have a small influence when compared to Marangoni stresses.

In this thesis, we aim at giving insight into the complexity of the coupling between the flow inside the microchannel and the dynamics of these surfactants. The surfactants that will be considered are those for which surface viscosity can be neglected, i.e., small non charged molecules present in small amounts. For this purpose, the numerical code JADIM, developed at Institut de Mécanique des Fluides de Toulouse (IMFT) is used and is further developed to simulate two phase flows with surfactants.

## 2.4 Objectives of the thesis and structure of the manuscript

The advantage that microfluidics offers for gas-liquid absorption, both through the bubbly flow regime and the Taylor flow regime, and the wide use of surfactants in microfluidics has motivated us to fix the following objectives:

1. Understand and indentify the parameters controlling the thickness of the lubrication film in the Taylor flow regime.
2. Characterize the coupling between the dynamics of surfactants and the flow inside microchannels.

This work is based on experiments, numerical simulations and analytical modelling. The experiments and analytical modelling have been performed at TIPs and PU, while the numerical simulations have been carried out with the JADIM code developed at IMFT. Several stays, of few months each, were performed at IMFT in order to contribute to the development of JADIM and to perform the simulations. This work contains 2 parts, and is organized around 8 chapters.

The first part focuses on the dynamics of a bubbly flow inside a microchannel containing surfactants. The first part contains the Chapters 3,4,5,6 and 7.

Chapter 3 introduces the equations governing two phase flow with soluble surfactants. In this chapter, a particular attention is held on the transport equation of surfactants on a moving and deforming surface. In particular, an Eulerian formulation of the transport equation of a scalar along a moving and deforming interface is presented. Some key features of this equation are emphasized.



Chapter 4 introduces the numerical methods used in this work and the development made, including the implementation of the Eulerian formulation of the transport equation of surfactants on an interface, the implementation of a source term inside the bulk transport equation accounting for the adsorption flux of surfactants towards this interface, and the calculation of the Marangoni stresses induced by the inhomogeneous distribution of surfactants on the interface.

Chapter 5 presents validation tests regarding surfactant transport and Marangoni stresses. In this chapter, each term appearing in the implemented equations are validated separately, by comparing the numerically obtained solution to an exact analytical solution.

Chapter 6 presents results obtained with the code presented in the previous chapters, regarding the analysis of the dynamics of deformable bubbles translating along a microchannel filled with a liquid that contains surfactants. The chapters 5 and 6 are part of an article that has just been accepted for publication in *Langmuir*.

Chapter 7, makes the transition with the second part of the thesis. In this chapter, a work conducted in a frame of a collaboration with Prof. Roberto Zenit from Universidad Nacional Autonoma de Mexico (UNAM) is presented. In this work, an ancient technique used to assess the alcohol content of Mezcal, a traditional Mexican alcoholic beverage, is studied, using JADIM. This technique relies on the extended lifetime of superficial bubbles inside a cup filled with Mezcal, this extended lifetime being partly caused by organic molecules acting as surfactants. An attempt is made to gain insight into the mechanisms controlling the extended lifetime of these bubbles using JADIM. An article is being prepared on this subject in collaboration with the team of Prof. Roberto Zenit.

The second part focuses on the dynamics of a Taylor flow inside a microchannel. It contains the chapters 8,9 and 10.

Chapter 8 is a brief introduction to Taylor flows.

Chapter 9 presents a methodology developed during this thesis at ULB, allowing to measure the thickness of the lubrication film forming around a pancake-like bubble using a single instantaneous bright-field image of a bubble. The method is developed and applied in this chapter. The experimental apparatus is presented, the technique is explained and used. An emphasis is brought on the few equipment it requires when compared to other methods. A discussion about the extension of the method to drops is presented. An article has been published in the journal *Applied Physics Letter* regarding this subject in october 2018.

Chapter 10 focuses on the effect of buoyancy on the Taylor flow regime. It is a work conducted in the frame of collaboration with Prof. Howard Stone from PU. It was performed at PU during an eight-month stay. The experimental apparatus and the image processing is explained. A theoretical prediction of the effect of buoyancy on the film thickness and bubble orientation is presented, and the experimental measurements are compared to the theoretical predictions. This work has been published in *Physical Review Fluids* in october 2017.

Finally, a conclusion presents the main results of this work and outlines some challenging perspectives such as the simulation of Taylor flows and Pancake bubbles with surfactants or the extension of the experimental method to measure the lubrication film thickness to different geometry and systems, and the study of the dynamics of dewetting of the lubrication film. Regarding this subject, in the continuation of the work performed with Prof. Howard Stone, a work has been published regarding the dewetting of Taylor bubbles in microchannels in *Langmuir* in december 2017.

The literature review regarding the study of the bubbly flow regime is presented in Chapter 6. In Chapter 8, a literature review concerning the Taylor flow regime is available and in Chapter 9 a survey of film thickness measurement techniques is available. In Chapter 10, the literature review concerning the effect of buoyancy on bubbles in tubes and microchannels is presented.

## **Part I**

# **Dynamics of bubbly flows in microchannels**

## CHAPTER 3

### Governing equations

#### 3.1 Introduction

In this chapter the equations governing the motion of a bubble transported by a liquid in a microchannel are presented. A specific attention is held on the equation governing the surfactant transport on the bubble interface.

#### 3.2 Mass conservation

The mass conservation for each phase  $k$  ( $k = c$  or  $k = d$ , with  $c$  the continuous liquid phase and  $d$  the dispersed gas phase) separated by the surface  $S$  is written as:

$$\frac{\partial \rho_k}{\partial t} + \nabla \cdot (\rho_k \mathbf{v}_k) = 0 \quad (3.1)$$

where  $\rho_k$  is the density of phase  $k$ ,  $\mathbf{v}_k$  is the velocity of phase  $k$  and  $\nabla$  is the nabla operator. The mass flux exiting phase  $k$ ,  $J_k$ , can be written in terms of the velocity of the phase  $k$ , evaluated at the interface, and the velocity of the interface,  $\mathbf{v}_I$ :

$$J_k = \rho_k (\mathbf{v}_k - \mathbf{v}_I) \cdot \mathbf{n}_k \quad (3.2)$$

where  $\mathbf{n}_k$  is the normal to the interface, pointing outside phase  $k$ .

**Kinematic condition without mass transfer at the interface:** If no mass transfer is allowed at the interface,  $J_k = 0$ . From equation 3.2, one can identify the following relationship between  $\mathbf{v}_k$  and  $\mathbf{v}_I$ , valid at the interface:

$$\mathbf{v}_k \cdot \mathbf{n}_k = \mathbf{v}_I \cdot \mathbf{n}_k \quad (3.3)$$

This equation establishes the fact that the normal component of the velocity is continuous across the interface. This hypothesis (no mass transfer at the interface) is an excellent approximation as long as there is no transfer of the main components of one of the phase across the interface.

**Kinematic condition with mass transfer at the interface:** When mass transfer is allowed at the interface (i.e., when one of the main components of both phases crosses the interface) the sum of the mass flux getting out of all phases should be equal to zero :

$$\sum_k J_k = 0 \quad (3.4)$$

### 3.3 Momentum conservation

The momentum conservation for an incompressible Newtonian fluid is written for each phase  $k$  as:

$$\frac{\partial \mathbf{v}_k}{\partial t} + \nabla \cdot (\mathbf{v}_k \otimes \mathbf{v}_k) = -\frac{1}{\rho_k} \nabla p_k + \frac{1}{\rho_k} \nabla \cdot \bar{\mathbf{T}}_k + \mathbf{g} \quad (3.5)$$

where  $\mu_k$  is the dynamic viscosity of phase  $k$ ,  $\bar{\mathbf{T}}_k$  is the viscous stress tensor of phase  $k$ , defined as:  $\bar{\mathbf{T}}_k = \mu_k (\nabla \mathbf{v}_k + (\nabla \mathbf{v}_k)^T)$ ,  $\otimes$  is the dyadic product,  $\mathbf{g}$  is the gravitational acceleration and  $p_k$  is the pressure inside phase  $k$ . The momentum conservation at the interface between both phases is written as follows:

$$\sum_k (J_k \mathbf{v}_k - \bar{\mathbf{M}}_k \cdot \mathbf{n}_k) = -\sigma (\nabla_s \cdot \mathbf{n}) \mathbf{n} + \nabla_s \sigma \quad (3.6)$$

where  $\sigma$  is the surface tension of the interface,  $\mathbf{n} = \mathbf{n}_l$  is the normal to the interface, pointing towards the gas phase,  $\bar{\mathbf{M}}_k$  is the total stress tensor given by  $\bar{\mathbf{M}}_k = (-p_k \bar{\mathbf{I}} + \bar{\mathbf{T}}_k)$ , where  $\bar{\mathbf{I}}$  is the identity tensor,  $\nabla_s = ((\bar{\mathbf{I}} - (\mathbf{n} \otimes \mathbf{n})) \cdot \nabla)$  is the surface gradient operator (Batchelor (1967)) and  $\nabla_s \cdot \mathbf{n}$  is the curvature of the bubble interface.

**Continuity of the shear stress:** The shear stress is continuous across the interface if there is no surface tension gradients:

$$\sum_k (\bar{\mathbf{T}}_k \cdot \mathbf{n}_k) \cdot \mathbf{t}_k = \nabla_s \sigma \cdot \mathbf{t}_k \quad (3.7)$$

where  $\mathbf{t}_k$  is a unit vector tangent to the interface.

### 3.4 Surfactant mass conservation on the bubble surface

In this subsection the equations describing the conservation of surfactant mass on a moving and deforming interface are presented. The main feature of these equations is the way to express the Lagrangian time derivative (or total time derivative) of  $\Gamma$ , the surfactant mass per unit area, a quantity associated to the moving surface.

#### 3.4.1 The general form

The conservation of  $\Gamma$  on the interface  $S$  is written as (Stone (1990)):

$$\frac{d}{dt} \int_{S(t)} \Gamma dS \equiv \int_{S(t)} \frac{d\Gamma}{dt} dS + \int_{S(t)} \Gamma \frac{d}{dt} dS = \int_{S(t)} D_s \nabla_s^2 \Gamma dS + \int_{S(t)} S_\Gamma dS \quad (3.8)$$

where  $S(t)$  refers to the surface,  $dS$  is the surface element,  $d/dt$  is the Lagrangian time derivative,  $D_s$  is the diffusion coefficient of the surfactants along the interface and  $S_\Gamma$  is the flux of surfactants from the liquid phase to the interface, due to the adsorption/desorption of the surfactants, i.e.,  $S_\Gamma = (D_c \mathbf{n} \cdot \nabla C_c)|_I$ , where the subscript  $I$  denotes the bubble-liquid interface and  $C_c$  is the concentration of surfactants in the liquid. This flux is given by Langmuir's kinetic law (Levich (1962); Muradoglu and Tryggvason (2008)):

$$S_\Gamma = k_a C_I (\Gamma_\infty - \Gamma) - k_d \Gamma \quad (3.9)$$

where  $k_a$  and  $k_d$  are adsorption and desorption kinetic constants, respectively, and  $C_I$  is the surfactant concentration in the liquid in contact with the interface. The main difference in the equations available in the literature describing the conservation of  $\Gamma$  on the surface  $S$  comes from the evaluation of the Lagrangian time derivative of  $\Gamma$ , i.e.,  $\frac{d\Gamma}{dt}$ . Two equivalent forms are presented in the following sections. The first one expresses the Lagrangian time derivative in terms of a “normal time derivative”, this terminology being explained below. The second one expresses the Lagrangian time derivative in terms of an “Eulerian time derivative”, this terminology being described in the corresponding section. The strategy employed in this section is to start from Eq. (3.8) and derive the two form discussed above.

### 3.4.2 The normal time derivative form

The equation proposed by Stone (1990) is presented in this subsection. The first step in the derivation is to express the Lagrangian time derivative of  $\Gamma$ , i.e.,  $\frac{d\Gamma}{dt}$  (see Eq. (3.8)), in terms of the “normal time derivative”. The normal time derivative is a partial time derivative of  $\Gamma$  with respect to time taken along the normal to the interface. For this purpose, Fig. 3.1 depicts 3 fixed points in the laboratory frame,  $M$ ,  $M'$ ,  $M''$ . At time  $t$ , the velocity on  $M$  is  $\mathbf{v}|_M$ . At time  $t$ ,  $M$  is on the interface (as depicted on Fig. 3.1 by the black solid line) and at time  $t + \Delta t$  the points  $M'$  and  $M''$  are on the interface. The position vector localizing the point  $M$  is:  $\mathbf{r}|_M$ . The velocity vector evaluated on  $M$ ,  $\mathbf{v}|_M$ , points towards  $M''$ . The component of  $\mathbf{v}|_M$  that is normal to the interface, i.e.,  $(\mathbf{v} \cdot \mathbf{n})|_M$ , points towards  $M'$ . The total derivative of  $\Gamma$  with respect to time is:

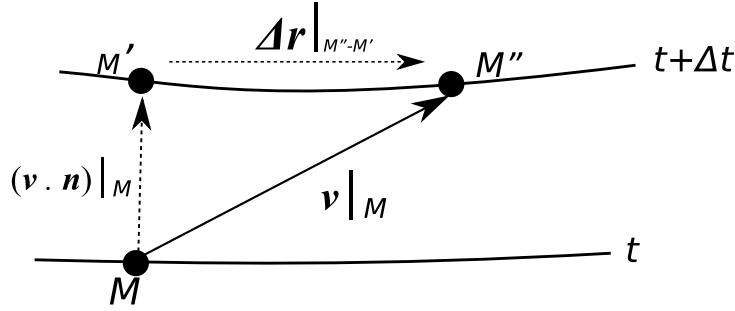


Figure 3.1: The interface at time  $t$  and  $t + \Delta t$ . The dots depict three fixed points in the laboratory frame:  $M$ ,  $M'$  and  $M''$ , respectively. The velocity evaluated on  $M$  is  $\mathbf{v}|_M$ .

$$\frac{d\Gamma}{dt} = \lim_{\Delta t \rightarrow 0} \frac{\Gamma(t + \Delta t)|_{M''} - \Gamma(t)|_M}{\Delta t} \quad (3.10)$$

The total time derivative of  $\Gamma$  is also given by:

$$\frac{d\Gamma}{dt} = \lim_{\Delta t \rightarrow 0} \frac{\Gamma(t + \Delta t)|_{M''} - \Gamma(t + \Delta t)|_{M'}}{\Delta t} + \lim_{\Delta t \rightarrow 0} \frac{\Gamma(t + \Delta t)|_{M'} - \Gamma(t)|_M}{\Delta t} \quad (3.11)$$

By definition, the normal time derivative is:

$$\frac{\partial \Gamma}{\partial t}|_n = \lim_{\Delta t \rightarrow 0} \frac{\Gamma(t + \Delta t)|_{M'} - \Gamma(t)|_M}{\Delta t} \quad (3.12)$$

The following notations are defined:  $\Delta \mathbf{r}|_{M''-M'} = \mathbf{r}|_{M''} - \mathbf{r}|_{M'}$  and  $\Delta \Gamma|_{M''-M'} = \Gamma|_{M''} - \Gamma|_{M'}$ . With these notations, an expression of  $\Gamma|_{M''}$  is given by:

$$\Gamma|_{M''} = \Gamma|_{M'} + \frac{\Delta \Gamma|_{M''-M'}}{\Delta \mathbf{r}|_{M''-M'}} \Delta \mathbf{r}|_{M''-M'} \approx \Gamma|_{M'} + \nabla_s \Gamma \cdot \Delta \mathbf{r}|_{M''-M'} \quad (3.13)$$

Injecting Eqs. (3.12) and (3.13) into Eq. (3.11) yields:

$$\frac{d\Gamma}{dt} = \frac{\partial \Gamma}{\partial t} \Big|_n + \lim_{\Delta t \rightarrow 0} \nabla_s \Gamma \cdot \frac{\Delta \mathbf{r}|_{M''-M'}}{\Delta t} \quad (3.14)$$

With the definition of  $\Delta \mathbf{r}|_{M''-M'}$  given above, one can deduce from Fig. 3.1 that  $\lim_{\Delta t \rightarrow 0} \frac{\Delta \mathbf{r}|_{M''-M'}}{\Delta t} = \mathbf{v}_s$ , where  $\mathbf{v}_s = \mathbf{v} - (\mathbf{v} \cdot \mathbf{n})\mathbf{n}$  is the liquid velocity tangent to the surface  $S$ . Thus, the following relationship is obtained:

$$\frac{d\Gamma}{dt} = \frac{\partial \Gamma}{\partial t} \Big|_n + \mathbf{v}_s \cdot \nabla_s \Gamma \quad (3.15)$$

In this way, we have expressed the Lagrangian time derivative of  $\Gamma$  (see Eq. (3.8)) in terms of a normal time derivative.

The second step in the derivation is to express the variation of the surface element,  $\frac{d}{dt} dS$  (see Eq. (3.8)). Stone (1990) showed that it can be expressed as:

$$\Gamma \frac{d}{dt} dS = \Gamma \nabla_s \cdot \mathbf{v} \quad (3.16)$$

As the procedure followed by Stone (1990),  $\mathbf{v}$  is decomposed as  $\mathbf{v} = \mathbf{v}_s + (\mathbf{v} \cdot \mathbf{n})\mathbf{n}$  and Eq. (3.16) yields:

$$\Gamma \frac{d}{dt} dS = \Gamma \nabla_s \cdot \mathbf{v}_s + \Gamma (\nabla_s \cdot \mathbf{n})(\mathbf{v} \cdot \mathbf{n}) \quad (3.17)$$

Injecting Eqs. (3.15) and (3.17) into Eq. (3.8) allows to recover the local form presented by Stone (1990):

$$\frac{\partial \Gamma}{\partial t} \Big|_n + \nabla_s \cdot (\Gamma \mathbf{v}_s) + \Gamma (\nabla_s \cdot \mathbf{n})(\mathbf{v} \cdot \mathbf{n}) = D_s \nabla_s^2 \Gamma + S_\Gamma \quad (3.18)$$

In this form, each term has an explicit physical interpretation. For example, the term  $\nabla_s \cdot (\Gamma \mathbf{v}_s)$  in Eq. (3.18) expresses the convective transport of  $\Gamma$  by the velocity tangent to the surface.  $D_s \nabla_s^2 \Gamma$  expresses the diffusion of  $\Gamma$  along the surface, from regions of higher values of  $\Gamma$  to regions of lower values of this variable. Finally,  $(\Gamma \nabla_s \cdot \mathbf{n})(\mathbf{v} \cdot \mathbf{n})$  is the product of the curvature of the surface (on a given point on the surface) with the normal component of the velocity field adjacent to the surface. The normal component of the velocity of the fluid adjacent to the surface changes the curvature of the interface (locally) and, for a given quantity of surfactants on the surface, this change in curvature dilutes or concentrates the surfactants. In the next subsection, an alternative formulation of Eq. (3.18) is derived which is convenient to solve using a fixed coordinate system.

### 3.4.3 The Eulerian form

The general form of the conservation equation is reminded (Eq. (3.8)):

$$\frac{d}{dt} \int_{S(t)} \Gamma dS \equiv \int_{S(t)} \frac{d\Gamma}{dt} dS + \int_{S(t)} \Gamma \frac{d}{dt} dS = \int_{S(t)} D_s \nabla_s^2 \Gamma dS + \int_{S(t)} S_\Gamma dS$$

The main feature of the form presented in this section is the way to evaluate the Lagrangian time derivative:  $\frac{d\Gamma}{dt}$  (see Eq. (3.8)). In fact, it is a form that is convenient to use when working with a fixed coordinate system. In this formulation, the Lagrangian time derivative of  $\Gamma$  is written in terms of an Eulerian partial time derivative. This necessitates a concept developed by Pereira and Kalliadasis (2008). This concept relies on extending the quantity  $\Gamma$  locally around the surface  $S$  and the time  $t$  to a field  $\tilde{\Gamma}$  so that when  $\tilde{\Gamma}$  is restricted to the surface  $S$ , it is equal to  $\Gamma$  at all time,  $t$ . The expression of the Lagrangian time derivative as a function of an Eulerian time derivative, proposed by Pereira and Kalliadasis (2008), is derived again here, using the same methodology as in the previous paragraph. Fig. 3.2 depicts 3 fixed points in the laboratory frame  $M$ ,  $M'$  and  $M''$ , respectively. At time  $t$ , the interface passes through the fixed point  $M$  and at time  $t + \Delta t$  it passes through the points  $M'$  and  $M''$ . The position vector  $\mathbf{r}$  localizes any points in a fixed coordinate system. The field  $\tilde{\Gamma}$  is defined as an arbitrary extension of  $\Gamma$  as follows:

1. At time  $t$ ,  $\Gamma$  is extended from  $M$ , which is on the surface  $S$ , towards the point  $M'$  to a field  $\tilde{\Gamma}$ . This field,  $\tilde{\Gamma}$ , has the property to be equal to  $\Gamma$  on the surface  $S$  and on the point  $M'$ . Those properties can be expressed with the following equation:  $\tilde{\Gamma}(t)|_M = \Gamma(t)|_M = \tilde{\Gamma}(t)|_{M'}$ .
2. At time  $t + \Delta t$ , the interface passes through the points  $M'$  and  $M''$ . Thus,  $\Gamma$  is defined on these points. Consequently, at  $t = t + \Delta t$  and on  $M''$  (on the surface,  $S$ ), the field  $\tilde{\Gamma}$  is equal to  $\Gamma$  which gives the following equation:  $\tilde{\Gamma}(t + \Delta t)|_{M''} = \Gamma(t + \Delta t)|_{M''}$ .
3. At time  $t + \Delta t$ , the interface passes through the points  $M'$  and  $M''$ . Thus,  $\Gamma$  is defined on these points. At time  $t = t + \Delta t$  and on  $M'$ ,  $\Gamma$  is extended from the surface  $S$  towards the point  $M$ , defining  $\tilde{\Gamma}$ . This can be expressed with the following equation:  $\tilde{\Gamma}(t + \Delta t)|_M = \Gamma(t + \Delta t)|_{M'}$ .

As it will be seen, the definition of the field  $\tilde{\Gamma}$  is necessary in order to express the Lagrangian time derivative of  $\Gamma$  in terms of an Eulerian time derivative.

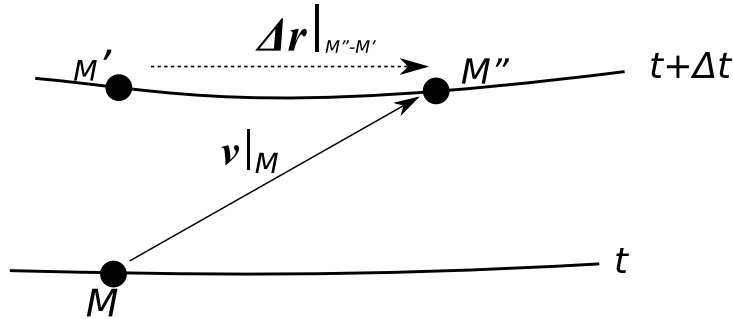


Figure 3.2: The interface at time  $t$  and  $t + \Delta t$

In order to express the Lagrangian time derivative of  $\Gamma$  in terms of an Eulerian time derivative, we begin by expressing the Eulerian partial time derivative of  $\tilde{\Gamma}$  at  $\mathbf{r}|_M$ :

$$\frac{\partial \tilde{\Gamma}}{\partial t}|_M = \lim_{\Delta t \rightarrow 0} \frac{\tilde{\Gamma}(t + \Delta t)|_M - \tilde{\Gamma}(t)|_M}{\Delta t} \quad (3.19)$$

Using the definition of  $\tilde{\Gamma}$ , the following equation is deduced from Eq. (3.19):

$$\frac{\partial \tilde{\Gamma}}{\partial t}|_M = \lim_{\Delta t \rightarrow 0} \frac{\Gamma(t + \Delta t)|_{M'} - \Gamma(t)|_M}{\Delta t} \quad (3.20)$$

This equation can be rewritten as:

$$\frac{\partial \tilde{\Gamma}}{\partial t}|_M = \lim_{\Delta t \rightarrow 0} \frac{\Gamma(t + \Delta t)|_{M''} - \Gamma(t)|_M}{\Delta t} + \lim_{\Delta t \rightarrow 0} \frac{\Gamma(t + \Delta t)|_{M'} - \Gamma(t + \Delta t)|_{M''}}{\Delta t} \quad (3.21)$$

It is noticed that  $\lim_{\Delta t \rightarrow 0} \frac{\Gamma(t+\Delta t)|_{M''} - \Gamma(t)|_M}{\Delta t} = \frac{d\Gamma}{dt}$ , which is the Lagrangian time derivative of  $\Gamma$ . Therefore:

$$\frac{\partial \tilde{\Gamma}}{\partial t} \Big|_M = \frac{d\Gamma}{dt} + \lim_{\Delta t \rightarrow 0} \frac{\Gamma(t+\Delta t)|_{M'} - \Gamma(t+\Delta t)|_{M''}}{\Delta t} \quad (3.22)$$

The right hand side of Eq. (3.22) is rewritten in terms of  $\tilde{\Gamma}$ :

$$\frac{\partial \tilde{\Gamma}}{\partial t} \Big|_M = \frac{d\Gamma}{dt} + \lim_{\Delta t \rightarrow 0} \frac{\tilde{\Gamma}(t+\Delta t)|_M - \tilde{\Gamma}(t+\Delta t)|_{M''}}{dt} \quad (3.23)$$

As in the previous paragraph the following notation is defined:  $\Delta \mathbf{r}|_{M''-M} = \mathbf{r}|_{M''} - \mathbf{r}|_M$ . A Serie Taylor expansion of  $\tilde{\Gamma}|_{M''}$  is given by:

$$\tilde{\Gamma}|_{M''} \approx \tilde{\Gamma}|_M + \nabla \tilde{\Gamma} \cdot \Delta \mathbf{r}|_{M''-M} \quad (3.24)$$

This allows to write Eq. (3.23) in the form:

$$\frac{\partial \tilde{\Gamma}}{\partial t} \Big|_M = \frac{d\Gamma}{dt} - \lim_{\Delta t \rightarrow 0} \frac{\nabla \tilde{\Gamma} \cdot \Delta \mathbf{r}|_{M''-M}}{\Delta t} \quad (3.25)$$

It is noticed that,  $\lim_{\Delta t \rightarrow 0} \frac{\Delta \mathbf{r}|_{M''-M}}{\Delta t} = \mathbf{v}|_M$ . Therefore, the total derivative of  $\Gamma$  can be expressed in terms of  $\tilde{\Gamma}$ :

$$\frac{d\Gamma}{dt} = \frac{\partial \tilde{\Gamma}}{\partial t} \Big|_M + \mathbf{v}|_M \cdot \nabla \tilde{\Gamma} \quad (3.26)$$

where  $M$  represents a fixed point in the laboratory frame. This is valid for any arbitrary extension of  $\Gamma$  from the interface  $S$  to the surrounding. As can be seen, the definition of a scalar field  $\tilde{\Gamma}$  allows to express the Lagrangian time derivative of  $\Gamma$ , which is defined only on the surface  $S$ , in terms of an Eulerian partial time derivative of  $\tilde{\Gamma}$  which is defined in the whole domain.

As a second step, the variation of the surface element, i.e.,  $\Gamma \frac{d}{dt} dS$  (see Eq. (3.8)) is expressed, as in the previous section as:

$$\Gamma \frac{d}{dt} dS = \Gamma \nabla_s \cdot \mathbf{v} \quad (3.27)$$

It can be shown that:

$$\nabla_s \cdot \mathbf{v} = \nabla \cdot \mathbf{v} - \mathbf{n} \cdot \nabla \mathbf{v} \cdot \mathbf{n} \quad (3.28)$$

Injecting Eq. (3.26) and (3.28) into Eq. (3.8) leads to:

$$\frac{\partial \tilde{\Gamma}}{\partial t} \Big|_M + \mathbf{v} \cdot \nabla \tilde{\Gamma} + \Gamma \nabla \cdot \mathbf{v} - \Gamma \mathbf{n} \cdot (\nabla \mathbf{v}) \cdot \mathbf{n} = D_s \nabla_s^2 \Gamma + S_\Gamma \quad (3.29)$$

Eq. (3.29) describes the transport of  $\Gamma$  on  $S$ , and expresses the Lagrangian time derivative of  $\Gamma$  in terms of the Eulerian partial time derivative of  $\tilde{\Gamma}$ , which is an arbitrary extension of  $\Gamma$ . In other words, in order to calculate the Lagrangian time derivative of a quantity  $\Gamma$  associated to a moving and deforming surface,  $d\Gamma/dt$ , an intermediate scalar is defined,  $\tilde{\Gamma}$ . This field has the property to be defined on the surface and on its surrounding and to be equal to  $\Gamma$  on the surface. In this way, it is possible to calculate  $d\Gamma/dt$  in terms on an Eulerian time derivative,  $\frac{\partial \tilde{\Gamma}}{\partial t} \Big|_M$ , where  $M$  is a fixed point in the laboratory frame of reference. Eq. (3.29) is not useful as it is. It is extended at the vicinity of the surface  $S$ , i.e., it is rewritten in terms of  $\tilde{\Gamma}$ :

$$\frac{\partial \tilde{\Gamma}}{\partial t} \Big|_M + \nabla \cdot (\mathbf{v} \tilde{\Gamma}) - \tilde{\Gamma} \mathbf{n} \cdot (\nabla \mathbf{v}) \cdot \mathbf{n} = D_s \nabla_s^2 \tilde{\Gamma} + S_{\tilde{\Gamma}} \quad (3.30)$$

It should be understood that, in this formulation, the transport of  $\Gamma$  is dealt by (i) expressing the Lagrangian time



derivative of  $\Gamma$  in terms of an Eulerian partial derivative of  $\tilde{\Gamma}$  and (ii) by extending Eq. (3.29) at the interface vicinity to have an equation with one variable only. Eq. (3.30) is the one that is used in this thesis. We emphasize on the fact that Eqs. (3.18 and 3.30) are two equivalent way to express the transport of a quantity along a moving and deforming interface.

### 3.5 Surfactant transport in the liquid bulk

The transport equation for the surfactants inside the liquid, for an incompressible fluids, is:

$$\left. \frac{\partial C_c}{\partial t} \right|_M + \mathbf{v} \cdot \nabla C_c = D_c \nabla^2 C_c \quad (3.31)$$

where  $C_c$  is the molar concentration of surfactants in the liquid and  $D_c$  is the diffusion coefficient of the surfactant inside the liquid. At the interface, the surfactant adsorbs on the surface which gives the following boundary condition:

$$\mathbf{n} \cdot \nabla C_c = S_\Gamma \quad (3.32)$$

### 3.6 Surface equation of state

It is assumed that the surface tension depends on the surfactant concentration on the interface according to an equation of state derived from the Langmuir adsorption isotherm (Levich (1962)):

$$\sigma = \sigma_0(T) + RT\Gamma_\infty \ln \left( 1 - \frac{\Gamma}{\Gamma_\infty} \right) \quad (3.33)$$

where  $R$  is the ideal gas constant,  $T$  is the absolute temperature,  $\sigma_0$  is the surface tension of the clean interface at the temperature  $T$ , and  $\Gamma_\infty$  is the maximum packing concentration of surfactants on the interface.

### 3.7 Conclusion

In this chapter, the system of equations to solve for the description of the motion of a bubble inside a microchannel in the presence of surfactants have been presented. A particular attention was held on the equation governing the transport of the surfactant concentration,  $\Gamma$ , on the bubble interface. Two different forms of this equation was presented, the difference between these two equations being the way to write the Lagrangian time derivative of  $\Gamma$ . The expression presented by Pereira and Kalliadasis (2008) allowing to write the Lagrangian time derivative of  $\Gamma$  in terms of an Eulerian partial time derivative has been derived. Finally, the equation governing the transport of surfactants on the bubble surface has been rewritten in terms of this Eulerian partial time derivative.

In the next chapter, the numerical code used to solve this system is presented. In particular, the implementation of the following equations and methodologies is presented:

1. An Eulerian formulation of the surfactant transport equation on the bubble surface.
2. A numerical methodology to account for the adsorption of surfactants towards the bubble surface.
3. A numerical methodology to compute the Marangoni stresses induced by surfactant concentration gradients

## CHAPTER 4

### The numerical code JADIM-LS

#### 4.1 Numerical methods for multiphase flows

The simulation of two phase dispersed flows is an active area of research and a tool in industry to analyze and design various processes. The methods for simulating dispersed two phase flows can be classified within “Front tracking” methods and “Volume tracking” methods. In the former case, the interface separating two phases is tracked explicitly through the use of markers associated to the interface (Unverdi and Tryggvason (1992); Popinet and Zaleski (1999)). Those method allow to calculate the geometric properties of the interface (its normal and its curvature) with a high accuracy, and the needs in terms of computational power is not too demanding. However, the extension of these methods to three dimensional flow configuration is difficult.

In Volume tracking methods, the interface between two fluids is defined implicitly by the means of a scalar field or the use of volumetric markers (Harlow and Welch (1965)). The transport of the interface is achieved through the transport of this scalar (or of these markers) within a fixed computational mesh. Within volume tracking methods, the well known Volume of Fluid (VOF) method has been used thoroughly to simulate various dispersed two phase flow (Hirt and Nichols (1981)). More specifically, the VOF method has been used to characterize several features of two phase dispersed flows in microchannels. For example, Khodaparast *et al.* (2015) performed experiments and numerical simulations using the VOF method, to characterize the hydrodynamics of small bubbles inside horizontal microchannels. They characterized the bubble velocity and shape as a function of  $Ca$ . Other works used VOF simulations to analyze the flow field in a Taylor flow inside microchannels (Taha and Cui (2006)). The mass transfer from Taylor bubbles towards the surrounding liquid and the flow boiling has also been investigated using VOF simulations (van Baten and Krishna (2004); Hassanvand and Hashemabadi (2012); Magnini and Thome (2016)). This method is well-known for its property allowing to conserve mass. However, it was pointed out that this method suffers from the generation of non-physical spurious currents. It was shown that the generation of these currents was due to errors in the calculation of the curvature of the interface, those errors being advected along with the interface, and possibly amplified after advection of the interface (Abadie *et al.* (2015)). This feature was tackled to some extent, for instance, by using a smoothing procedure when calculating the normal to the interface (Dupont and Legendre (2010)).

However, the Level-set method (LS) was shown to achieve a better calculation of the geometrical properties of the interface in some cases (Sussman *et al.* (1994, 1998)). This has a considerable importance for the simulation of microscale two phase flows. In microscale flows, viscous forces and surface tension forces are dominant when compared to inertial and buoyancy forces. Thus, the correct calculation of the surface tension forces are necessary to identify and characterize the main features of these flows. For example Abadie *et al.* (2015) showed that, at small  $Ca$ , i.e., when surface tension forces are dominant, the VOF method, coupled with the Continuum Surface Force (CSF) model for calculating surface tension forces and with the Flux Corrected Transport (FCT) scheme for advecting the interface, fails in predicting the correct flow pattern in a fully developed Taylor flow, as illustrated in Fig. 4.1. In this figure, the streamlines of a fully developed Taylor flow taking place inside a cylindrical tube at  $Ca = 0.005$  calculated using a VOF method (top) and Level-set method (bottom) are depicted. In the VOF method, an additional recirculation loop near the spherical cap of the bubble in the liquid is visible. It was shown that this additional loop arises from the generation of spurious current, through the coupled effect of inexact

curvature calculation and interface advection. This loop is not present in the Level-set simulation. This in turn has

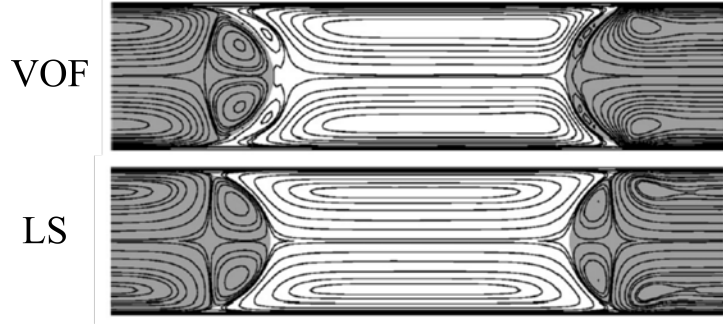


Figure 4.1: Streamlines in Taylor flow in a microchannel at  $Ca = 0.005$ , (top): VOF model, (bottom): Level-set model (adapted from Abadie *et al.* (2015))

an important influence when calculating the slip velocity, i.e.,  $W = (U - J_l)/U$ , where  $U$  and  $J_l$  are the bubble velocity and the mean flow velocity, respectively. This is illustrated in Fig. 4.2. In this figure, the slip velocity

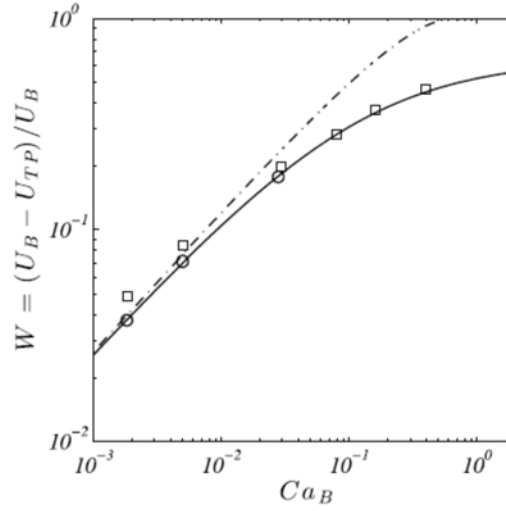


Figure 4.2: Slip velocity of the Taylor bubble as a function of  $Ca_b$  for VOF simulations (squares) and Level-set simulations (circles) (taken from Abadie *et al.* (2015)). The dashed-dotted line gives values of the theoretical prediction of Bretherton (1961) while the solid line gives value of the correlation of Aussillous and Quéré (2000).

of the Taylor bubble was calculated as a function of  $Ca_B = \mu U / \sigma$ , for VOF simulations (squares) and Level-set simulations (circles). The solid line is a correlation predicting  $W$  as a function of  $Ca$  proposed by Aussillous and Quéré (2000), and the dashed line is the theoretical prediction of Bretherton (1961). As quantitatively observed on Fig. 4.2, the Level-set method implemented in JADIM allows a more accurate description of the dynamics of Taylor flow than the VOF-CSF-FCT at low values of  $Ca_b$ , i.e., in surface tension dominated situations.

The natural choice for simulating two phase flows with soluble surfactants would be a Front Tracking method where a mesh associated to the interface is present. In this way, the location of the interface would be defined explicitly and surfactants would be straightforwardly transported along this mesh, for example, with the use of Eq. (3.18). However, it will be shown that the Level set method is also well suited for describing two phase flows with soluble surfactants. In particular, in Chapter 5, we provide a comparison of the results obtained within this thesis with the Level-set method and results of the literature that use a Front Tracking method in the case of a bubble rising in a liquid of infinite extent that contains surfactants.

In this chapter, a brief introduction to JADIM is presented, followed by the presentation of the Level-set modulus of JADIM. The contribution of this thesis to JADIM is presented in the third section. In particular, the numerical method allowing to solve the equations presented in Chap. (3) regarding the transport of surfactants on a moving interface (Eq. (3.29)), the source term in the surfactant transport equation inside the liquid phase (Eq. 3.32)), and the Marangoni stress (Eq. (3.6)) are presented. The spatial and time discretization schemes are presented.

## 4.2 The JADIM code

The numerical code used to solve the equations presented in the previous section is the JADIM code, which has been developed at IMFT. It has been developed to simulate dispersed two-phase flows including hydrodynamics and transfer phenomena around spherical bubbles (Legendre (1996)) and deformable interfaces with a VOF technique (Benkenida (1999)), and later with a Level-set method (Abadie *et al.* (2015)). These methods, and in particular the VOF, and more recently the Level-set method, for computing moving interfaces on a fixed grid, have been validated and used to simulate various multiphase flow systems (Benkenida (1999); Bonometti and Magnaudet (2007); Haroun *et al.* (2010); Dupont and Legendre (2010); Legendre and Maglio (2013); Abadie *et al.* (2012, 2015)). In the VOF and the Level-set methods, the interface is captured by an Eulerian description of each phase on a fixed grid with variable density and viscosity.

### 4.2.1 One fluid formulation

Under the assumptions that (i) the fluids are Newtonian and incompressible, (ii) there is no mass transfer through the interface, (iii) the flow is isothermal, the velocity field  $\mathbf{v}$  and the pressure  $p$  satisfy the classical one-fluid formulation of the Navier–Stokes equations (Scardovelli and Zaleski (1999)):

$$\frac{\partial \mathbf{v}}{\partial t} + \mathbf{v} \cdot \nabla \mathbf{v} = -\frac{1}{\rho} \nabla p + \frac{1}{\rho} \nabla \cdot \bar{\mathbf{T}} + F_{\sigma,c} \delta_I + F_{\sigma,m} \delta_I \quad (4.1)$$

$$\nabla \cdot \mathbf{v} = 0 \quad (4.2)$$

$$\mu = \mu_c (1 - F) + \mu_d F \quad (4.3)$$

$$\rho = \rho_c (1 - F) + \rho_d F \quad (4.4)$$

where  $\bar{\mathbf{T}} = \mu \left( \nabla \mathbf{v} + (\nabla \mathbf{v})^T \right)$  is the viscous stress tensor;  $\rho$ ,  $\mu$ ,  $\sigma$  are the density, the dynamic viscosity and the surface tension, respectively;  $\mathbf{n}$  is a unit vector normal to the interface, arbitrarily chosen pointing towards the liquid phase and  $\delta_I$  is the Dirac distribution associated to the interface. In this formulation, the capillary contribution,  $F_{\sigma,c} = -\frac{\sigma}{\rho} (\nabla \cdot \mathbf{n}) \mathbf{n}$ , and the Marangoni stress,  $F_{\sigma,m} = -\frac{1}{\rho} \nabla_s \sigma$ , appear as volumetric forces acting at the interface vicinity. The local viscosity and density,  $\mu$  and  $\rho$ , are calculated from the volume fraction of the gas phase,  $F$ , by a linear interpolation as shown on Eqs. (4.3) and (4.4), where  $\mu_c$ ,  $\mu_d$ ,  $\rho_c$  and  $\rho_d$  are the viscosity and density of the liquid ( $c$ ) and gas ( $d$ ) phases, respectively. An harmonic mean between the viscosity (or density) of the liquid and of the gas is sometime used to calculate the viscosity associated to the computational cells that contain the interface. However, in the presence of Marangoni stresses on the interface, it has been shown that the harmonic mean of the viscosity of each phase does not give the correct jump in tangent viscous stress at the interface, i.e.,  $\sum_k (\bar{\mathbf{T}}_k \cdot \mathbf{n}_k) \cdot \mathbf{t}_k = \nabla_s \sigma \cdot \mathbf{t}_k$  (Hayashi and Tomiyama (2012)).

### 4.2.2 The projection method

The projection method is used to solve the Navier–Stokes equation, i.e., Eq. (4.1) together with the continuity equation, i.e., Eq. (4.2). This method is presented here for an explicit time scheme. An intermediate velocity field,  $\tilde{\mathbf{v}}$ , is first calculated at time  $t = (n + 1) \Delta t$ ; with  $n$  the number of time step  $\Delta t$ :

$$\frac{\tilde{\mathbf{v}}^{n+1} - \mathbf{v}^n}{\Delta t} = -(\mathbf{v} \cdot \nabla \mathbf{v})^n - \frac{1}{\rho} \nabla p^n + \left( \frac{1}{\rho} \nabla \cdot \bar{\mathbf{T}} \right)^n + (F_{\sigma,c} \delta_I)^n + (F_{\sigma,m} \delta_I)^n \quad (4.5)$$

This intermediate velocity does not satisfy the continuity equation. To calculate the divergence free velocity field, an auxiliary potential is introduced,  $\Phi$ :

$$\frac{\mathbf{v}^{n+1} - \tilde{\mathbf{v}}^{n+1}}{\Delta t} = -\frac{1}{\rho} \nabla \Phi^{n+1} \quad (4.6)$$

The divergence of this equation is taken and  $\nabla \cdot \mathbf{v}^{n+1} = 0$  is injected to obtain the equation that gives  $\Phi^{n+1}$ :

$$-\nabla \cdot \frac{1}{\rho} \nabla \Phi^{n+1} = \frac{1}{\Delta t} \nabla \cdot \tilde{\mathbf{v}}^{n+1} \quad (4.7)$$

Solving Eq. (4.7) gives the field  $\Phi^{n+1}$  from which the pressure is obtained:

$$p^{n+1} = p^n + \Phi^{n+1} \quad (4.8)$$

and the velocity field at time  $t = (n + 1) \Delta t$  is deduced from the updated pressure field:

$$\frac{\mathbf{v}^{n+1} - \mathbf{v}^n}{\Delta t} = -(\mathbf{v} \cdot \nabla \mathbf{v})^n - \frac{1}{\rho} \nabla p^{n+1} + \left( \frac{1}{\rho} \nabla \cdot \bar{\mathbf{T}} \right)^n + (F_{\sigma,c} \delta_I)^n + (F_{\sigma,m} \delta_I)^n \quad (4.9)$$

### 4.2.3 The Level-set method

The Level-set method was introduced in JADIM by Abadie (2013). In this method, the location of each phase with respect to the interface is given by the signed distance function to the interface (or Level-set function),  $\phi(\mathbf{x}, t)$ . This distance function obeys to the following transport equation (Osher and Sethian (1988)):

$$\frac{\partial \phi}{\partial t} + \mathbf{v} \cdot \nabla \phi = 0 \quad (4.10)$$

In this work,  $\phi$  is defined as being positive in the gas phase and negative in the liquid phase. A classical redistancing equation is applied to the Level-set function at each time step:

$$\frac{\partial \phi}{\partial \tau} + \text{sign}(\phi)(|\nabla \phi| - 1) = 0 \quad (4.11)$$

where  $\tau$  is a fictitious time. The sign function is (Xu and Zhao (2003)):

$$\text{sign}(\phi(\mathbf{x}, t)) = \frac{\phi}{\sqrt{\phi^2 + \Delta x^2}} \quad (4.12)$$

where  $\Delta x$  is the grid size.

The normal to the interface,  $\mathbf{n}$ , and its curvature,  $\kappa$ , are computed with the Level-set function as follows:

$$\mathbf{n} = -\frac{\nabla\phi}{\|\nabla\phi\|} \quad (4.13)$$

$$\kappa = -\nabla \cdot \left( \frac{\nabla\phi}{\|\nabla\phi\|} \right) \quad (4.14)$$

where  $\mathbf{n}$  is pointing towards the liquid phase. The tangent to the interface,  $\mathbf{t}$ , is calculated such that  $\mathbf{t} \cdot \mathbf{n} = 0$ . Its specific calculation will be presented in the fifth chapter, in the case of an axisymmetric geometry. The volume fraction of the gas phase,  $F$ , in a given computational cell is computed from the Level-set function using a smooth Heaviside function:

$$F = H(\phi) = \begin{cases} 0 & \text{if } \phi(\mathbf{x}) < -\epsilon \\ \frac{1}{2} \left( 1 + \frac{\phi}{\epsilon} + \frac{1}{\pi} \sin\left(\frac{\pi\phi}{\epsilon}\right) \right) & \text{if } -\epsilon < \phi(\mathbf{x}) < \epsilon \\ 1 & \text{if } \phi(\mathbf{x}) > \epsilon \end{cases} \quad (4.15)$$

where  $\epsilon = \sqrt{2}\Delta x$  is the half numerical thickness of the interface.

#### 4.2.4 Spatial discretization

##### Navier stokes solver

Eqs. (4.1) and (4.2) are discretized on staggered grids using a finite volume method. The spatial derivative are discretized using second order centered schemes (Magnaudet *et al.* (1995); Legendre and Magnaudet (1998)). The staggered grids are depicted in Fig. 4.3. In this figure, the black cells are the cells centered on pressure points, which are called “pressure cells”, the green cells are the cells centered on  $u$ , and the red cells are the cells centered on  $v$ , where  $u = \mathbf{e}_x \cdot \mathbf{v}$  and  $v = \mathbf{e}_y \cdot \mathbf{v}$ , where  $\mathbf{e}_x$  and  $\mathbf{e}_y$  are the unit vector associated to the Cartesian mesh (see Fig. 4.3).

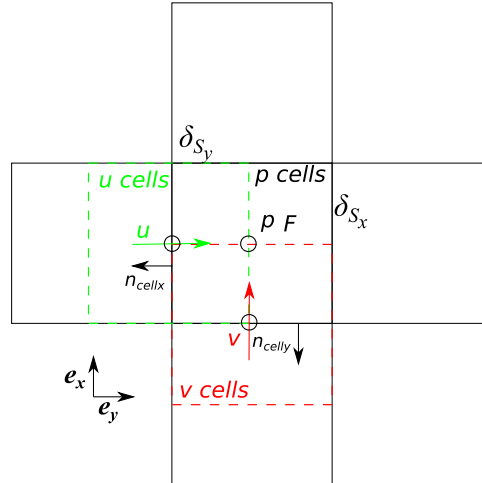


Figure 4.3: Staggered grids in JADIM for 2D. The position of the pressure,  $p$ , the volume fraction,  $F$ , and the  $x$  and  $y$  components of the velocity,  $u$  and  $v$ , respectively, are indicated as circles in this figure. The pressure cells are drawn in black, the velocity cells are drawn in green and red for the  $u$  and  $v$  components respectively.

In JADIM, the interfacial stresses are calculated as volumetric forces acting at the vicinity of the interface,

following the method of Brackbill *et al.* (1992). The capillary pressure jump,  $F_{\sigma,c}$ , is calculated, in the Level-set framework as follows (Abadie *et al.* (2015)):

$$F_{\sigma,c} = -\frac{\bar{\sigma}}{\rho V_p} \nabla F \int_{\delta_S} \left( \frac{\nabla \phi}{\|\nabla \phi\|} \right) \cdot \mathbf{n}_{cell} dS \quad (4.16)$$

where  $\bar{\sigma}$  is the average value of the surface tension in the cell centered on the velocity points,  $\nabla F$  is the average value of  $\nabla F$  in the cell centered on the velocity points,  $V_p$  is the volume of the pressure cell,  $\delta_S = 2\delta_{Sx} + 2\delta_{Sy}$  denotes the surface of the faces of a pressure cell and  $\mathbf{n}_{cell}$  is the unit normal to the faces of the pressure cell.

### Transport of the Level-set function

The advective terms are discretized using a conservative form of the fifth order WENO scheme (Liu *et al.* (1994); Couderc (2007)). It is based on the fact that the velocity field is divergence free:  $\mathbf{v} \cdot \nabla \phi = \nabla \cdot (\phi \mathbf{v})$ . Integrating in the control volume centered on the pressure cells yields:  $\int_{V_p} \nabla \cdot (\phi \mathbf{v}) dV_p = \int_{\delta_S} \mathbf{n} \cdot (\phi \mathbf{v}) dS$ , with  $\int_{\delta_S} \mathbf{n} \cdot (\phi \mathbf{v}) dS$  being approximated as:

$$\int_{\delta_S} \mathbf{n} \cdot (\phi \mathbf{v}) dS \approx Q_x + Q_y \quad (4.17)$$

where  $Q_x$ ,  $Q_y$ , are the fluxes over the cell faces having the normals  $\mathbf{n}_{cellx}$  and  $\mathbf{n}_{celly}$ , respectively (see Fig. 4.3). The fluxes over the cell faces are computed using the conservative form of the fifth order WENO scheme (WENO5c) which allows better mass conservation than the classical WENO5 scheme (Couderc (2007)). The algorithm of this scheme is shown for the  $x$  spatial direction and at a given time  $t = n\Delta t$ , the extension to the other direction being straightforward. The fluxes across the cell faces with the normal  $x$  is  $Q_x = Q_{i+\frac{1}{2}} - Q_{i-\frac{1}{2}}$ . The fluxes  $Q_{i+\frac{1}{2}}$  and  $Q_{i-\frac{1}{2}}$ , where  $i$  is an indice along the  $x$  direction for the center of the pressure cells, are computed using an upwind formulation:

$$Q_{i+\frac{1}{2}} = \begin{cases} u_{i+\frac{1}{2}} \phi_{i-1}^+ & \text{if } u_{i+\frac{1}{2}} > 0 \\ u_{i+\frac{1}{2}} \phi_i^- & \text{if } u_{i+\frac{1}{2}} < 0 \end{cases} \quad (4.18)$$

The values  $\phi_i^\pm$  are computed by weighting the values  $\phi_i$  around the cell face of interest on three stencils

$$\phi_i^\pm = \omega_0^\pm \phi_i^{\pm 0} + \omega_1^\pm \phi_i^{\pm 1} + \omega_2^\pm \phi_i^{\pm 2} \quad (4.19)$$

The  $+$  or  $-$  signs refer to the upwind direction that is chosen to build the stencils and the values  $\omega_0^\pm \phi_i^{\pm 0,1,2}$

$$\begin{cases} \phi_{i+\frac{1}{2}}^{\pm 0} = \frac{1}{3} r_1^\pm - \frac{7}{6} r_2^\pm + \frac{11}{6} r_3^\pm \\ \phi_{i+\frac{1}{2}}^{\pm 1} = -\frac{1}{6} r_2^\pm + \frac{5}{6} r_3^\pm + \frac{1}{3} r_4^\pm \\ \phi_{i+\frac{1}{2}}^{\pm 2} = +\frac{1}{3} r_3^\pm + \frac{5}{6} r_4^\pm - \frac{1}{6} r_5^\pm \end{cases} \quad (4.20)$$

where  $r^\pm$  are given by

$$\begin{cases} r_1^- = \phi_{i-2,j}, r_1^+ = \phi_{i+3,j}, r_2^- = \phi_{i-1,j}, r_2^+ = \phi_{i+2,j}, r_3^- = \phi_{i,j} \\ r_3^+ = \phi_{i+1,j}, r_4^- = \phi_{i+1,j}, r_4^+ = \phi_{i,j}, r_5^- = \phi_{i+2,j}, r_5^+ = \phi_{i-1,j} \end{cases} \quad (4.21)$$

where the weights  $\omega_0^\pm, \omega_1^\pm, \omega_2^\pm$  are given by

$$\begin{cases} \omega_0^\pm = \frac{\alpha_0^\pm}{\alpha_0^\pm + \alpha_1^\pm + \alpha_2^\pm} \\ \omega_1^\pm = \frac{\alpha_1^\pm}{\alpha_0^\pm + \alpha_1^\pm + \alpha_2^\pm} \\ \omega_2^\pm = \frac{\alpha_2^\pm}{\alpha_0^\pm + \alpha_1^\pm + \alpha_2^\pm} \end{cases} \quad (4.22)$$

so that the weighting is consistent,  $\omega_0^\pm + \omega_1^\pm + \omega_2^\pm = 1$ , and where  $\alpha_0^\pm, \alpha_1^\pm, \alpha_2^\pm$  given by

$$\begin{cases} \alpha_0^\pm = \frac{1}{10} \left( \frac{1}{\epsilon + IS_0^\pm} \right)^2 \\ \alpha_1^\pm = \frac{6}{10} \left( \frac{1}{\epsilon + IS_1^\pm} \right)^2 \\ \alpha_2^\pm = \frac{3}{10} \left( \frac{1}{\epsilon + IS_2^\pm} \right)^2 \end{cases} \quad (4.23)$$

where  $\epsilon$  is generally fixed to  $10^{-6}$  to avoid the denominator to be null, and where the  $IS^\pm$  represent the regularity indicators:

$$\begin{cases} IS_0^\pm = \frac{13}{12} (q_1^\pm - 2q_2^\pm + q_3^\pm)^2 + \frac{1}{4} (q_1^\pm - 4q_2^\pm + 3q_3^\pm)^2 \\ IS_1^\pm = \frac{13}{12} (q_2^\pm - 2q_3^\pm + q_4^\pm)^2 + \frac{1}{4} (q_2^\pm - q_4^\pm)^2 \\ IS_2^\pm = \frac{13}{12} (q_3^\pm - 2q_4^\pm + q_5^\pm)^2 + \frac{1}{4} (3q_3^\pm - 4q_4^\pm + q_5^\pm)^2 \end{cases} \quad (4.24)$$

### Redistanciation of the Level-set function

The redistanciation equation, Eq. (4.11), is discretized using the classical fifth order WENO scheme (WENO5) (Liu *et al.* (1994)). It is presented in appendix.

### 4.2.5 Temporal discretization

The time scheme used to compute the advective terms in Eqs. (4.1), (4.10), (4.11) is a third-order Runge–Kutta scheme. The viscous stresses in Eq. (4.1) are computed using a semi-implicit Crank–Nicolson method (Magnaudet *et al.* (1995); Legendre and Magnaudet (1998)).

## 4.3 Numerical methodology to account for surfactants

The Level-set modulus of JADIM deals with the transport of the interface in an Eulerian framework, i.e., in a fixed mesh. Thus, it is the Eulerian formulation of the surfactant transport equation on a surface, Eq. (3.29), that is used to transport surfactants on the surface. Furthermore, as the computational mesh is fixed, it is a challenge to deal with soluble surfactants. In fact, the boundary condition of the surfactant transport equation inside the bulk phase, i.e., Eq. (3.32), needs to be evaluated in the liquid in contact with the surface. However, there is no grid points attached to the surface in the Level-set method implemented in JADIM. Muradoglu and Tryggvason (2008) first



proposed a method to consider soluble surfactants using a front tracking method. This method was extended for volume tracking methods by Hayashi and Tomiyama (2012). The method they propose, though approximate, is implemented, validated and used in this work for simulating soluble surfactants.

The Marangoni stress, induced by surfactant concentration gradients on the surface, is computed using the classical Continuum Surface Force model developed by Brackbill *et al.* (1992).

In the following sections, the numerical methods used to deal with surfactants are presented, including the spatial and temporal discretization schemes.

#### 4.3.1 Transport of surfactants on the surface

As seen in Chapter 3, in an Eulerian description of a gas-liquid interface, and for incompressible fluids, the transport equation of surfactants on the interface is given by:

$$\left. \frac{\partial \tilde{\Gamma}}{\partial t} \right|_M + \mathbf{v} \cdot \nabla \tilde{\Gamma} - \tilde{\Gamma} \mathbf{n} \cdot (\nabla \mathbf{v}) \cdot \mathbf{n} = D_s \nabla_s^2 \tilde{\Gamma} + S_{\tilde{\Gamma}} \quad (4.25)$$

where  $\tilde{\Gamma}$  is an arbitrary extension of  $\Gamma$ , the surfactant concentration field on the interface and where  $S_{\tilde{\Gamma}} = k_a C_I (\Gamma_\infty - \tilde{\Gamma}) - k_d \tilde{\Gamma}$ . The extension is performed perpendicularly to the interface by solving the following Partial Differential Equation (PDE) after each physical time step of the numerical procedure, with the initial condition  $\tilde{\Gamma}^*(\mathbf{x}, \tau = 0) = \tilde{\Gamma}(\mathbf{x}, t)$  (Xu and Zhao (2003)):

$$\frac{\partial \tilde{\Gamma}^*}{\partial \tau} + \text{sign}(\phi) \frac{\nabla \phi}{\|\nabla \phi\|} \cdot \nabla \tilde{\Gamma}^* = 0 \quad (4.26)$$

where  $\tau$  is a fictitious time. As pointed out by Xu and Zhao (2003), it has been observed that 5 iterations are sufficient when solving Eq. (4.26), for  $\tilde{\Gamma}^*$  to reach its converged values with respect to  $\tau$ . Indeed, we have checked that the relative variation of the values of  $\tilde{\Gamma}^*$  is less than 0.5% when the number of fictitious-time step was increased from 4 to 8. Eqs. (4.25 and 4.26) are solved together to achieve the transport of  $\Gamma$  along the gas-liquid interface.

#### Temporal schemes

A third order Runge-Kutta (RK3) scheme is used to discretize Eqs. (4.25) and (4.26) with respect to time. The application of this scheme to Eq. (4.25) is presented. Using the following notation:  $L(\tilde{\Gamma}) = \frac{\partial \tilde{\Gamma}}{\partial t}$ , this scheme can be written as follows:

$$\begin{cases} \tilde{\Gamma}^1 = \tilde{\Gamma}^m + \Delta t L(\tilde{\Gamma}^m) \\ \tilde{\Gamma}^2 = \frac{3}{4} \tilde{\Gamma}^m + \frac{1}{4} (\tilde{\Gamma}^1 + L(\tilde{\Gamma}^1)) \\ \tilde{\Gamma}^{m+1} = \frac{1}{3} \tilde{\Gamma}^m + \frac{2}{3} (\tilde{\Gamma}^2 + L(\tilde{\Gamma}^2)) \end{cases} \quad (4.27)$$

with  $0 \leq m \leq 2$ , is the number of intermediate time step within a physical time step of the numerical procedure.

## Spatial discretization

**Expansion term:** The spatial discretization of the expansion term is performed using a centered scheme. In a Cartesian mesh, it is computed as follows:

$$\mathbf{n} \cdot \nabla \mathbf{v} \cdot \mathbf{n} = n_x^2 \frac{du}{dx} + n_y^2 \frac{dv}{dy} + n_x n_y \frac{du}{dy} + n_x n_y \frac{dv}{dx} \quad (4.28)$$

where  $n_x$  and  $n_y$  are the  $x$  and  $y$  components of  $\mathbf{n}$ , i.e.,  $n_x = \mathbf{n} \cdot \mathbf{e}_x$  and  $n_y = \mathbf{n} \cdot \mathbf{e}_y$ . A staggered grid is used in JADIM where the pressure ( $p$ ), the Level-set function ( $\phi$ ), the surface concentration ( $\tilde{\Gamma}$ ) are defined on the center of the central grid ( $i, j$ ), the  $x$  component of the velocity vector ( $u$ ) is defined on the cell faces having their normal along  $x$ , and the  $y$  component of the velocity ( $v$ ) is defined on the cell faces having their normal along  $y$ . In this configuration the derivatives are computed as:

$$\frac{du}{dx} \approx \frac{u_{i+\frac{1}{2},j} - u_{i-\frac{1}{2},j}}{\Delta x} \quad (4.29)$$

$$\frac{dv}{dy} \approx \frac{v_{i,j+\frac{1}{2}} - v_{i,j-\frac{1}{2}}}{\Delta y} \quad (4.30)$$

$$\frac{du}{dy} \approx \frac{u_{i,j+\frac{1}{2}} - u_{i,j-\frac{1}{2}}}{\Delta y} \quad (4.31)$$

$$\frac{dv}{dx} \approx \frac{v_{i+\frac{1}{2},j} - v_{i-\frac{1}{2},j}}{\Delta x} \quad (4.32)$$

where

$$u_{i,j+\frac{1}{2}} = \frac{1}{4} \left( u_{i+\frac{1}{2},j} + u_{i+\frac{1}{2},j+1} + u_{i-\frac{1}{2},j} + u_{i-\frac{1}{2},j+1} \right) \quad (4.33)$$

and

$$u_{i,j-\frac{1}{2}} = \frac{1}{4} \left( u_{i+\frac{1}{2},j} + u_{i+\frac{1}{2},j-1} + u_{i-\frac{1}{2},j} + u_{i-\frac{1}{2},j-1} \right) \quad (4.34)$$

The location of  $u_{i,j+\frac{1}{2}}$  is depicted on Fig.(4.4).

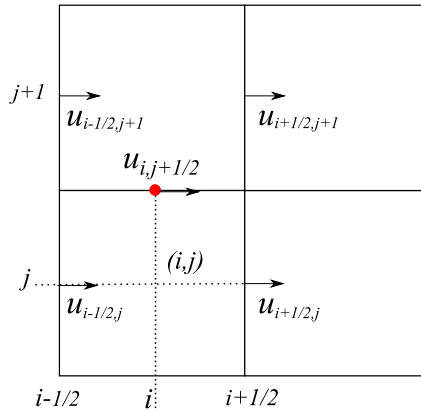


Figure 4.4: Location of  $u_{i,j+\frac{1}{2}}$ .

**Advection term:** The spatial discretization of the advection term,  $\mathbf{v} \cdot \nabla \tilde{\Gamma}$ , is done in a conservative manner using the fact that the velocity field is divergence free:

$$\mathbf{v} \cdot \nabla \tilde{\Gamma} = \nabla \cdot (\tilde{\Gamma} \mathbf{v}) \quad (4.35)$$

Integrating in the control volume centered on the pressure cells yields:

$$\int_V \nabla \cdot (\tilde{F} \mathbf{v}) dV = \int_{S_{\text{cell}}} \mathbf{n} \cdot (\mathbf{v} \tilde{F}) dS_{\text{cell}} \approx Q_x^F + Q_y^F \quad (4.36)$$

The mass fluxes over the cell faces,  $Q_x^F$  and  $Q_y^F$  are computed using the WENO5c scheme. This scheme was presented in section 4.2.4 for fluxes of momentum.

**Diffusion along the surface:** The term accounting for the diffusion along the surface is rewritten in the form:

$$D_s \nabla_s^2 \tilde{F} = D_s \left[ \nabla^2 \tilde{F} - \kappa \nabla \tilde{F} \cdot \mathbf{n} - \mathbf{n} \cdot \mathbf{D}^2 \tilde{F} \cdot \mathbf{n} \right] \quad (4.37)$$

where  $\mathbf{D}^2 \tilde{F}$  is the Hessian matrix of  $\tilde{F}$ . It is defined as:

$$\mathbf{D}^2 \tilde{F} = \frac{\partial^2 \tilde{F}}{\partial x_i \partial x_j} \quad (4.38)$$

with  $i$  and  $j$  equal to 0 or 1 with  $x_1 = x$  and  $x_2 = y$ . Finally,  $\kappa = \nabla \cdot \frac{\nabla \phi}{|\nabla \phi|}$  is the curvature of the surface. The first term in Eq. (4.37) accounts for an isotropic diffusion, i.e.,  $\nabla^2 \tilde{F}$ , from which the diffusion along the normal to the interface,  $\kappa \nabla \tilde{F} \cdot \mathbf{n} + \mathbf{n} \cdot \mathbf{D}^2 \tilde{F} \cdot \mathbf{n}$  is subtracted (Xu and Zhao (2003)). The diffusion term is integrated in the control volume centered on pressure cells as follows:

$$\int_{V_p} D_s \nabla_s^2 \tilde{F} dV_p = \int_{V_p} D_s \nabla \cdot \nabla \tilde{F} dV_p - \int_{V_p} D_s \left[ \kappa \nabla \tilde{F} \cdot \mathbf{n} + \mathbf{n} \cdot \mathbf{D}^2 \tilde{F} \cdot \mathbf{n} \right] dV_p \quad (4.39)$$

Note that the isotropic diffusion term, i.e.,  $\nabla^2 \tilde{F}$ , is not transformed into a surface integral. This choice was made in order to be consistent with the spatial discretization of the diffusion along the normal, i.e.,  $\kappa \nabla \tilde{F} \cdot \mathbf{n} + \mathbf{n} \cdot \mathbf{D}^2 \tilde{F} \cdot \mathbf{n}$ . All the spatial derivatives are computed using a second order centered scheme. As an example, Fig. 4.5a and b shows where the derivatives  $\frac{\partial^2 \tilde{F}}{\partial x^2}$  and  $\frac{\partial^2 \tilde{F}}{\partial x \partial y}$ , appearing in the term  $\mathbf{n} \cdot \mathbf{D}^2 \tilde{F} \cdot \mathbf{n}$ , are located.

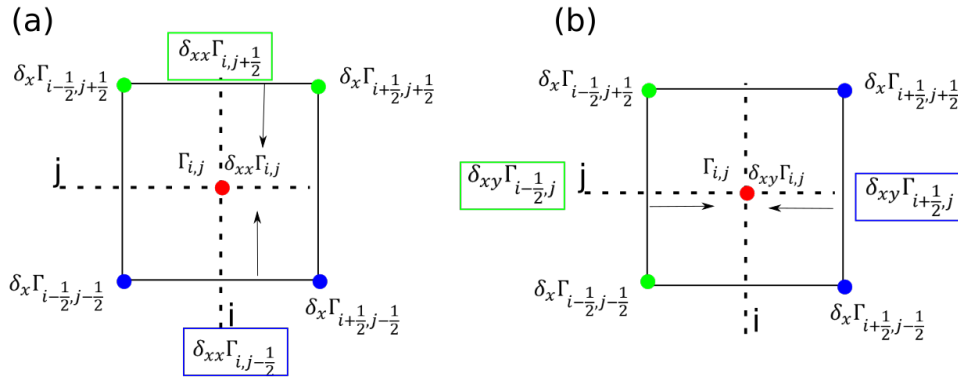


Figure 4.5: Schematic explaining the computation of (a)  $\frac{\partial^2 \tilde{F}}{\partial x^2}$  and (b)  $\frac{\partial^2 \tilde{F}}{\partial x \partial y}$ .

**Extension equation (Eq. (4.26))** The term  $\text{sign}(\phi) \frac{\nabla \phi}{\|\nabla \phi\|} \cdot \nabla \tilde{F}$ , is discretized using an upwind formulation. The term  $\text{sign}(\phi) \frac{\nabla \phi}{\|\nabla \phi\|}$  can be seen as the extension velocity of  $\tilde{F}$  from the interface to the surrounding. The discrete equivalent of the following derivatives:  $\frac{\partial \tilde{F}}{\partial x}(\mathbf{x}, t)$ ,  $\frac{\partial \tilde{F}}{\partial y}(\mathbf{x}, t)$ ,  $\frac{\partial \phi}{\partial x}(\mathbf{x}, t)$  and  $\frac{\partial \phi}{\partial y}(\mathbf{x}, t)$ , at a specific time  $n\Delta t$ , where  $n$  is an integer are written as:  $(\tilde{F}_{i,j}^n)_x$ ,  $(\tilde{F}_{i,j}^n)_y$ ,  $(\phi_{i,j}^n)_x$  and  $(\phi_{i,j}^n)_y$ . The upwind approximations of the derivatives

are then given by:

$$\begin{cases} (\tilde{T}_{i,j}^n)_x \approx D_x^- \tilde{T}_{i,j}^n & \text{if } \text{sign}(\phi_{i,j}^n)(\phi_{i,j}^n)_x > 0 \\ (\tilde{T}_{i,j}^n)_x \approx D_x^+ \tilde{T}_{i,j}^n & \text{if } \text{sign}(\phi_{i,j}^n)(\phi_{i,j}^n)_x < 0 \\ (\tilde{T}_{i,j}^n)_y \approx D_y^- \tilde{T}_{i,j}^n & \text{if } \text{sign}(\phi_{i,j}^n)(\phi_{i,j}^n)_y > 0 \\ (\tilde{T}_{i,j}^n)_y \approx D_y^+ \tilde{T}_{i,j}^n & \text{if } \text{sign}(\phi_{i,j}^n)(\phi_{i,j}^n)_y < 0 \end{cases} \quad (4.40)$$

where  $D_x^- \tilde{T}_{i,j}^n$  et  $D_x^+ \tilde{T}_{i,j}^n$  are the upwind approximations of  $\frac{\partial \tilde{T}}{\partial x}(\mathbf{x}, t)$ , that depend on the sign of  $\text{sign}(\phi_{i,j}^n)(\phi_{i,j}^n)_x$ . The upwind approximations of  $\frac{\partial \tilde{T}}{\partial x}(\mathbf{x}, t)$  and  $\frac{\partial \tilde{T}}{\partial y}(\mathbf{x}, t)$  are computed using the fifth order WENO scheme. This scheme is presented in appendix.

For the computation of the approximation of the  $x$  and  $y$  components of  $\nabla \phi$ , that is,  $(\phi^n|_{i,j})_x$  and  $(\phi^n|_{i,j})_y$ , a classical second-order centered scheme is used.

### 4.3.2 Transport of surfactants inside the bulk phase

Following Muradoglu and Triguvason (2008) and Hayashi and Tomiyama (2012), Eq.(6.5) is solved under a no flux boundary condition at the interface:  $(D_c \mathbf{n} \cdot \nabla C_d)|_I = 0$ . Consequently, the boundary condition of Eq.(6.5),  $S_\Gamma = (D_c \mathbf{n} \cdot \nabla C_c)|_I$ , is included in the bulk transport equation as an interfacial source term  $S_{\tilde{\Gamma}} \delta_I$ :

$$\frac{\partial C_c}{\partial t} + \mathbf{v} \cdot \nabla C_c = \nabla \cdot (D_c \nabla C_c) - S_{\tilde{\Gamma}} \delta_I \quad (4.41)$$

The no flux condition is enforced by extrapolating  $C_c$  from the interface to the gas phase, solving the following PDE at each physical time step, with the initial condition  $C_c^*(\mathbf{x}, \tau = 0) = C_c(\mathbf{x}, t)$ :

$$\frac{\partial C_c^*}{\partial \tau} + \text{sign}(\phi) \frac{\nabla \phi}{\|\nabla \phi\|} \cdot \nabla C_c^* = 0 \quad (4.42)$$

This technique allows simulating the transfer of surfactants from the bulk phase to a surface when no mesh is associated to this surface. In particular, the extrapolation procedure of  $C_c$  from the interface towards the gas phase allows to impose the no flux boundary condition on the interface, i.e.,  $(D_c \mathbf{n} \cdot \nabla C_d)|_I = 0$ .

### 4.3.3 Marangoni stress

The term accounting for the Marangoni effect appears as an additional source term in the one fluid formulation of the Navier–Stokes equation:

$$F_{\sigma,m} = \nabla_s \sigma \delta_I. \quad (4.43)$$

The numerical method used to solve the interfacial force is the Continuum Surface Force model (CSF) proposed by Brackbill et al. [1992]. This method consists in spreading the Marangoni stress along the numerical thickness of the interface,  $\epsilon$ . The surface gradient of the surface tension,  $\nabla_s \sigma$ , is calculated by first computing the gradient of the surface tension, and second by removing its normal component to the interface

$$\nabla_s \sigma \delta_I = \left[ \nabla \sigma - \frac{\nabla \phi}{\|\nabla \phi\|} \left( \frac{\nabla \phi}{\|\nabla \phi\|} \cdot \nabla \sigma \right) \right] \left( \frac{2\rho}{\rho_c + \rho_d} \right) \delta(\phi)_I \quad (4.44)$$

where  $\delta(\phi)_I$  is a smoothed Dirac function which allows to spread the effect of the Marangoni stress over the numerical thickness of the interface. It is defined as:

$$\begin{cases} \delta(\phi)_I = \frac{1}{2\epsilon} \left[ 1 + \cos\left(\frac{\pi\phi}{\epsilon}\right) \right] & |\phi| < \epsilon \\ \delta(\phi)_I = 0 & \text{otherwise} \end{cases} \quad (4.45)$$

The Marangoni stress,  $F_{\sigma,m}$ , is computed at the center of the cells centered on the velocity nodes (see Fig. 4.3) as illustrated in Fig. 4.6. In this figure, pressure cells are drawn as black squares, cells centered on the velocity nodes  $u$  and  $v$  are drawn as green and red squares, respectively. The Marangoni stress acts along the whole numerical thickness of the interface,  $\epsilon$ . The  $x$  component of the Marangoni stress is computed at the center of the cells centered on  $u$ , as illustrated by the green arrows on Fig. 4.6. The  $y$  component of the Marangoni stress is computed at the center of the cells centered on  $v$ , as illustrated by the red arrows on Fig. 4.6. The computation

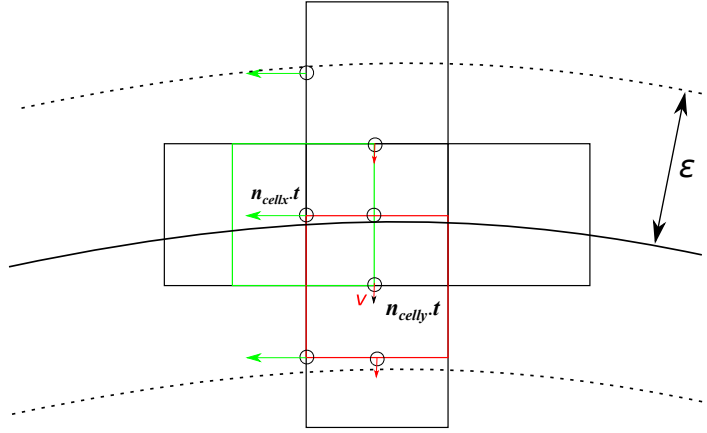


Figure 4.6: Schematic representation of the Marangoni force computation on staggered grids.

of the derivatives of  $\sigma$  and  $\phi$  appearing in Eq. (4.44) i.e.,  $\frac{\partial \sigma}{\partial x}(\mathbf{x}, t)$ ,  $\frac{\partial \sigma}{\partial y}(\mathbf{x}, t)$ ,  $\frac{\partial \phi}{\partial x}(\mathbf{x}, t)$  and  $\frac{\partial \phi}{\partial y}(\mathbf{x}, t)$  is done using a classical second-order centered scheme.

## 4.4 Conclusion

In this chapter, the implementation of the equations that are necessary to account for surfactants, in the Level-set modulus of JADIM, was detailed. The transport equation of surfactants on the bubble surface was written in an Eulerian formulation. In order to be able to solve this equation, it is extended at the interface vicinity, perpendicularly to the interface, into a volume of few cells thick. This extension is performed at every time step of the numerical procedure.

The sink term accounting for the adsorption flux of surfactants from the liquid to the bubble surface is included in the surfactant transport equation inside the liquid as an interfacial source term. Consequently, a no flux condition is imposed on the bubble-liquid interface. This condition is enforced by extrapolating the surfactant concentration,  $C_c$ , from the liquid in contact with the interface towards the gas phase, such that:  $\nabla C_d \cdot \mathbf{n} = 0$ .

Finally, the Marangoni stress is distributed along the numerical thickness of the interface following the idea of the Continuum Surface Force model

A simplified schematic of the successive steps performed during one physical time step of the numerical procedure is presented on Fig. 4.7. The algorithm starts with the transport of the interface and the transport of

surfactants on the bubble interface as well as inside the liquid. The capillary contribution, the Marangoni stress and the other terms in the Navier Stokes equations are computed and added inside the momentum balance equation and an intermediate velocity field is obtained. This velocity field does not satisfy the continuity equation. The projection method is used to deduce the pressure at the following time step, from which an updated velocity field is obtained.

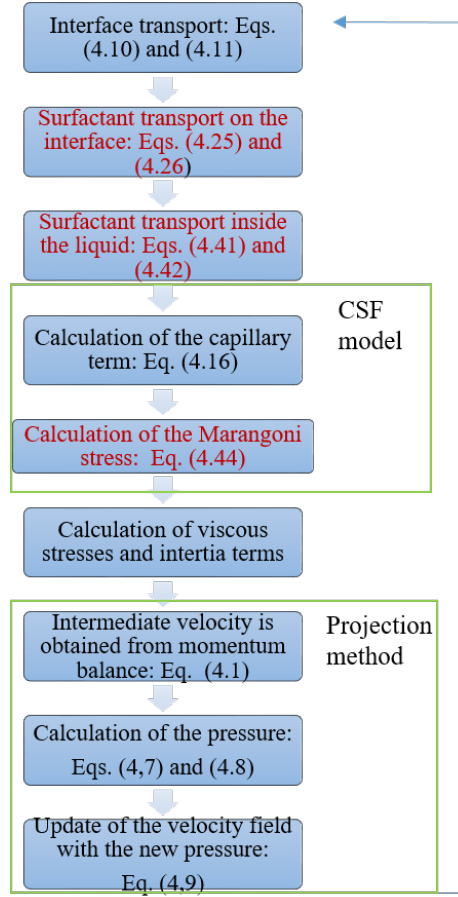


Figure 4.7: Schematic of the successive steps of the numerical procedure

In the next chapter, the implementation of each of these terms in the different equations is validated.

## CHAPTER 5

### Validation of the numerical procedure

The LS modulus of JADIM has been validated previously (Abadie et al 2013, Abadie et al 2015). In this chapter, validation tests regarding surfactants and the Marangoni stress are reported. More precisely, those tests aim to validate the numerical implementation of (i) the different terms in the equation describing the surfactant transport on the gas-liquid interface and (ii) the computation of the Marangoni stress. Concerning (i), several test cases are performed, in particular situations where  $\partial \tilde{\Gamma} / \partial t$  and only one other term of Eq. (4.25) are involved. For each test case, Eqs. (4.25 and 4.26) are solved together and compared to a reference solution. For each test case, the ability of the simulation to reproduce a reference solution is verified by computing the error based on the classical  $L_1$  and  $L_\infty$  norms:

$$\epsilon_1 = \frac{1}{T_f} \sum_{i=0}^n |N(i\Delta t) - A(i\Delta t)| \Delta t \quad (5.1)$$

$$\epsilon_\infty = \max (|N(i\Delta t) - A(i\Delta t)|) \quad (5.2)$$

where  $N(i\Delta t)$  is the solution computed with JADIM at time  $t = i\Delta t$ ,  $A(i\Delta t)$  is the reference solution of the test case at time  $t = i\Delta t$ ,  $\Delta t$  is the constant time step used for sampling and  $T_f = n\Delta t$  is the final simulation time, with  $n$  an integer.  $A(i\Delta t)$  is the exact analytical solution of the test case when it exists. For the test case presented in Sec. (5.3), for which an approximate analytical solution exists, or for the test case presented in Sec. (5.2), for which the numerical method is an approximate one,  $A(i\Delta t)$  is the numerical solution computed with the finest mesh, or smallest time step. For each test case, the evolution of the errors with the time step and mesh size is presented, unless the contrary is explicitly mentioned. It should be noted that the curves relating  $\epsilon_1$  or  $\epsilon_\infty$  to  $\Delta x$  or  $\Delta t$  characterize both the speed at which the numerically computed solution converges and its ability to reproduce the exact solution. In that sense, the convergence rates that are reported in this chapter do not strictly characterize the convergence of the spatial and temporal discretization scheme that were used.

### 5.1 Validation of the numerical procedure used to transport surfactants on the bubble surface

#### 5.1.1 Expansion test

The test case presented here is inspired from Stone (1990). A two-dimensional bubble is initialized at the center of the computational domain. A polar coordinate system is placed at the center of the bubble:  $r$  is the radial coordinate and  $\theta$  the angular one.  $e_r$  is the radial unit vector. In Eq. (4.25), the term  $\tilde{\Gamma} \mathbf{n} \cdot \nabla \mathbf{v} \cdot \mathbf{n}$  is a term accounting for the change of the local curvature of the surface (Stone (1990)). To test its proper implementation, a growing bubble with an homogeneous surfactant concentration field on its surface is simulated. There is neither adsorption nor desorption of surfactants to/from the bubble interface from/to the bulk phase. A non-zero divergence velocity field  $\mathbf{v} = Kre_r$  is imposed, where  $K$  is a constant. It should be noted that Eq. (4.25) is only valid for incompressible flows. However, the spatial discretization of the convective term,  $\mathbf{v} \cdot \nabla \tilde{\Gamma}$ , is done in a conservative manner using the fact that the velocity field is divergence free:  $\mathbf{v} \cdot \nabla \tilde{\Gamma} = \nabla \cdot (\tilde{\Gamma} \mathbf{v})$ . Integrating  $\nabla \cdot (\tilde{\Gamma} \mathbf{v})$  on the control

volume centered on a pressure cell yields  $\int_V \nabla \cdot (\tilde{I} \mathbf{v}) dV = \int_S \mathbf{n} \cdot (\mathbf{v} \tilde{I}) dS$ . Therefore, Eq. (4.25) becomes valid for compressible flows as well. The computational setup and the flow field are presented in Fig. 5.1.

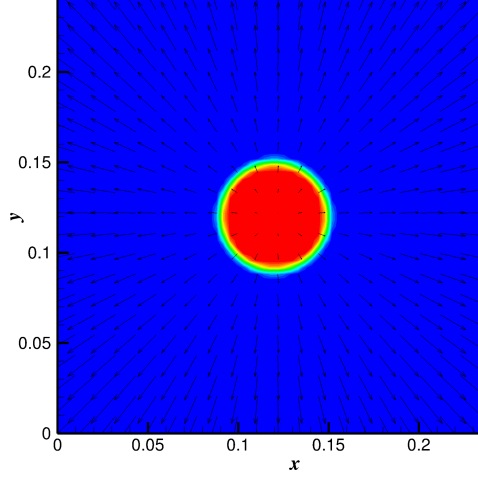


Figure 5.1: A two-dimensional bubble is placed in a square domain. The bubble interface is expanded with the velocity field  $\mathbf{v} = K r \mathbf{e}_r$ . The velocity field  $\mathbf{v}$  is plotted by the means of vectors. The color characterizes the value of the function  $F$  (red=gas; blue=liquid).

The differential equation governing  $\tilde{I}$  is obtained by injecting the expression of  $\mathbf{v}$  into Eq. (4.25):

$$\frac{d\tilde{I}}{\tilde{I}} = -K dt \quad (5.3)$$

which yields:

$$\tilde{I} = I_0 e^{-Kt} \quad (5.4)$$

where  $\tilde{I}(t=0) = I_0$ .  $\tilde{I}$  is presented as a function of the time in Fig. 5.2a, with  $I_0 = 1 \text{ mol/m}^2$ . The solid line is the analytical solution (Eq. (5.4)) and the crosses are values of  $\tilde{I}$  computed with JADIM, with a computational domain containing  $64 \times 64$  computational cells. It can be observed that the agreement between the computation performed with JADIM and the analytical solution given by Eq. (5.4) is excellent. The errors  $\epsilon_1$  and  $\epsilon_\infty$  are presented in Fig. 5.2b as functions of the grid size  $\Delta x$ . In order to guide the eye, a small solid black line is plotted in Fig. 5.2b that shows a second-order convergence. It is observed that both  $\epsilon_1$  and  $\epsilon_\infty$  follow a similar trend as the solid black line. Note that the time step was fixed to  $\Delta t = 1.4 \cdot 10^{-4} \text{ s}$  for all the computational grids.

The convergence of the numerical solution towards the solution given by Eq. (5.4), with the integration time step has also been verified. The time step convergence is shown in Fig. 5.3. In order to guide the eye, a small solid black line is drawn in Fig. 5.3 that shows a third-order convergence. It is observed that both  $\epsilon_1$  and  $\epsilon_\infty$  follow a similar trend as the solid black line. This is consistent with the third-order Runge–Kutta scheme that was used for the time discretization of Eq. (4.25).

### 5.1.2 Advection test

The proper implementation of the advection term,  $\mathbf{v} \cdot \nabla \tilde{I}$ , in Eq. (4.25) is verified with the following test case. A two-dimensional circular bubble is initialized at the center of the computational domain. A polar coordinate system is defined, with an origin at the center of the bubble:  $\theta$  is the angular coordinate and  $r$  the radial one;  $\mathbf{e}_\theta$  is the angular unit vector. The following velocity field is imposed:  $\mathbf{v} = \omega r \mathbf{e}_\theta$ , where  $\omega$  is a constant. There is



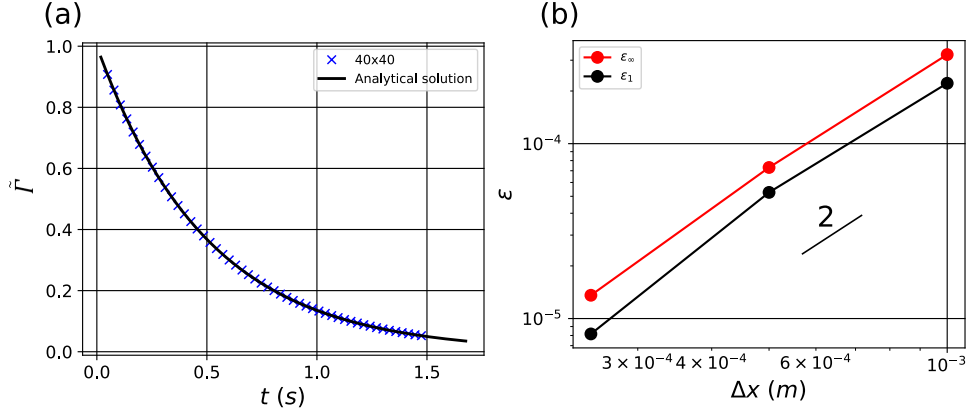


Figure 5.2: This figure refers to the validation test presented in section 5.1.1. (a)  $\tilde{\Gamma}$  as a function of the time for the configuration depicted in Fig. 5.1. The continuous line gives the analytical solution (Eq. (5.4)) and the crosses give values computed with JADIM with a grid containing  $64 \times 64$  cells. (b)  $\epsilon_1$  and  $\epsilon_\infty$  as functions of the cell size  $\Delta x$ . In order to guide the eye, a small solid black line is drawn that shows a second order convergence.

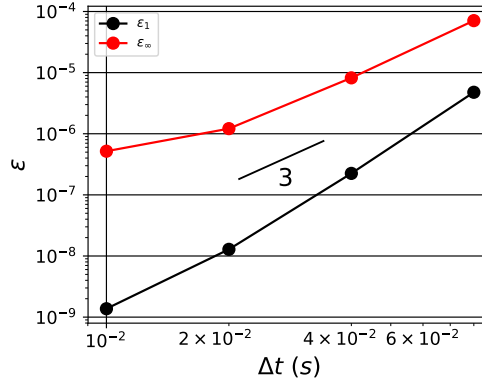


Figure 5.3: The errors,  $\epsilon_1$  and  $\epsilon_\infty$  as functions of the integration time step,  $\Delta t$ . The solid black line shows a third-order convergence.

neither diffusion along the surface nor adsorption/desorption of surfactants. For this test case, it can be verified that Eq. (4.25) reduces to:

$$\frac{\partial \tilde{\Gamma}}{\partial t} + \omega \frac{\partial \tilde{\Gamma}}{\partial \theta} = 0 \quad (5.5)$$

The following initial condition is chosen:  $\tilde{\Gamma}(\theta, t = 0) = \sin(\theta) + 2$ . The analytical solution of Eq. (5.5) with this initial condition can be found using the method of characteristics:

$$\tilde{\Gamma} = \sin(-t\omega + \theta) + 2 \quad (5.6)$$

The computational setup, the initial concentration field and the velocity field are presented in Fig. 5.4. For stability reasons, for this test case, the integration time step is fixed to  $\Delta t = \Delta x / (\omega R)$ , where  $R$  is the bubble radius. The solution given by Eq. (5.6) is plotted in Fig. 5.5a as a solid line, for  $\theta = \frac{\pi}{2}$  and  $\omega = 1$ . Values computed with JADIM, using 160 cells along the  $x$  and  $y$  directions, are plotted as crosses. It can be observed that the agreement between the computation performed with JADIM and the analytical solution given by Eq. (5.6) is excellent. The errors  $\epsilon_1$  and  $\epsilon_\infty$  are plotted in Fig. 5.5b as functions of the grid size  $\Delta x$ . In order to guide the eye, a small solid red line is plotted in Fig. 5.5b that shows a convergence rate of 1.5.

It is noticed in this test case that, if the mesh is not fine enough, the peaks of  $\tilde{\Gamma}$  are getting smaller as it is transported. This is depicted in Fig. 5.6. In this figure,  $N = \omega t / (2\pi)$  is the number of rotation that  $\tilde{\Gamma}$  performs

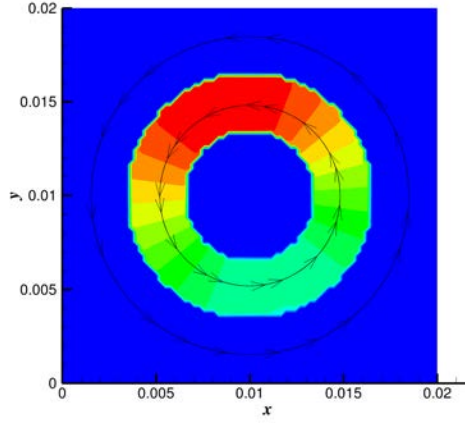


Figure 5.4: A two-dimensional bubble is placed in a square domain. The streamlines corresponds to the following velocity field:  $\mathbf{v} = \omega r e_\theta$ . The contour plot characterizes  $\tilde{T}$  at a given time  $t$ . This computation was performed with 80 cells along the  $x$  and  $y$  directions.

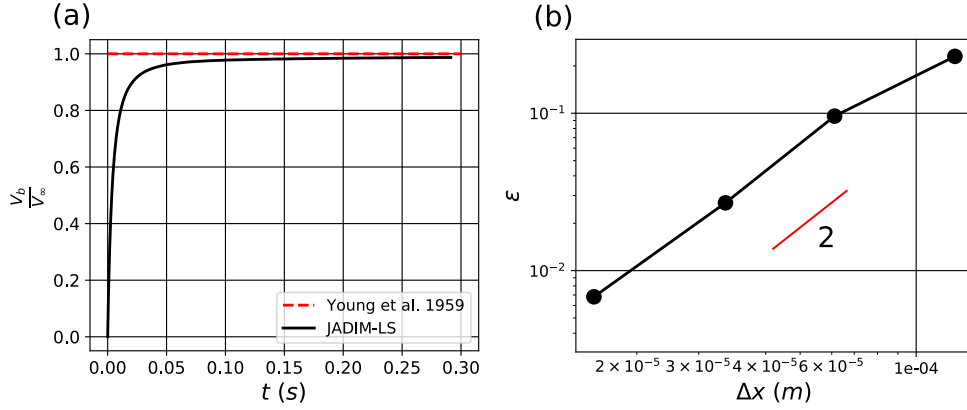


Figure 5.5: This figure refers to the validation test presented in section 5.1.2. (a) Comparison, for  $\theta = \frac{\pi}{2}$  and  $\omega = 1$ , between the solution given by Eq. (5.6) (black line) and values calculated with JADIM (crosses), using a grid having 160 cells along the  $x$  and  $y$  directions. (b) The errors,  $\epsilon_1$  and  $\epsilon_\infty$ , as functions of the cell size. The red line shows a convergence rate of 1.5.

around the perimeter of the bubble. It can be observed that when the mesh is coarse, the solution computed with JADIM follows the solution of Eq. (5.6) for  $N = 0.1$ . However, as  $N$  increases, the peaks of the sinus function tend to disappear. When the mesh is refined, the solution computed with JADIM follows the analytical solution even for  $N = 13$ .

In this test case, it has been observed that, if the mesh size is fixed, decreasing the time step (starting from  $\Delta t = \Delta x/(\omega R)$ ) does not improve the solution calculated by JADIM. On the contrary, the peaks of the sinus function gets smaller as  $\Delta t$  gets smaller, for a fixed value of  $t = n\Delta t$ , where  $n$  is an integer. This is depicted in Fig. 5.7, where the maximum value of  $\tilde{T}$  is plotted as a function of  $N$ , for a mesh characterized by 40 cells along the  $x$  and  $y$  directions. It is observed that the maximum value of  $\tilde{T}$  decreases with time, this decrease being more pronounced as  $\Delta t$  is decreased. This is due to numerical diffusion that is known to increase as the ratio of  $(\Delta x)^2/\Delta t$  increases. We believe that the numerical diffusion observed for this test case is responsible for the convergence order of 1.5.

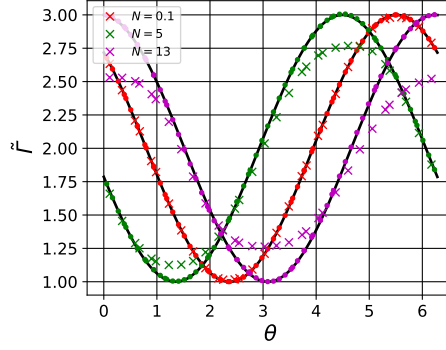


Figure 5.6: (a) Comparison between the solution given by Eq. (5.6) (black line) and values calculated with JADIM at different times. Two grids are used for the computations. A grid having 32 cells along the  $x$  and  $y$  directions (crosses) and a grid having 64 cells along the  $x$  and  $y$  directions (dots).

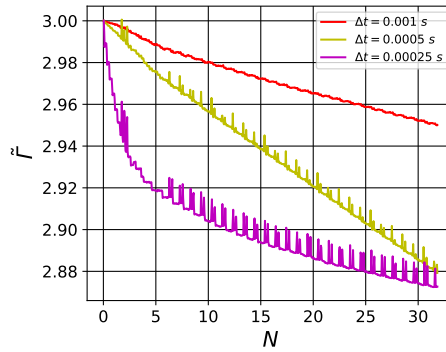


Figure 5.7: Maximum value of  $\tilde{\Gamma}$  as a function of the number of rotation that  $\tilde{\Gamma}$  performs around the perimeter of the bubble ( $N = \omega t / (2\pi)$ )

### 5.1.3 Adsorption/desorption test

The proper implementation of the source term,  $K_a C_I (\Gamma_\infty - \tilde{\Gamma}) - K_d \tilde{\Gamma}$ , in Eq. (4.25), is verified with the following test case. A stagnant liquid pool with a free surface contains surfactants, with a constant concentration  $C_0$ . The free surface contains surfactants, with an initial concentration  $\Gamma_0$ . In this situation, Eq. (4.25) reduces to an ordinary differential equation:

$$\frac{d\tilde{\Gamma}}{dt} = K_a C_0 (\Gamma_\infty - \tilde{\Gamma}) + K_d \tilde{\Gamma} \quad (5.7)$$

whose solution is:

$$\tilde{\Gamma} = \frac{K_a C_0 \Gamma_\infty - e^{-(t+Q)(K_a C_0 + K_d)}}{K_a C_0 + K_d} \quad (5.8)$$

where  $Q = -\frac{1}{K_a C_0 + K_d} \ln(K_a C_0 \Gamma_\infty - \Gamma_0 (K_a C_0 + K_d))$  is an integration constant. Fig. 5.8 presents the computational domain. Eq. (5.8) is plotted as a solid line in Fig. 5.9a, together with values of  $\tilde{\Gamma}$  calculated with JADIM, for  $K_a = 1 \text{ mol} \times \text{m}^3 \cdot \text{s}^{-1}$ ,  $K_d = 1 \text{ s}^{-1}$ ,  $\Gamma_0 = 1 \text{ mol/m}^2$ ,  $\Gamma_\infty = 5 \text{ mol/m}^2$  and  $C_0 = 2 \text{ mol/m}^3$ . In Fig. 5.9b,  $\epsilon_1$  and  $\epsilon_\infty$  are plotted as functions of the integration time step used in JADIM. The solid line shows a third-order convergence. This is consistent with the third-order Runge–Kutta scheme used for the time discretization of Eq. (4.25).

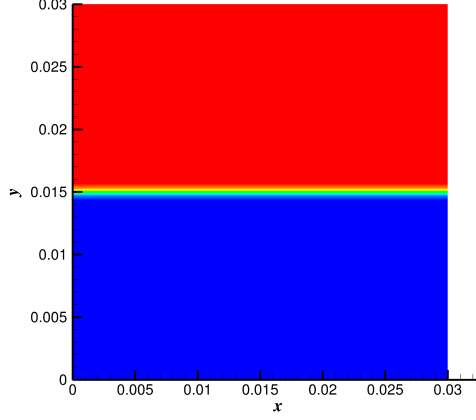


Figure 5.8: Computational setup for the simulation of a stagnant liquid pool containing surfactants. 64 square cells are placed along the  $x$  and  $y$  directions. The colors characterize the value of the function  $F$  (blue=liquid phase, red=gas phase).

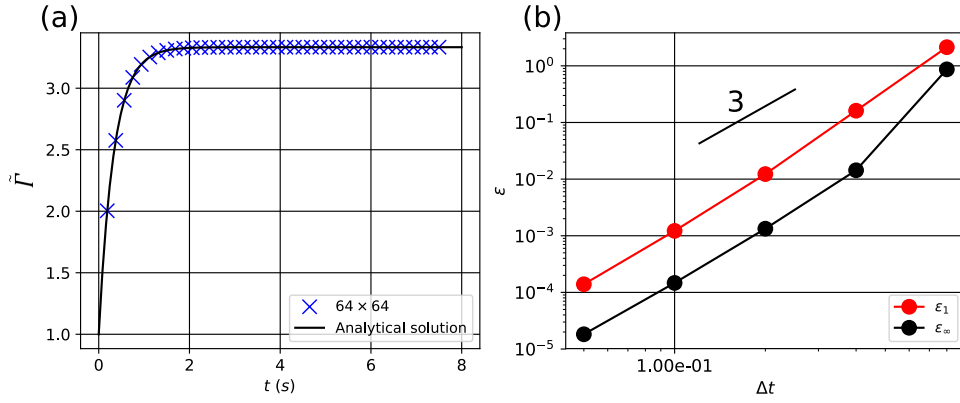


Figure 5.9: This figure refers to the validation test presented in section 5.1.2. (a) Surface concentration,  $\tilde{\Gamma}$ , as a function of the time  $t$ . The black solid line is the solution given by Eq. (5.8) and crosses give values computed with JADIM. (b)  $\epsilon_1$  and  $\epsilon_\infty$  as functions of the integration time step  $\Delta t$ . The solid line shows a convergence rate of 3.

### 5.1.4 Diffusion test

The proper implementation of the term accounting for surface diffusion in Eq. (4.25) is verified with the following test case, proposed by Xu and Zhao (2002). For reminder, the surface diffusion is discretized in the following form:

$$D_s \nabla_s^2 \tilde{\Gamma} = D_s \left[ \nabla^2 \tilde{\Gamma} - \kappa \nabla \tilde{\Gamma} \cdot \mathbf{n} - \mathbf{n} \cdot \mathbf{D}^2 \tilde{\Gamma} \cdot \mathbf{n} \right] \quad (5.9)$$

A two-dimensional circular and stagnant bubble of radius  $r_0$  is initialized at the center of the computational domain. A polar coordinate system is placed at the center of the bubble:  $r$  is the radial coordinate and  $\theta$  is the angular one. Without adsorption/desorption flux of surfactants to/from the interface, and using the polar coordinate system, Eq. (4.25) reduces to:

$$\frac{\partial \tilde{\Gamma}}{\partial t} = \frac{1}{r_0^2} D_s \frac{\partial^2 \tilde{\Gamma}}{\partial \theta^2} \quad (5.10)$$

This PDE is completed by a periodic boundary condition:  $\tilde{\Gamma}(0, t) = \tilde{\Gamma}(2\pi, t)$ . The following initial condition is used:  $\tilde{\Gamma}(\theta, t = 0) = \sin \theta + 2$ .

Eq.(5.10) can be solved using separation of variables. It gives:

$$\tilde{r}(\theta, t) = 2 + \exp\left(\frac{-D_s t}{r_0^2}\right) \sin \theta \quad (5.11)$$

For stability reasons, for this test case, the integration time step is fixed to:  $\Delta t = \Delta x^2/D_s$ . The surface con-

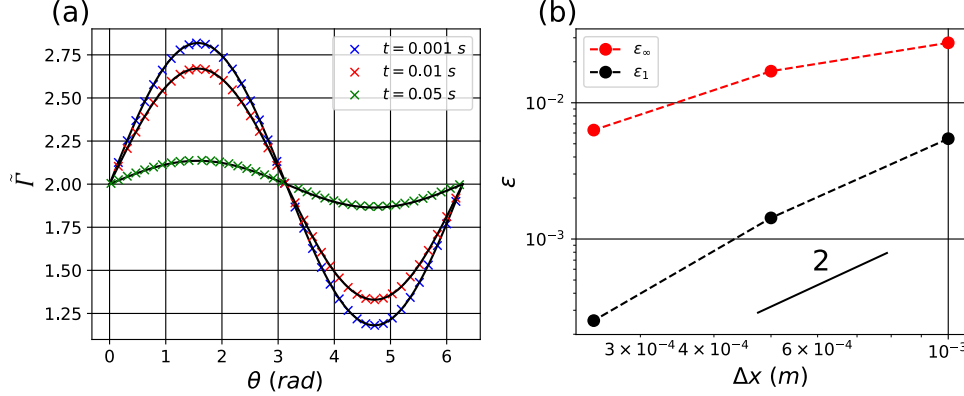


Figure 5.10: (a)  $\tilde{r}(\theta)$  at different times. The black solid lines are the solutions given by Eq. (5.10) at  $t = 0.005$  s,  $t = 0.01$  s and  $t = 0.05$  s, while crosses give values computed with JADIM. (b)  $\epsilon_\infty$  and  $\epsilon_1$  at time  $t = 0.01$  s as functions of the mesh size  $\Delta x$ . The solid black line shows a second-order convergence.

centration profile  $\tilde{r}(\theta, t)$  is shown in Fig. 5.10a, at different times. In this figure, the solid lines represent the solution given by Eq. (5.11) and the crosses give values computed with JADIM. The grid used for the computation contains 80 cells along both directions. Fig. 5.10b presents  $\epsilon_1$  and  $\epsilon_\infty$  as functions of mesh size  $\Delta x$ . Note that for this test case,  $\epsilon_1$  and  $\epsilon_\infty$  are defined as:  $\epsilon_1 = \frac{1}{2\pi} \sum_{i=0}^n |N(t_i, i\Delta\theta) - A(t_i, i\Delta\theta)|\Delta\theta$  and  $\epsilon_\infty = \max(|N(t_i, i\Delta\theta) - A(t_i, i\Delta\theta)|)$ , where  $t_i$  denotes a specific time in the simulation. The solid black line shows a second order convergence.

The convergence with the integration time step is also verified. The mesh size is fixed to  $\Delta x = 0.003125$  m and the time step is varied. The diffusion coefficient is set to  $D_s = 0.01 \text{ m}^2/\text{s}$ . The result is presented in Fig. 5.11a. In this figure, it is clearly seen that the solution computed with JADIM gets closer to the solution given by Eq. (5.1.4) as the integration time step is reduced. The convergence rate is shown in Fig. 5.11b. A second order convergence with the integration time step,  $\Delta t$ , is observed.

### 5.1.5 Discussion

In this section, the convergence of the numerical procedure used to solve Eqs. (4.25 and 4.26) was verified. In general, the convergence rate of the solution computed with JADIM towards an analytical solution with respect to  $\Delta x$  was close or smaller than two. In particular, the expansion and the diffusion tests showed a convergence rate close to two, which is consistent with the spatial discretization schemes of these terms (see chapter 4). Concerning the advection test (see section (5.1.2), the convergence rate with  $\Delta x$  is close to 1.5. It is hypothesized that this lower convergence rate when compared to the other test cases might be due to the numerical diffusion observed for this test case. Further investigations need to be conducted to confirm this hypothesis.

The convergence of the solution computed with JADIM towards an analytical solution with respect to  $\Delta t$  was also characterized. A convergence rate close to three was observed for the adsorption test (see section 5.1.3) and the expansion test (see section 7.2). This is consistent with the use of the third-order Runge-kutta scheme for the time discretization of Eqs. (4.25 and 4.26). Concerning the diffusion test, a convergence rate close to two was observed. The reason of this lower convergence rate has not been investigated and is unknown.

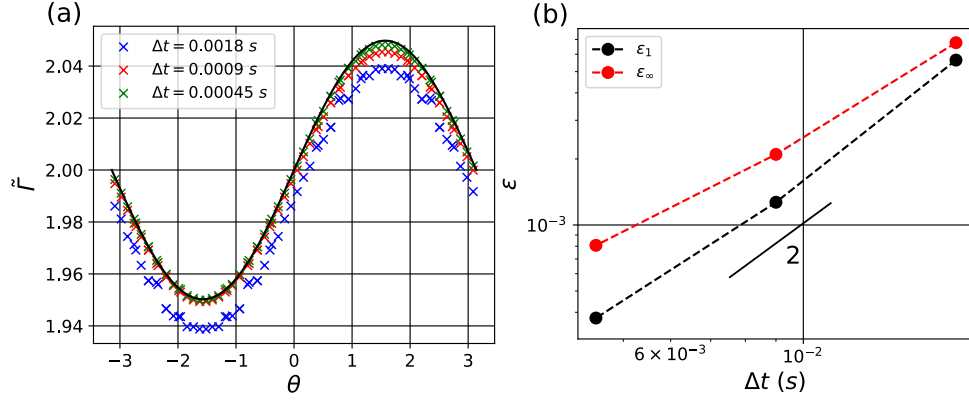


Figure 5.11: This figure refers to the validation test presented in section 5.1.4. (a)  $\tilde{I}(\theta)$  at  $t = 0.27$  s. The black solid line is the solutions given by Eq. (5.10) at  $t = 0.27$  s while crosses give values computed with JADIM for  $\Delta t = 0.018$  s,  $\Delta t = 0.009$  s and  $\Delta t = 0.0045$  s. (b)  $\epsilon_\infty$  and  $\epsilon_1$  at time  $t = 0.27$  s as functions of the integration time step,  $\Delta t$ . The solid black line shows a second order convergence.

It is expected that the term that exhibits the lowest convergence rate will dictate the convergence rate of the whole numerical procedure, as it will be seen later.

## 5.2 Exchange term in the surfactant transport equation inside the bulk phase

As pointed out in the section presenting the numerical method, the adsorption/desorption flux of surfactants towards/from the surface is dealt as an interfacial source term inside the bulk transport equation (Eq. (4.41)) and a no-flux condition towards the dispersed phase is imposed. In this subsection, we verify that this technique can reproduce analytical results within an acceptable error margin. The following test case is designed for this purpose.

A flat horizontal interface is initialized inside a two-dimensional rectangular domain. The computational domain is the same as in Fig. 5.8, but the red color corresponds to the liquid phase and the blue color corresponds to the gas phase. The upper boundary is a wall where the bulk concentration is fixed to  $C = C_1$ . The surfactant concentration on the gas-liquid interface is fixed to  $\tilde{\Gamma} = \Gamma_1$ . The side boundaries are walls with noflux boundary conditions for the surfactants. The distance between the upper (lower) boundary and the interface is  $H_1$  ( $H_2$ ). At equilibrium (i.e., for  $t \rightarrow \infty$ ) the surfactant diffusion flux in the upper phase is equal to the net surfactant flux to the interface:  $S_{\tilde{\Gamma}} = (D_c \mathbf{n} \cdot \nabla C_c)|_I$ . Therefore, an equilibrium concentration at the vicinity of the interface,  $C_I$ , exists, and can be expressed as follows:

$$C_I = \frac{-\frac{D_1 C_1}{H_1} + K_d \Gamma_1}{-\frac{D_1}{H_1} + K_a (\Gamma_\infty - \Gamma_1)} \quad (5.12)$$

The diffusion coefficient of the surfactants in the upper (liquid) phase is set to  $D_1 = 10^{-3} \text{ m}^2/\text{s}$ . The adsorption and desorption constants of the surfactants are fixed to  $K_a = 1 \text{ mol} \times \text{m}^3/\text{s}$ ,  $K_d = 1 \text{ s}^{-1}$  and  $\Gamma_1 = 2 \text{ mol}/\text{m}^2$ . Eq. (5.12) is plotted as a solid line in Fig. 5.12a, whereas the values obtained with JADIM are plotted as crosses. The values obtained with JADIM are obtained by solving Eqs. (4.41) and (4.42). The computation is performed with 128 cells along the  $x$  and  $y$  directions. The computation is able to reproduce the analytical solution with less than 2% of error, when  $t \rightarrow \infty$ . The convergence is verified by comparing the values of  $C_I$  computed with JADIM to the one computed with the finest grid. This is shown in Fig. 5.12b. To guide the eye, a small black solid line is drawn that shows a first order convergence. It seems that the method of imposing the no-flux boundary condition

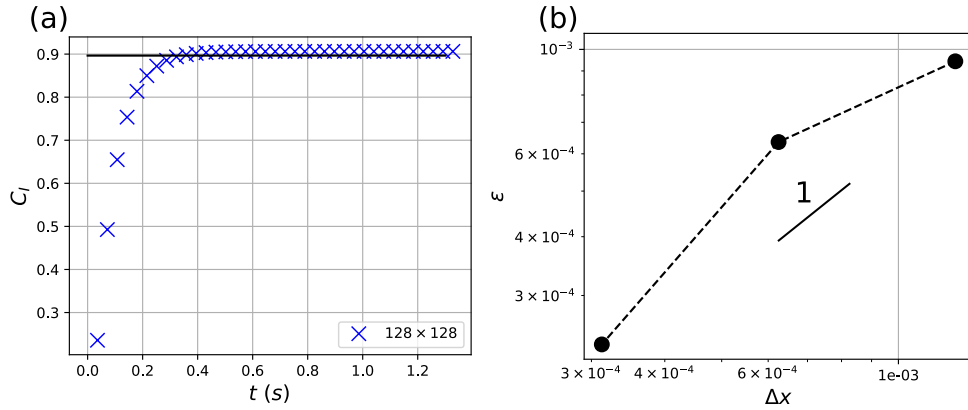


Figure 5.12: This figure refers to the validation test presented in section 5.2. (a)  $C_I$  as a function of the time  $t$ . The black solid line is the solution given by Eq. (5.12) and the crosses are the values computed with JADIM. (b)  $\epsilon_1$  as a function of grid size  $\Delta x$ .

at the interface by solving Eq. (4.42) only in the gas phase leads to a solution that is in satisfactory agreement with the analytical solution, however, the convergence rate of the solution is lower than what is expected.

The sensitivity of the solution calculated with JADIM to the number of pseudo time step ( $n$ ) when solving Eq. (4.42) was verified. It was observed that the solution computed with JADIM varies less than 0.6% when  $n$  is

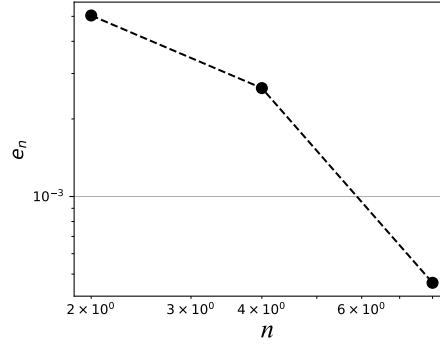


Figure 5.13: The parameter  $e_n = (C_I(\tau) - C_I(\tau = 16)) / C_I(\tau = 16)$  as a function of the number of pseudo-time step.

increased from 2 to 16. This is illustrated in Fig. 5.13, where  $e_n = (C_I(\tau) - C_I(\tau = 16)) / C_I(\tau = 16)$  is plotted as a function of  $\tau$ . In the rest of the work performed in this thesis, the number of pseudo-time step performed when solving Eq. (4.42) is  $n = 5$ .



### 5.3 Marangoni stress

The proper implementation of the CSF model for the computation of the Marangoni stress is verified by simulating an axisymmetric bubble subjected to a constant surface tension gradient:  $\sigma = \sigma_0 (1 - \beta \frac{z}{L})$ , where  $\beta$  is a constant. The analytical expression of the terminal velocity of the bubble is given, in the creeping flow limit, i.e., for  $Re_b = \frac{\rho_c d V_b}{\mu_c} \rightarrow 0$ , for a spherical bubble, i.e., for  $Ca_b = \frac{\mu_c V_b}{\sigma_0} \rightarrow 0$ , for vanishing Marangoni number, i.e.,  $\frac{\beta d}{L} \rightarrow 0$ , and in an unbounded medium, by Young *et al.* (1959):

$$V_b = \frac{1}{3} \frac{-\sigma_0 d \frac{\beta}{L}}{(2\mu_c + 3\mu_d)} \quad (5.13)$$

The computational setup is presented in Fig. 5.14. The numerical solution obtained with JADIM by solving Eqs. (3-4) is compared to Eq. (5.13) in Fig. 5.16a, with  $\mu_d = \mu_c = 0.2$  Pa.s,  $\rho_c = \rho_d = 0.02$  kg.s<sup>-1</sup>,  $d = 1$  m,  $\sigma_0 = 10$  N.m<sup>-1</sup> and  $\beta = 0.27$ . The numerical solution is computed with a mesh characterized by a ratio of the bubble diameter to the mesh size  $d/\Delta x$  equal to 64. It is calculated that  $Re_b = 0.0889$  and  $Ca_b = 0.017$ . This confirms that Eq. (5.13) can be applied to predict  $V_b$  in this specific configuration. The difference between the bubble velocity computed with Eq. (5.13) and the one computed with JADIM is less than 2 % and falls below 1% when the size of the mesh is  $\Delta x = d/128$ . The convergence is characterized by comparing the values of  $V_b$  computed with JADIM to the one computed with the finest grid. This is shown in Fig. 5.16b. The solid line shows a second order convergence.

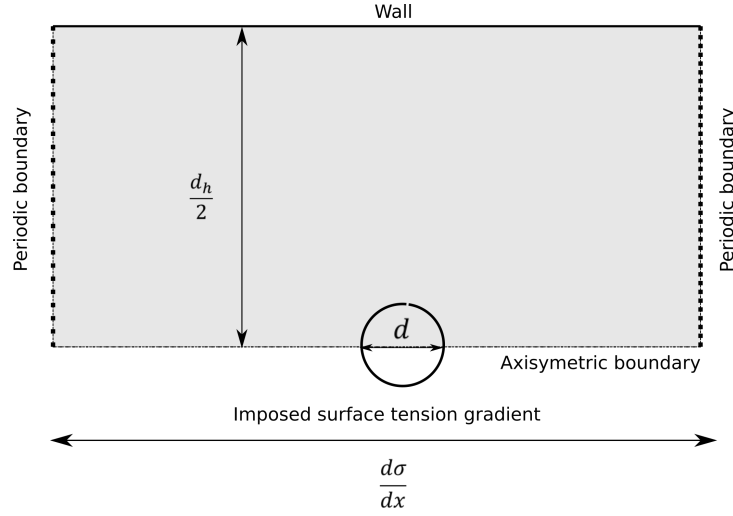


Figure 5.14: Computational setup for the axisymmetric simulation of a bubble subjected to a constant surface tension gradient.

The convergence of the numerical procedure with the integration time step has also been verified. The values of  $V_b$  are calculated with a mesh characterized with  $d/\Delta x = 64$  and different values of  $\Delta t$ . The convergence is evaluated by comparing the values of  $V_b$  computed with JADIM with a given value of  $\Delta t$  to the one computed with the smallest value of  $\Delta t$ . A third order convergence with the integration time step is observed, as expected from a third order Runge–kutta scheme.

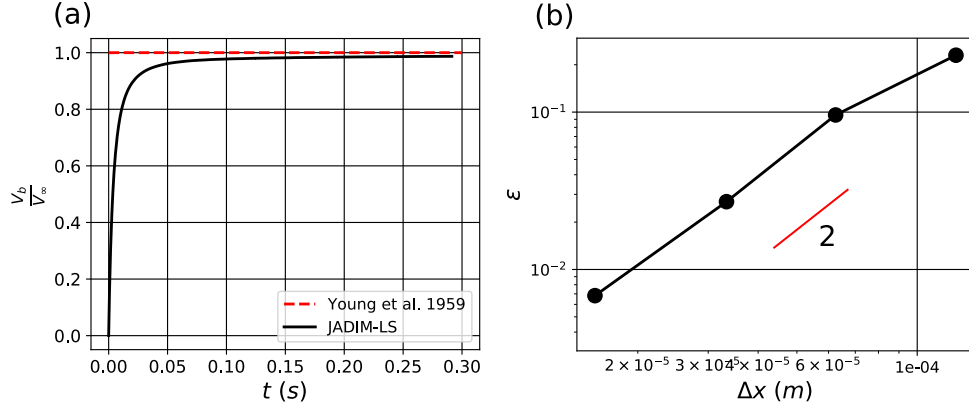


Figure 5.15: This figure refers to the validation test presented in section 5.3. (a) Bubble velocity as a function of the time computed with JADIM (solid line) and steady state bubble velocity given by Eq. (5.13) (dashed line). (b) Relative error with respect to the finest mesh as a function of the mesh size ( $\Delta x$ ). The solid line shows a second order convergence.

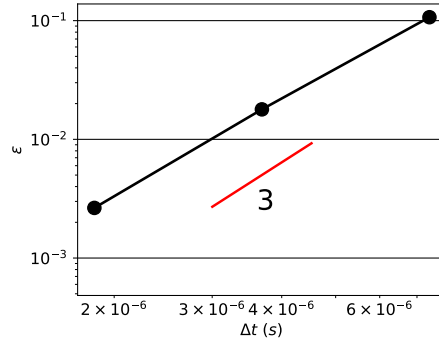


Figure 5.16: This figure refers to the validation test presented in section 5.3. Relative error with respect to the smallest time step as a function of the integration time step ( $\Delta t$ ). The solid line shows a third order convergence.

## 5.4 Bubble rising in an infinite stagnant liquid

In this section, the validation of the whole numerical procedure is done, with the following test case:

A bubble is initialized at the center of an axisymmetric domain. The domain and the boundary conditions are presented in Fig. 5.17. The upper boundary of the domain is a wall, an axisymmetric boundary condition is imposed on the lower boundary and periodic boundary conditions are imposed on the side boundaries of the domain. Gravity acts along the negative  $z$  axis (see Fig. 5.17) and, consequently, the bubble rises along the  $z$ -axis due to its density difference with the surrounding liquid. The bubble interface is initially clean, i.e.,  $\tilde{\Gamma}(\mathbf{x}, t = 0) = 0$ . The surfactant concentration is initially uniform in the liquid  $C(\mathbf{x}, t = 0) = C_0$ . The non dimensional numbers characterizing the studied system can be summarized as follows:

$$\text{Re} = \frac{\rho_c \mathcal{UL}}{\mu_c}, \text{Bo} = \frac{\rho g(d)^2}{\sigma_0}, \text{Mo} = \frac{(\rho_c - \rho_d) g \mu_c^4}{(\rho_c^2 \sigma^3)}, m = \frac{\rho_d}{\rho_c}, \lambda = \frac{\mu_d}{\mu_c}$$

$$E = \frac{RT\Gamma_\infty}{\sigma_0}, \text{La} = \frac{k_a C_\infty}{k_d}, \text{Da} = \frac{\Gamma_\infty}{\mathcal{L} C_\infty}, \alpha = \frac{k_a C_\infty \mathcal{L}}{\mathcal{U}}, \text{Pe} = \frac{\mathcal{UL}}{D_c}, \text{Pe}_s = \frac{\mathcal{UL}}{D_s}$$

where  $\text{Re}$ ,  $\text{Bo}$ ,  $\text{Mo}$ ,  $E$ ,  $\text{La}$ ,  $\text{Da}$ ,  $\alpha$ ,  $\text{Pe}$ ,  $\text{Pe}_s$ ,  $m$ ,  $\lambda$  are the Reynolds number, the Bond number, the Morton number,

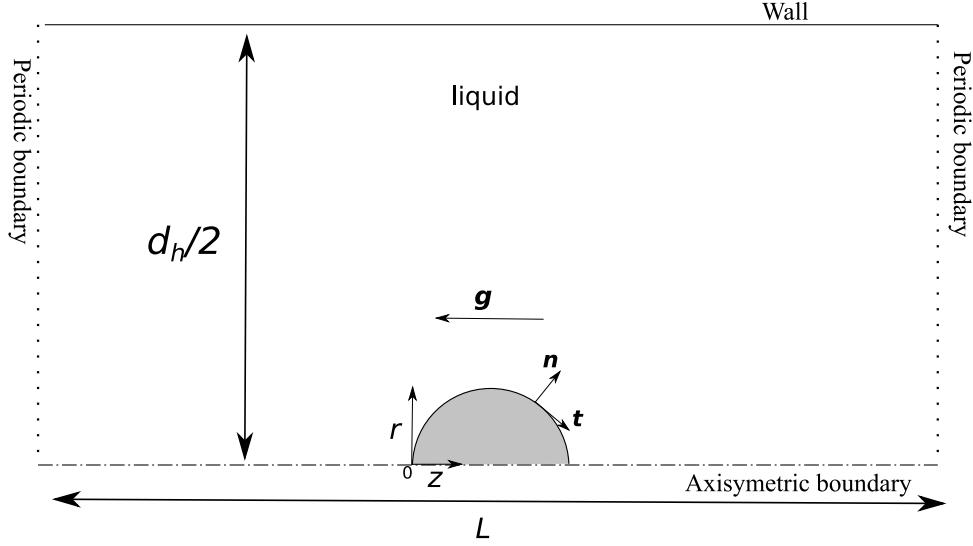


Figure 5.17: Computational domain for the simulation of a bubble rising in a stagnant liquid. The length of the periodic domain is  $L$ . The boundary conditions are indicated on the figure.

the elasticity number, the Langmuir number, the Damkohler number, the dimensionless adsorption rate, the Peclet number based on the bulk surfactant diffusivity, the Peclet number based on the interfacial surfactant diffusivity, the ratio of the gas viscosity ( $\mu_d$ ) to the liquid viscosity ( $\mu_c$ ) and the ratio of the gas density ( $\rho_d$ ) to the liquid density ( $\rho_c$ ), respectively. The velocity scale is set to  $\mathcal{U} = V_{hr}$ , where  $V_{hr}$  is the terminal velocity given by Hadamard–Rybczynski solution for a spherical bubble in the low Reynolds number limit moving in an infinite domain (Clift *et al.* (1978)):

$$V_{hr} = \frac{2}{3} \frac{g(d/2)^2(\rho_c - \rho_d)}{\mu_c} \frac{\mu_c + \mu_d}{2\mu_c + 3\mu_d} \quad (5.14)$$

The length scale is set to the bubble radius  $\mathcal{L} = d/2$ . This length scale sets two additional number characterizing the geometry:  $L/d$  and  $d_h/d$ . The parameters are fixed to:  $E = 0.5$ ,  $Da = 10$ ,  $\alpha = 20$ ,  $Pe = 10$ ,  $Pe_s = 100$ ,  $m = 0.1$ ,  $\lambda = 0.025$ ,  $Bo = 1$ ,  $Mo = 0.1$ ,  $L/d = 20$ ,  $d_h/d = 15$  and  $La$  is set to 0 or 1. The terminal bubble velocity computed with JADIM is compared to values computed by Tasoglu *et al.* (2008), who solved the same problem using a Finite Difference/Front-Tracking method. For the chosen parameters, a clean buoyant bubble is spherical (Clift *et al.* (1978)). The terminal values of the bubble Reynolds number,  $Re_b = \rho_c V_b d / \mu_c$ , obtained by Tasoglu *et al.* (2008) for a clean bubble ( $La = 0$ ) and a contaminated one ( $La = 1$ ) are  $Re_b = 0.241$  and  $Re_b = 0.164$ , respectively. Those values are plotted as the blue and red solid lines in Fig. 5.18a, respectively. On this figure, the instantaneous values of  $Re_b$  computed with JADIM, for  $La = 0$  and  $La = 1$ , are presented as the blue and red dashed lines, respectively. The following scale is used to define a dimensionless time:  $t^* = t / \sqrt{d/g}$ .  $Re_b$  is plotted against  $t^*$  in Fig. 5.18a. It is observed that the clean bubble accelerates and reaches smoothly its terminal velocity. It appears that the terminal value of  $Re_b$  computed with JADIM ( $Re_b = 0.239$ ) is in excellent agreement with the one reported by Tasoglu *et al.* (2008). The contaminated bubble (i.e.,  $La = 1$ ) decelerates after an initial acceleration, as surfactants adsorb on the bubble surface. The terminal bubble Reynolds number computed with JADIM,  $Re_b = 0.161$ , is again in very good agreement with the one reported by Tasoglu *et al.* (2008). The convergence rate is verified by computing  $e = (V_b - V_{ref}) / V_{ref}$ , where  $V_b$  is the bubble terminal velocity computed with JADIM with a given mesh, and  $V_{ref}$  is the bubble terminal velocity computed with the finest mesh;  $e$  is presented as a function of  $\Delta x$  in Fig. 5.18b. To guide the eye, a small black solid line is drawn that shows a convergence rate of 1.5. The points on this curve seems to follow this rate. This convergence rate characterizes the whole numerical procedure presented in chapter 4, including the transport of surfactant along

the gas-liquid interface and inside the liquid phase (Eqs. 4.25 and 4.41), the computation of the capillary pressure jump, of the marangoni stress, of the viscous and inertial terms (Eq. 4.1), and the use of the projection method to account for the incompressibility equation (Eq. 4.2). The lowest convergence rate observed in this chapter was close to 1 for the “exchange term”. However, the influence of this terms on the convergence rate of the terminal velocity of the buoyant bubble seems to be limited. The convergence rate of the procedure seems to be dictated by the advection term in Eq. 4.25. Further investigation of this feature is out of the scope of this thesis.

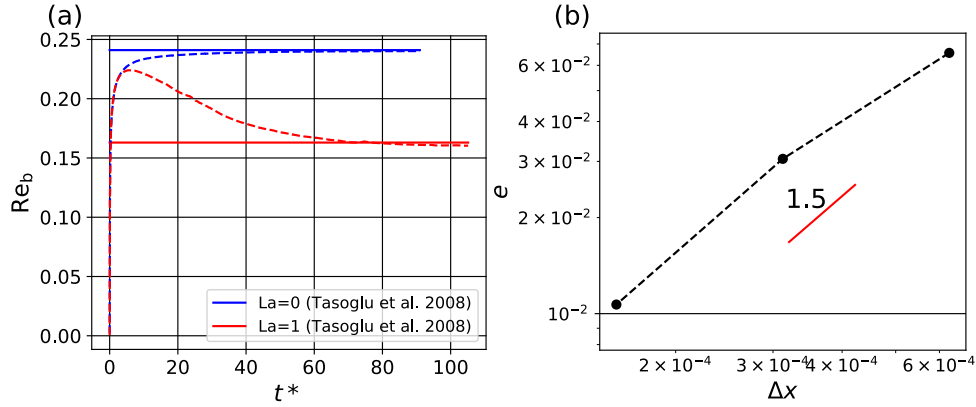


Figure 5.18: This figure refers to the validation test presented in section 5.4. (a) Bubble Reynolds number  $Re_b$  as a function of the dimensionless time computed with JADIM, for  $La = 0$  (dashed blue) and  $La = 1$  (dashed red). Blue and red solid lines: terminal values of  $Re_b$  computed by Tasoglu et al. (2008) using a Finite Difference/Front Tracking method. (b) Convergence parameter  $e$  as a function of  $\Delta x$ .

Simulations were also performed varying  $Eu$ ,  $Mo$  and  $La$ . The drag force acting on the bubble,  $F_d$ , has been computed using the cylindrical coordinate system  $(r, z)$  as follows:

$$F_d = 2\pi \int_{z_r}^{z_f} \left( \tau_{nt}(z, r_I(z)) - \left( -p_c(z, r_I(z)) + \tau_{nn}(z, r_I(z)) \right) r'_I(z) \right) r_I(z) dz \quad (5.15)$$

where  $z_r$  and  $z_f$  are the axial coordinates localizing the back and the front of the bubble, respectively,  $r_I(z)$  is the radial coordinate localizing the gas-liquid interface,  $r'_I = \frac{dr_I}{dz}$ ,  $\tau_{nt} = (\bar{\mathbf{T}} \cdot \mathbf{n}) \cdot \mathbf{t}$  is the tangent viscous stress,  $\tau_{nn} = (\bar{\mathbf{T}} \cdot \mathbf{n}) \cdot \mathbf{n}$  is the normal viscous stress and  $p_c$  is the periodic component of the pressure inside the liquid (i.e.,  $p_c = p + \rho g z$ ). In order to evaluate  $F_d$ , the values of  $\tau_{nt}$  and  $\tau_{nn}$  are first calculated at the center of the computational cells and then interpolated on the gas-liquid interface. Using the coordinate system  $(r, z)$ , the unit tangent vector to the gas-liquid interface is calculated as  $\mathbf{t} = -\frac{1}{\|\nabla\phi\|} \left( \frac{\partial\phi}{\partial r}, -\frac{\partial\phi}{\partial z} \right)$ . The drag coefficient of the spherical bubble, based on the terminal bubble velocity and its diameter, is then computed for each simulation as:

$$C_D = F_d / \left( 0.5 \rho_c \pi (d/2)^2 V_b^2 \right) \quad (5.16)$$

In Fig. 5.19, drag coefficients computed with JADIM are compared to correlations predicting  $C_d$  as a function of  $Re_b$  for a clean spherical bubble (Mei et al. (1994)):

$$C_d = \frac{24}{Re_b} \left( \frac{2}{3} + \left( \frac{12}{Re_b} + 0.75 \left( 1 + \frac{3.315}{Re_b^{1/2}} \right) \right)^{-1} \right) \quad (5.17)$$

and for a rigid sphere (Schiller and Naumann (1935)):

$$C_d = \frac{24}{Re_b} (1 + 0.15 Re_b^{0.687}) \quad (5.18)$$

It can be observed in Fig. 5.18 that varying  $La$  from 0 to 1 allows obtaining a bubble rising with a drag coefficient characterizing a spherical bubble with a clean interface (for  $La = 0$ ) or characterizing a rigid sphere (for  $La = 1$ ).

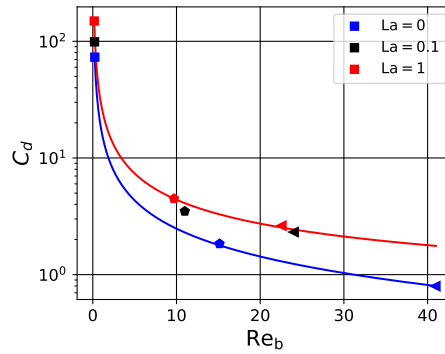


Figure 5.19: Drag coefficient,  $C_d$ , of a buoyant bubble as a function of its Reynolds number (terminal value). Squares, pentagons and triangles are values of the drag coefficient of the bubble computed with JADIM for values of the Bond number and Morton number equal to:  $(Bo = 1; Mo = 0.1)$ ,  $(Bo = 1; Mo = 10^{-5})$  and  $(Bo = 0.1; Mo = 10^{-9})$ , respectively. Blue, black and red symbols are values corresponding to  $La = 0$ ,  $La = 0.1$  and  $La = 1$ , respectively. The blue and red solid lines give values of the drag coefficient predicted by the correlations given in Eqs. (5.17) and (5.18), respectively.

Table 5.1: Validation tests: a summary

Test name	Validated equation number	Order of convergence with $\Delta x$	Order of convergence with $\Delta t$
<i>Expansion test: section 7.2</i>	Eqs. (4.10, 4.11, 4.25 and 4.26)	$\approx 2$	$\approx 3$
<i>Advection test: section 5.1.2</i>	Eqs. (4.25 and 4.26)	$\approx 1.5$	/
<i>Adsorption test: section 5.1.3</i>	Eqs. (4.25 and 4.26)	/	$\approx 3$
<i>Diffusion test: section 5.1.4</i>	Eqs. (4.25 and 4.26)	$\approx 2$	$\approx 2$
<i>Exchange term in the surfactant transport equation inside the bulk phase: section 5.2</i>	Eqs. (4.41 and 4.42)	$\approx 1$	/
<i>Marangoni stress: section 5.3</i>	Eqs. (4.1, 4.10, 4.11)	$\approx 2$	$\approx 3$
<i>Bubble rising in an infinite stagnant liquid: section 5.4</i>	Eqs. (4.1, 4.10, 4.11, 4.25, 4.26, 4.41 and 4.42)	$\approx 1.5$	/

## 5.5 Conclusion

In this section, the implementation of the different terms in the equation describing the surfactant transport on the gas-liquid interface and the computation of the Marangoni stress has been validated. A summary of the test cases and the order of convergence is presented in Table 5.1.

In the next section, the code is applied to study the influence of soluble surfactants on the dynamics of deformable bubble inside horizontal microchannels.

## CHAPTER 6

### Influence of soluble surfactants and deformation on the dynamics of centered bubbles in cylindrical microchannels

This chapter presents a work that has been accepted for publication in the journal entitled *Langmuir* (Atasi *et al.* (2018b)).

#### 6.1 Introduction

Investigation of microscale flows is relevant for many microfluidic applications such as micro-heat exchangers, micro-absorbers and micro-extractors (Han *et al.* (2012); Kashid *et al.* (2011)). In recent years, bubble micro-absorbers were developed for industrial applications and, consequently, the motion of bubbles in microchannels was investigated thoroughly. In such a gas-liquid microscale flow, inertial effects are often negligible while surface tension and viscous forces dominate the system. The relative importance of inertial to viscous forces is assessed by the means of the Reynolds number:  $Re = \rho J_l d / \mu$ , where  $\rho$ ,  $\mu$ ,  $J_l$  and  $d$  are the density and viscosity of the liquid, the mean flow velocity and the bubble diameter, respectively. The Reynolds number characterizing these microscale flows is often close or smaller than unity. The relative importance of viscous forces to surface tension forces is assessed by the means of the capillary number:  $Ca = J_l \mu / \sigma$ , where  $\sigma$  is the surface tension of the gas-liquid interface.

Among the investigations regarding the motion of bubbles in microchannels, the dynamics of bubbles with a volume equivalent diameter,  $d$ , larger than the channel equivalent diameter,  $d_h$ , has received considerable attention (Hassanvand and Hashemabadi (2012); Abiev (2013); Abadie *et al.* (2012); Gupta *et al.* (2010a); Yu *et al.* (2007)). The bubble equivalent diameter is defined as  $d = (6V/\pi)^{1/3}$ , where  $V$  is the bubble volume. For example, it was shown that the mass transfer in those systems is considerably enhanced due to recirculation of the liquid in between bubbles, promoting mixing (Hassanvand and Hashemabadi (2012)). On the other hand, the motion and dissolution of small bubbles in microchannels, i.e., bubbles with  $d/d_h < 1$ , has received less attention. Cubaud *et al.* (2012) studied experimentally and globally the dissolution of spherical bubbles within microchannels. Feng (2010) studied the effect of  $Re$  and  $Ca$  on the dynamics of an isolated small bubble in a horizontal channel. Khodaparast *et al.* (2015) studied, with experiments and numerical simulations, the motion of bubbles inside horizontal channels. In their work,  $Re$  and  $Ca$  were varied (in the ranges  $10^{-3} < Re < 10^3$  and  $10^{-4} < Ca < 10^{-1}$ ) and the shape and the velocity of the bubble,  $V_b$ , was monitored. For  $d/d_h < 1$ , they observed that  $V_b/J_l$  decreases as  $d/d_h$  is increased. The same behavior was observed by Kurimoto *et al.* (2013) for buoyancy driven bubbles in vertical pipes. Stan *et al.* (2011) studied the influence of Archimedes' thrust on the vertical position of spherical bubbles within a horizontal and straight rectangular microchannel. They also observed that, for neutrally buoyant bubbles characterized by small  $Re$  and moderate  $Ca$ , the equilibrium position of the bubble is near the symmetry axis of the channel. At larger  $Re$ , they observed that inertial migration forces shift this position off the horizontal symmetry plane of the channel.

When surfactants are introduced in the liquid, they may adsorb on the bubble surface and alter the surface tension of the gas-liquid interface. Consequently, an inhomogeneous distribution of the surfactants on the interface causes Marangoni stresses, influencing the dynamics of the bubble (Bel Fdhila and Duineveld (1996); Cuenot *et al.*

(1997); Tasoglu *et al.* (2008); Takagi *et al.* (2009); Fukuta *et al.* (2008)). This property of surfactants make them widely used in microfluidics to stabilize emulsions or to favor the formation of bubbles or droplets (Baret *et al.* (2009); Riaud *et al.* (2018)). Regarding the dynamics of small bubbles translating along microchannels, Mikaelian *et al.* (2015) performed direct numerical simulations of spherical bubbles, i.e., for  $Ca \rightarrow 0$ , translating along a horizontal channel. They investigated the effect of bubble confinement, through varying the parameter  $d/d_h$ , on the bubble velocity. They considered two limiting situations to model the presence of surfactants. They imposed a zero shear stress on the gas-liquid interface in order to model the case of a clean interface. The presence of surfactants was accounted for by imposing a no slip condition on the gas-liquid interface (i.e., by imposing that the bubble behaves as a rigid sphere). They established correlations to calculate the ratio of the bubble velocity to the mean flow velocity,  $V_b/J_l$ , as a function of  $d/d_h$ , for the case of a clean interface:

$$\frac{V_b}{J_l} = 1 + \exp \left( -1.83 \left( \frac{d}{d_h} \right)^5 \right) \quad (6.1)$$

and for a bubble behaving as a rigid sphere:

$$\frac{V_b}{J_l} = 1 + \exp \left( -1.92 \left( \frac{d}{d_h} \right)^{\frac{9}{4}} \right) \quad (6.2)$$

These correlations were established in the range  $0 < d/d_h \leq 0.75$ . Note that Rivero-Rodriguez and Scheid (2018) extended the explored numerical range to  $0 < d/d_h \leq 0.9$  and used polynomial fittings to express  $V_b/J_l$  as a function of  $d/d_h$ .

The effect of the surfactants on the velocity of the liquid adjacent to the bubble surface depends on their distribution on the gas-liquid interface. This distribution can be determined by solving the complete set of coupled partial differential equations governing the transport of surfactants on the bubble surface and in the liquid. In a microchannel bubbly flow, due to the bubble confinement created by the channel walls, the distribution of surfactants on the gas-liquid interface is expected to be fundamentally different from their distribution in the case of a bubble rising in an infinite liquid medium. To the best of our knowledge, the distribution of surfactants on the surface of a bubble translating in a horizontal microchannel has not been studied yet. Furthermore, the effect of the bubble deformability (i.e., the effect of  $Ca$ ) on  $V_b/J_l$  in the presence of surfactants has not been studied in previous works.

Accordingly, in this study, we investigate, by direct numerical simulations, the combined effect of the bubble deformability, the presence of surfactants and the bubble confinement on the dynamics of isolated small bubbles (i.e.,  $d/d_h < 1$ ) transported by a liquid in a horizontal microchannel. We consider the presence of surfactants by simulating their transport on the surface of the bubble and inside the liquid phase. We compute the Marangoni stress induced by their inhomogeneous distribution on the surface. The numerical code used for this study is the JADIM code, which has been developed to simulate dispersed two-phase flows (Cuenot *et al.* (1997); Dupont and Legendre (2010); Abadie *et al.* (2015); Legendre and Magnaudet (1998); Legendre *et al.* (2003)). Our analysis emphasizes on several parameters characterizing the system: the bubble shape, the ratio of the bubble velocity to the mean flow velocity,  $V_b/J_l$ , the drag coefficient of the bubble,  $C_d$ , the fluid velocity tangent to the bubble surface,  $V_s/V_b$  and the surfactant distribution on the interface,  $\Gamma$ . Our goal is to highlight and quantify the key phenomena governing the studied system.



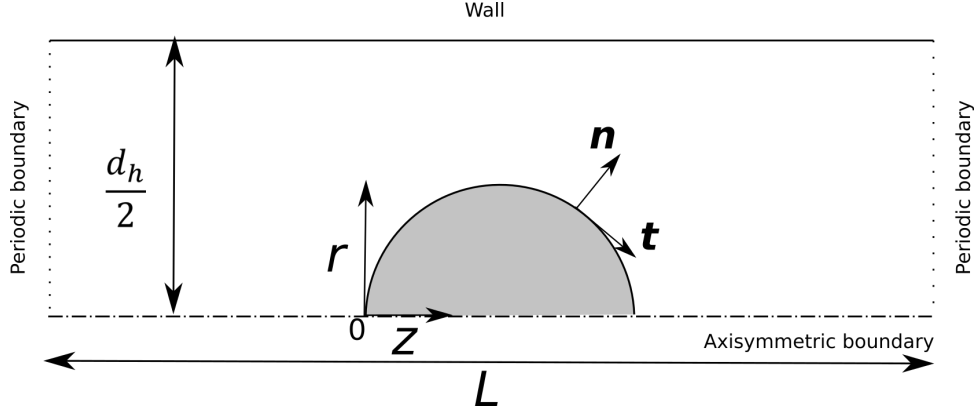


Figure 6.1: Axisymmetric bubble of density  $\rho_d$  and viscosity  $\mu_d$  immersed in a viscous liquid of density  $\rho_c$  and viscosity  $\mu_c$  inside a cylindrical microchannel of length  $L$  and diameter  $d_h$ . The unit vector normal to the gas-liquid interface,  $\mathbf{n}$ , and the unit vector tangent to the gas-liquid interface,  $\mathbf{t}$ , are sketched in this figure.

## 6.2 Problem statement

### 6.2.1 Geometry

We consider an axisymmetric bubble of diameter  $d$  moving in a horizontal and rectilinear microchannel with a circular cross section (referred to as a cylindrical microchannel in this work) of diameter  $d_h$ , as sketched in Fig. (6.1). The channel has a length  $L$  and a pressure difference  $\Delta p > 0$  is imposed between the left and the right boundaries of the domain. The bubble is centered in the channel. Rivero-Rodriguez and Scheid (2018) have recently shown that centered bubbles are stable provided that  $d/d_h$  is larger than 0.85 or that the Ohnesorge number  $\text{Oh} = \sqrt{\text{Ca}/\text{Re}}$  is larger or equal to 0.2 for bubbles with  $d/d_h < 0.85$ . In addition, they showed that, regardless of the value of  $\text{Oh}$ ,  $V_b/J_l$  and the bubble shape are not affected by  $\text{Re}$  provided that  $\text{Re} \lesssim 8$ . In this study, a particular attention is held to ensure that  $\text{Oh} \geq 0.2$ , so that the bubble can be considered as centered. The liquid and the bubble surface contain surfactants with initial concentrations  $C_0$  and  $\Gamma_0$ , respectively.

### 6.2.2 Equations and modeling assumptions

The governing equations are reminded in this section and the modeling assumptions are presented. The numerical method to solve these equations have been presented in Chap. (5). Under the assumptions that (i) the fluids are newtonian and incompressible, (ii) there is no gas-liquid mass transfer through the interface, (iii) the flow is isothermal, the velocity field  $\mathbf{v}$  and the pressure  $p$  satisfy the classical one-fluid formulation of the Navier–Stokes equations (Scardovelli and Zaleski (1999)):

$$\nabla \cdot \mathbf{v} = 0 \quad (6.3)$$

$$\frac{\partial \mathbf{v}}{\partial t} + \mathbf{v} \cdot \nabla \mathbf{v} = -\frac{1}{\rho} \nabla p + \frac{1}{\rho} \nabla \cdot \bar{\mathbf{T}} - \frac{\sigma}{\rho} (\nabla \cdot \mathbf{n}) \mathbf{n} \delta_I - \frac{1}{\rho} \nabla \sigma \delta_I \quad (6.4)$$

where  $\rho$ ,  $\mu$ ,  $\sigma$  are the density, the dynamic viscosity and the surface tension, respectively.  $\bar{\mathbf{T}}$  is the viscous stress tensor,  $\mathbf{n}$  is a unit vector normal to the interface, arbitrarily chosen pointing towards the liquid phase and  $\delta_I$  is the Dirac distribution associated to the bubble-liquid interface.

The transport equations of the surfactants in the liquid phase and on the gas-liquid interface are given by (Stone

(1990); Cuenot *et al.* (1997)):

$$\frac{\partial C}{\partial t} + \mathbf{v}_c \cdot \nabla C = \nabla \cdot (D_c \nabla C) \quad (6.5)$$

$$\frac{\partial \Gamma}{\partial t} + \nabla_s \cdot (\mathbf{v}_s \Gamma) = D_s \nabla_s^2 \Gamma + S_\Gamma \quad (6.6)$$

where  $C$  is the surfactant concentration in the liquid phase,  $\Gamma$  is the surfactant concentration on the gas-liquid interface,  $D_c$  and  $D_s$  are the diffusion coefficients in the liquid phase and on the interface, respectively,  $\mathbf{v}_c$  is the velocity field of the liquid phase ( $\mathbf{v}_c = \mathbf{v}$  when in the liquid phase),  $\mathbf{v}_s$  is the component of  $\mathbf{v}_c$  tangent to the interface and  $\nabla_s = (\bar{\mathbf{I}} - (\mathbf{n} \otimes \mathbf{n})) \cdot \nabla$  (Batchelor (1967)).  $S_\Gamma$  is the flux of surfactants from the liquid phase to the interface, due to the adsorption/desorption of the surfactants, i.e.,  $S_\Gamma = (D_c \mathbf{n} \cdot \nabla C)|_I$ , where the subscript  $I$  denotes the bubble-liquid interface. It is given by (Cuenot *et al.* (1997); Muradoglu and Tryggvason (2008)):

$$S_\Gamma = k_a C_I (\Gamma_\infty - \Gamma) - k_d \Gamma \quad (6.7)$$

where  $k_a$  and  $k_d$  are adsorption and desorption kinetic constants, respectively, and  $C_I$  is the surfactant concentration in the liquid in contact with the interface. It is assumed that the surface tension depends on the surfactant concentration on the interface according to an equation of state derived from the Langmuir adsorption isotherm (Levich (1962)):

$$\sigma = \sigma_0 + RT\Gamma_\infty \ln \left( 1 - \frac{\Gamma}{\Gamma_\infty} \right) \quad (6.8)$$

where  $R$  is the ideal gas constant,  $T$  is the absolute temperature,  $\sigma_0$  is the surface tension of the clean interface and  $\Gamma_\infty$  is the maximum packing concentration of surfactants on the interface.

Considering the boundary conditions, periodicity is imposed between the inlet and the outlet of the domain, simulating therefore a train of bubbles, a no-slip condition with zero transfer rate is imposed on the wall and a symmetry condition is imposed on the symmetry axis:

$$\begin{cases} \mathbf{v}|_{z_{\text{left}}} = \mathbf{v}|_{z_{\text{right}}} \\ \mathbf{v}|_{r=d_h/2} = 0 \\ \mathbf{v} \cdot \mathbf{n}_a|_{r=0} = 0 \end{cases} \quad (6.9)$$

$$\begin{cases} C|_{z_{\text{left}}} = C|_{z_{\text{right}}} \\ \nabla C \cdot \mathbf{n}_w|_{r=d_h/2} = 0 \\ \nabla C \cdot \mathbf{n}_a|_{r=0} = 0 \end{cases} \quad (6.10)$$

$$\begin{cases} \Gamma|_{z_{\text{left}}} = \Gamma|_{z_{\text{right}}} \\ \nabla \Gamma \cdot \mathbf{n}_a|_{r=0} = 0 \end{cases} \quad (6.11)$$

$$\left\{ p \right\}_{z_{\text{left}}} = \left\{ p \right\}_{z_{\text{right}}} + \Delta p \quad (6.12)$$

where  $\mathbf{n}_w$  is the unit vector normal to the channel wall,  $\mathbf{n}_a$  is the unit vector normal to the symmetry axis,  $(z, r)$  are the axial and radial coordinates, respectively (see Fig. (6.1)) and  $z_{\text{left}}$  and  $z_{\text{right}}$  are the axial coordinates localizing the left and right boundaries of the computational domain, respectively.

### 6.2.3 Dimensional analysis

The governing equations are solved in their dimensional forms and the results are expressed in terms of relevant dimensionless parameters. Let  $\mathcal{L}$  and  $\mathcal{U}$  be appropriately defined length and velocity scales, respectively. The number of dimensional parameters, 16, minus the number of dimensions, 4, results in 12 dimensionless numbers allowing to characterize the problem. Two of them characterize the geometry of the system, while 10 others characterize its dynamics. These 10 dimensionless numbers are defined as follows:

$$\begin{aligned} \text{Re} &= \frac{\rho_c \mathcal{U} \mathcal{L}}{\mu_c}, \text{Ca} = \frac{\mu_c \mathcal{U}}{\sigma_0}, m = \frac{\rho_d}{\rho_c}, \lambda = \frac{\mu_d}{\mu_c} \\ E &= \frac{RT\Gamma_\infty}{\sigma_0}, \text{La} = \frac{k_a C_\infty}{k_d}, \text{Da} = \frac{\Gamma_\infty}{\mathcal{L} C_\infty}, \alpha = \frac{k_a C_\infty \mathcal{L}}{\mathcal{U}}, \text{Pe} = \frac{\mathcal{U} \mathcal{L}}{D_c}, \text{Pe}_s = \frac{\mathcal{U} \mathcal{L}}{D_s} \end{aligned}$$

where  $\text{Re}$ ,  $\text{Ca}$ ,  $E$ ,  $\text{La}$ ,  $\text{Da}$ ,  $\alpha$ ,  $\text{Pe}$ ,  $\text{Pe}_s$ ,  $m$ ,  $\lambda$  are the Reynolds number, the Capillary number, the Elasticity number, the Langmuir number, the Damkohler number, the dimensionless adsorption rate, the Peclet number based on the bulk surfactant diffusivity, the Peclet number based on the interfacial surfactant diffusivity, the ratio of the gas viscosity ( $\mu_d$ ) to the liquid viscosity ( $\mu_c$ ) and the ratio of the gas density ( $\rho_d$ ) to the liquid density ( $\rho_c$ ), respectively.

The velocity scale  $\mathcal{U}$  is set equal to the mean velocity of the monophasic liquid Poiseuille flow that would have been generated by the imposed pressure gradient,  $\Delta p/L$ :  $\mathcal{U} = J_{l\text{ref}} = \Delta p d_h^2 / (32\mu_c L)$ , and the length scale is set as  $\mathcal{L} = d$ . This length scale sets the two dimensionless numbers characterizing the geometry:  $d/d_h$  and  $L/d$ . It has been verified that the difference between  $J_{l\text{ref}}$  and the actual value of  $J_l$  obtained in the simulations varies between 0.8% and 2.8%, confirming that the chosen scale is appropriate for the setup considered in this work. The Capillary number, the Langmuir number and the ratio of the bubble equivalent diameter to the tube diameter are varied in the range:  $10^{-2} < \text{Ca} < 1$ ,  $0 < \text{La} < 10$  and  $0.15 < d/d_h < 0.75$ , respectively. The other parameters are set to values usually encountered for surfactants in bubbly flows:  $\text{Da} = 0.1$ ,  $E = 0.12$ ,  $\alpha = 0.1$ ,  $\text{Pe}_s = \infty$  (Takemura (2005); Takagi *et al.* (2009)). Furthermore the parameters  $m$  and  $\lambda$  are set to  $m = 10^{-3}$  and  $\lambda = 10^{-2}$ , which are typical values encountered in bubbly flows. In order to satisfy the criterion  $\sqrt{\text{Ca}/\text{Re}} \geq 0.2$ , the value of  $\text{Re}$  is either set equal to 1 if  $\text{Ca} \geq 0.04$ , or to  $\text{Ca}/0.04$  if  $\text{Ca} < 0.04$ . As discussed earlier, the bubble shape and  $V_b/J_l$  do not depend on  $\text{Re}$  for  $\text{Re} \lesssim 8$ . The value of  $\text{Pe}$  sets the thickness of the surfactant diffusion boundary layer around the bubble. A particular attention has to be paid to capture the surfactant concentration gradients within this boundary layer. As a consequence, the value of  $\text{Pe}$  is set to a moderate value,  $\text{Pe} = 500$ , in order to avoid too large computational costs. The value of  $L/d$  is increased gradually, starting from 4, until  $V_b/J_l$  becomes independent of  $L/d$ .

## 6.3 Results

In this section, the dynamics of an isolated small bubble inside a horizontal microchannel is studied. Initially, i.e., at  $t = 0$  s, the bubble is at the center of the computational domain, as sketched in Fig. (6.1). The liquid surrounding the bubble contains surfactants with an initially homogeneous concentration,  $C_\infty$ . The independency of the bubble terminal velocity on the initial surfactant concentration on the bubble-liquid interface,  $\Gamma_0$ , has been verified. To illustrate this statement, the instantaneous bubble velocity,  $V_b$ , is presented in Fig. (6.2) as a function of the time  $t$ , for different values of  $\Gamma_0$ , as compared to the equilibrium value  $\Gamma_{\text{eq}} = \Gamma_\infty \frac{\text{La}}{1+\text{La}}$ . For  $\Gamma_0 = 0$ , it can

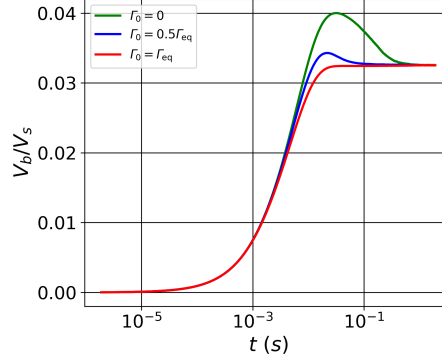


Figure 6.2:  $V_b$  as a function of the time for different values of the initial concentration of surfactants on the gas-liquid interface:  $\Gamma_0 = 0$ ,  $\Gamma_0 = 1/2\Gamma_{eq}$  and  $\Gamma_0 = \Gamma_{eq}$ , for  $Ca = 0.01$ ,  $d/d_h = 0.75$  and  $Re = 0.25$ .

be observed that the bubble first accelerates. Then, as surfactants adsorb on the bubble-liquid interface,  $V_b$  begins to decrease until it reaches its terminal value. When  $\Gamma_0$  is increased, the bubble reaches its terminal velocity at an earlier time. It is observed that this terminal velocity is not affected by the value of  $\Gamma_0$ . Therefore, in all the numerical simulations presented in this work, the initial concentration of surfactants on the bubble-liquid interface is set to the equilibrium value:  $\Gamma_0 = \Gamma_{eq}$ . In this way, the effective simulation time is reduced.

The mass of surfactants is monitored on the bubble surface as:  $M(t) \equiv \int_{S(t)} \tilde{\Gamma} dS(t)$ , following the method of Xu and Zhao (2002). In appendix, we provide more information about the calculation of  $M(t)$  and how it evolves along the simulation. The simulations are stopped when  $\|\frac{dM(t)}{dt}\|/M(t) < 0.01$  and  $\|\frac{dV_b(t)}{dt}\|/V_b(t) < 0.01$ . Unless explicitly mentioned, all the results presented in this section relate to a stationary state of the studied system.

In the first part of the result section, the dynamics of an isolated spherical bubble, i.e.,  $Ca \ll 1$ , inside a horizontal microchannel is studied. The second part deals with the shape and the flow field around a deformable bubble, in the absence of surfactants. Finally, the combined effect of surfactants and bubble deformability on the bubble dynamics is analyzed.

### 6.3.1 Spherical bubbles

Fig. (6.3) presents the steady state surface concentration field of the surfactants,  $\tilde{\Gamma}$ , (presented at the vicinity of the bubble surface only), bulk concentration field of the surfactants,  $C$ , and velocity streamlines in a reference frame attached to the bubble mass center, for  $Re = 0.25$ ,  $Ca = 10^{-2}$ ,  $d/d_h = 0.75$ ,  $La = 0$  (Fig. (6.3a)),  $La = 0.1$  (Fig. (6.3b)),  $La = 1$  (Fig. (6.3c)) and  $La = 10$  (Fig. (6.3d)). The bubble moves from the left to the right in a laboratory reference frame. As expected, for  $Ca = 10^{-2}$  and for  $Re \sim 1$ , the bubble is spherical. As it can be observed in Fig. (6.3), the structure of the liquid flow in the microchannel appears to differ significantly from the one observed when a bubble rise in a liquid of infinite extend. More specifically, it is observed that the flow structure generates a convergent stagnation point at the front of the bubble (point A in Fig. (6.4)) and a divergent stagnation point at the rear of the bubble (point B in Fig. (6.4)). Moreover, the flow generates a convergent stagnation circle on the back half of the bubble side (C in Fig. (6.4)) and a divergent stagnation circle on the front half of the bubble side (D in Fig. (6.4)). Consequently, on the surface, the surfactants accumulate near the convergent point/circle and are depleted near the divergent point/circle. This is clearly observed in Fig. (6.3).

The surfactants reduce the surface tension and, consequently, their inhomogeneous distribution on the bubble-liquid interface induces surface tension gradients that are expected to alter the fluid velocity along the interface.

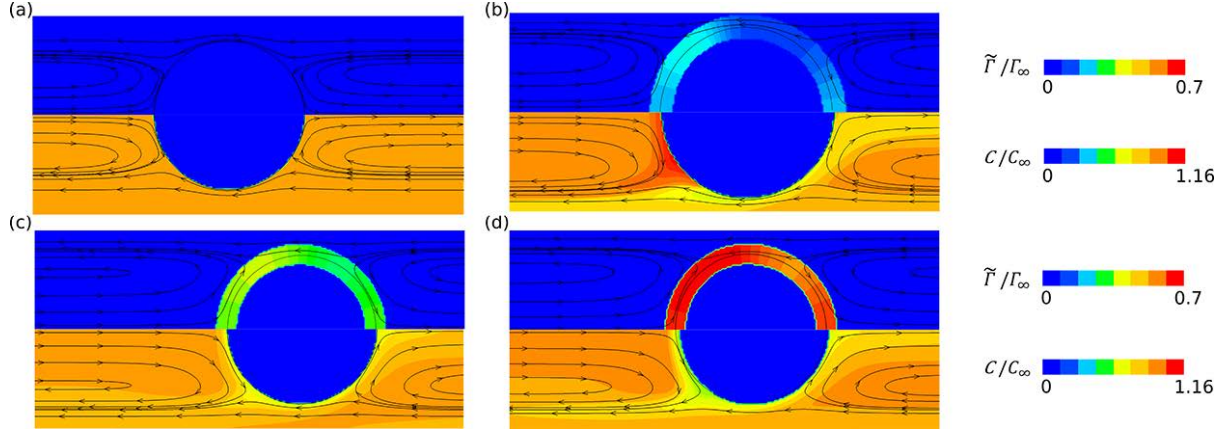


Figure 6.3: Contour plots of (top) the surfactant concentration field on the bubble surface,  $\tilde{\Gamma}$ , and (bottom) the bulk surfactant concentration field,  $C$ . Velocity streamlines are drawn in a reference frame translating with the bubble. The bubble moves from the left to the right. (a)  $La = 0$ , (b)  $La = 0.1$ , (c)  $La = 1$  and (d)  $La = 10$ .

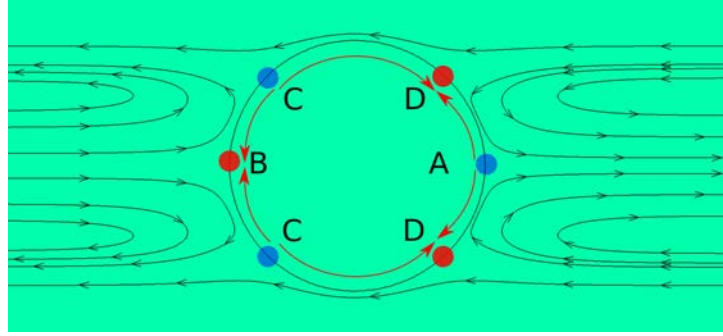


Figure 6.4: A spherical bubble inside a microchannel. The bubble goes from left to right. Red dots depict a divergent stagnation point/circle on the bubble surface, where consequently the surface tension is high. Blue dots depict a convergent stagnation point/circle on the bubble surface where the surface tension is low. Velocity vectors, in black, are drawn in a reference frame attached to the bubble mass center. Red arrows depict the direction of the Marangoni stress.

In Figs. (6.5a-d), the dimensionless surfactant concentration on the bubble surface,  $\tilde{\Gamma}/\Gamma_\infty$ , the dimensionless tangent shear stress on the bubble surface,  $\tau_{nt}d/(V_b\mu_c)$ , the dimensionless surfactant concentration inside the liquid adjacent to the bubble surface,  $C/C_\infty$ , and the dimensionless gas-liquid relative velocity on the bubble surface,  $V_s/V_b$ , where  $V_s = (V_b - \mathbf{v} \cdot \mathbf{t})$ , are plotted as functions of the axial coordinate,  $z$ , for different values of  $La$  and with  $Re = 0.25$ ,  $Ca = 0.01$  and  $d/d_h = 0.75$ . Note that the origin of the axial coordinate,  $z = 0$ , is at the back of the bubble. As described previously, the recirculating flow in between bubbles causes surfactants to accumulate near the convergent stagnation point/circle on the bubble surface and to deplete near the divergent stagnation point/circle. This is confirmed by Fig. (6.5a). Notably, for  $La = 0.1$ , the adsorption flux of surfactants towards the bubble surface is not sufficient to maintain surfactants around the divergent stagnation circle on the front half of the bubble side (point D in Fig. (6.4)) and, consequently, the bubble surface is almost clean of surfactants near this divergent stagnation circle. The tangent shear stress distribution on the bubble surface is shown on Fig. (6.5b). It can be observed that the shear stress increases as  $La$  is increased. The shear stress is positive on the side of the bubble and becomes negative at the back and at the front of the bubble. At the front of the bubble, near the convergent stagnation point on the bubble surface (point A in Fig. (6.4)), surfactants accumulate. On the contrary, near the divergent stagnation circle on the front half of the bubble (point D in Fig. (6.4)), surfactants are depleted. This creates a Marangoni stress directed towards the back of the bubble, as sketched on Fig. (6.4), leading to the negative values of  $\tau_{nt}$  at the front of the bubble for  $La > 0$  (see Fig. (6.5b)).

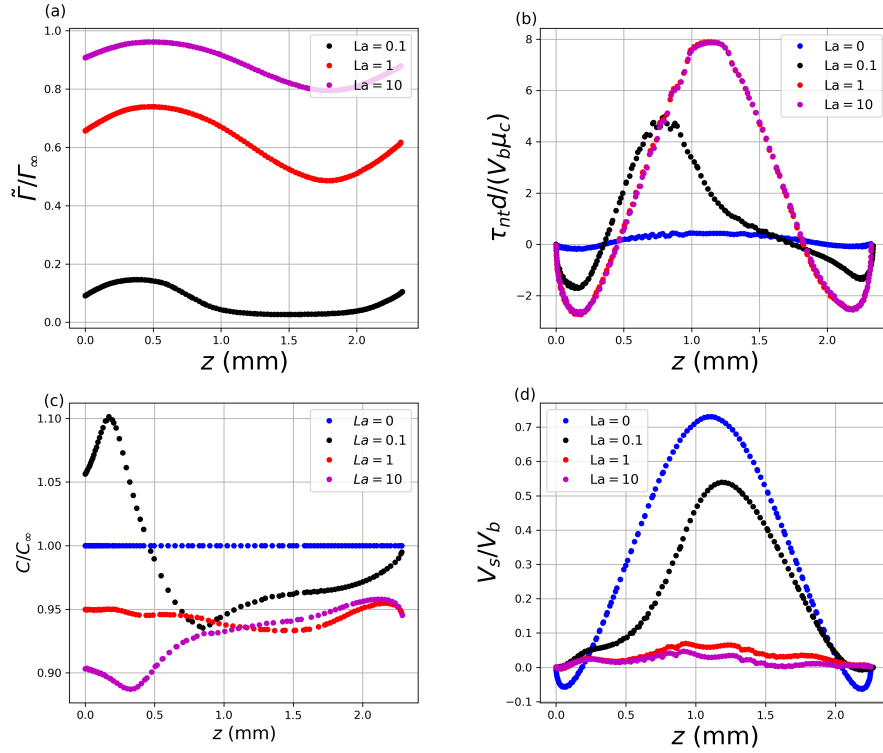


Figure 6.5: (a) Dimensionless surfactant concentration on the bubble surface,  $\tilde{\Gamma}/\Gamma_\infty$ , (b) dimensionless shear stress tangent to the bubble surface,  $\tau_{nt}d/(V_b\mu_c)$ , (c) dimensionless surfactant concentration inside the liquid adjacent to the bubble surface,  $C/C_\infty$ , (d) dimensionless liquid velocity tangent to the bubble surface,  $V_s/V_b$ , as functions of the axial coordinate,  $z$ , for different value of  $La$ ;  $z = 0$  is at the back of the bubble. The other dimensionless numbers are fixed to  $Re = 0.25$ ,  $Ca = 0.01$  and  $d/d_h = 0.75$ .

A Marangoni stress directed towards the back of the bubble is also generated between C and B, for  $La > 0$  (see Fig. (6.5b)). On the other hand, as shown in Fig. (6.5b), on the side of the bubble, for  $La > 0$ , a Marangoni stress induced in between the divergent stagnation circle and the convergent one is directed towards the front of the bubble, as sketched in Fig.(6.4). It is observed in Fig. (6.5b) that the tangent shear stress reaches a maximum on the side of the bubble, where the gap between the bubble and the channel wall is the smallest. For  $La = 0.1$ , as discussed previously, the surfactant adsorption towards the interface is small when compared to the advective flux of surfactant from the divergent stagnation circle to the convergent stagnation one. As a consequence, the shear stress on the bubble surface does not increase significantly on the front part of the bubble when  $La$  is increased from 0 to 0.1. It is observed on Fig. (6.5b) that the tangent shear stress,  $\tau_{nt}$ , becomes independent of  $La$  when  $La > 1$ . It should be noted that, as it might have been expected,  $\tau_{nt}d/(V_b\mu_c)$  reaches its maximum value at locations on the bubble surface where  $\nabla\tilde{\Gamma}$  is high. For instance, the shear stress profile on the bubble surface presented on Fig. (6.5b), for  $La = 0.1$ , exhibits a maximum at  $z \approx 0.75$  mm. At that location on the bubble surface,  $\tilde{\Gamma}/\Gamma_\infty$  exhibits an important gradient, as it can be observed in Fig. (6.5a), for  $La = 0.1$ . It might be expected that the Marangoni stresses induced by the interaction between the flow structure and the surfactants tend to immobilize (in a reference frame attached to the bubble) the bubble surface for large values of  $La$ . This is characterized in Fig. (6.5d), where  $V_s/V_b$  is plotted against the axial coordinate,  $z$ . When  $La = 0$ , the surface velocity is positive on the side of the bubble, and changes sign near the front and the back of the bubble due to the recirculating flow. When  $La$  is increased to 0.1, the fluid velocity is significantly reduced on the side of the bubble. Moreover,  $V_s$  is also significantly modified on the front/back of the bubble. For instance,  $V_s/V_b$  reaches almost the value of 0 in between the convergent stagnation point and the divergent stagnation circle on the front half of the

bubble side (between A and D in Fig. (6.4)): the Marangoni stress induced in between the convergent stagnation point and the divergent stagnation circle tends to immobilize the interface, in this region, when  $La$  is increased from 0 to 0.1. As  $La$  is increased to 1,  $V_s$  approaches 0 everywhere on the bubble surface: the Marangoni stress created in between the convergent stagnation circle (C in Fig. (6.4)) and the divergent one (D in Fig. (6.4)) leads almost to the interface immobilization.

The surfactants induce an immobilization of the bubble surface (in a reference frame attached to the bubble) through the mechanisms discussed in the previous paragraph. Thus, it might be expected that the surfactants have a significant impact on the velocity of the spherical bubble. An important parameter in microfluidic bubbly flow is the ratio of the bubble velocity,  $V_b$ , to the mean flow velocity,  $J_l$ . Mikaelian *et al.* (2015) established correlations, valid for an isolated spherical bubble (i.e., for  $Ca \rightarrow 0$ ), to calculate this ratio as a function of  $d/d_h$ , for two limiting situations. (i) They imposed a stress-free condition on the bubble surface to model a situation without surfactants. They proposed Eq. (6.1) to calculate  $V_b/J_l$  in this limiting situation. (ii) They imposed a no slip condition at the bubble surface to model the influence of surfactants. They proposed Eq. (6.2) to calculate  $V_b/J_l$  in this situation. The ratio  $V_b/J_l$  is presented on Fig. (6.6) as a function of  $d/d_h$ , for different values of  $La$  and for  $Ca = 0.01$  and  $Re = 0.25$ . Eq. (6.1) and (6.2) are represented on this figure as the blue and red solid lines, respectively. Squares give values calculated with JADIM for  $La = 0, 0.1, 1$  and  $10$ . It is observed that the two limiting cases are well reproduced by our simulations, for  $La = 0$  and  $La = 1$ . An intermediate value of  $V_b/J_l$  is obtained for  $La = 0.1$ . In line with the observations in the previous paragraph,  $V_b/J_l$  becomes independent of  $La$  for  $La > 1$ : the value of  $V_b/J_l$  that characterizes a bubble behaving as a rigid sphere is obtained for  $La > 1$ . It is worth pointing out that, as seen in the previous section, a spherical bubble rising in a stagnant liquid of infinite extent containing surfactants behaves also as a rigid sphere regarding its velocity when  $La \geq 1$ . The analysis of the velocity field for the different cases shows that recirculations at the front and at the back of the bubble are present for all the cases presented in Fig. (6.6), except for the one with  $La = 0$  and  $d/d_h = 0.15$ . This is coherent with the results of Mikaelian *et al.* (2015).

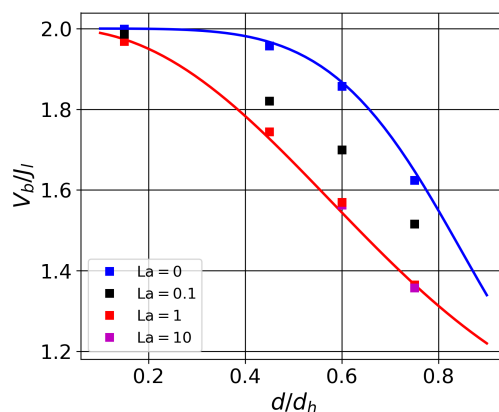


Figure 6.6: Ratio of the bubble velocity to the mean flow velocity,  $V_b/J_l$ , as a function of the ratio of the bubble diameter to the channel diameter,  $d/d_h$ . Blue and red solid lines are the correlations established numerically by Mikaelian *et al.* (2015) for a stress free and an immobile interface, respectively. Squares give values obtained with JADIM, for different values of  $La$  and for  $Re = 0.25$  and  $Ca = 0.01$

### 6.3.2 Deformable bubble without surfactants

In this subsection, the bubble shape, the bubble drag coefficient,  $C_d$ , and the ratio of the bubble velocity to the mean flow velocity,  $V_b/J_l$ , are analyzed without surfactants. Accordingly,  $Ca$  is varied between 0.01 and 1, with

$La = 0$ . The bubble shape is characterized by plotting the  $(r, z)$  coordinates of the bubble interface as well as by computing the curvature of its interface:  $\kappa = -\nabla \cdot (\nabla \phi / \|\nabla \phi\|)$ . Results regarding the bubble shape are presented on Figs. (6.7a,b and c), for  $d/d_h = 0.45, 0.6$  and  $0.75$ , respectively. The red ( $Ca = 0.01$  and  $Re = 0.25$ ), blue ( $Ca = 0.1$  and  $Re = 1$ ) and green ( $Ca = 1$  and  $Re = 1$ ) symbols give values of the  $(r, z)$  coordinates of the bubble interface. It is observed that the shape of the bubble is nearly spherical for  $Ca = 0.01$  and  $Ca = 0.1$ , for all values of  $d/d_h$ . However, when  $Ca = 1$ , the bubble is elongated and takes a “bullet shape”. This shape is further characterized on Figs. 6.7(d,e and f), where the curvature,  $\kappa$ , of the gas-liquid interface is plotted as a function of the axial coordinate,  $z$ . The curvature  $\kappa$  is normalized by the curvature of a spherical bubble that has the same volume:  $2/d$ . When  $Ca = 0.01$ , the curvature of the bubble is constant and equal to  $2/d$ , regardless of the value of  $d/d_h$ , as depicted by the red dots on Figs. (6.7d,e and f). When  $Ca = 0.1$ ,  $\kappa$  is not constant along the bubble interface. For example, the dimensionless curvature profile shown on Fig. (6.7f) for  $Ca = 0.1$  ( $Re = 1$ ,  $d/d_h = 0.75$ ) exhibits a value larger than one at  $z \approx 0.5$  mm ( $\kappa d/2 \approx 1.5$ ) and a value smaller than one at  $z \approx 1.5$  mm ( $\kappa d/2 \approx 0.75$ ). At the front of the bubble,  $\kappa d/2$  is also larger than one and, at the back, it is smaller than one. For  $Ca = 1$  ( $Re = 1$ ,  $d/d_h = 0.75$ , Fig. (6.7f)), the normalized curvature is reduced all along the body of the bubble except near its front and its back.

The dimensionless normal viscous stress on the interface,  $\tau_{nn}d/(V_b\mu_c)$ , is plotted against the axial coordinate,  $z$ , on Figs. (6.7g,h and i), for  $d/d_h = 0.45, 0.6$  and  $0.75$ , respectively. Note that a negative value of  $\tau_{nn}d/(V_b\mu_c)$  indicates a stress directed from the liquid toward the bubble interface (i.e., “pushing” the interface). On the contrary, a positive value of  $\tau_{nn}d/(V_b\mu_c)$  indicates a normal stress directed from the interface towards the liquid phase (i.e., “pulling” the interface). It is observed that  $\tau_{nn}d/(V_b\mu_c)$  is below zero near the divergent stagnation circle on the bubble surface on the front half of the bubble. On the contrary,  $\tau_{nn}d/(V_b\mu_c)$  is higher than zero near the convergent stagnation circle on the bubble surface, on the back half of the bubble. Finally, on Figs. (6.7j,k and l), the periodic component of the dimensionless pressure in the liquid on the interface,  $p_c d/(V_b\mu_c)$ , where  $p_c = p + \frac{\Delta p}{L}z$ , is plotted as a function of  $z$ . It is observed that  $-p_c$  and  $\tau_{nn}$  roughly follow the same trends,  $-p_c$  being significantly smaller than  $\tau_{nn}$  for the cases reported here. The normal stress balance at the bubble-liquid interface is written, for moderate values of  $Re$ , neglecting the viscosity of the gas phase, in dimensionless form, as:

$$\bar{p}_d - \bar{p}_c + \bar{\tau}_{nn} \approx \frac{1}{Ca_b} \bar{\kappa} \quad (6.13)$$

where  $\bar{p}_d = p_d d/(V_b\mu_c)$  is the periodic component of the dimensionless pressure in the gas on the interface,  $\bar{p}_c = p_c d/(V_b\mu_c)$ ,  $\bar{\tau}_{nn} = \tau_{nn}d/(V_b\mu_c)$ ,  $\bar{\kappa} = \kappa d$  and  $Ca_b = \mu_c V_b/\sigma_0$ . Eq. (6.13) shows that, as  $\bar{p}_d$  is almost constant, an increase of  $\bar{p}_c$  or a decrease of  $\bar{\tau}_{nn}$  leads to a decrease of  $\bar{\kappa}$ . Reciprocally, a decrease of  $\bar{p}_c$  or an increase of  $\bar{\tau}_{nn}$  leads to an increase of  $\bar{\kappa}$ . This can be observed by comparing Figs. (6.7d and g), Figs. (6.7e and h) and Figs. (6.7f and i). The recirculating flow in between bubbles generates points (or circles) on the bubble surface where the normal viscous stress is locally negative, near the divergent stagnation point (or circle), or positive, near the convergent stagnation point (or circle). Thus, Eq. (6.13) shows that, as  $Ca_b$  (or similarly  $Ca$ ) is increased, the inhomogeneous distribution of the normal viscous stress (and pressure) on the bubble surface, generated by the recirculating flow, causes the curvature of the bubble surface to decrease near the divergent stagnation point (or circle) and to increase near the convergent stagnation point (or circle). This leads to the elongation of the bubble as  $Ca$  is increased.

Due to the recirculating flow in between bubbles, the bubble elongates as  $Ca$  is increased in contrast to the case of a bubble rising in a stagnant liquid of infinite extent where the bubble is flattened. Thus, the drag coefficient of the bubble  $C_d = 4F_d / \left( \frac{1}{2} (V_b - J_l)^2 \pi d^2 \right)$  based on the bubble equivalent diameter and the relative velocity  $(V_b - J_l)$ , is expected to be affected by the deformability of the bubble in a particular way. The drag coefficient of the bubble is computed as presented in the validation section. It is plotted in Fig. (6.8a) as a function of  $Ca$ , for  $d/d_h = 0.15, 0.45, 0.6$  and  $0.75$ , respectively. Note that the values of the drag coefficient computed with JADIM



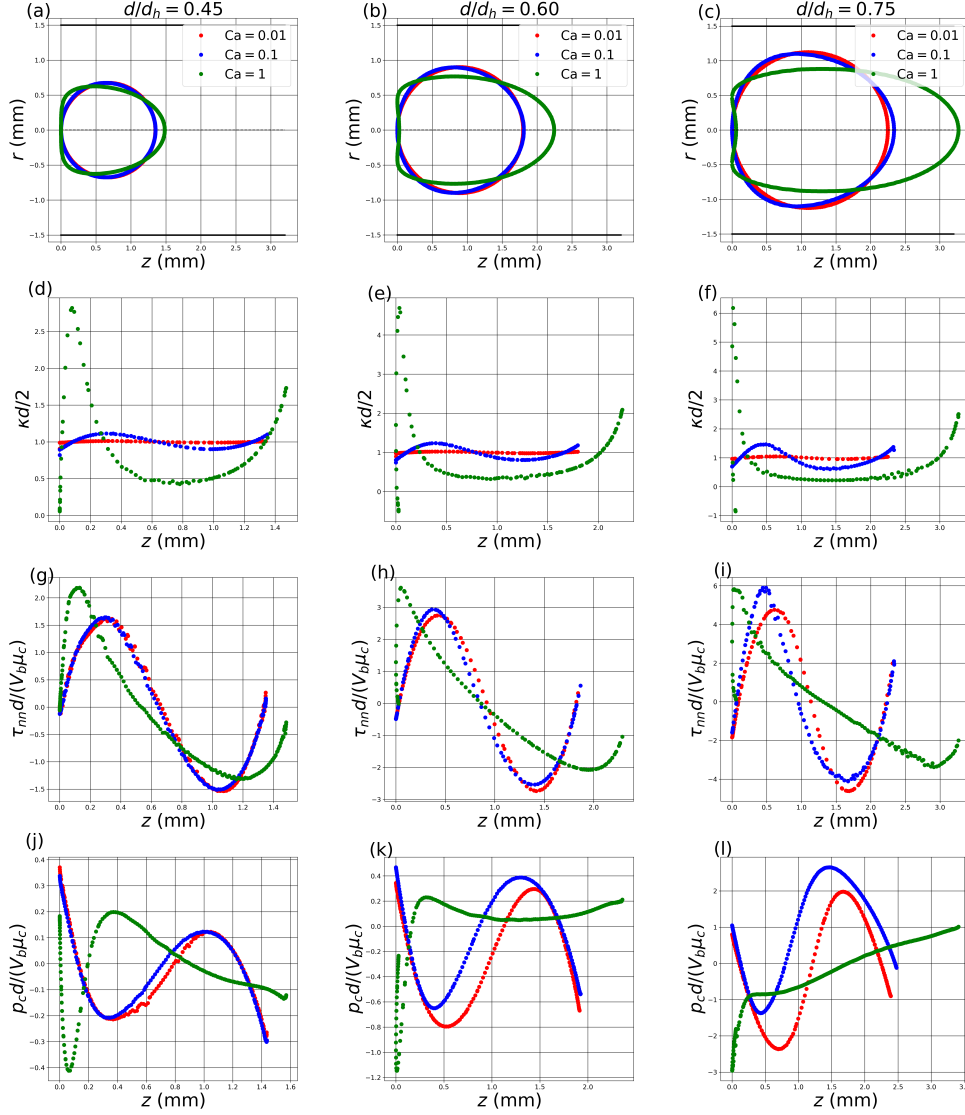


Figure 6.7: (first row) Radial position of the interface as a function of  $z$ . (second row) Normalized curvature,  $\kappa d/2$ , as a function of  $z$ . (third row) Dimensionless normal viscous stress on the bubble surface,  $\tau_{nn}d/(V_b\mu_c)$ , as a function of  $z$ . (fourth row) Dimensionless liquid pressure on the bubble surface,  $p_cd/(V_b\mu_c)$ , as a function of  $z$ . The different columns correspond to: (first column)  $d/d_h = 0.45$ , (second column)  $d/d_h = 0.6$  and (third column)  $d/d_h = 0.75$ , respectively. Red dots:  $Ca = 0.01$ , blue dots:  $Ca = 0.1$ , green dots:  $Ca = 1$ . These results have been obtained for a clean interface, i.e.,  $La = 0$ .

are in good agreement with the ones deduced from calculations obtained by Rivero-Rodriguez and Scheid (2018). It is observed that, in general, the drag coefficient of the bubble decreases as  $d/d_h$  decreases. It is observed that  $C_d$  is almost constant with respect to  $Ca$  when  $d/d_h < 0.45$ . However, for larger values of this ratio,  $C_d$  decreases when  $Ca$  gets larger than 0.1. To understand this effect, the radius of the projection of the bubble on a plane perpendicular to the  $z$  axis,  $r_p$ , is plotted against  $Ca$  in a small insert in Fig. (6.8a). As the capillary number is increased from 0.1 to 1,  $r_p$  decreases from  $d/2$  to less than  $0.8d/2$ . As discussed in the previous paragraph, the recirculating flow in between bubbles causes the bubble to elongate for  $Ca \sim 1$ . As the bubble elongates,  $r_p$

decreases leading to the reduction of the drag force acting on the bubble. This partly explains why  $C_d$  decreases when  $Ca$  is increased, as  $C_d$  is defined using the equivalent diameter,  $d$ . An alternative drag coefficient can be defined using  $\pi r_p^2$  as the reference surface:  $C_d^* = F_d / (0.5 (V_b - J_l)^2 \pi r_p^2)$ . This alternative drag coefficient is plotted as a function of  $Ca$  in Fig. (6.8b). It is observed that  $C_d$  and  $C_d^*$  exhibits the same kind of evolution with respect to  $Ca$ , though  $C_d^*$  is slightly less affected by  $Ca$  than  $C_d$ . This indicates that the change in the distribution of the pressure and of the normal viscous stress on the bubble surface induced when increasing  $Ca$  (see Figs. (6.7g,h,i,j,k and l)) is mainly responsible of the reduction of  $C_d$ . Notably, it is shown in the next section that the convergent stagnation circle on the front half of the bubble disappear when  $Ca$  is increased beyond  $Ca \sim 0.5$ .

$C_d$  is reduced as  $Ca$  is increased, especially for values of  $d/d_h > 0.6$ . Thus, the effect of  $Ca$  on  $V_b/J_l$  is expected to be significant, especially for values of  $d/d_h > 0.6$ . In Fig. (6.9),  $V_b/J_l$  is plotted as a function of  $d/d_h$ , for  $Ca = 0.01$ ,  $Ca = 0.1$ ,  $Ca = 0.5$  and  $Ca = 1$ .  $V_b/J_l$  decreases as  $d/d_h$  increases when  $Ca = 0.01$  and  $Ca = 0.1$ . However, when  $Ca = 0.5$  or  $Ca = 1$ , it is observed that  $V_b/J_l$  increases and takes a value larger than 2 as  $d/d_h$  is increased. Furthermore, at a constant value of  $d/d_h$ , increasing  $Ca$  leads to an increase of  $V_b/J_l$ . For instance, when  $d/d_h = 0.75$ ,  $V_b/J_l$  increases from 1.6 to 2.2 when  $Ca$  is increased from  $10^{-2}$  to 1.

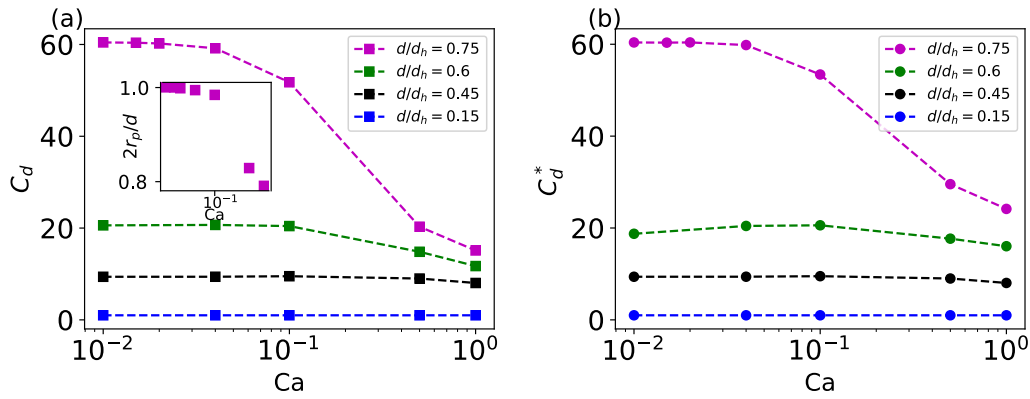


Figure 6.8: (a) Drag coefficient,  $C_d = 4F_d / (0.5 (V_b - J_l)^2 \pi d^2)$ , as a function of  $Ca$ , for  $La = 0$  and for different values of  $d/d_h$ . (b) Drag coefficient based on the effective projection area of the bubble on a plane perpendicular to the main flow direction,  $C_d^* = F_d / (0.5 (V_b - J_l)^2 \pi r_p^2)$ , as a function of  $Ca$ , for  $La = 0$  and for different values of  $d/d_h$ .

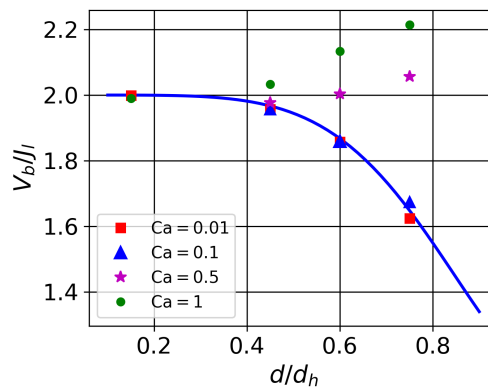


Figure 6.9:  $V_b/J_l$  as a function of  $d/d_h$ , for  $Ca = 0.01$ ,  $Ca = 0.1$ ,  $Ca = 0.5$  and  $Ca = 1$  depicted by squares, triangles, stars and circles, respectively. There is no surfactant in the system. The blue solid line is the correlation established numerically by Mikaelian et al. (2015), predicting the value of  $V_b/J_l$  for a bubble having a clean surface.

### 6.3.3 Deformable bubble with surfactants

In this subsection, the combined effect of  $La$  and  $Ca$  on the bubble dynamics is analyzed for  $d/d_h = 0.75$ . The steady state surfactant concentration on the surface,  $\tilde{\Gamma}$ , (presented at the vicinity of the bubble surface only) and in the liquid,  $C$ , are presented on Fig. (6.10), for  $d/d_h = 0.75$ ,  $Re = 1$ ,  $Ca = 0.5$ , (a)  $La = 0$ , (b)  $La = 0.1$ , (c)  $La = 1$  and (d)  $La = 10$ . It is observed that the bubble is elongated and that recirculations have disappeared

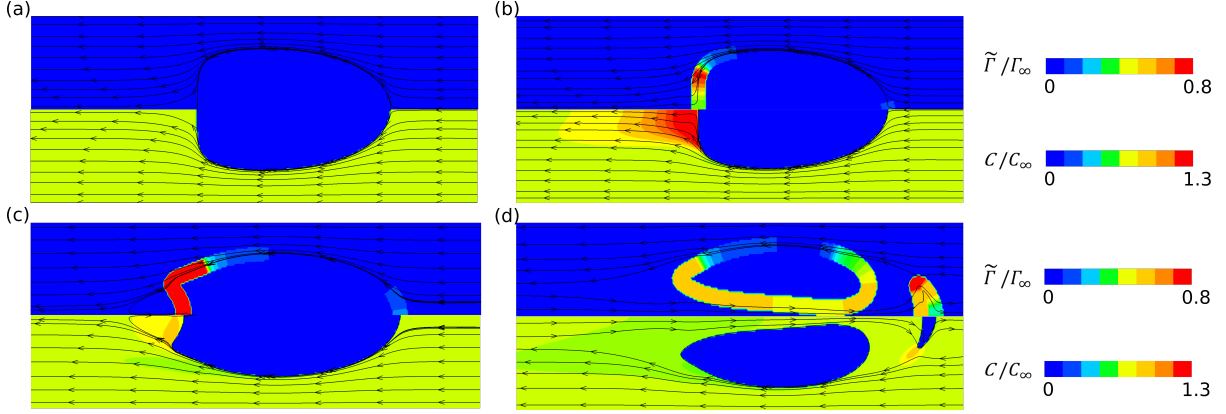


Figure 6.10: Contour plots of the surfactant concentration field,  $\tilde{\Gamma}$ , (upper part) and the bulk surfactant concentration field,  $C$  (lower part), for  $Ca = 0.5$ ,  $d/d_h = 0.75$  and (a)  $La = 0$ , (b)  $La = 0.1$ , (c)  $La = 1$  and (d)  $La = 10$ . Velocity streamlines are drawn in a reference frame translating with the bubble velocity. The bubbles move from left to right. Note that the bubble sketched in (d) has burst and might not have reached its terminal shape.

when compared to the cases presented in Fig. (6.3). As a consequence, only two stagnation points remain on the bubble surface, one at the front of the bubble and one at the back. Surfactants are swept to the back of the bubble and accumulate there, leading to a clean interface on the front half of the bubble. Consequently, surfactants desorb from the surface at the back of the bubble leading to their accumulation in the liquid adjacent to the back of the bubble. As  $La$  is increased from 0.1 to 1, more surfactants are adsorbed on the bubble surface and, consequently, more surfactants accumulate at the back of the bubble. This leads to a slight invagination of the back of the bubble. When  $La = 10$ , it appears that the invagination proceeds towards the front of the bubble and finally leads to the bursting of the bubble. Due to the change in the flow structure, the divergent stagnation circle on the bubble surface, where the liquid pressure,  $p_c$ , and the normal viscous stresses,  $\tau_{nn}$ , were contributing to increase the drag coefficient of the bubble (see Fig. (6.7)) disappears. This might explain the diminution of the drag coefficient  $C_d^*$  when  $Ca$  is increased (see Fig. (6.8)), and the consequent increase in  $V_b/J_L$ .

The results presented in Fig. (6.10) show that the deformation of the bubble, when  $Ca = 0.5$ , has a strong influence on the structure of the flow near the bubble, when compared to a spherical bubble. This, in turn, has a significant influence on the distribution of the surfactants on the surface of the bubble. To give more insights into this,  $\tilde{\Gamma}/\Gamma_\infty$  is plotted as a function of the axial coordinate,  $z$ , with  $z = 0$  at the back of the bubble, in the first column of Fig. (6.11), for  $Ca = 0.04$  (first row),  $Ca = 0.1$  (second row) and  $Ca = 0.5$  (third row), for  $d/d_h = 0.75$  and for different values of  $La$ . For  $Ca = 0.04$ , the bubble is almost spherical and, as mentioned previously, it is observed that the surfactants accumulate near the convergent stagnation point/circle on the bubble surface and are depleted near the divergent stagnation point/circle. When  $Ca$  is equal to 0.1, a similar distribution of the surfactants on the surface of the bubble is observed, but with steeper gradients. Finally, when  $Ca$  is equal to 0.5, it is observed that the surfactants are totally swept to the back of the bubble.

Increasing  $Ca$  induces a change in the flow field around the bubble and a consequent change in the surfactant distribution on the bubble surface. Thus, it might be expected that the tangent shear stress distribution on the

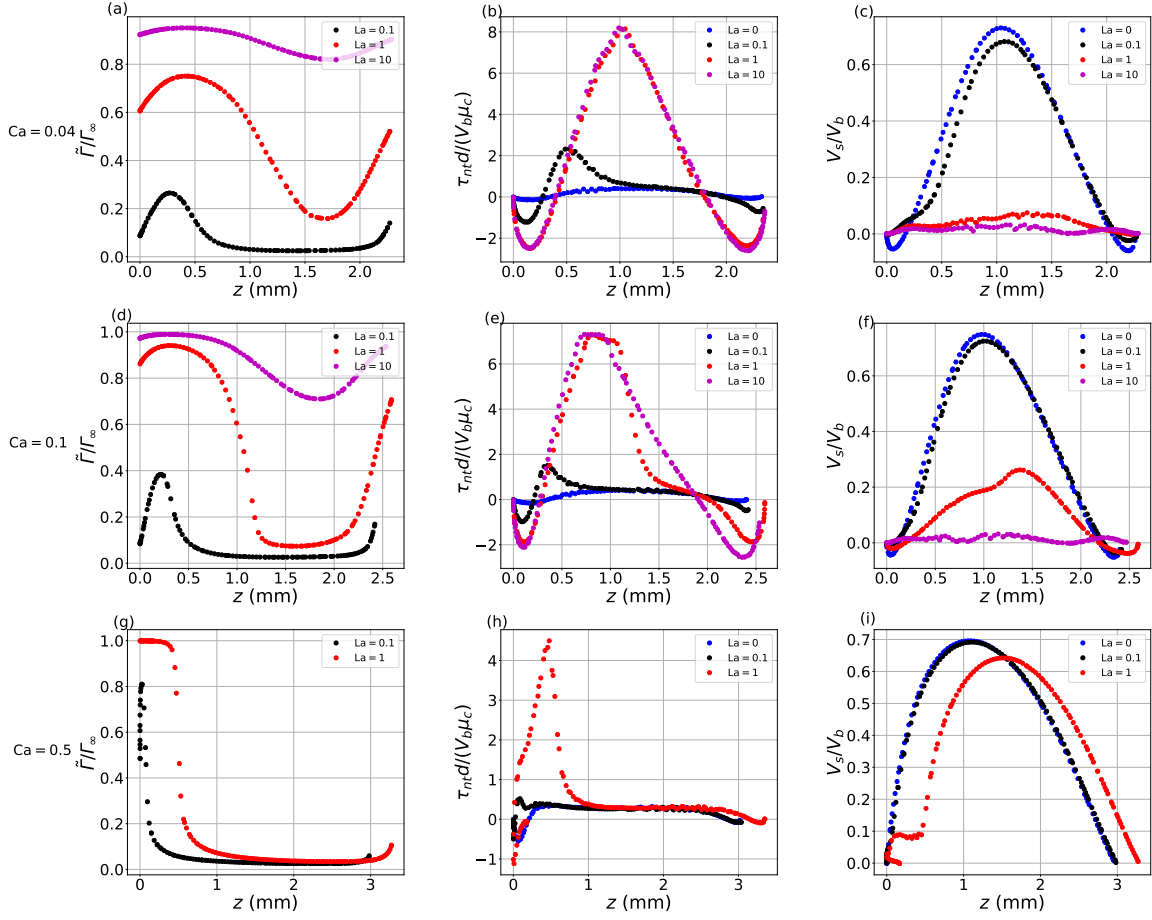


Figure 6.11: (first column) Surfactant concentration on the surface of the bubble,  $\tilde{\Gamma}/\Gamma_\infty$ , (second column) viscous shear stress along the tangent to the bubble surface,  $\tau_{nt}d/(V_b\mu_c)$ , and (third column) ratio of the liquid velocity tangent to the bubble surface to the bubble velocity,  $V_s/V_b$ . (first line)  $Ca = 0.04$ , (second line)  $Ca = 0.1$  and (third line)  $Ca = 0.5$ .

bubble surface,  $\tau_{nt}d/(V_b\mu_c)$ , is also strongly affected by an increase of  $Ca$ . On the second column of Fig. (6.11)  $\tau_{nt}d/(V_b\mu_c)$  is presented as a function of the axial coordinate,  $z$ , for different values of  $Ca$  and  $La$ . As  $Ca$  increases from 0.04 to 0.1, the surfactant concentration decreases near the divergent stagnation circle on the front part of the bubble side, causing a decrease of the shear stress at that location, for  $La = 1$  and  $La = 10$ . As  $Ca$  is increased further, all the surfactants accumulate at the back of the bubble leading to a clean surface on the most part of the bubble, except at the back.

The tangent shear stress distribution on the bubble surface is expected to affect the interface velocity. On the third column of Fig. (6.11),  $V_s/V_b$  is presented as a function of  $z$ , for different values of  $Ca$  and  $La$ . It is observed that, in general, increasing  $La$  leads to the reduction of  $V_s/V_b$ . It is reduced at locations where the shear stress on the bubble surface is high. For example, the shear stress profile observed for  $Ca = 0.04$  and  $La = 0.1$  (black dots on Fig. (6.11b)) exhibits a peak at  $z \approx 0.5$ , where the concentration profile of surfactants exhibits an important gradient (black dots on Fig (6.11a)). The influence of  $La$  on  $V_s/V_b$  is reduced for  $Ca = 0.5$  (see Fig. (6.11i)). As mentioned previously, as  $Ca$  is increased, surfactants are swept to the back of the bubble and, consequently, have a smaller influence on  $V_s/V_b$ .

The drag coefficient of the bubble,  $C_d = 4F_d / \left( 0.5\rho_c (V_b - J_l)^2 \pi d^2 \right)$ , is also expected to be less influenced by the presence of surfactants when  $Ca$  is increased. The effect of  $Ca$  and  $La$  on the drag coefficient of the bubble is analyzed on Fig. (6.12a), where  $C_d$  is plotted as a function of  $Ca$  for several values of  $La$  and for  $d/d_h = 0.75$ . It is observed that, in general, the drag coefficient of the bubble increases with  $La$ . As it might have been expected, when  $Ca$  is larger than approximately 0.5, the drag coefficient of the bubble becomes almost independent of  $La$ . As for  $C_d$ ,  $V_b/J_l$  becomes also independent of  $La$  when  $Ca$  is larger than 0.5, as it can be observed in Fig. (6.12b).

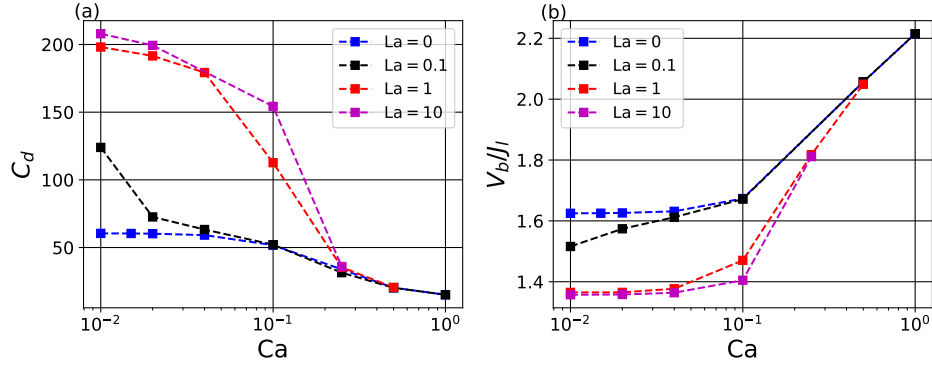


Figure 6.12: (a) Drag coefficient as a function of  $Ca$  for  $d/d_h = 0.75$  and different values of  $La$ . (b)  $V_b/J_l$  as a function of  $Ca$  for  $d/d_h = 0.75$  and different values of  $La$ .

The bubble velocity and the drag coefficient becomes independent of  $La$  as  $Ca$  reaches values close to unity, for  $d/d_h = 0.75$ . At this point, surfactants accumulate at the back of the bubble and reduce locally the surface tension of the gas-liquid interface. This causes the back of the bubble to deform, as illustrated in Fig. (6.13). Increasing

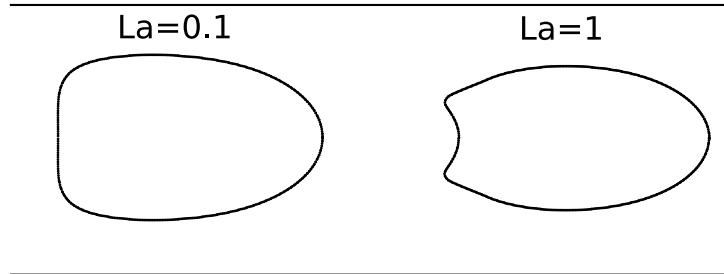


Figure 6.13: Contours of the bubble for  $La = 0.1$  and  $La = 1$ . The other parameters are set to  $Ca = 0.5$  and  $d/d_h = 0.75$ .

$La$  further causes the back of the bubble to invaginate. This can even cause the bubble to burst, as presented in Fig. (6.14). This unsteady bursting phenomenon reported in Fig. (6.14) was also observed in previous experimental and numerical studies that considered the effect of viscosity ratio ( $\lambda$ ) on the shape and bursting behavior of drops (Olbricht and Kung (1992); Nath *et al.* (2017)). In the previous section, Eq. (6.13) was used to discuss the change in bubble shape with  $Ca$ . The same equation can be used to discuss the effect of  $La$  on the bubble shape. As seen in the previous paragraph, as  $Ca$  reaches values close to 0.5, surfactants are swept to the back of the bubble and consequently, reduces locally the surface tension of the gas-liquid interface. If Eq. (6.13) is evaluated at the back of a bubble (a bubble such as the one in Figs. (6.13a or b)), with  $\kappa \sim 2/r_c$ , where  $r_c$  is the radius of curvature of the back of the bubble, an expression of  $r_c$  can be obtained:

$$r_c = \frac{2d}{(\bar{p}_d - \bar{p}_c + \bar{\tau}_{nn}) Ca_b \frac{\sigma_0}{\sigma}} \quad (6.14)$$

In contrast to Eq. (6.13), the presence of surfactant is considered, and consequently, the effective surface tension

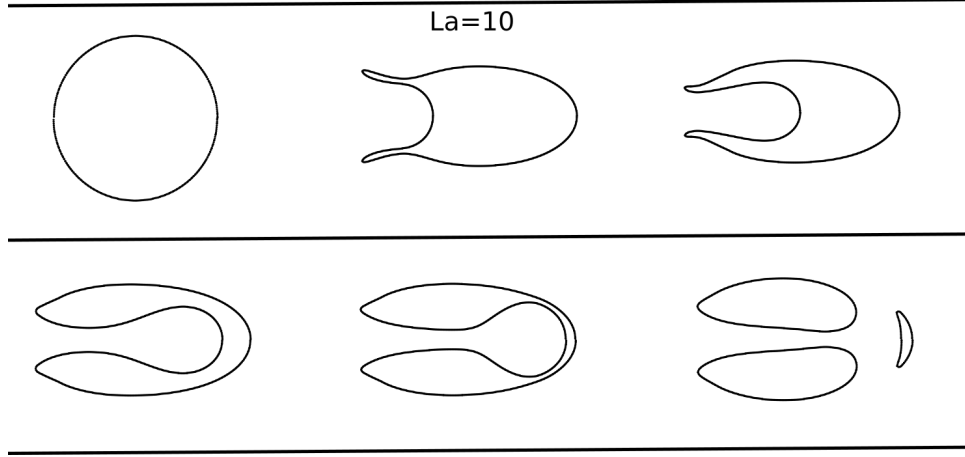


Figure 6.14: Contours of the bubble at different time for  $La = 10$ ,  $d/d_h = 0.75$  and  $Ca = 0.5$ .

of the gas-liquid interface appears in Eq. (6.14). The periodic component of the pressure inside the gas can be estimated as:  $p_d = 4\sigma/d$ . In dimensionless form, it gives:  $\bar{P}_d = 4/(Ca_b\sigma_0/\sigma)$ . Thus, Eq. (6.14) yields:

$$r_c = \frac{2d}{4 + (-\bar{p}_c + \bar{\tau}_{nn}) Ca_b \frac{\sigma_0}{\sigma}} \quad (6.15)$$

It should be noted that when  $Ca_b \rightarrow 0$ , the bubble is spherical and  $r_c = d/2$  is recovered from Eq. (6.15). At the back of the bubble,  $-\bar{p}_c + \bar{\tau}_{nn}$  is negative (see Fig. (6.7)). Thus, as  $Ca_b$  increases, the normal stresses at the back of the bubble cause  $r_c$  to increase, and consequently the back of the bubble flattens. As it is increased further,  $r_c$  might change sign if  $|(-\bar{p}_c + \bar{\tau}_{nn}) Ca_b \sigma_0/\sigma| > 4$ . This causes the back of the bubble to invaginate. As it can be seen in Eq. (6.15), the same effect can be caused by surfactants accumulating at the back of the bubble, since the presence of surfactants increase  $\sigma_0/\sigma$ . This is visible in Fig. (6.13). Eq. (6.15) also shows that the increase of  $Ca_b$  and/or  $\sigma_0/\sigma$  can lead to the bubble bursting if  $r_c$  approaches negative values close to zero. In Fig. (6.15),  $r_c$  is plotted as a function of  $Ca$ , for  $\sigma/\sigma_0 = 0$  and  $0.5$ . In this figure,  $-\bar{p}_c + \bar{\tau}_{nn}$  is imposed to  $-3$ .  $-\bar{p}_c + \bar{\tau}_{nn} = -3$  characterizes the normal viscous stresses at the back of a bubble with  $d/d_h = 0.75$  and  $Ca = 0.01$  and  $0.1$  (see Figs. (6.7)i and l). The blue and red vertical lines depict the critical value of  $Ca$  from which the back of the bubble begins to invaginate. In Fig. (6.15), it is visible that increasing  $Ca$  causes the back of the bubble to flatten, and to invaginate. If there are surfactants in the system,  $0 < \sigma_0/\sigma < 1$ . The case of  $\sigma/\sigma_0 = 0.5$  is presented on Fig. (6.15). In this case, for  $Ca \rightarrow 1$ ,  $r_c$  approaches 0 (being negative) indicating a bubble with a severe invagination on its back. In this case, the bubble probably bursts.

As an example, a diagram presenting the different regimes obtained in the simulations for  $d/d_h = 0.75$  is presented on Fig. (6.16). In this plot, 3 distinct regions can be identified, corresponding to classical bubble motion with  $V_b/J_l < 2$ , bubble with velocity larger than the maximum velocity in the liquid, i.e.,  $V_b/J_l > 2$ , and unstable bubble, leading to burst. This figure illustrates a transition between a bursting bubble and a stable bubble (red solid line in Fig. (6.16)). As it can be observed, this transition depends upon the bubble deformability (i.e., upon  $Ca$ ), and surfactants (i.e., upon  $La$ ). This transition might also depend on other non dimensional numbers characterizing the surfactants. However a complete parametric study is beyond the scope of this paper.

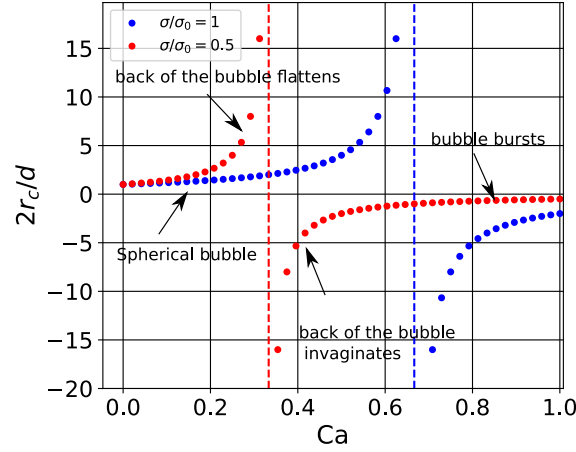


Figure 6.15:  $r_c$  as a function of  $Ca$  for different values of  $\sigma/\sigma_0$ . The dashed vertical lines depict vertical asymptots

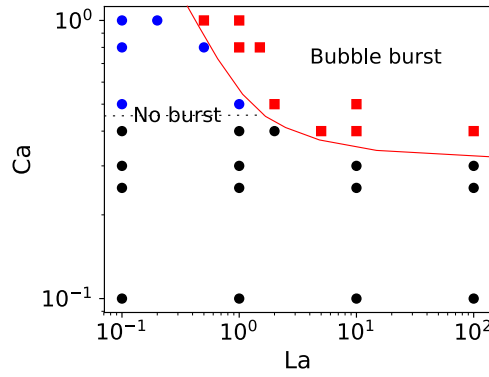


Figure 6.16: Bubble stability diagram for  $d/d_h = 0.75$ . Black, blue and red symbols represent a simulation where  $V_b/J_l < 2$ ,  $V_b/J_l > 2$ , and where the bubble bursts, respectively.

## 6.4 Conclusion

We performed a numerical study to investigate the effect of soluble surfactants and deformability on the dynamics of an isolated bubble translating in a horizontal microchannel of circular cross section. We use a Level-Set method to capture the gas-liquid interface. The capillary pressure jump and the Marangoni stress are computed using the Continuum Surface Force model. The transport of surfactants on the bubble surface is dealt in an Eulerian framework and is coupled to its transport in the liquid.

In line with previous studies, we observed that when the bubble is spherical, the liquid recirculates in between bubbles. As a consequence, surfactants accumulate on convergent stagnation point/circle on the bubble surface and deplete on divergent stagnation point/circle. For a Langmuir number larger than 1, this causes the bubble interface to get almost immobilized in between convergent and divergent stagnation point/circle (in a reference frame attached to the bubble), due to Marangoni stresses induced by surface tension gradients; regarding its relative velocity to the liquid, the bubble behaves as a solid sphere when  $La > 1$ . The ratio of the bubble velocity to the mean flow velocity decreases as the ratio of the bubble diameter to the tube diameter increases. Furthermore, when the bubble is spherical, it is shown that surfactants can increase the drag coefficient of the bubble by a factor of 2.

When the bubble is allowed to deform, i.e., when the capillary number is of order of unity, the curvature of its interface is reduced near the divergent stagnation circle on the front part of the bubble side, where the viscous stress normal to the bubble surface is high. This is due to the recirculating flow, which “hits” the bubble at this location, and locally increases this stress. Consequently, it reduces the curvature of the bubble interface. Therefore, the bubble elongates as  $Ca$  is increased. As the bubble elongates, it is shown that its drag coefficient decreases due to the modification of the flow structure around the bubble. Consequently, the ratio of its velocity to the mean liquid velocity,  $V_b/J_l$ , increases and can be larger than 2. For  $d/d_h = 0.75$ , if  $Ca$  becomes larger than approximately 0.5, recirculations in between bubbles disappear and surfactants are swept towards the back of the bubble. They have less influence on the drag coefficient of the bubble and on its velocity,  $V_b/J_l$ , than for a spherical bubble. Increasing the amount of surfactant adsorbing to the bubble surface can eventually cause the back of the bubble to invaginate and possibly the bubble to burst.



## CHAPTER 7

### A numerical investigation of the lifetime of superficial bubbles inside Mezcal

This chapter presents a work performed in a frame of a collaboration with Prof. Roberto Zenit from Universidad Nacional Autonoma de Mexico. A paper has been submitted to the journal Proceedings of the National Academy of Science regarding this work (Rage *et al.* (2018)).

#### 7.1 Introduction

Superficial bubbles or surface bubbles are encountered in countless of natural environments such as in the case of “ocean foams”, or “bubble nests”. In the former case, free gas bubbles are produced in the sea by the decomposition of detrital matter or the impact of raindrops (Garrett (1967)). In the presence of natural or anthropic surfactants, those bubble create stable foams that can accumulate on the shores. An example of such foams is shown on the left of Fig. 7.1. In the latter, the Catfish for instance uses bubbles as nests for its larvae (Hostache and Mol (1998)). The fish stabilizes those bubble with surfactants it produces. Such bubbles are shown on the right of Fig. 7.1.



Figure 7.1: (left) Ocean foams at Ocean Beach in San Francisco (image taken from the website of the National Oceanic and Atmospheric Administration). (right) Bubble nest on the surface of a pond (image taken from Hostache and Mol (1998)) .

Surface bubbles are also encountered in beverages, such as beer, champagne or Mezcal, a traditional distilled alcoholic beverage from Mexico. Mezcal is obtained by fermentation of agave, a plant living in arid climates. Sample agave plants are shown in Fig. 7.2. The process of production of Mezcal begins by harvesting the plants and extracting the “pina”, or heart, by cutting off the plant’s leaves and roots. The pinas are cooked for approximately three days in earthen ovens, giving mezcal its intense and distinctive smoky flavor (Rage (2017)). The cooked pinas are then crushed and mashed (traditionally by the means of a stone wheel rotated by a horse) (Rage (2017)). The obtained cooked and crushed agave is then left to ferment in large barrels with water added (Rage (2017)). After fermentation, two distillations are performed in order to obtain a mixture containing between 40 and 55 % of alcohol (volume content). The beverage is often aged between one month and four years.

Once the Mezcal is produced, a traditional technique to asses the alcohol content in Mezcal is performed. In this technique, the “Mezcalero” pours a stream of the beverage into a small vessel. As the vessel fills up with the liquid, splashing of the stream with the liquid produces bubbles. If the alcohol content is correct, stable bubbles



Figure 7.2: Agave plants (taken from [hDp://turismo.mexplora.com](http://turismo.mexplora.com) and [hDp://www.taringa.net.](http://www.taringa.net.))

form at the surface and float beneath the surface. Traditionally, the stream is formed by pouring Mezcal into a reed having an opening of 2 mm in diameter. The successive steps of this procedure is shown in Fig. (7.3).

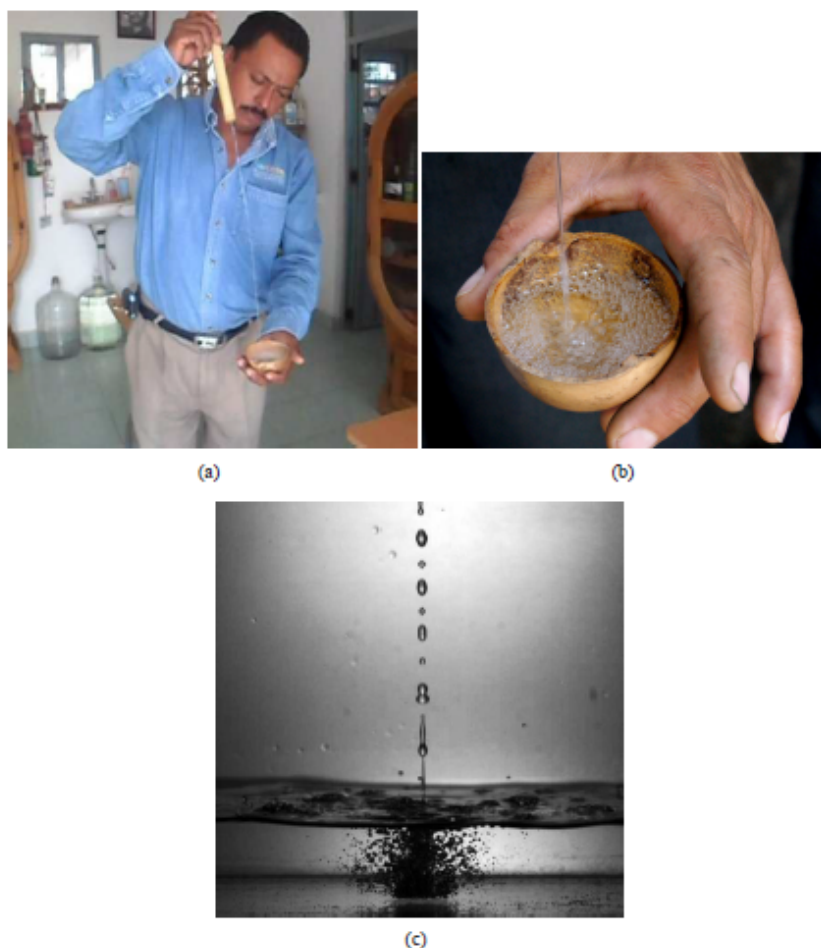


Figure 7.3: Traditional technique to asses the alcohol content of Mezcal. (a) The Mezcalero produces a stream of the liquid with a small reed. (b) the stream splashes onto the stagnant liquid inside the vessel and produces stable bubbles. (c) Images of the splashing of the stream with the liquid inside the vessel (images are taken from Rage *et al.* (2018)).

The time that these bubbles “rests” under the surface, their lifetime, can be divided in two stages, namely, the bouncing stage, and the film drainage stage (Kosior *et al.* (2014); Malysa *et al.* (2005)). Surfactants can alter the lifetime of those surface bubbles by playing on both stages. For example, Kosior *et al.* (2014) performed experi-

ments of a single air bubble rising in stagnant water contaminated with octanol. They showed that, depending on the octanol concentration inside the water, the bouncing time changed from 10 ms to 90 ms. They identified that this behavior was due to the change in both the bubble velocity before impacting the free surface and the bubble shape. Surfactants also affect the lifetime of the bubble under the free surface by increasing the time taken for the film to drain by immobilizing its surface (Wang *et al.* (2017)).

In this chapter, the problem of Mezcal is studied. In particular, several questions are addressed regarding the lifetime of the bubbles beneath the surface of the vessel:

1. Does the traditional technique work? In particular, when the Mezcal contains the desired concentration of alcohol (i.e., between 45 % and 55% volume content), does the bubble exhibit an extended lifetime beneath the surface of the vessel? To answer this question, the team of Roberto Zenit performed controlled experiments that are briefly explained and reported in section 7.2
2. What are the mechanisms controlling the lifetime of the bubbles? To answer this question, the first step used in this work is to idealize the Mezcal as a mixture of water and alcohol that contains surfactants. The second step is to perform numerical simulation using this idealized system in an attempt to put into light some of the mechanisms that control the lifetime of the bubbles under the free surface.

In this way, the problem of the traditional technique to assess the alcohol content in Mezcal is addressed both using experiments and numerical simulations, in a complementary manner.

## 7.2 Experimental observations

Experiments were performed by the team of Prof. Roberto Zenit in order to verify if this traditional technique actually works. First, measurement of the properties of a water-alcohol mixture are reported in Fig. 7.4a. In this figure, the properties of the mixture,  $\rho_c$ ,  $\mu_c$  and  $\sigma$  are plotted as a function of the alcohol volume fraction of the mixture,  $x_v$ . The values of each of these properties is scaled by the properties of water. Interestingly, it is observed that the maximum of viscosity is observed for  $x_v = 55\%$  while other quantities are less affected. The concentration of alcohol has a strong influence on the viscosity, with a maximum corresponding to the Mezcal properties indicating that the longer lifetime of bubbles inside Mezcal and the peak in viscosity at  $x_v = 55\%$  are certainly correlated.

Second, an experimental setup that mimics this traditional technique was prepared. The reed used in the traditional technique (see Fig. 7.3) was reproduced and the mean diameter of the bubble formed using the procedure explained in the introduction was determined,  $d \approx 2$  mm. Solutions were prepared by mixing pure Mezcal (Mezcal Sanchez, see for example <https://www.mezcalreviews.com/mezcal/la-herencia-de-sanchez-ponche-de-frutas/>), with water or ethanol to change its alcohol content, pure Mezcal containing 55 % of alcohol (volume content). The diluted Mezcal is referred in this text to as altered Mezcal. The properties of Mezcal Sanchez was measured by the team of Roberto Zenit:  $\rho_c = 919.0$  kg/m<sup>3</sup>,  $\mu_c = 3.07$  Pa.s and  $\sigma = 30.6$  mN/m was obtained. The lifetime obtained in the mixtures is presented in Fig. 7.4b. In this figure, the black circle presents the lifetime of a bubble in pure Mezcal. It is observed that diluting Mezcal with alcohol or water leads to the reduction of the lifetime of the bubbles (as materialized by the red circles in Fig. 7.4b). The experiments of the team of Prof. Roberto Zenit show that the traditional technique works. It was supposed that the extended lifetime of the bubbles inside the vessel that contains pure Mezcal when compared to diluted Mezcal is due to: (i) high viscosity of a water/alcohol mixtures at around 55 % alcohol content (ii) and to the surfactants naturally present in Mezcal that are diluted if water or ethanol is added in it.

In order to confirm these hypothesis (i and ii), we perform numerical simulations using JADIM. In particular, those are the questions we aim to address

1. How can Mezcal be idealized in order to perform numerical simulations of a bubble rising in a cup filled with it?
2. Can the peak of lifetime as a function of alcohol content be reproduced using this model and JADIM
3. If yes, can we identify some of the mechanisms in play that controls the lifetime of the bubbles under the free surface.

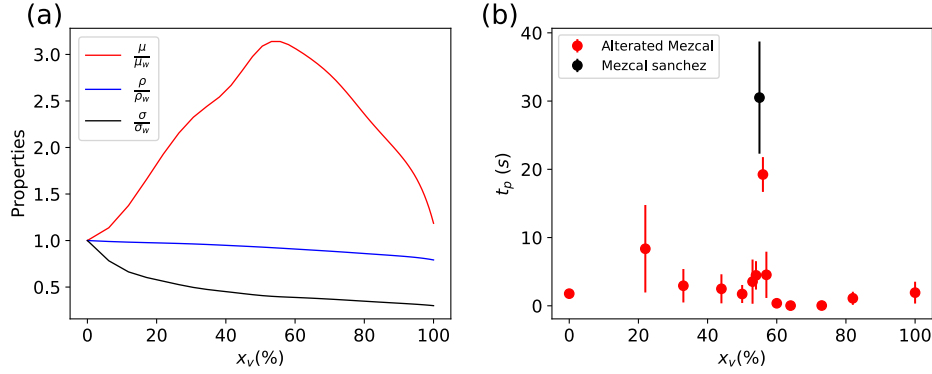


Figure 7.4: (a): Properties of the water alcohol mixture as a function of alcohol volume content measured by the team of Roberto Zenit. (b): Life time of bubbles inside pure mezcal (red square), and altered mezcal with either ethanol or water.

In order to address these questions, the rest of this chapter is organized as follows. Section 7.3 presents the idealization of the Mezcal that we propose. Section 7.4 briefly presents the computational setup for the simulations and outlines some features regarding the requirement in terms of mesh refinement. Section 7.5 shows the role of surfactants in determining the lifetime of the bubbles. Section 7.6 presents the results of the simulations. In particular, it presents results regarding the lifetime of bubbles as a function of alcohol content obtained in the simulations and identifies some physical mechanism that play a role in determining the lifetime of the bubbles.

### 7.3 Problem statement

Mezcal is a mixture of ethanol, water, and numerous organic compounds including methanol, acetic acid, ethyl acetate, higher alcohols, esters, ketones, terpenes, among others (López (2010)). It was shown that long chain alcohols such as octanol or dodecan-diol adsorb on an interface between air and an aqueous solutions and reduce its surface tension (Srinivas and Ghosh (2012); Giribabu and Ghosh (2007); Chang and Franses (1995)). In this study, the Mezcal is considered as a mixture of water and ethanol that contains surfactants with a bulk concentration  $C_0$ . The properties of the water-alcohol mixtures are:  $\rho_c(x_v)$ ,  $\mu_c(x_v)$ ,  $\sigma(\sigma_0(x_v), C_0)$ , where  $\rho_c$  is the density of the mixture,  $\mu_c$  is the viscosity of the mixture,  $\sigma$  is the surface tension of the interface between the mixture and the air and  $x_v$  is the volume fraction of alcohol inside the mixture;  $\sigma_0$  is the surface tension of the interface of the pure water-alcohol mixture, i.e., that does not contain surfactants. The properties of the surfactants are:  $\Gamma_\infty$ ,  $k_a$ ,  $k_d$ ,  $D_s$ , where  $\Gamma_\infty$  is the maximum packing concentration of surfactants on the interface,  $k_a$  and  $k_d$  are adsorption and desorption constants, respectively and  $D_s$  is the diffusion coefficient of the surfactants along the air/liquid interface. As can be seen, in the model we propose the properties of the water-alcohol mixture depend upon the alcohol volume fraction inside the mixture ( $x_v$ ). The surface tension  $\sigma$  depends upon the volume fraction of alcohol  $x_v$  that fixes the values of  $\sigma_0$  and the concentration of surfactants inside the water-alcohol mixture  $C_0$ . The properties  $\rho(x_v)$ ,  $\mu(x_v)$ ,  $\sigma_0(x_v)$ , have been measured by the team of Prof. Roberto Zenit (see Fig. 7.4a). Those values are used as input parameters for the simulations.

In the next section the computational setup for the simulations is presented.

## 7.4 Setup for the simulations

### 7.4.1 Domain

The computational domain of the simulations is presented in Fig. 7.5. An initially stagnant and spherical bubble

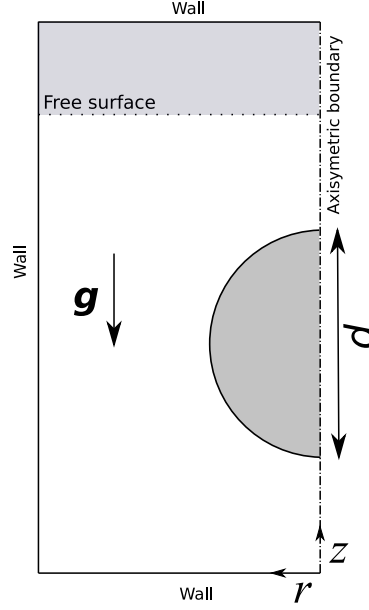


Figure 7.5: Computational domain for the simulation of bubbles inside Mezcal

of diameter  $d = 3.1$  mm is depicted. The centroid of the bubble is initially at  $z = d$  (see Fig. 7.5). A free surface is placed at  $z = 2d$ . Gravity acts along the negative  $z$  axis. Walls are placed on three boundary of the domain as illustrated in Fig. 7.5 and a symmetry axis is placed along the  $z$  axis, therefore simulating an axisymmetric configuration.

### 7.4.2 Mesh

The mesh used for the computations is organized in three blocks as depicted in Fig. 7.6. The blocks have lengths of  $l_1 = 1.75d$ ,  $l_2 = 0.5d$  and  $l_3 = 0.25d$ , each block containing  $N_1$ ,  $N_2$  and  $N_3$  computational cells along the  $z$ -axis respectively. The computational domain contains  $N_z = N_1 + N_2 + N_3$  and  $N_r$  computational cells along the  $z$  and  $r$  axis, respectively. The first block (depicted in Fig. 7.6 with the symbol “I”) is characterized with a decreasing cell size along the  $z$  direction. An arithmetic sequence is used to generate the mesh along the  $z$  direction in the first block:

$$\begin{cases} \Delta z_i = \Delta z_0 + q \cdot i \\ l_1 = \sum_{i=1}^{N_1} \Delta z_i \end{cases} \quad (7.1)$$

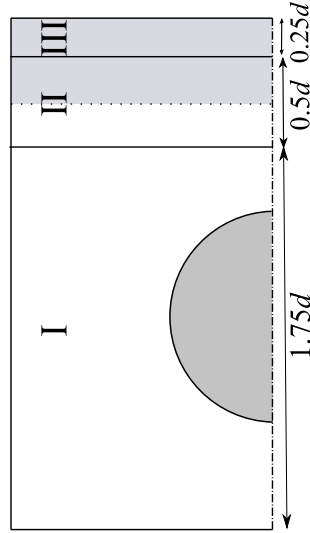


Figure 7.6: Subdivision of the computational domain into three subregions

The length of block I,  $l_1$ , the minimum value of  $\Delta z$ , i.e.,  $\Delta z_0$ , and the desired number of cells in block I along the  $z$ -axis,  $N_1$  are known. Thus, in order to generate the mesh inside block I, the unknown  $q$  is deduced:

$$q_1 = 2 \frac{l_1 - N_1 \Delta z_0}{N_1(N_1 + 1)} \quad (7.2)$$

The block II contains the free surface (see Fig. 7.6). The cells in this block have a uniform size of  $\Delta z = \Delta z_0 = l_2/N_2$ , where  $N_2$  is the desired number of cells along the  $z$ -axis in block II. The mesh in this region needs to be fine enough to capture the dynamics of the drainage of the film between the top of the bubble and the free surface. This is illustrated below.

In block III, the cell size along the  $z$ -axis increases gradually as  $z$  increases following an arithmetic evolution given by Eq. (7.2), where the subscript 1 are replaced by 3.

Four mesh were tested in order to identify the proper one allowing to capture the drainage dynamics of the film. The characteristics of each mesh are given in table 7.1. More specifically, a mesh convergence study has been

Table 7.1: Values of the parameters characterizing the computational meshes

$N_x$	$N_r$	$d/\Delta z_0$	$q_1$	$q_3$
100	50	76.58	$2.66 \times 10^{-6}$	$6.73 \times 10^{-6}$
200	100	153.16	$6.73 \times 10^{-7}$	$1.76 \times 10^{-6}$
400	200	306.32	$1.69 \times 10^{-7}$	$4.51 \times 10^{-7}$
800	400	612.64	$4.240 \times 10^{-8}$	$1.14 \times 10^{-7}$

conducted in order to identify the refinement that is required in order to capture the dynamics of the film drainage. In particular, simulations have been performed with the setup presented in Fig. 7.5. The distance between the tip of the bubble and the free surface,  $h_0$ , was monitored for the four meshes as a function of time. The results are presented in Fig. 7.7. It is visible that  $h_0$  decreases with time, as the bubble rises and approaches the free surface for all the meshes. However, for the two coarsest meshes, the computations are not able to capture the film drainage and coalescence occurs instantly when the bubble approaches the free surface (black and green curves in Fig. 7.7). The two other meshes are able to capture the bounce of the bubble on the free surface and the film drainage, these two phenomena being discussed in the results section. The film rupture occurs when its thickness

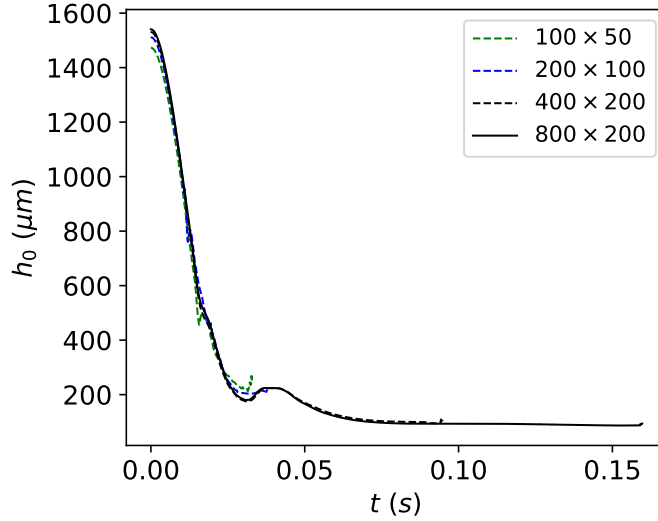


Figure 7.7: Vertical distance between the tip of the bubble and the free surface as a function of time,  $t$ . The computations were performed with four different meshes.

is of the order of the cell size. For this reason, the exact time at which the bubble coalesces does not converge satisfactorily towards a fixed value when the mesh is refined for the range of meshes used in this study. However, it is clearly visible that the shape of the curve  $h_0(t)$  converges. This feature indicates that in the present simulations, the physics governing the lifetime of the bubble is satisfactorily captured when the mesh is characterized with 400 and 200 cells along the  $z$  and  $r$  directions respectively. In the remaining, simulations are performed with the mesh characterized with  $N_x = 400$  and  $N_r = 200$  (see table 7.1). This mesh is characterized by  $\Delta z_0 \approx 10 \mu\text{m}$ , which sets the coalescence thickness to approximately  $h_c \approx 50 \mu\text{m}$ . This thickness was observed to be approximately the same for all the simulations performed within this project.

The team of Prof. Roberto Zenith inferred the rupture thickness of the film in their experiments from the speed at which the leading piercing edge moves as the bubble bursts (Culick (1960)). This thickness was determined by the team of Roberto Zenith to be:  $h_r = 24 \pm 4 \mu\text{m}$ . Due to computing limitations, the minimum grid size we could apply in the numerical simulations was  $\Delta z_0 \approx 10 \mu\text{m}$  which sets the coalescence thickness to  $h_c \approx 50 \mu\text{m}$ . In the case of a film drainage between two rigid interfaces, and in the limit  $Bo \ll 1$ , the thinning at the apex follows  $h \propto t^{1/2}$  (Scheid *et al.* (2012)). Consequently, a decrease by a factor two for the critical film rupture should imply an increase by a factor four of the lifetime. Though this correction factor is certainly a good approximation, the numerically obtained bubble lifetimes have not been corrected with this factor. The reason for this is that the drainage dynamics with surfactants can significantly differ from the one between rigid interfaces. In conclusion, the goal of the present study is to highlight the key phenomena governing the bubble lifetime under the free surface rather than obtaining quantitative values of bubble lifetime.

## 7.5 Results

### 7.5.1 Determination of the lifetime

As mentioned in the introduction, three stages can be observed when a bubble rises in a stagnant liquid: the rising, the bouncing and the film drainage stages (Kosior *et al.* (2014); Malysa *et al.* (2005)). In the simulations performed in this work, these three stage have been observed. They are illustrated in Fig. 7.8. In this figure, the bubble



velocity is plotted against time, for a simulation characterized with:  $\rho_c = 966.61 \text{ kg/m}^3$ ,  $\mu_c = 0.0022 \text{ Pa.s}$ ,  $\sigma = 0.038 \text{ N/m}$ ,  $k_a = 3 \text{ m/(mol.s)}$ ,  $k_d = 1 \text{ s}^{-1}$  and  $C_\infty = 0.025 \text{ mol/m}^3$ . In this figure, it is observed that

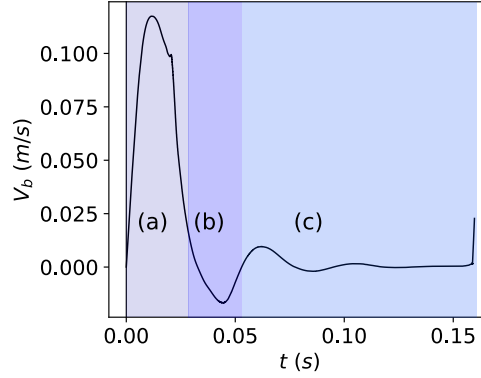


Figure 7.8: Bubble velocity,  $V_b$ , as a function of time,  $t$ .

during the rising stage, the bubble velocity first increases. As the bubble gets closer to the free surface, it begins to decelerate. This stage is annotated with the letter “a” in Fig. 7.8. The bouncing stage happens in some cases, when the bubble velocity is large enough when impacting the surface. In fact, the bubble dismisses the excess kinetic energy into the deformation of its surface and backward motion, resulting into bounces (Zawala *et al.* (2007); Sunol and González-Cinca (2010); Kosior *et al.* (2014)). This stage is depicted with the letter “b” in Fig. 7.8. In the case presented in Fig. 7.8, several bounces with decreasing intensity are visible. In this work, the film drainage stage is defined after the first bounce till the coalescence occurs. The film drainage stage is annotated with the letter “c” in Fig. 7.8. In this work, the lifetime of the bubble is therefore defined as the time taken for the film to drain after the first bounce (stage c in Fig. 7.8).

## 7.5.2 Role of surfactants

The role of surfactants in this system is illustrated in this subsection. Fig. 7.9 presents the contours of a bubble and of the free surface at time  $t = 0.055 \text{ s}$ , after it bounced one time under the interface. The mixture is characterized with the following properties:  $\rho_c = 927.3 \text{ kg/m}^3$ ,  $\mu_c = 0.0030 \text{ Pas}$  and  $\sigma_0 = 0.030 \text{ N/m}$ , which corresponds to  $x_v = 0.50$ . The angle  $\theta$  is defined in Fig. 7.9, with the origin of the polar coordinate system defined on the bubble mass center. As illustrated,  $\theta = 0$  refers to the symmetry axis of the problem. The role of surfactants in

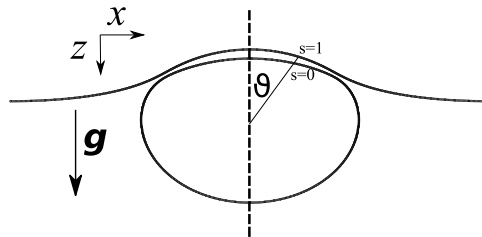


Figure 7.9: Contour of the air-liquid interfaces, at time  $t = 0.055 \text{ s}$

this system is illustrated by plotting  $v_s = (V_b - \mathbf{v} \cdot \mathbf{t})$ , where  $\mathbf{t}$  is the unit tangent vector to the gas/liquid interface and  $V_b$  is the bubble velocity, for  $\theta = 0.35 \text{ rad}$ , as a function of the normal distance to the bubble surface which is called  $s$ . Surfactants reduce the liquid velocity especially near the bubble surface (i.e., at  $s = 0$ ), and consequently, increase the drainage time of the film. It also induces a flow in the opposite direction of the main drainage flow direction, near the bubble surface, as can be seen in Fig. 7.10 at  $s \approx 0$ . It should be noted that simulations with



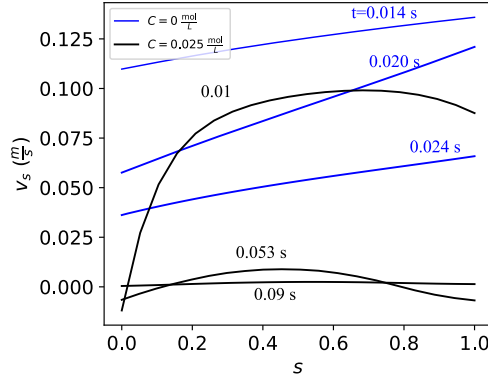


Figure 7.10:  $v_s$  as a function of the normal distance to the interface for  $\theta = 0.35\text{rad}$ .  $s = 0$  corresponds to the bubble surface and  $s = 1$  refers to the free surface.

other amount of surfactants have also been performed. Above a threshold value of  $C_0$ , the same kind of velocity profile as the black lines in Fig. 7.10 was observed. Below this threshold value, the velocity profiles in the film was like if there were no surfactants in the system. Those threshold values depend upon several parameters of the system, including  $k_a$ ,  $k_d$ ,  $\mu_c$  among others.

The reduction of the drainage velocity near both surfaces induced by surfactants drastically increase the film drainage time, when compared to the case where no surfactants are present. This can be rationalized as follows:

In the absence of surfactants, the force balance in the film is approximately given by:

$$\rho_c g \sim \mu_c \frac{d^2 u}{dx^2} \quad (7.3)$$

where  $x$  is the coordinate along the horizontal direction, as sketched in Fig. 7.9,  $u$  is the velocity component along  $x$  and scale as  $u \sim d/t_p$ , where  $t_p$  is the time taken for the film to drain. Thus the balance can be approximated by:

$$\rho_c g \sim \frac{\mu_c d}{d^2 t_p} \quad (7.4)$$

The drainage time of the film is deduced:

$$t_p \sim \frac{\mu}{\rho g d} \quad (7.5)$$

In the presence of surfactants, as observed in Fig. 7.9, the liquid velocity is reduced on the bubble surface and on the free surface. Thus, the shear stress resists the gravitational drainage:

$$\rho_c g \sim \mu_c \frac{d^2 u}{dy^2} \quad (7.6)$$

where  $y$  is the coordinate along the vertical direction (see Fig. 7.9). Inside the film,  $y$  scale with the thickness of the film,  $h$ , thus the drainage time of the film scales as:

$$t_p \sim \frac{\mu d}{\rho g h^2} \quad (7.7)$$

The ratio of the drainage time of the film in the absence of surfactants to the drainage time in the presence of surfactants is nothing else than the square of the aspect ratio  $\epsilon = h/d$ , also referred to as the film parameter.

In the preliminary simulations performed in this work, it was observed that  $h$  varies from 150 microns towards 30 microns, the thickness at which the film ruptures. Taking  $h$  as 100 microns yields  $h/d \approx 0.03$ . This scaling

Table 7.2: Values of the parameters characterizing the liquid for case 1 (black pentagons in Figs. 7.11,7.12a and b)

$x_v$ (%)	$\rho_c g$ (N/m <sup>3</sup> )	$\sigma$ (N/m)	$\mu$ (Pa.s)	$t_p$ (s)	$t_p^*$	Bo
6.19	9691.28	0.057	0.0011	0.05	1316.75	1.62
11.87	9621.70	0.048	0.0014	0.059	1275.50	1.902
17.11	9570.71	0.044	0.0017	0.063	1114.98	2.08
21.95	9527.07	0.041	0.0019	0.064	972.20	2.2189
26.43	9482.50	0.039	0.0022	0.069	931.58	2.36
30.6	9433.14	0.036	0.0023	0.076	950.80	2.49
34.48	9377.34	0.035	0.0024	0.081	958.30	2.59
38.11	9318.37	0.034	0.0025	0.0812	920.25	2.66
41.51	9260.33	0.033	0.0027	0.094	1011.38	2.73
47.7	9151.17	0.031	0.0030	0.10	973.97	2.87
50.52	9097.68	0.030	0.0031	0.11	996.87	2.92
53.18	9043.87	0.029	0.0031	0.11	957.45	2.96
55.70	8990.46	0.029	0.0031	0.010	881.02	2.98
66.46	8753.38	0.028	0.0029	0.085	796.98	3.04
81.7	8382.92	0.025	0.0023	0.084	951.40	3.19

analysis shows that, the reduction of the fluid velocity on the bubble surface and on the free surface caused by surfactants increases the drainage time of the film by a factor of 900, when compared to a case where surfactants are not present. When surfactants were not present in the simulations, the bubble coalesced instantaneously when it approached the free surface. In order to capture the dynamics of the drainage without surfactants, both the cell size and the time step used in the computations has to be decreased drastically. This is out of the scope of this work. From now on, the parameters concerning surfactants are fixed to the values characterizing octanol in an aqueous solution:  $k_a/k_d = 3 \text{ m}/(\text{mol})$ ,  $C_\infty = 0.025 \text{ mol}/\text{m}^3$  and the influence of alcohol volume fraction is studied. The ratio  $\Gamma_\infty/\sigma_0$  is the parameter relating the surface tension,  $\sigma$ , to the surfactant concentration on the interface,  $\tilde{\Gamma}$ . In this study, the parameter  $\Gamma_\infty/\sigma_0(x_v)$  is kept constant in between the simulations. This means that when  $x_v$  is varied,  $\sigma_0$  varies, and,  $\Gamma_\infty$  is adapted such that  $\Gamma_\infty/\sigma_0(x_v)$  remains constant. This is done in order to keep the dimensionless numbers concerning the surfactants constant in between simulations (i.e.,  $E = RT\Gamma_\infty/\sigma_0$ ) and to analyze only the influence of fluid properties on the lifetime of the bubbles.

### 7.5.3 Lifetime of bubbles as a function of the alcohol volume fraction.

In this section, we test if the idealization of mezcal that we propose together with the numerical method implemented in this thesis is capable of reproducing the evolution trend of the lifetime as a function of alcohol content observed in the experiments.

For this purpose simulations are performed varying  $x_v$ , the other parameters being fixed:  $\Gamma_\infty/\sigma_0 = 0.1/(RT)$ , where  $R$  is the ideal gas constant and  $T$  is the absolute temperature,  $k_a = 3 \text{ m}/(\text{mol.s})$ ,  $k_d = 1 \text{ s}^{-1}$ ,  $C_\infty = 0.025 \text{ mol}/\text{m}^3$ ,  $D = 10^{-9} \text{ m}^2/\text{s}$  and  $D_s = 10^{-14} \text{ m}^2/\text{s}$ . Throughout this study, the bubble equivalent diameter is set to  $d = 3 \text{ mm}$ . The properties of the water alcohol mixture as a function of alcohol content is summarized in Table 7.2.

The lifetime of the bubbles obtained in the simulations are plotted as a function of  $x_v$  in Fig. 7.11b. It is observed that the lifetime of the bubbles under the free surface increase gradually as  $x_v = 6.19\%$  towards  $x_v = 55\%$ . Beyond  $x_v = 55\%$ , the lifetime of the bubbles decreases as  $x_v$  is increased. As in the experiments,

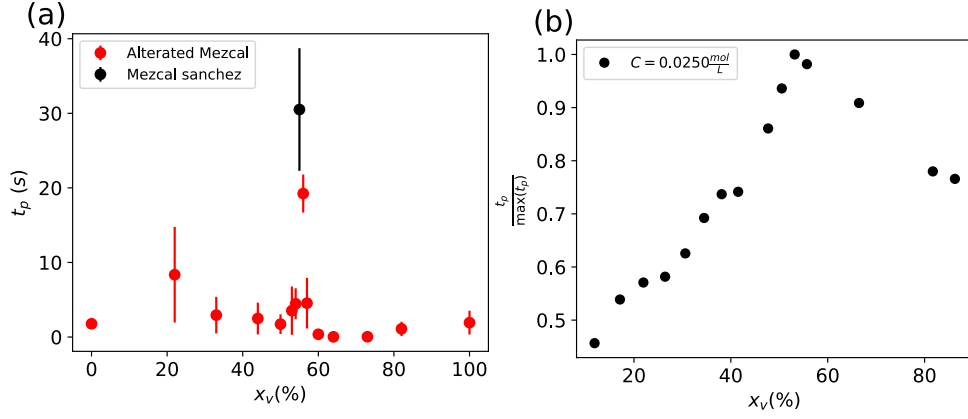


Figure 7.11: (a) Lifetime of the bubbles under the surface measured in the experiments performed by the team of Prof. Zenit, inside pure mezcal (red square) and altered mezcal (black squares). (b) Simulated lifetimes of the bubbles under the surface as a function of alcohol volume fraction

the maximum lifetime of the bubbles is obtained for an intermediate alcohol concentration of  $x_v = 55\%$ . It should be noted that the lifetime obtained with the numerical simulations follow the same evolution trend with respect to the alcohol volume fraction as the viscosity (see Fig. 7.4). This suggests that in the simulations, the lifetime of the bubble at the surface of the liquid is set at leading order by the competition between gravitational drainage, and viscous forces which slows down the drainage. It is worth saying that simulations with other concentrations of surfactants ( $C_0$ ) have been performed. It was observed that the lifetime increases with increasing surfactant concentration in the range of values of  $C_0$  that was tested. However, the mechanisms by which this effect occurs was not investigated, and thus the data are not reported here. They can be found in Rage *et al.* (2018).

The conclusion in this subsection is that the idealization we propose for the mezcal together with the implemented numerical method allows to obtain a trend for the evolution of the lifetime as a function of  $x_v$  that is comparable to the evolution trend of the viscosity with the alcohol volume fraction. This conclusion is also in agreement with the prediction of Eq. (7.7) that arises from a scaling analysis that considers that the lifetime is governed by the competition between gravity and shear stress.

#### 7.5.4 Scaling analysis

It was observed in the previous section that the lifetime of the bubbles in the simulations performed in this work is governed by the competition between gravitational drainage and viscous shear. A time scale can be build by balancing these two effects, using Eq. (7.7) and the definition of  $\epsilon = h/d$ :  $t_{scale} = \epsilon^{-2} \mu_c / (\rho_c g d)$ . This time scale is based on a dynamic balance that takes place inside the thin film, between gravitational drainage and viscous shear. However, a static balance between capillary force and gravitational forces is also taking place in the system the outcome of which dictates the shape of the bubble and of the free surface. Those shapes are expected to affect the lifetime of the bubbles. The Bond number can be build with the ratio of this two effects:  $Bo = (\rho g d^2) / \sigma_0$ . Now, the lifetime of the bubble is expected to follow the following evolution trend:

$$t_p = \epsilon^{-2} \frac{\mu_c}{\rho_c g d} F(Bo) \quad (7.8)$$

According to this analysis, for fixed surfactant properties, the lifetime of a bubble under the surface depends upon a time scale which is set by the competition of gravitational drainage and viscous effects :  $\epsilon^{-2} \mu_c / \rho_c g d$ . This time scale is modulated by a function of the Bond number  $Bo = \frac{\rho g d^2}{\sigma_0}$ . In the next paragraph, we first verify if this analysis applies to our simulations. We then try to understand the physical meaning of the function  $F(Bo)$ .

Two sets of simulations are performed to test if the scaling applies to the simulations. First, the alcohol volume fraction of the mixture is varied and  $t_p$  is monitored. The lifetime obtained from these simulations is plotted as black pentagons in Fig. 7.12a as a function of Bo. These simulations are referred as “case 1”. The values of  $x_v$ ,  $\rho g$ ,  $\sigma$ ,  $t_p$  and  $t_p^* = t_p \epsilon^{-2} \rho g d / \mu_c$  associated to each black pentagon in Fig. 7.12a are summarized in Table 7.2.

In Fig. 7.12, the lifetime obtained with the data in Table 7.2 show no clear trend with Bo. This is expected since, if the analysis presented in the previous paragraph is valid, then  $t_p$  is a function of Bo and of the time scale  $\mu_c / (\rho_c g d)$ .

This is why a second series of simulations are performed, where the parameters  $\rho_c g$ ,  $\mu_c$  and  $\sigma$  are varied arbitrarily regardless of  $x_v$ . The lifetime obtained from these simulations are plotted as green pentagons in Fig. 7.12a. As it can be observed from this figure, for the same value of Bo, different values of lifetime are obtained. However, if  $t_p$  is normalized by the timescale  $\epsilon^{-2} \mu_c / (\rho_c g d)$ , the black and green pentagons now collapse onto

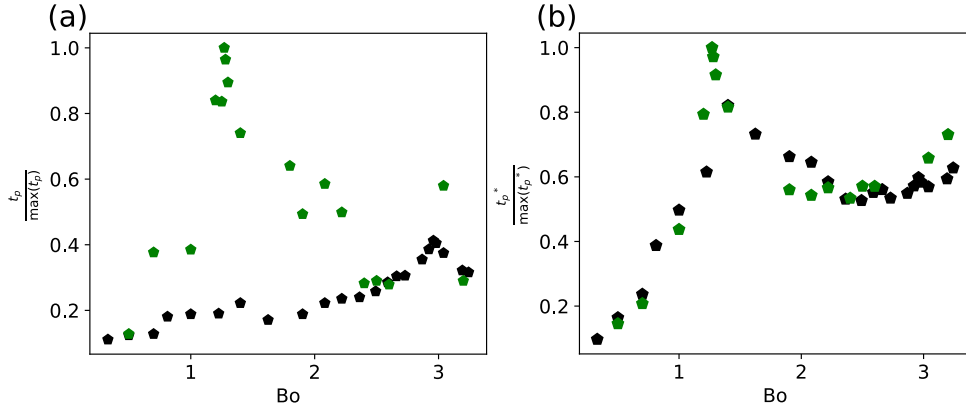


Figure 7.12: (a) Relative lifetime of the bubble under the surface ( $t_p / \max(t_p)$ ) as a function of the Bond number. (b) Scaled lifetime,  $t_p^* / \max(t_p^*)$  as a function of the Bond number. The scale is given by Eq. (7.8). Note that in Fig. 7.12b, few black symbols are hidden behind green symbols.

a single curve as clearly shown in Fig. 7.12b. Thus, the non-dimensional lifetime, i.e  $t_p^* = \epsilon^{-2} t_p \rho_c g d / \mu_c$ , is a function of the Bond number. We would like to note that in between simulations, the thickness at which the film ruptured was always approximately 30 microns, i.e., when the bubble surface and the free surface are separated by 3 computational cells. We note also that, when experimental data regarding the lifetime of bubbles inside altered mezcal is non dimensionalized with the time scale  $\epsilon^{-2} \mu_c / (\rho_c g d)$ , the data shows the same evolution trend with Bo, i.e.,  $t_c^*$  increases with Bo for  $Bo \lesssim 1$  and decreases for  $Bo \gtrsim 1$ . Those data not presented here can be found in Rage *et al.* (2018). In the next paragraph, the physical meaning of the function  $F(Bo)$  is investigated.

The Bond number characterizes the competition between gravitational forces that deform the bubble as well as the free surface, and surface tension force that counters the deformation of those surfaces. Thus, the influence of the Bond number on the bubble shape and free surface shape is analyzed. The contour of the bubble is plotted

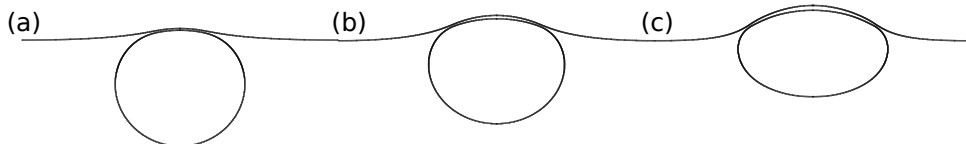


Figure 7.13: Bubble shapes while “resting” under the surface : (a) Bo = 0.5, (b) Bo = 1.5 and (c) Bo = 3.2

in Fig. 7.13 for  $\mu = 0.002$  Pa.s,  $\rho = 930$  Kg/m<sup>3</sup>  $d = 3.1$ mm and  $g = 9.81$  for different values of Bo: Bo = 0.5 (Fig. 7.13a), Bo = 1.5 (Fig. 7.13b) and Bo = 3.2 (Fig. 7.13c). The values of Bo are varied by changing  $\sigma_0$ . In this way, the timescale  $\mu_c / (\rho_c g d)$  is kept constant between the simulations. The bubble shapes presented in

Fig. 7.13 are in good qualitative agreement with theoretical and experimental results of Teixeira *et al.* (2015). In fact, in their work, they propose a theoretical model, validated with experiments of the shape of bubbles “resting” under a free surface in a solution containing surfactants. They show that, as  $Bo$  is increased, the bubble loses progressively its spherical shape, and in particular, the bottom part of the bubble flattens. This behavior is clearly observed in Fig. 7.13. In addition, the drainage dynamics associated to the deformability of the interfaces makes the film non-uniform along the bubble. In particular, a neck region occurs for sufficiently large Bond number, associated to a local thinning of the film (Fig. 7.13b). And the position of the neck changes position from the top of the bubble toward the liquid bath, as the Bond number increases (Fig. 7.13c). As a consequence, the position where coalescence occurs gets farther from the symmetry axis of the bubble. This is characterized by computing the position of the minimum film thickness during the drainage phase at a time for which the bubble shape seem at “rest”, i.e., after the bouncing phase. This position is measured with the polar angle  $\theta$  introduced in Fig. 7.9. It is observed that as  $Bo$  increases from 0.5 towards 3,  $\theta$  passes from less than 0.2 rad towards more than 1 rad, with a sharp increase in between  $Bo = 1 - 2$ . As  $Bo$  increases, the film drains faster near the side of the bubble than

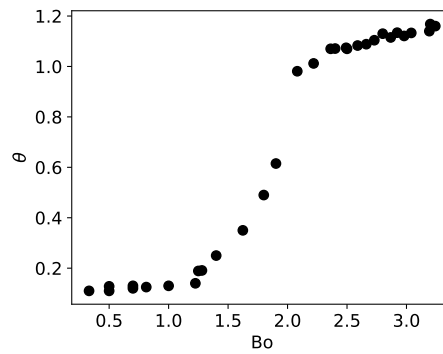


Figure 7.14: Angular position,  $\theta$ , of the minimum film thickness while the bubble “rests” under the surface ( $\theta$ ) as a function of  $Bo$ .

close to its symmetry axis, leading to a coalescence occurring at the bubble side. To understand this phenomena, the curvature of the free surface,  $\kappa = -\nabla \cdot \mathbf{n}$ , is plotted as a function of  $\theta$  in Fig (7.15a) for three values of  $Bo$ . The curvature is maximum at  $\theta = 0$ , near the symmetry axis of the free surface for all values of  $Bo$ . However, the curvature profile  $\kappa(\theta)$  changes with  $Bo$ . It seems that as  $Bo$  increases, the curvature of the free surface gets constant near the symmetry axis of the problem and displays a steep gradient farther from this axis.

In the liquid film, near the free surface, the pressure is given by  $p_l \approx p_g + \kappa\sigma$ , where  $\kappa$  is the curvature of the free surface. Taking the derivative of this expression, assuming  $p_g$  constant, gives:  $\frac{dp_l}{d\theta} \approx \sigma \frac{d\kappa}{d\theta}$ . Thus, any variation of curvature of the free surface result in an additional pressure gradient that creates a flow inside the film. In the configurations depicted in Fig. 7.13a,b and c, the curvature variation produces a capillary induced drainage of the film. In order to identify the dependency of this capillary induced drainage on  $Bo$ , the maximum value of  $\frac{d\kappa}{d\theta}$  is plotted as a function of  $Bo$  in Fig. 7.15b. In this figure, it is visible that at  $Bo \approx 1.2$ , the variation of the curvature of the free surface is minimum. This means that at this  $Bo$ , the capillary induced drainage is minimum, leading to a maximum in the dimensionless lifetime of the bubble (as shown in Fig. 7.12b). Now, a bubbles formed using the traditional technique to asses the alcohol content has a diameter close to  $d \approx 2$  mm. Inside a water-alcohol mixture of  $x_v \approx 50\%$ , those bubbles are characterized with a Bond number of  $Bo \approx 1.2$ . In this situation the bubbles benefit both of a maximum viscosity (as shown in Fig. 7.4) and a minimum capillary induced drainage (as shown in Fig. 7.15b), thus “rests” the longest under the free surface.

This analysis seems convincing and seems to apply for the simulations. Of course, in the experiments, several other important effects might play a role in determining the lifetime of the bubbles. In particular, ethanol evapo-

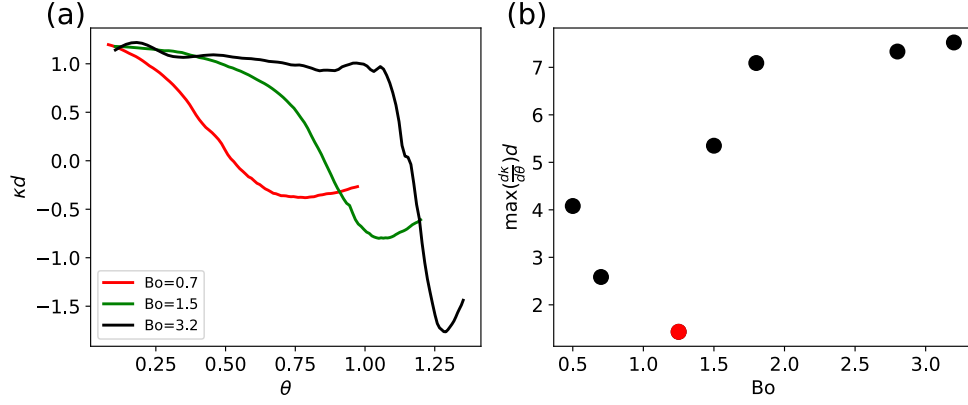


Figure 7.15: (a): Non-dimensional curvature profile of the free surface for different values of Bond. (b): Maximum value of the curvature variation of the free surface as a function of  $Bo$ .

rates at room temperature. Thus, especially inside the thin film between the bubble surface and the free surface, its concentration might be less than near the side of the bubble. The surface tension of an interface between air and a mixture of water and alcohol increases as its alcohol content diminishes as shown in Fig. 7.4. Thus, this evaporation of alcohol might induce a marangoni stress directed from the side of the bubble towards the thin film, that might play a role in determining the lifetime of the bubble. Of course, the exact effect of this Marangoni stress on the lifetime of the bubble is not easy to predict and depend upon many parameters such as the speed at which the alcohol diffuses from the side of the bubble towards the thin film or the evaporation rate of the alcohol inside the film. Those parameters will dictate if sufficient surface tension gradients will be induced by the evaporation of alcohol inside the thin film. Direct numerical simulations could be used in future works to investigate the effect of the evaporation of alcohol on the lifetime of the bubbles. The evaporation of alcohol inside the thin film will also induce a decrease of the liquid temperature which in turn might also generate Marangoni stresses directed from the bubble side towards the thin film. However, at first sight, surfactants and alcohol evaporation seem to induce Marangoni stresses directed from the side of the bubble towards the thin film between the bubble and the free surface. As a result, it seems that the simulations performed on this idealized system (Mezcal = Water/alcohol + surfactants) contains the main ingredients that determine the lifetime of the surface bubbles inside Mezcal: Gravitational drainage of the thin film, capillary induced drainage of the thin film, viscous stresses resisting the drainage and Marangoni stresses immobilizing the bubble surface and the free surface.

## 7.6 Conclusion and perspective

In this chapter, the numerical method has been used to understand the physical mechanisms controlling the lifetime of superficial bubbles inside Mezcal. For this purpose, the Mezcal has been idealized as a mixture of water and alcohol containing surfactants. The simulations were ran using experimental data regarding the properties of a mixture of water and ethanol, and the properties of octanol as a surfactants.

The simulations were run for a single value of the surfactant concentration. It was observed that, the bubbles exhibit a maximum lifetime for an intermediate concentration of alcohol, i.e.,  $x_v = 0.55$ , as in the experiments.

It was first shown that, in the idealized system, surfactants increase the time taken for the film to drain by immobilizing the surface of the bubble and the free surface. A classical scaling analysis showed that when both surfaces are immobilized, the lifetime of the bubbles is given by  $t_p \sim \frac{\mu R}{\rho g h^2}$ , which is obtained by balancing viscous forces to gravitational forces. This scaling analysis is pushed further using the physical argument that surface tension should play a role in determining the lifetime of the bubbles. Performing simulations show that

indeed, in the idealized system, in addition to gravitational drainage, a capillary induced drainage exists and affects the lifetime of the bubbles. Simulations results show that this capillary induced drainage reaches a minimum at a value of  $Bo \approx 1.2$ . The minimum of the capillary induced drainage is materialized by a peak on the curve relating by  $t_p \rho_c g d / \mu_c$  to  $Bo$ . This peak is also observed on the experiments performed by the team of Roberto Zenit, the data being available in Rage *et al.* (2018). This study has shown that the mechanism controlling the lifetime of a bubble beneath the free surface separating air and Mezcal are: gravitational drainage of the thin film, capillary induced drainage of the thin film, viscous stresses resisting the drainage and Marangoni stresses immobilizing the bubble surface and the free surface (induced by surfactants and alcohol evaporation).

## **Part II**

# **Dynamics of Taylor flow in Microchannels**



# CHAPTER 8

## Introduction

The motion of confined bubbles in capillaries or microchannels is a hydrodynamic problem with a large variety of applications in industry, medicine and in everyday life. In recent years, microfluidics witnessed a large attention in industry with the development of micro-heat exchangers, micro-absorbers and micro-extractors. These devices often imply the translation of a bubble (or drop) of low viscosity, through a higher viscosity liquid, resulting in the so-called Taylor flow regime. In such a microscale flow, inertial and buoyancy effects are often negligible while surface tension and viscous forces dominate the system. The relative importance of inertial to viscous forces is assessed by the means of the Reynolds number:  $Re = \rho U a / \mu$ , where  $\rho$ ,  $\mu$ ,  $U$  and  $a$  are the density and viscosity of the liquid, the bubble velocity and the microchannel half height (or radius of the capillary), respectively. The relative importance of buoyancy to surface tension effects is assessed by the means of the Bond number:  $Bo = \rho g a^2 / \sigma$ , where  $\rho$  and  $\sigma$  are the density of the liquid and the surface tension of the interface, respectively. The Reynolds number and the Bond number characterizing these microscale flows is often small when compared to unity. Finally, the relative importance of viscous forces to surface tension forces is assessed by the means of the capillary number:  $Ca = U \mu / \sigma$ , which is the relevant parameter characterizing these microscale flows.

The pioneering work on this problem was conducted by Fairbrother and Stubbs (1935). They noticed that a tube filled with a viscous liquid cannot be emptied by pushing a less viscous fluid through the tube because of the deposition of a lubrication film on the tube walls. Following this work, Taylor (1961) measured the thickness of this film,  $h_\infty$ . It was observed that  $h_\infty$  increases with  $Ca$ . This observation was rationalized by the theoretical work of Bretherton (1961). The author showed that for  $Ca^{1/3} \ll 1$  the thickness of the film was given by:

$$h_\infty = 1.337 a Ca^{2/3} \quad (8.1)$$

where  $a$  is the half height of the microchannel (or the radius of the capillary) Later, some authors extended the applicability of Eq. (8.1) to values of  $Ca$  up to 2 (Aussillous and Quéré (2000); Klaseboer *et al.* (2014)).

The analysis performed by Bretherton (1961) rely on the lubrication approximation of the momentum conservation equations. In the following section, the lubrication approximation is presented, and the main features of the derivation of  $h_\infty$  proposed by Bretherton (1961) are presented as well as the extension proposed by Aussillous and Quéré (2000) and Klaseboer *et al.* (2014).

## 8.1 Lubrication approximation

The lubrication approximation is used to describe the flow in narrow gaps. In these configurations, the characteristic dimension of the system in the main flow direction,  $l$ , is large when compared to the dimension in the crosswise direction,  $h_\infty$ . The ratio of these two length scales being  $\epsilon = h_\infty / l \ll 1$ . These two length scales are used to non dimensionalize the variables:

$$\bar{x} = \frac{x}{l}, \bar{y} = \frac{y}{h_\infty}, \bar{u} = \frac{u}{U}, \bar{v} = \frac{v}{V}, \bar{t} = \frac{t}{t_c}, \bar{p} = \frac{p}{\Delta p}$$

where  $x$  is the coordinate along the main flow direction,  $y$  is the coordinate along the crosswise direction,  $\mathcal{U}$  is the typical velocity along the main flow direction,  $\mathcal{V}$  is the typical velocity along the crosswise direction,  $t_c$  is the characteristic time scale of the system, and  $\Delta p$  is the typical pressure drop in the system. Typically, since  $x$  is the main flow direction, the velocity scale along  $y$  is set to  $\mathcal{V} = \epsilon \mathcal{U}$ . The time scale is set to  $t_c = h_\infty/\mathcal{V} = l/\mathcal{U}$ . The  $x$  and  $y$  component of the momentum equations as well as the continuity equations, Eqs. (3.1 and 3.5), are written in terms of these dimensionless variables, for a Cartesian coordinate system  $(x, y)$  as:

$$\frac{\partial \bar{u}}{\partial \bar{x}} + \frac{\partial \bar{v}}{\partial \bar{y}} = 0 \quad (8.2)$$

$$\epsilon \text{Re} \left( \frac{\partial \bar{u}}{\partial \bar{t}} + \bar{u} \frac{\partial \bar{u}}{\partial \bar{x}} + \bar{v} \frac{\partial \bar{u}}{\partial \bar{y}} \right) = -\frac{h_\infty^2 \Delta p}{\mathcal{U} \mu l} \frac{\partial \bar{p}}{\partial \bar{x}} + \frac{\partial^2 \bar{u}}{\partial \bar{y}^2} + \epsilon^2 \frac{\partial^2 \bar{u}}{\partial \bar{x}^2} \quad (8.3)$$

$$\epsilon^3 \text{Re} \left( \frac{\partial \bar{v}}{\partial \bar{t}} + \bar{u} \frac{\partial \bar{v}}{\partial \bar{x}} + \bar{v} \frac{\partial \bar{v}}{\partial \bar{y}} \right) = -\frac{h_\infty^2 \Delta p}{\mathcal{U} \mu l} \frac{\partial \bar{p}}{\partial \bar{y}} + \epsilon^4 \frac{\partial^2 \bar{v}}{\partial \bar{x}^2} + \epsilon^2 \frac{\partial^2 \bar{v}}{\partial \bar{y}^2} + \epsilon \frac{\rho g h_\infty^2}{U \mu} \quad (8.4)$$

$$(8.5)$$

where  $\text{Re} = \frac{\rho \mathcal{U} h_\infty}{\mu}$  is the Reynolds number associated to the flow inside the gap. As it can be observed, the typical pressure drop inside the gap is  $\Delta p = \frac{\mathcal{U} \mu l}{h_\infty^2}$ . In the lubrication approximation,  $\text{Re} \ll 1$  and  $\epsilon \ll 1$ , keeping only the 0'th and 1'st order terms, and with  $\rho g h_\infty \ll (\mathcal{U} \mu l)/h_\infty$  leads to the classical lubrication equations. In dimensional form it gives:

$$\frac{\partial u}{\partial x} + \frac{\partial v}{\partial y} = 0 \quad (8.6)$$

$$0 = -\frac{\partial p}{\partial x} + \mu \frac{\partial^2 u}{\partial y^2} \quad (8.7)$$

$$0 = \frac{\partial p}{\partial y} \quad (8.8)$$

Part II of this thesis mainly relies on Eqs. (8.6), (8.7) and (8.8). In the next section, the pioneering work of Bretherton (1961) that predicts the thickness of the lubrication film around a Taylor bubble is presented. In Chapter 9, an experimental method allowing to determine the thickness of this film is developed. Finally, in Chapter 10, a variation of the theory of Bretherton (1961) is presented. In particular, the effect of gravity on the film thickness is considered. In fact, when buoyancy effects are significant, the condition  $\rho g h_\infty \ll (\mathcal{U} \mu l)/h_\infty$  leading to Eq. (8.8) is not satisfied and, consequently, Eq. (8.8) becomes inadequate to describe the problem. It needs to be modified to account for buoyancy effects. Experiments are performed to test the validity of the proposed theory.

## 8.2 The analysis of Bretherton

A typical Taylor bubble translating inside a microchannel is sketched in Fig. 8.1. In the classical analysis of Bretherton (1961), the front of the bubble is divided into three distinct regions, (I): the capillary static region, also referred to as the static meniscus, where surface tension forces are dominant and consequently the front cap of the bubble forms a sphere of radius  $R$ . (II): the transition region, also referred to as the dynamical meniscus, where viscous forces begin to be significant and are balanced by surface tension forces. Between (I) and (II), a matching region is present where the interface shape of (I) and (II) match. (III): the thin film region, where a lubrication film of constant thickness,  $h_\infty$ , deposits on the microchannel wall. Bretherton (1961) first developed an analytical expression of  $h_\infty$  that relies on the lubrication approximation. The main features of the analysis of Bretherton (1961) leading to the expression of  $h_\infty$  are presented here. The analysis relies on dividing the front of the bubble into the aforementioned regions, treat the transition region (or dynamical meniscus) and connect the solution of this region to the static meniscus in a common overlap region.

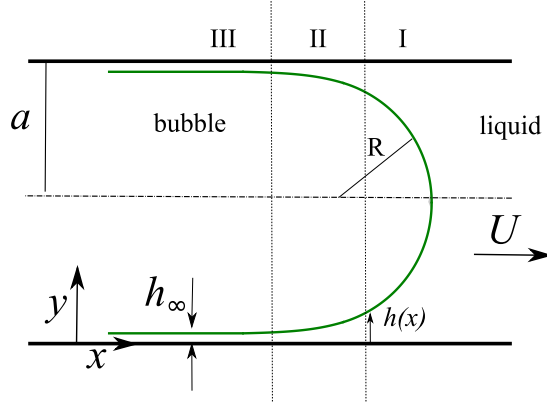


Figure 8.1: A Taylor bubble translates inside a microchannel at constant velocity  $U$ . The microchannel height is  $2a$ . The bubble is divided in three regions: (I) indicates the capillary static region, where the tip of the bubble forms a sphere of radius  $R$ . (II) indicates the transition region in which the viscous forces are balanced by the capillary forces due to the variation of the curvature along the interface. Between (I) and (II), a matching region is present where the interface shape of (I) and (II) match. As the bubble translates, a lubrication film of thickness,  $h_\infty$  is deposited on the microchannel wall.

In region II, it is assumed that viscous effect are significant together with surface tension effects. Eq. (8.7) holds and is used. Considering the problem in a reference frame translating with the bubble velocity,  $U$ , integrating Eq. (8.7) with the no slip condition on the microchannel wall, i.e.,  $y = 0$ , and the no shear condition at the gas-liquid interface, i.e.,  $y = h$ , leads to:

$$u(y) = -U + \frac{1}{2\mu} \frac{\partial p}{\partial x} (y^2 - 2yh) \quad (8.9)$$

where  $U$  is the translating bubble velocity. From continuity, the flux across the lubrication film (region III) is equal to the flux across region II, thus:

$$-Uh_\infty = -Uh - \frac{h^3}{3\mu} \frac{\partial p}{\partial x} \quad (8.10)$$

In the lubrication approximation, the normal stresses are dominated by pressure, thus the normal stress balance on the gas-liquid interface reduces to:

$$p_g - p = \sigma \kappa \quad (8.11)$$

where  $\sigma$  is the surface tension,  $p_g$  is the pressure inside the gas which is set to  $p_g = 0$  and  $\kappa$  is the curvature of the gas-liquid interface:

$$\kappa = \frac{\partial_{xx} h}{\left(1 + (\partial_x h)^2\right)^{\frac{3}{2}}} \quad (8.12)$$

Using the scales  $h_\infty$  and  $l$ , with  $\epsilon = \frac{h_\infty}{l} \ll 1$  to non dimensionalize  $x$  and  $y$  leads to:

$$\bar{\kappa} = \frac{\partial_{\bar{x}\bar{x}} \bar{h}}{\left(1 + \epsilon^2 (\partial_{\bar{x}} \bar{h})^2\right)^{\frac{3}{2}}} \quad (8.13)$$

where  $\bar{\kappa} = \kappa l$ . Since  $\epsilon^2 \ll 1$ ,  $\kappa \approx \partial_{xx} h$  is obtained and consequently the normal stress balance reduces to:

$$p = -\sigma \partial_{xx} h \quad (8.14)$$

From Eq. (8.10), the differential equation governing the shape of the gas-liquid interface in region II is deduced:

$$3\text{Ca} \frac{(h - h_\infty)}{h^3} + \partial_{xxx} h = 0 \quad (8.15)$$

where  $\text{Ca} = U\mu/\sigma$  is the capillary number. Defining  $H = h/h_\infty$  and  $X = \text{Ca}^{1/3}x/(h_\infty)$  leads to the classical Bretherton equation:

$$\frac{(H - 1)}{H^3} + \partial_{XXX} H = 0 \quad (8.16)$$

The curvature of the gas-liquid interface  $\kappa \approx \partial_{xx} h$  is written in terms of the variables characterizing region II as:

$$\partial_{xx} h = \frac{\partial_{XX} H \text{Ca}^{2/3}}{h_\infty} \quad (8.17)$$

In region I, the distance between the gas-liquid interface and the wall is of the order of the tube radius,  $a$ . In this situation, viscous effects vanish and in the absence of buoyancy effects, the curvature of the gas-liquid interface is constant. Furthermore, if the film thickness is small when compared to the microchannel height, i.e.,  $h_\infty/a \ll 1$ , the spherical cap of the bubble fills approximately the entire gap between the microchannel wall. In this situation the radius of curvature of the spherical cap of the bubble can be approximated as  $R \approx a$ . In this situation, the curvature of the front cap of the bubble is given by:  $\frac{1}{a}$ .

The curvature of the gas-liquid interface in region II and in region I should match in a common overlap region in which one can write:

$$\frac{1}{h_\infty} \lim_{X \rightarrow \infty} \partial_{XX} H \text{Ca}^{2/3} = \frac{1}{a} \quad (8.18)$$

where a numerical solution of Eq. (8.16) shows that  $\lim_{X \rightarrow \infty} \partial_{XX} H = 1.337$  (Bretherton (1961)), which leads to:

$$\frac{h_\infty}{a} = 1.337 \text{Ca}^{\frac{2}{3}} \quad (8.19)$$

This equation gives  $h_\infty/a$  as a function of  $\text{Ca}$  for  $h_\infty/a \ll 1$ .

### 8.3 Extension of the Bretherton model

Aussillous and Qu  r   (2000) and later Klaseboer *et al.* (2014) accounted for the contribution of the lubrication film in defining the curvature of the front cap of the bubble. If  $R_f$  is the radius of curvature of the front cap of the bubble, the matching condition (Eq. 8.18) becomes:

$$\frac{1}{h_\infty} \lim_{X \rightarrow \infty} \partial_{XX} H \text{Ca}^{2/3} = \frac{1}{R_f} \quad (8.20)$$

where  $R_f < a$ , is the radius of curvature of the front cap of the bubble. The thickness of the lubrication film is then given by:

$$\frac{h_\infty}{R_f} = 1.337 \text{Ca}^{\frac{2}{3}} \quad (8.21)$$

$R_f$  is an unknown. The distance between the cell/tube centerline and the interface in the matching region  $R_f$  and the liquid thickness  $C_N h_\infty$  should fit the radius of the tube. This gives an additional equation as proposed by Klaseboer *et al.* (2014)

$$a = C_N h_\infty + R_f \quad (8.22)$$

where  $C_N$  is a constant. Combining Eqs. (8.21 and 8.22) allows to obtain an expression of  $h_\infty/a$ :

$$\frac{h_\infty}{a} = \frac{1.337 \text{Ca}^{\frac{2}{3}}}{1 + 1.337 C_N \text{Ca}^{\frac{2}{3}}}, \quad (8.23)$$

The value of  $C_N$  depends upon the geometry of the problem (tube of circular cross section or microchannel with a rectangular cross section) and is not clearly defined. For example, for a tube of circular cross section, Aussillous and Quéré (2000) found that  $C_N = 2.5$  by fitting Eq. (8.23) to the experimental measurements of Taylor (Taylor (1961)). Later, Klaseboer *et al.* (2014) pointed out that the exact value of  $C_N$  depends upon where  $R_f$  is evaluated in the matching region and can take a value up to 2.9 if  $R_f$  is evaluated for  $H > 10^6$ , i.e  $X > 10000$ , and 2.34 if it is evaluated for  $H = 6 \times 10^2$ , i.e  $X = 50$ . Finally in the case of a planar geometry, the correlation established by Balestra *et al.* (2018) by performing 2D stokes simulations of a bubble translating along a planar channel showed that  $C_N = 2.19$ . In this thesis, theoretical considerations regarding the value of  $C_N$  is not considered, and Eq. 8.23 is used with  $C_N = 2.5$  when a tube of circular cross section is considered, and  $C_N = 2.19$  when a microchannel of rectangular cross section is considered.

## 8.4 Conclusion

In this chapter, the basic equations governing the flow in thin films have been introduced, namely Eqs. (8.6), (8.7) and (8.8). The classical analysis of Bretherton (1961) allowing to obtain Eq. (8.1) which predicts the thickness of the lubrication film around a bubble and a microchannel was presented. The extensions of the original analysis to larger values of Ca (Eq. (8.23)) was introduced (Aussillous and Quéré (2000); Klaseboer *et al.* (2014); Balestra *et al.* (2018)).

In the next chapter, we develop a method to measure the thickness of a lubrication film in Taylor bubbles. In particular an equation that is analogous to Eq. (8.23) is developed and its validity is tested.

## CHAPTER 9

### How to measure the thickness of a lubrication film in a pancake bubble with a single snapshot?

This chapter is part of a paper that has been published in the journal *Applied Physics Letters* in October 2018 (Atasi *et al.* (2018a)).

#### 9.1 Introduction

Large air bubbles translating inside confined geometries, or pancake bubbles, are encountered in countless situations including oil extraction, gas-liquid absorption and treatment of pulmonary disorders. The dynamics of these bubbles relies on the lubrication film in between the bubble and the walls of the channel in which they translate.

Numerous experimental works aimed at measuring the thicknesses of lubrication films formed between a bubble or drop and a solid surface. Direct measurement of film thickness have been performed extensively, using Interferometric imaging in various situations, including the thickness of thin vapor film in Leidenfrost drops (Tran *et al.* (2012)), or the thickness of air film trapped beneath a drop impacting a solid surface (Driscoll and Nagel (2011)).

Direct measurement methods of the film thickness forming between a pancake bubble and the walls of a microchannel also requires interferometric top-view imaging (Han *et al.* (2011); Chen *et al.* (2015); Huerre *et al.* (2015a)) or bright-field side-view imaging (Atasi *et al.* (2017)). Indirect measurement methods rely instead on a model that relates another measured quantity to the film thickness itself. The most classical indirect method consists in measuring the bubble velocity and recovering the film thickness via a Bretherton-like model (with the use of Eq. (8.1) or (8.23) (Warnier *et al.* (2008); Howard *et al.* (2011); Khodaparast *et al.* (2018)). This *classical method* requires a temporal sequence of images and the knowledge of the channel height as well as the fluid properties, such as the viscosity and the surface tension. Other indirect measurement methods have also been used to infer the thickness of the lubrication film around bubbles in microchannels. For instance, Chen (1986) exploited the link between the conductivity across a channel containing a bubble and the thickness of the lubrication film. We propose in this work a *new method*, also indirect, that only requires a single instantaneous bright-field image of the bubble and the sole knowledge of the refractive indices of the fluids.

Numerous techniques based on bright-field images allow to characterize the geometrical properties of bubbles or drops. For example, a raytracing technique has been used to relate the optical pattern viewed on brightfield images of layered bubbles to the geometry of these layers (van der Net *et al.* (2007)). Some researchers used the lensing effect of a drop deposited on a solid substrate, illuminated with a laser or a low aperture light, to measure the contact angle of the drop. In fact, the drop both refracts and reflects bright circles on the image, their diameter being related to the contact angle of the drop (Allain *et al.* (1985); Zhang and Chao (2002, 2003); Campbell and Christenson (2018)).

The method we propose relies on the location of specific intensity peaks, called glare points, created on the image of a bubble illuminated using a light beam (e.g., emitted from a laser or diffusive light source) (Hulst and Wang (1991)). These intensity peaks correspond to different interaction orders of the beam with the bubble. When

two of these intensity peaks are visible on the brightfield image of a spherical bubble, the distance between these two points can be used to obtain the bubble diameter. This technique is entitled Glare Point Velocimetry and Sizing (GPVS) (Dehaeck *et al.* (2005)) and has been used to size particles or measure the refractive index of liquids. A typical optical setup used for GPVS measurements is shown in Fig. 9.1. A spherical bubble is illuminated with a laser from the bottom of the scene. Observation is performed at angle of  $96^\circ$  with respect to the vertical direction (see Fig. 9.1). Two intensity peaks are visible on the bright-field image at the right of the scene. The point C arises from the rays that are reflected once on the bubble surface and that reach the objective. These rays produce an intensity maximum that is indicated with the letter C. The point B arises from rays that interact three times with the bubble before hitting the objective lens. The trajectory of these rays is drawn in grey in Fig. 9.1. In this technique, the bubble diameter can be inferred from the distance B-C, if the refractive indices of the bubble and of the liquid surrounding the bubble are known. In GPVS, the glare points are visualized in focus. When these

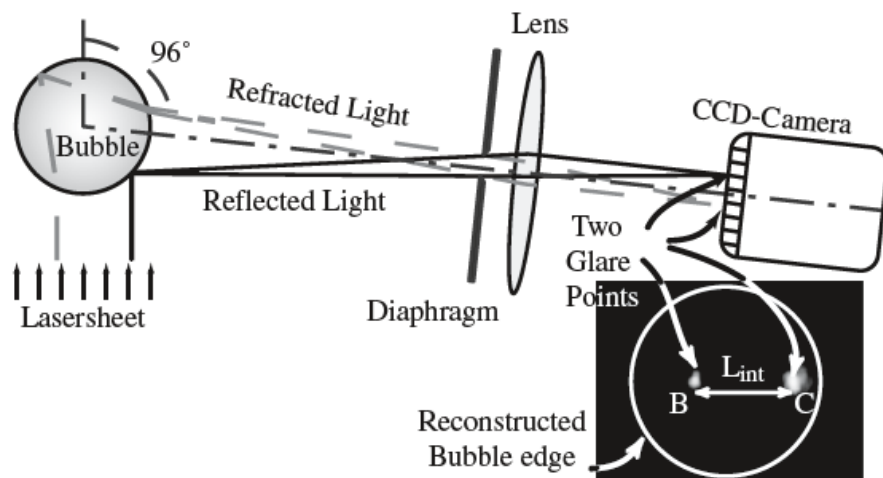


Figure 9.1: An optical setup allowing to observe two glare points on the bright-field image of a spherical bubble. This image was taken from Dehaeck *et al.* (2005).

glare points are visualized out of focus, interference patterns form on the image. The period of these interference fringes is used to size particles in suspensions or sprays (König *et al.* (1986); Glover *et al.* (1995)). This technique is entitled Interferometric Laser Imaging for Droplet Sizing (ILIDS). In contrast to the above techniques, we use in this paper an in-line configuration. In this case, the glare points connect to form a glare ring or circle as described in Dehaeck and van Beeck (2007). In the case of spherical bubbles, Dehaeck and van Beeck (2007) established an analytical expression correlating the radius of the glare ring to the radius of the spherical bubble:

$$R_g = \frac{1 + \sqrt{1 + 8n_1^2/n_2^2}}{4n_1^2/n_2^2} R_e \quad (9.1)$$

where  $n_1$  is the refractive index of the liquid surrounding the bubble, and  $n_2$  is the refractive index of the gas. Even though in-line measurements of these glare points have been used to size bubbles (with the use of Eq. (9.1)) (Dehaeck and van Beeck (2007)) and measure refractive indices (Gavrilovic (2017)), to our knowledge, they have not yet been used to measure the thickness of lubrication films.

In this chapter, a new method to measure the thickness of lubrication films is developed. This method requires a single brightfield image of a bubble translating in a microchannel, as the one presented on the left of Fig. 9.2. This image was recorded with a standard transmission microscope. A schematic of the optical setup allowing to obtain the images on Fig. 9.2 is shown on Fig. 9.3. The microchannel, of width  $w$  and height  $2a$ , is illuminated

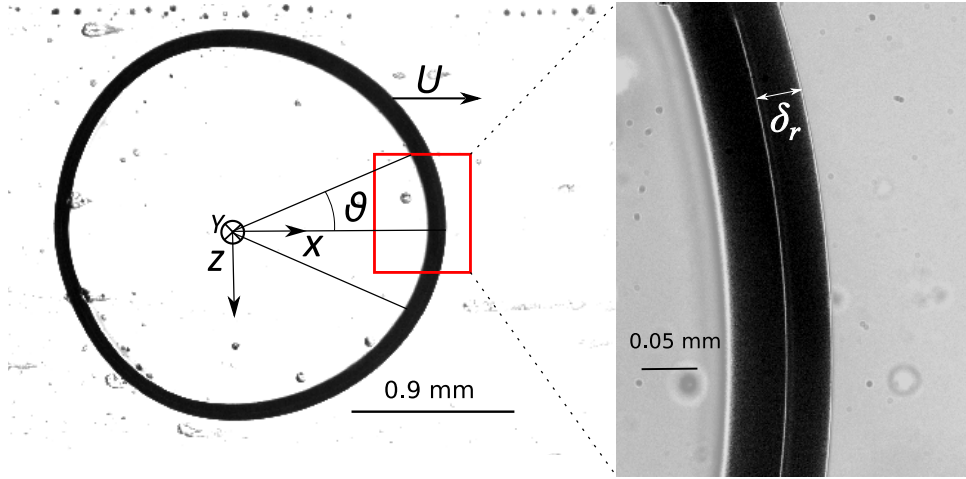


Figure 9.2: (Left) Top-view bright-field image of a pancake bubble inside a microchannel. (Right) Zoom on the glare ring inside the shadow region, the contrast of which has been enhanced for visualization purpose.

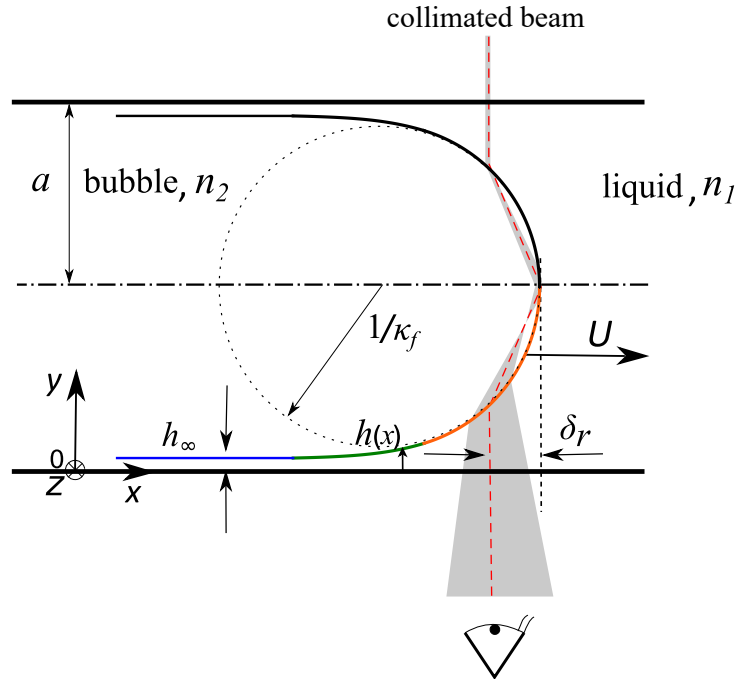


Figure 9.3: Side-view of a pancake bubble inside a microchannel of half height  $a$ . The bubble translates with a velocity  $U$  and generates on the walls a lubrication film of constant thickness,  $h_\infty$ . The static meniscus (orange line) of constant radius  $1/\kappa_f$  is connected to the lubrication film (blue line) through a dynamic meniscus (green line). The light rays (in gray) producing the glare ring on the bright-field image have been reconstructed by raytracing,  $n_1$  and  $n_2$  being the refractive index of each phase. The ray that exits the channel perpendicularly (red dashed line) is used to determine  $\delta_r$ .

with a collimated light source from the top of the scene and in-line observation is performed from the bottom with a standard transmission microscope. The rays producing the glare ring on the bright-field image are refracted on the bubble-liquid interface, reflected and refracted a second time before exiting the bubble from the bottom of the scene. The ray that exits the microchannel perpendicularly is depicted in red in Fig. 9.3. The distance between the position at which this ray exits the bubble and the bubble edge is denoted as  $\delta_r$  (see Figs. 9.2 and 9.3). As it can be intuitively understood,  $\delta_r$  correlates with the curvature  $\kappa_f$  of the bubble interface, which itself can be linked to the thickness of the lubrication film,  $h_\infty$ , through a model.



## 9.2 Methodology

The methodology followed in this work is (i) to establish numerically a relationship between  $\delta_r$  and  $h_\infty$  and (ii) to perform experiments in order to validate the established correlation. For (i), a raytracing algorithm is developed and validated. The raytracing algorithm is applied to a shape function describing the bubble interface:

$$F(x, y, z) = 0 \quad (9.2)$$

where  $(x, y, z)$  define the Cartesian coordinate system as represented in Figs. 9.2 and 9.3. This raytracing algorithm allows to calculate  $\delta_r/a$  for a given value of  $m = n_1/n_2$  and  $h_\infty/a$ , where  $n_1$  and  $n_2$  are the refractive indices of outer and inner phases, respectively (see Fig. 9.2). Applying the algorithm for different values of  $m$  allows us to build the correlation. (ii) The accuracy of the correlation is verified by performing experiments of a single air bubble translating inside a microchannel of rectangular cross section.

In this section, first the experimental setup is presented including the microchannel fabrication process, the optical setup allowing the visualization of the bubbles and the image processing procedure allowing to extract the parameter  $\delta_r$  and the bubble velocity. Secondly, the raytracing algorithm, developed in this thesis, allowing to establish the relationship between  $\delta_r/a$ ,  $h_\infty/a$  and  $m$  is presented. Finally, the model that is used to construct the shape of a pancake bubble translating along a microchannel, on which the ray-tracing algorithm is applied, is presented.

### 9.2.1 Experimental setup

Experiments are performed at room temperature, using mineral oil and silicon oil as working fluids. Air is used to produce bubbles inside these fluids.

#### Microchannel

The microchannel fabrication process is sketched in Fig. 9.4. It is based on a method proposed by Carofiglio *et al.* (2008). Two glass slides having a thickness of 0.9 mm and one photo-lithography mask are used. The mask is transparent to ultraviolet light (UV), except on an area where it is black. This area contains the pattern of the microchannel. The microchannel contains one flow-focusing device, as described by Garstecki *et al.* (2005), and one rectilinear channel of width  $w = 3$  mm.

1. Four holes are drilled on one glass sheet on locations where the fluid will be injected in the channel and withdrawn (glass A on Fig. 9.4)
2. Four spacers of 200 microns thickness are glued on 4 corners of the other glass sheet (glass B). The back of the glass B (the side that does not contain the spacers) is covered with black tape. This step avoids reflection of ultraviolet light during the insolation of the channel.
3. An optical glue, Norton Optical Adhesive (NOA), is then poured on the front of glass B and glass A is deposited on it.
4. The photolithography mask is deposited on glass A. Glycerol is poured on glass A before depositing the mask to avoid air bubbles to get trapped between the glass and the mask
5. The structure is insolated with UV light for 2-3 seconds with the glass A on the top.
6. Nanoports are glued to the holes that were drilled during the first step.

7. The NOA that has not been exposed to UV light is still fluid and is sucked-up through the nanoports using a vacuum pump. Ethanol and acetone is injected through the nanoports to help evacuate the NOA.
8. The chip is then insolated with UV light for 3 minutes and then left in an oven at 50°C during 12 hours.

A schematic of a side view of the obtained channel is presented on Fig. 9.4. As can be seen, the top and bottom walls of the channel are composed of glass. The side walls are composed of NOA. The distance between

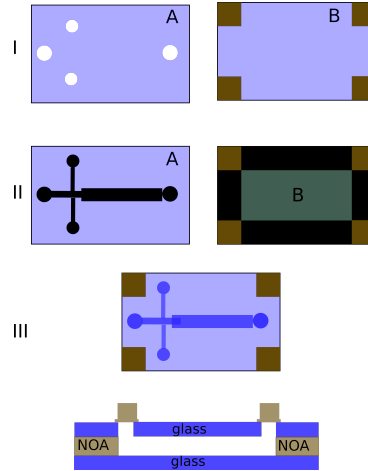


Figure 9.4: Microchannel fabrication process

the two glass plates inside the channel,  $2a$ , has been measured using a 3D microscope. The height distribution obtained is shown on Fig. 9.5.  $a = 109 \pm 3 \mu\text{m}$  is obtained. This procedure allows to produce a microchannel

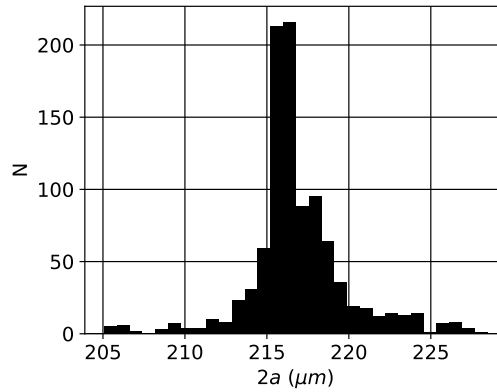


Figure 9.5: Number of measurements as a function of channel height.

with good optical quality for the visualization of a bubble and, in particular, of the glare-circle.

## Optics

Brightfield microscopy is used to visualize the bubbles. A collimated beam is mounted on an optical microscope. The in-line bright-field image of the bubble is recorded using a 12 bit camera having an acquisition speed of 11 frame per second and a pixel size of  $3.45 \mu\text{m}$ . A schematic of the optical setup is shown in Fig. 9.6. The bubble is illuminated from the top of the scene with parallel illumination. Light rays travel across the bubble and exit the bubble from the bottom of the scene after multiple interactions. The rays that interact three time with the bubble form a bright ring within the shadow region of the brightfield image. A schematic of the output image is shown at the bottom of the scene. This optical setup allowed visualization and detection of a sharp interface between the gas

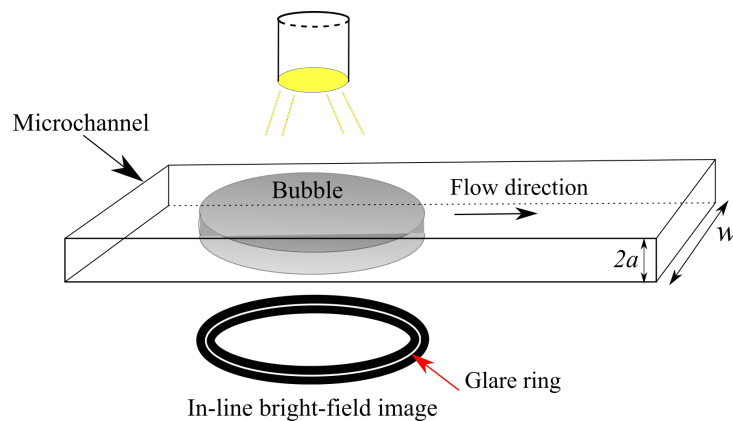


Figure 9.6: A bubble translates inside an horizontal microchannel of height  $2a$  and width  $w$ . A collimated light beam is used to illuminate the bubble and the microchannel from the top of the scene. The bubble is observed from the bottom of the scene using a magnification lens (2x and 10x) and a camera.

and the liquid phases as well as the glare-circle on the brightfield image using a 10x magnification (Khodaparast *et al.* (2013)). The image processing procedure is detailed below.

## Image processing

The bubble velocity,  $U$ , and the parameter  $\delta_r$  are extracted by the following procedure.

The bubble velocity is measured by tracking the nose of the bubble on consecutive images. Consecutive images such as the one on the left of Fig. 9.2 are used for this purpose. These images are obtained by the means of a 2x magnification lens.

The parameter  $\delta_r$ , is determined on images such as the one on the right of Fig. 9.2. Those images are obtained by the means of a 10x magnification lens. The procedure used to measure  $\delta_r$  on images can be summarized as follows: The images are scanned and only images containing the front part of the bubble are kept. The objective lens is moved such that the field of view is characterized by approximately  $-15^\circ \lesssim \theta \lesssim 15^\circ$ , where  $\theta$  is the angle between the channel axis and the normal to the bubble-liquid interface (see Fig. 9.2). The contour of the front part of the bubble is detected using a "Canny edge detection" algorithm. The glare points are detected using an intensity threshold. A second-order polynomial is fitted on a sufficiently high number of points that have been identified as belonging to the exterior contour (for reminder, this identification is performed with the use of the Canny algorithm). The normal to this polynomial is computed and the closest point to this normal, that has been identified as a glare point,  $g_p$ , is identified (for reminder, the identification of the glare points is done using an intensity threshold). A second-order polynomial is fitted on a sufficiently high number of points, evenly distributed at both side of  $g_p$ . This polynomial is a part of the glare ring. The intersection between the normal to

the bubble edge and the glare ring is calculated and the distance between the points on both polynomial that are joint by the normal is calculated. This procedure is done on evenly space points that have been identified as being part of the exterior contour of the bubble. As an example, a processed image is presented on Fig. 9.7. In this figure, the red line is a second-order polynomial that has been fitted to the locations of the glare points (forming therefore a part of the glare ring). The blue line is a second-order polynomial that has been fitted to the bubble contour. The distance  $\delta_r$  is depicted in this figure.

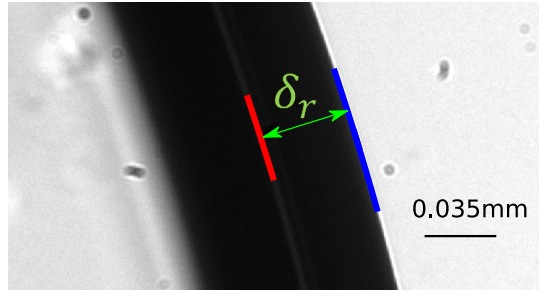


Figure 9.7: A bubble translates inside an horizontal microchannel of half height  $a$ , from left to right, with  $Ca = 0.005$ . The bubble is observed with a magnification of 10x.

Once  $\delta_r$  is extracted from the bright-field images, in order to infer the film thickness from values of  $\delta_r$ , a correlation relating  $\delta_r$  to  $h_\infty$  needs to be established. This is done by applying a ray-tracing algorithm on a model of the bubble shape. In the next section, the ray-tracing algorithm developed in this thesis is presented and validated.

## 9.2.2 Raytracing

We developed an algorithm that allows to simulate the interaction between a bundle of parallel light rays and an interface separating two media. The algorithm is then used to simulate the path of the light rays across the bubble.

Let us consider the interaction between a light ray and an interface between 2 media. The refraction and the reflection of the ray on the interface are described by the Snell-Descartes equations:

$$\begin{cases} n_1 \sin \theta_1 = n_2 \sin \theta_2 & (\text{refraction}) \\ \theta_1 = \theta_2 & (\text{reflection}) \end{cases} \quad (9.3)$$

where  $n_1$  and  $n_2$  are the refractive index of medium 1 and 2 respectively,  $\theta_1$  is the angle between the incoming ray and the normal to the interface and  $\theta_2$  is the angle between the refracted/reflected ray and the normal to the interface.

A ray is described with the equation:  $R^j(x, y) = y - a_r^j x - b_r^j = 0$ , where  $a_r^j$  and  $b_r^j$  are two parameters and  $j$  is an integer accounting for the interaction order of a ray with an interface. The interface is described in the general form:  $F(x, y) = 0$ . The normal to the interface is given by  $\mathbf{n} = \frac{\nabla F}{\|\nabla F\|}$ .

The algorithm is composed of 2 main steps:

1. the calculation of the intersection between the incoming ray ( $R^j(x, y)$ ) and the interface ( $F(x, y)$ ).
2. The calculation of the refracted and reflected rays

The input parameters of the algorithm are the  $(x, y)$  coordinates of the geometrical shape with which the rays will interact, and the refractive index of the two media that are separated by the interface.

The first step of the algorithm is to compute the intersection between the incoming rays,  $R^j(x, y) = y - a_r^j x - b_r^j = 0$ , and the geometrical shape,  $F(x, y) = 0$ . This is performed in two steps, first the point of the geometrical shape  $(x_i, y_i)$  that is the closest to the incoming ray is identified. Second, the function  $F$  is defined at the location  $(x_i, y_i)$  as:  $F_i = a_i x_i^2 + b_i x + c_i = 0$ , where  $a_i, b_i, c_i$  are fitting parameters. The fitting parameters are found by applying the least square method on the 3 points  $(x_{i-1}, y_{i-1}), (x_i, y_i), (x_{i+1}, y_{i+1})$ . The exact intersection point is computed by equating  $F(x_I, y_I) = R^j(x_I, y_I)$ , where  $x_I$  is the abscissa of the intersection and  $y_I$  is the ordinate of the intersection. The abscissa of the intersection is equal to:

$$x_I = \frac{1}{2} \left( -\frac{b_i - a_r^j}{a_i} \pm \sqrt{\left( \left( \frac{b_i - a_r^j}{a_i} \right)^2 - 4 \frac{c_i - b_r^j}{a_i} \right)} \right) \quad (9.4)$$

The ordinate of the intersection is deduced by evaluating  $R^j(x_I, y_I) = 0$ :  $y_I = a_r^j x_I + b_r^j$ .

The second step of the algorithm deals with reflection/refraction of the ray on the interface. For this purpose, the slope of the normal to the interface at the position  $(x_i, y_i)$  is computed:  $A_i = -(2a_i x_i + b_i)^{-1}$ . The angle between the incoming ray and the normal to the interface,  $\theta_1$  is deduced:  $\theta_1 = \arctan(A_i)$ . Eqs. (9.5) are applied to calculate  $\theta_2$ . The refracted/reflected ray are then constructed by calculating their slope:

$$a_r^j = \begin{cases} \tan(\theta_1 - \pi + \theta_2) & \text{if } A_i > 0 \\ \tan(\theta_1 - \pi - \theta_2) & \text{if } A_i < 0 \end{cases} \quad (9.5)$$

The parameter  $b_r^j$  is deduced:  $b_r^j = y_I - a_r^j x_I$ . The new ray is constructed using the parameters  $a_r^j$  and  $b_r^j$  and the new intersection between the geometrical shape and the ray is calculated.

It should be noted that, during step 1 of the algorithm, once the the point of the geometrical shape,  $(x_i, y_i)$ , that is the closest to the incoming ray has been identified, the following variables are defined:  $\Delta x = x_i - x_{i+1}$  and  $\Delta y = y_i - y_{i+1}$ . If  $|\Delta x| \geq |\Delta y|$ , then the procedure described above is done. On the other hand, if  $|\Delta x| \leq |\Delta y|$ , then the function  $F$  is defined at the location  $(x_i, y_i)$  as:  $F_i = a_i y_i^2 + b_i y_i + c_i = 0$  and the rest of the procedure of step 1 and 2 is done by replacing  $x_i$  by  $y_i$  and reciprocally. This allow to apply the raytracing algorithm on closed curves, line a circle or an ellipse.

The raytracing algorithm has been validated with the following test case: a circle of radius  $R_e$  is intiallized as sketched in Fig. 9.8. Light rays are thrown towards the circle from the top of the scene. These rays are depicted in grey in Fig. 9.8. The trajectory of the rays that interact three time with the circle is calculated. The position at which those rays exit the bubble vertically,  $R_g$  is determined. The value of  $R_g$  computed with the ray-tracing algorithm is compared the prediction of Eq. (9.1).

Eq. (9.1) is plotted as a solid line in Fig. 9.9, for  $n_1 = 1.467$  and  $n_2 = 1$ . Stars give values of  $R_g$  computed with the raytracing algorithm developed for this work. As it can be observed, there is a good match between the prediction of Eq. (9.1) and the algorithm.

Now, the algorithm has been developed and validated, it is ready to use on a model of a bubble shape. In the next section, two models for the shape of the bubble are presented.

### 9.2.3 Model of the bubble shape

In order to establish the relationship predicting  $h_\infty/a$  as a function of  $\delta_r/a$  and  $m$  the raytracing algorithm presented above is applied on a model for the bubble shape.

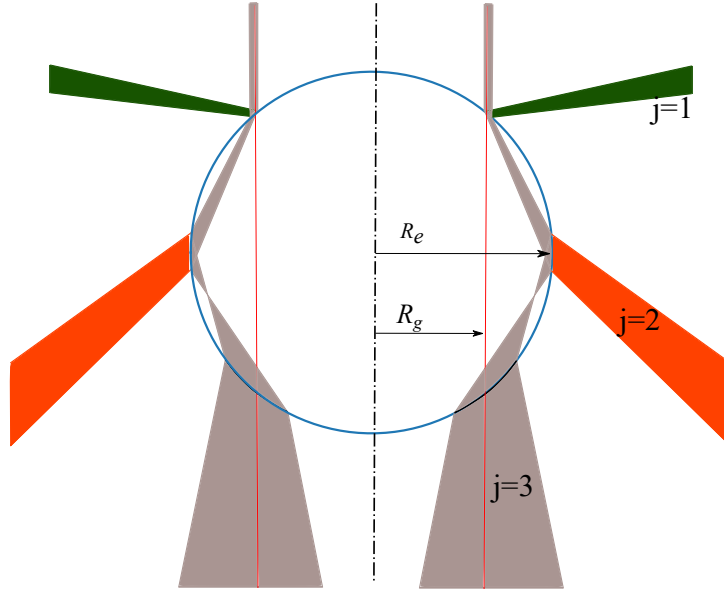


Figure 9.8: Trajectory of the rays that interact with a circle. The rays are incident upon the bubble from the top of the scene. Green rays are reflected on the circle after the first interaction ( $j=1$ ), orange rays are refracted at the second interaction ( $j=2$ ) and gray rays are refracted after the third interaction ( $j=3$ ). The rays that exit the bubble vertically form the glare points. These rays are depicted in red.

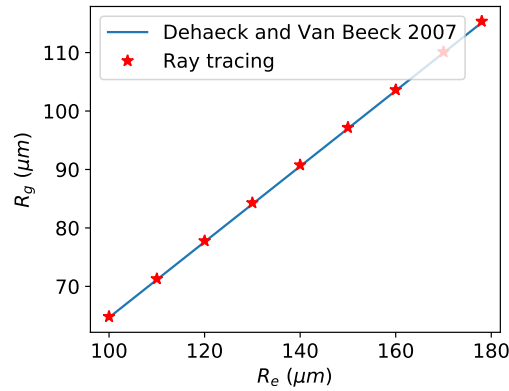


Figure 9.9:  $R_g$  as a function of  $R_e$  for a circle. The solid line is calculated using Eq. (9.1), whereas stars give values calculated with the raytracing algorithm.

### Bretherton model for the bubble shape

For the sake of simplicity, the bubble shape function  $F(x, y, z)$  is considered at the plane  $z = 0$ , i.e.,  $F(x, y, z = 0)$  and, by symmetry about the axis  $y = a$ , where  $a$  is the half height of the channel, only the bottom half of the shape is considered. As sketched in Fig. 9.3, this shape is composed of a dynamic meniscus of thickness  $h(x)$  connecting the flat lubrication film of thickness  $h_\infty$  and the static meniscus of constant curvature  $\kappa_f$  at the front of the bubble. In the frame of the lubrication approximation, i.e., for  $h_\infty/a \ll 1$ , as seen in the previous chapter,  $h(x)$  can be obtained by solving the Bretherton equation that balances the capillary and viscous forces:

$$h^3 \kappa' = 3U \frac{\mu}{\sigma} (h - h_\infty) \quad (9.6)$$

where the prime denotes the  $x$ -derivative,  $\kappa$  is the surface curvature,  $\mu$  is the viscosity of the liquid and  $\sigma$  is the surface tension of the bubble/liquid interface. In virtue of the least degeneracy principle (Van Dyke (1964)), the

full expression of the curvature  $\kappa = h'' (1 + h'^2)^{-3/2}$  is used to patch the curvatures between the dynamic and the static menisci (see Eq. (8.12)). Balestra *et al.* (2018) performed 2D numerical simulations of the Stokes equation and established a correlation for the curvature of the static meniscus,

$$a \kappa_f = \frac{1 + 2.925 \text{Ca}^{2/3}}{1 + 0.495 \text{Ca}^{2/3}} \quad (9.7)$$

as well as for the thickness of the lubrication film, as discussed in the previous chapter:

$$\bar{h}_\infty(U) \equiv \frac{h_\infty}{a} = \frac{1.337 \text{Ca}^{2/3}}{1 + 1.337 \times 2.19 \text{Ca}^{2/3}} \quad (9.8)$$

The model of Balestra and the correlations (9.7) and (9.8) have been proven to be valid for  $\text{Ca} \lesssim 5 \cdot 10^{-2}$  Balestra *et al.* (2018). Now, given a certain value of  $\text{Ca}$ , Eq. (9.6) is solved as an initial value problem, with  $h(0) = h_\infty + \epsilon$ ,  $h'(0) = h'(0) = \epsilon$ , using  $\epsilon = 10^{-3}$  and Eq. (9.8) to calculate  $h_\infty$ . The equation is solved until the patch of curvatures is reached (i.e., when  $\kappa = \kappa_f$ , with  $\kappa_f$  calculated with Eq. (9.7)). The corresponding bubble shape  $F(x, y)$  is then reconstructed and implemented in the raytracing algorithm, from which the value of  $\delta_r/a$  is obtained for a given value of the refractive index ratio  $m = n_1/n_2$ . Even though for gases  $n_2 \approx 1$ , the use of  $m$  makes the method also applicable to inviscid pancake drops, as discussed later. The procedure is repeated for various values of  $\text{Ca}$  and  $m$ .

### Simplified model for the bubble shape

Another shape function of the bubble is also considered, composed of a static meniscus of radius  $R = a - h_\infty$  connected to a flat lubrication film of thickness  $h_\infty$ . This model, though not based on rigorous physical grounds, is considered here because of its simplicity. In fact, using Eq. (9.1), this model gives rise to an analytical expression predicting  $h_\infty/a$ :

$$\frac{h_\infty}{a} = 1 + \frac{\delta_r}{a} \left( \frac{4m^2}{1 + \sqrt{1 + 8m^2} - 4m^2} \right) \quad (9.9)$$

### Comparison of the two models

We want to test if the simplified model can be used to correlate  $h_\infty/a$  and  $\delta_r/a$  instead of applying the ray-tracing algorithm on the Bretherton model to build this correlation. For this purpose, values of  $\delta_r/a$  calculated by applying the ray-tracing algorithm on the Bretherton model are compared to Eq. (9.9) in Fig. 9.10. As it can be seen on this figure, the simplified model over-predicts  $h_\infty/a$  for a given value of  $\delta_r/a$  as compared to the Bretherton model. The discrepancy between the prediction of these two models being enhanced as  $\delta_r/a$  decreases. For example, for  $\delta_r/a = 0.30$ , the the simplified model predicts a value of  $h_\infty/a$  twice larger than the value predicted by the Bretherton model. This shows that the simplified model (i.e, Eq. (9.9)) cannot be used to deduce values of  $h_\infty/a$  from values of  $\delta_r/a$ . To do so, a correlation needs to be build relating  $\delta_r/a$  to  $h_\infty/a$  based on a more accurate model.

This is why in the first part of the next section, this correlation is build by applying the ray-tracing algorithm on the Bretherton model (presented in the first subsection of Section 9.2.3). After building the correlation, the method we propose consists in using this correlation to infer the lubrication film thickness from a single snapshot of the bubble. This is presented in the second part of the result section.

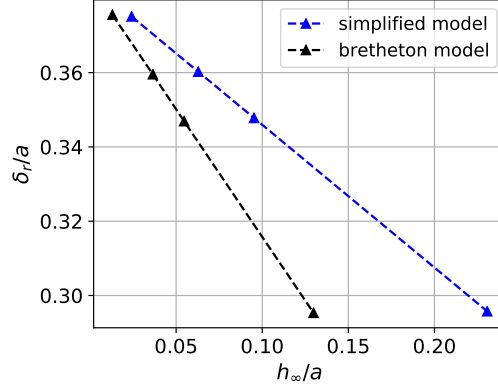


Figure 9.10: Position of the glare circle relative to the bubble edge,  $\delta_r/a$ , as a function of the lubrication film thickness,  $h_\infty/a$ , for  $m = 1.46$ . Th

### 9.3 Results and discussion

The results section is divided into two subsection. In the first subsection, the relationship correlating  $h_\infty/a$  to  $\delta_r/a$  and  $m$  is established. In the second subsection, the accuracy of the correlation is verified. Measurements of  $\delta_r/a$  performed in the experiments are used to calculate  $h_\infty/a$  using the established correlation.

#### 9.3.1 Establishment of an alternative equation for measuring the thickness of the lubrication film and the channel height

In order to relate  $\delta_r/a$  to  $h_\infty/a$  the following procedure is followed: given a certain value of  $Ca$ , a dimensionless bubble profile,  $F(x, y)/a = 0$ , is calculated using Eqs. (9.6), (9.7) and (9.8). The raytracing algorithm, presented in the methodology section, is applied on  $F(x, y)/a = 0$  and the value of  $\delta_r/a$  is calculated, for a fixed value of  $m$ . This procedure is done for several values of  $Ca$  and  $m$ .

The curves relating  $\delta_r/a$  to  $h_\infty/a$  are obtained, and are plotted in Fig. 9.11 for different values of  $m$ . It is observed that  $\delta_r$  is linearly correlated to  $h_\infty$ . Notably, for a static bubble, i.e., for  $Ca \rightarrow 0$ , the film becomes very thin, i.e.,  $h_\infty \rightarrow 0$ , (see Eq. 8.23). Thus, the front of the bubble forms a circle of radius  $R = a$ . In this situation, using Eq. (9.1), one has an expression relating  $a$  to  $\delta_{r,0}$ :

$$a(\delta_{r,0}) = \frac{\delta_{r,0}}{1 - \frac{1 + \sqrt{1 + 8m^2}}{4m^2}} \equiv \frac{\delta_{r,0}}{\xi(m)}, \quad (9.10)$$

As it can be seen, by only measuring  $\delta_{r,0}$  on an image of a static bubble, the channel height can be calculated. It should be noted that in practice, even for a static bubble, a lubrication film stabilized by Van Der Waals interactions is still present. However, the thickness of these films is known to be around a hundred nanometer therefore can be assumed to be zero in the frame of the present method. The empty symbols in Fig. 9.11 are given by Eq. (9.10). Finally, a new correlation based on the data of Fig. 9.11 can be written, as

$$\bar{h}_\infty(\delta_r) \equiv \frac{h_\infty}{a(\delta_{r,0})} = \frac{\xi(m)}{f(m)} \left( 1 - \frac{\delta_r}{\delta_{r,0}} \right), \quad (9.11)$$

where  $f(m) = Am^2 + Bm + C$  with  $A = -1.41 \pm 0.05$ ,  $B = 4.9 \pm 0.2$  and  $C = -3.5 \pm 0.1$  being the best fitted coefficients together with their standard deviations (see insert of Fig. 9.11). Note that this correlation



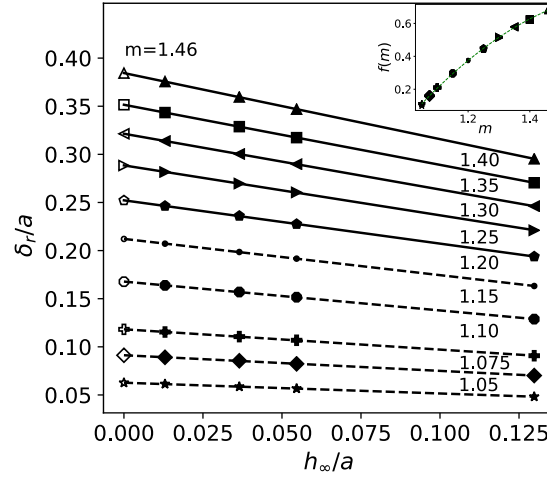


Figure 9.11: Position of the glare ring relative to the bubble edge,  $\delta_r/a$ , as a function of the lubrication film thickness,  $h_\infty/a$  for various values of the ratio of refractive indices  $m$ . Full symbols give values of  $\delta_r/a$  computed with our raytracing algorithm and empty symbols are calculated with Eq. (9.10). Lines for usual values of  $m$  corresponding to bubbles (resp., drops) are solid (resp., dashed). The insert depicts value of the function  $f(m)$  appearing in Eq. (9.11) and its best second-order polynomial fit (green dashed line)..

is established using only perpendicular rays (see dashed red line in Fig. 9.3), i.e., for an acceptance angle of the objective equal to 0:  $\alpha \equiv \arcsin(\text{NA}) = 0$ , where NA is the numerical aperture of the objective lens. For finite acceptance angles of the acquisition system (see gray area in Fig. 9.3), corrections based on the numerical aperture (NA) of the objective are derived below. For the configuration used here, it leads to a bias of about 3% in  $\delta_r$  or  $a(\delta_r)$ , which is comparable to their experimental determination uncertainties. Nevertheless, for the calculation of  $\bar{h}_\infty(\delta_r)$ , this error cancels out as can be inferred from Eq. (9.11).

In the next section, values of  $\bar{h}_\infty(\delta_r)$  are compared to values of  $\bar{h}_\infty(U)$  (obtained by measuring the bubble velocity and using Eq. (9.8)).

### 9.3.2 Experimental measurements

We remind that experiments were performed at room temperature using mineral and silicon oils as working liquids. Air bubbles are produced inside a microchannel filled with these liquids, hence  $m = n_1$ . A constant pressure difference is applied along the channel to induce the translation of bubbles. The bubble velocity and the parameter  $\delta_r$  are measured during these experiments (as explained in the methodology section).

First measurement of  $\delta_r/a(\delta_{r,0})$  is reported for the two fluids, where  $a(\delta_{r,0})$  is obtained with Eq. (9.10). It is observed in Fig. 9.12 that  $\delta_r/a(\delta_{r,0})$  is a decreasing function of Ca. The shift between the curves obtained with the two different fluids is due to the difference in refractive indices.

At this stage, the two correlations (9.8) and (9.11) can be used independently for the indirect measurement of the lubrication film thickness,  $h_\infty$ . In the following, they are referred to as the *Classical* and the *New* methods, respectively. It is worth noting that the two methods do not require the same set of input parameters as summarized in Table 9.1, in which the parameter values obtained using appropriate instruments are provided. It should be noted for instance that  $a$  is an input parameter for the classical method and has been measured with a 3D confocal microscope over a wide area of the channel. Contrarily,  $a$  is an output parameter for the new method and has been obtained by measuring  $\delta_{r,0}$  at one (or several) specific  $(x, z)$  location for a quiescent bubble. Yet the two measurements of the channel depth are in excellent agreement. Now, since both  $U$  and  $\delta_r$  were measured during

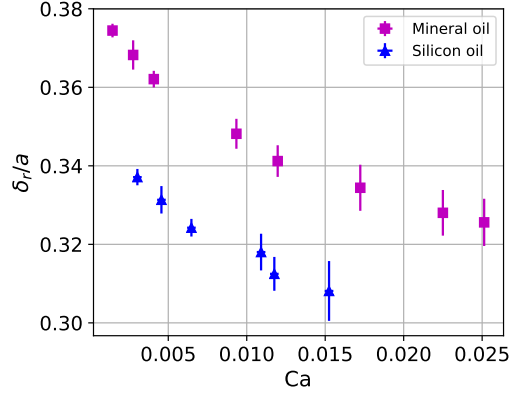


Figure 9.12: Measurement of  $\delta_r/a(\delta_{r,0})$  as a function of  $Ca$  where the channel height  $a(\delta_{r,0})$  is inferred from Eq. (9.11).

Table 9.1: Summary of the indirect measurement of  $\bar{h}_\infty = h_\infty/a$  with the classical and new methods. The measurement techniques and the corresponding instruments used for the input parameters are: (a) rheometer (Rheosens), (b) Tensiometer (KRUS DSA 100), (c) 3D confocal microscope (Keyence VK-X 200), (d) Bright-field microscope (Nikon eclipse Ti-5), (e) Standard camera (ALLIED GC2540), and (f) Refractometer (ATAGO DR-A1). The lines corresponding to the output parameters are in bold face.

Method	Parameters	Mineral oil	Silicon oil	Technique
<i>Classical</i>	$\mu$ (mPa/s)	$22 \pm 0.5$	$19 \pm 0.5$	(a)
	$\sigma$ (mN/m)	$29.8 \pm 0.1$	$20.6 \pm 0.1$	(b)
	$a$ ( $\mu\text{m}$ )	$109 \pm 3.1$		(c)
	$U$ ( $\mu\text{m/s}$ )	$U \pm \Delta U$		(d,e)
	$\bar{h}_\infty(U)$	<b>see Fig. 9.13</b>		<b>Eq. (9.8)</b>
<i>New</i>	$m$	1.4638	1.402	(f)
	$\delta_r$ ( $\mu\text{m}$ )	$\delta_r \pm \Delta\delta_r$		(d,e)
	$a(\delta_{r,0})$ ( $\mu\text{m}$ )	$110 \pm 1.5$	$111.5 \pm 0.2$	<b>Eq. (9.10)</b>
	$\bar{h}_\infty(\delta_r)$	<b>see Fig. 9.13</b>		<b>Eq. (9.11)</b>

the experiments, the two methods can directly be compared, as plotted in Fig. 9.13. The excellent agreement with the parity line thus validates the approach.

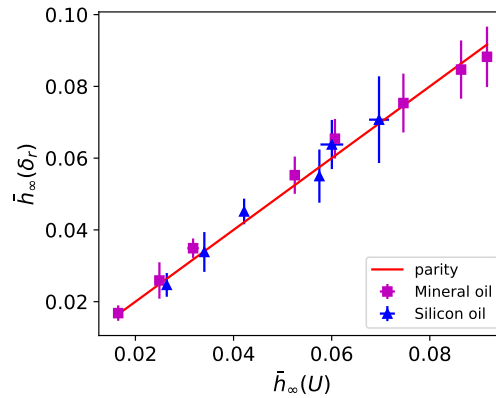


Figure 9.13: Comparison of indirect measurements of the lubrication film thickness  $\bar{h}_\infty = h_\infty/a$ , between the classical method using Eq. (9.8) and the new method using Eq. (9.11).

Furthermore, by equating Eqs. (9.11) and (9.8), the new method can be used to measure the velocity  $U$  of the

Table 9.2: Measured values of the visco-capillary velocity using direct techniques as given in Table 9.1 and (in bold) the indirect method that combines the classical and the new methods.

	Mineral oil	Silicon oil	
$\frac{\sigma}{\mu}$ (m/s)	$1.35 \pm 0.03$ <b><math>1.26 \pm 0.26</math></b>	$1.08 \pm 0.029$ <b><math>1.08 \pm 0.09</math></b>	see Table 9.1 <b>Eqs. (9.8, 9.10, 9.11)</b>

bubble, provided the ratio  $\sigma/\mu$  is added to the set of input parameters. As the new method necessitates only a single snapshot of the bubble, it can be advantageous when the velocity of the bubble is not uniform or when a high speed camera is not available. More interestingly, if  $U$  and  $\delta_r$  are measured simultaneously, combining the methods enables to measure the ratio  $\sigma/\mu$ , referred to as the visco-capillary velocity:

$$\frac{\sigma}{\mu} = 1.337^{\frac{3}{2}} U \frac{\left(1 - 2.19 \frac{\xi(m)}{f(m)} \left(1 - \frac{\delta_r}{\delta_{r,0}}\right)\right)^{\frac{3}{2}}}{\left(\frac{\xi(m)}{f(m)} \left(1 - \frac{\delta_r}{\delta_{r,0}}\right)\right)^{\frac{3}{2}}} \quad (9.12)$$

Nevertheless, as it can be observed in Fig. 9.13, the uncertainties associated to the calculation of  $\bar{h}_\infty(\delta_r)$  are smaller for the lower values of this variable due to slight blurring of the images at higher translation velocities. For this reason, the precision on the calculation of  $\sigma/\mu$  is larger for small values of  $\bar{h}_\infty(\delta_r)$ , and here, only the data points corresponding to a translation velocity lower than 0.00701 m/s have been kept for validation purpose. Results are again in excellent agreement with independent techniques as shown in Table 9.2.

Note that to increase the accuracy on  $\delta_r$ , we have used the value averaged over the range of angles  $\vartheta \approx \pm 15^\circ$ , as represented on the right of Fig. 9.2. Despite the fact that the shape function  $F(x, y)$  used in this work is strictly valid for  $\vartheta = 0$ , the corresponding variation made on the shape for small variations along the perimeter of the bubble remains small. Indeed, using the model of Burgess and Foster (1990), we have estimated the maximum of the variation  $\Delta h/a$  at  $\pm 0.004$ , i.e., well below the uncertainty of our experimental measurements, as it can be deduced from the amplitude of the error bars in Fig. 9.13. This said, our method can easily be adapted to other situations such as a pancake drop instead of a pancake bubble, at the sole condition that  $m > 1$ . To this purpose, the new shape function should be constructed depending additionally on the viscosity ratio, denoted  $\lambda = \mu_d/\mu$ , between the viscosity of the drop,  $\mu_d$ , and the one of the surrounding liquid (Balestra *et al.* (2018)). Updating the raytracing algorithm with these new shapes should allow to extend the correlating function in Eq. (9.11) for non-zero viscosity ratio, i.e.,  $f(m, \lambda)$ . Nevertheless, as mentioned earlier, the correlating function  $f(m)$  is already valid for inviscid pancake droplets. Practically, Balestra *et al.* (2018) have demonstrated that the shape of droplets for  $\lambda \lesssim 10^{-2}$  is almost identical to the shape obtained for  $\lambda = 0$ , as it has been considered in this work. This said, it is worth mentioning that the ratio of refractive indices  $m$  being lower for droplets than for bubbles, the sensitivity of the method would also be lower, as inferred from Fig. 9.11.

The raytracing and analytical determination of the glare ring position so far assumed an effective numerical aperture (NA) equal to 0, i.e. only perpendicular rays enter the system and are able to enter the camera. In the last section, we will examine what happens when a finite acceptance angle of the microscope objective is present.

### 9.3.3 Effect of a finite numerical aperture

A representative sketch of the setup is shown in Fig. 9.14. In the experiments, the microscope illumination path is made as parallel as possible, whereas the NA of the used 10x objective is 0.3. Thus, all outgoing rays with an angle below  $\alpha \equiv \arcsin(\text{NA}) = 17.4^\circ$  after refraction at the glass-air interface enter the microscope (see Fig.

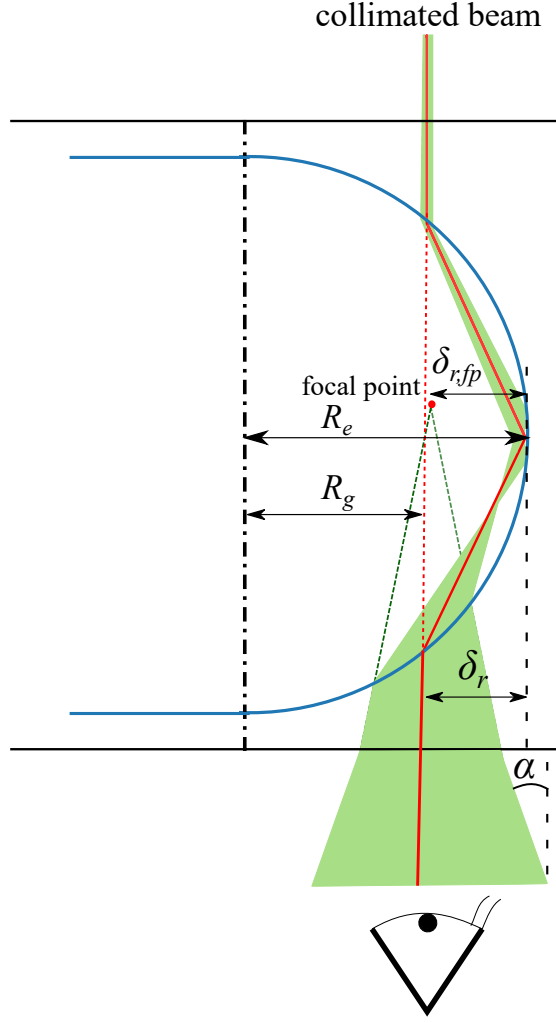


Figure 9.14: Trajectory of the rays that interact three times with a circular interface. The radius of the circle is  $R_e$ . The ray that exits the bubble perpendicularly defines  $R_g$ , as described in Eq. (9.1). This ray is depicted in red.

9.14). As it can be seen, this leads to a broadening of the glare ring. In the experiments, the microscope objective is focused on the middle of the channel in order to have a sharp bubble edge. From Fig. 9.14, it can be noticed that the axial rays delimiting the glare ring converge towards a focal point nearby (red dot in Fig. 9.14). Therefore, on the experimental images of the bubble, the thickness of the glare ring is small and its center can be assumed to be at the focal point  $\delta_{r,fp}$  of the axial rays delimiting the glare ring.

Following raytracing simulations, the induced error  $(\delta_{r,fp} - \delta_r)/\delta_r$  is plotted as a function of the NA of the used objective in Fig. 9.15. The curves in this plot were calculated for silicon oil and accounting for the fact that the objective is immersed in air. The curves show that as NA increases, the shift between the focal point and the perpendicular ray increases. For  $NA = 0.3$ , this shift reaches 3.4%. However, this shift does not depend significantly on  $h_\infty/a$  for  $NA = 0.3$  in the range of values of  $h_\infty/a$  obtained in the experiments. As a result, the bias on the calculation of  $\delta_r$  and  $\delta_{r,0}$  is approximately equal and almost cancels out in the calculation of  $h_\infty/a$  (see Eq. (9.11)). In conclusion of this section, raytracing simulations for a finite acceptance angle of the objective indicate that the bias could be approximately of 3% in the present case. This was calculated based on the position of the focal point of the axial rays delimiting the glare ring. However, not all rays in the glare ring will go through this point and the experimental location of the focal plane is also difficult to determine. As such, it seems unrealistic to present corrections on the given correlation based on the NA of the used objective. In addition, the

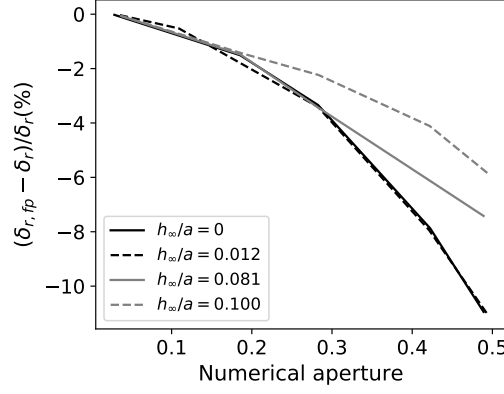


Figure 9.15: Relative shift between the position of the ray that exits the bubble perpendicularly and the focal point of the rays exiting the bubble as a function of the numerical aperture of the lens for  $m = 1.402$ .

corrections would tentatively be similar or smaller than the experimental uncertainty in the determination of  $\delta_r$ . Therefore such corrections have not been taken into account.

## 9.4 Conclusion

In conclusion, we have shown how one can measure the lubrication film thickness around a pancake bubble or inviscid drop, from a single bright-field image, as can be typically obtained with a transmission microscope. We also demonstrated how one can combine this technique with the measurement of the bubble velocity to extract a measure of the visco-capillary velocity. It is believed that the new method presented in this work can be of wide use in the future as it requires a standard microscope and a visual inspection of a single image, hence a smaller amount of less sophisticated instruments, as outlined in Table 9.1.

In this chapter, buoyancy effects were neglected because of the small dimensions of the studied system. In the next chapter, the effect of buoyancy on the motion of a long bubble translating inside an horizontal and cylindrical microchannel is studied with experiments and theoretical analysis. In particular the influence of buoyancy on lubrication film thickness and on the bubble orientation is analyzed.

## CHAPTER 10

### Effect of buoyancy on the motion of a long bubble in a horizontal tube

This chapter presents a work that was conducted at Princeton University during an eight month stay (1st February 2016 - 30<sup>th</sup> September 2016). It has been performed at the department of Mechanical and Aerospace Engineering (MAE) in the “Complex Fluid Lab” directed by Prof. Howard A. Stone. The aim of this work is to analyze by the means of experiments and theory, the effect of buoyancy on the dynamics of Taylor Flows. As briefly discussed in chapter 8, the presence of buoyancy affects the system by adding a hydrostatic pressure contribution to Eq. (8.8). As it will be shown, this has an influence on the thickness of the lubrication film. This collaboration between ULB and PU gave rise to papers in the journals entitled *Physical Review fluids* and *Langmuir* (Atasi *et al.* (2017); Khodaparast *et al.* (2018)). Only the work regarding the effect of buoyancy on the dynamics of Taylor flows is presented in this chapter because of its relevance with the previous chapter. The second publication studies the dynamics of the dewetting of the lubrication film in microchannels and is mentioned in the conclusion of this thesis. These two works were conducted in collaboration with Sepideh Khodaparast, a former Post-doc in the Complex Fluid Lab.

#### 10.1 Introduction

The motion of elongated bubbles in small liquid-filled confined geometries is a hydrodynamic problem with a large variety of industrial and medical applications in lubrication, heat and mass transfer, oil extraction and treatment of pulmonary disorders. The problem involves translation of a low viscosity fluid at average speed  $U$  into a higher viscosity liquid with density, viscosity and surface tension of  $\rho$ ,  $\mu$  and  $\gamma$ , respectively; the density of the bubble is negligible relative to that of the continuous liquid phase (Fig. 10.1). Characterization of the motion and the shape of the bubble requires consideration of the Reynolds number,  $Re = \frac{\rho U a}{\mu}$ , where  $a$  is the radius of the tube, in order to characterize the relative magnitudes of inertial and viscous effects, the Bond number,  $Bo = \frac{\rho g a^2}{\gamma}$ , where  $g$  denotes the gravitational acceleration, in order to characterize buoyancy effects relative to interfacial tension effects, and the capillary number,  $Ca = \frac{\mu U}{\gamma}$ , in order to assess the relative magnitudes of viscous and interfacial tension effects. In microscale geometries, the effects of buoyancy and inertia are often negligible ( $Bo, Re \ll 1$ ) and the motion of elongated bubbles can be described by a single dimensionless number, namely the capillary number  $Ca$ . However, as the dimensions of the geometry increase to millimeter lengths, gravitational effects have significant impacts on the shape and dynamics of the bubbles. In this paper, we aim to quantify such effects for long bubbles in millimeter diameter tubes at moderate capillary numbers and in the absence of inertia.

It was first observed by Fairbrother and Stubbs (1935) that in a circular tube filled with liquid a bubble moves slightly faster than the bulk liquid due to the formation of a thin liquid film between the bubble and the boundary. In other words, the deposition of a thin liquid film on the wall does not allow the entire volume of the more viscous liquid to be pushed out of a closed geometry using a less viscous fluid. The amount of liquid left on the tube wall is observed to increase with the velocity of the bubble. Accurate determination of the volume of liquid left on the bounding walls of the geometry was pioneered by the theoretical work of Bretherton (1961) and experimental measurements of Taylor (1961). Bretherton’s theory predicts the thickness of the liquid film  $h$  to increase with

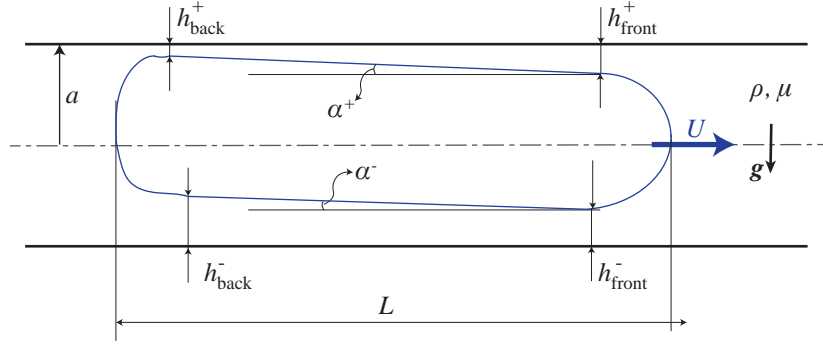


Figure 10.1: Schematic of a typical elongated bubble translating at capillary number  $Ca \approx 10^{-2}$  in a horizontal tube of radius  $a$ . The bubble is immersed in a viscous liquid of density  $\rho$  and viscosity  $\mu$ . Here  $U$  and  $L$  are the velocity and the length of the bubble, respectively. A spherical cap is present at the front of the bubble for low to moderate capillary numbers, followed by a transition region and a lubrication film. Because gravity  $g$  acts perpendicular to the tube axis, the bubble is inclined and the thin film has different thicknesses at the front ( $h^+_{\text{front}}$  and  $h^-_{\text{front}}$ ) compared to the back ( $h^+_{\text{back}}$  and  $h^-_{\text{back}}$ ). At the back of the bubble, a capillary wave is present (Bretherton (1961)).

$Ca^{2/3}$  for  $Ca < 10^{-3}$  in the visco-capillary regime

$$\bar{h}_{Br} = \frac{h}{a} = 1.337 Ca^{2/3}. \quad (10.1)$$

Later, Aussillous and Quéré (2000) provided a scaling analysis to extend Bretherton's theory to a wider range of  $Ca$  by considering the contribution of the liquid film thickness in defining the curvature at the front of the bubble:

$$\bar{h} = \frac{h}{a} = \frac{1.337 Ca^{2/3}}{1 + 3.35 Ca^{2/3}}. \quad (10.2)$$

The empirical coefficient in the equation above, 3.35, was found by fitting the result of their scaling analysis to the experimental measurements of Taylor for capillary numbers up to  $Ca = 2$  (Taylor (1961)).

More recently, several attempts have been made to investigate the gravitational effects on different features of the shape and the dynamics of confined elongated bubbles (Suresh and Grotberg; Zheng *et al.* (2007); de Lózar *et al.* (2008); Han and Shikazono (2009); Gupta *et al.* (2010b); Leung *et al.* (2012)). Such effects were generally neglected in the small horizontal geometries discussed above. A summary of the most relevant works, including studies of the motion of semi-infinite low viscosity air fingers progressing in liquid flows, is presented in Table 10.1. In general, two main features have been reported in the literature:

1. In the cross-sectional plane, buoyancy causes asymmetry in the distribution of the liquid film around the bubble. In two-dimensional geometries, this effect simply leads to a thinner liquid film at the top compared to the bottom of the tube. For example, Jensen *et al.* (1987) showed that for  $Ca < 10^{-3}$  the liquid film at the front of a long finger of gas translating in viscous liquid can be predicted analytically by  $\bar{h}^{\pm} = \frac{\bar{h}_{Br}}{1 \pm Bo}$ , where the  $+$  and  $-$  superscripts correspond to the top and the bottom of the channel, respectively. However, this model has not been tested against experimental measurements performed at finite  $Bo$ . Thus, here we modify the theory proposed by Jensen *et al.* to account for finite values of  $Ca$  and test its validity against experimental measurements for long bubbles in a tube of circular cross-section.
2. In the direction of the flow, a bubble is inclined with respect to the horizontal axis of symmetry; see the schematic in Fig. 10.1. As a result, a uniform film thickness region between the front and the back menisci, as predicted by Bretherton, no longer exists when gravitational effects are significant. Leung *et al.* (2012) showed that the inclination of a bubble is caused by the drainage of the liquid in the thin film region from the top to the bottom of the tube. Their experimental quantification of the drainage volume followed well the predictions of a mass balance analysis proposed in their study for  $Bo \leq 0.25$ . The inclination angle was observed to be fairly constant along the length of the bubble (Han and Shikazono (2009); Leung *et al.*

Table 10.1: Previous research on the motion of bubbles in horizontal and inclined channels with significant gravitational effects.

Ref.	Problem and geometry	Approach	Flow parameters	Focus of study
Jensen <i>et al.</i> (1987)	Saffman-Taylor finger* 2D (Hele-Shaw)	Theory, experiments	$Ca < 10^{-3}$ , $0 < Bo < 3.3$	Effect of $Ca$ and $Bo$ on the shape of the front meniscus, pressure jump across the interface and the film thickness at the front.
Brener <i>et al.</i> (1993)	Saffman-Taylor finger, 2D (Hele-Shaw)	Theory, experiments	-	Effect of buoyancy on the shape of the front meniscus in tilted channels.
Suresh and Grotberg	liquid slug bounded between 2 air bubbles, 2D	Theory	$0 < Ca < 0.05$ , $0 < Bo < 2$ , $0 < \theta^{**} < 180^\circ$	Effect of buoyancy on the shape of the front meniscus in tilted channels.
Zheng <i>et al.</i> (2007)	liquid slug bounded between 2 air bubbles, 2D	Numerics	$0.03 < Ca < 0.4$ , $0 < Bo < 0.6$ , $0 < \theta < 180^\circ$	Effect of buoyancy on the flow pattern in the liquid plug region.
de L��zar <i>et al.</i> (2008)	infinite finger, 3D (rectangular cross-section)	Numerics	$0.002 < Ca < 20$ , $Bo = 0, 1, 2.5$ , $1 < A_R^{***} < 8$	Effect of channel aspect ratio $A_R$ , $Ca$ and $Bo$ on the cross-sectional shape of the bubble and pressure jump across the front meniscus.
Han and Shikazono (2009)	slug flow, 3D (circular cross-section)	Experiments	$10^{-4} < Ca < 0.4$	Effect of $Ca$ , $Bo$ , $Re$ on the distribution of the liquid film thickness around the bubble.
Leung <i>et al.</i> (2012)	slug flow, 3D (circular cross-section)	Theory, experiments	$0.03 < Ca < 0.2$ , $Bo = 0.07, 0.17, 0.25$	(I) Effect of buoyancy on the distribution of the liquid film thickness around the bubble. (II) Velocity measurement in the liquid plug.
Present study	isolated elongated bubble, 3D (circular cross-section)	Theory, experiments	$10^{-3} < Ca < 0.15$ , $0.05 < Bo < 0.42$ , $10 < L^{****} < 35$	(I) Effect of $Ca$ and $Bo$ on the inclination angle and the film thickness. (II) Effect of bubble length on the film thickness.

\* The Saffman-Taylor problem refers to the motion of a low viscosity fluid displacing a higher viscosity fluid in a Hele-Shaw geometry.

\*\*  $\theta$  is defined as the angle between the orientation of the channel and the vertical direction for a tilted channel.

\*\*\*  $A_R$  is the aspect ratio of the cross-section of the channel defined as the ratio of the width to the height.

\*\*\*\*  $L$  is the length of the bubble divided by the channel radius.

(2012)), however, direct experimental quantification of the angle and its correlation with the flow parameters has not been reported. In this chapter we quantify the angle of the inclination for finite values of  $Bo$  and a range of  $Ca$ . Due to the inclination, the length of the bubble is expected to be an important parameter in determining the thickness of the film along the bubble, which we demonstrate and quantify below.

In a continuous train of bubbles separated by slugs of liquid on the orders of the tube radius and when buoyancy effects are significant, consecutive bubbles are observed to influence one another due to hydrodynamic interactions (Zheng *et al.* (2007)). This effect modifies the flow pattern in front of a translating bubble and therefore alters the shape of the front meniscus and the film thickness with respect to that of a single translating isolated bubble. To avoid such hydrodynamic interactions, here we study isolated independent bubbles in horizontal tubes of circular cross-section.

We provide a theoretical analysis by combining the available models in the literature for different geometrical and flow parameters, which predicts the evolution of the liquid film thickness around an elongated air bubble in a horizontal tube of circular cross-section. Also, we report experimental data to quantify the buoyancy effects on the motion of confined elongated bubbles. In particular, we perform bright-field side-view microscopy to directly observe the asymmetries in the flow caused by buoyancy. This approach allows direct quantification of the inclination angle and the distribution of the film thickness along the length of the bubble. Different  $Ca$  and  $Bo$  numbers are tested by systematically varying the velocity of the liquid phase and tube diameter. We also identify the influence of bubble length.



## 10.2 Experimental setup

### 10.2.1 Refractive index matching

Experiments were performed in glass capillaries of radii  $a = 0.51, 0.75, 1.15, 1.51\text{mm}$  and length  $L = 10\text{ cm}$ , which were submerged in a refractive index matching box filled with glycerol. The diameters of the tubes were measured optically using pre-calibrated microscope objectives. The region of interest (ROI) was observed through the straight side wall of the box (Fig. 10.2). This approach, together with the identical refractive indices of the working fluid, tube material and surrounding glycerol pool ( $n = 1.47$ ), ensured no optical distortions of the ROI due to light refraction at the outer and inner curved walls of the capillary (Budwig (1994)). Moreover, the refractive index matching design prevented total internal reflections, and thus allowed us to resolve the thin liquid film formed between the two-phase interface and the inner tube wall.

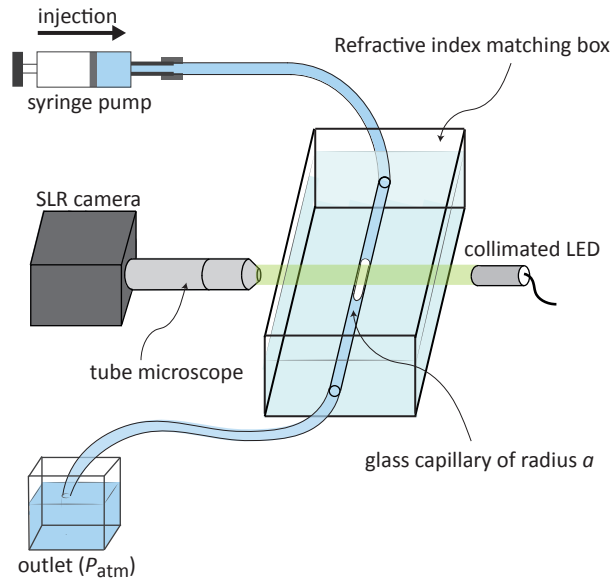


Figure 10.2: Schematic of the experimental setup showing a capillary placed in a box filled with refractive index matching liquid to eliminate optical distortions.

### 10.2.2 Experiments

All experiments were performed at  $T = 25^\circ\text{C}$  using glycerol as the continuous liquid phase (viscosity  $\mu = 0.84\text{ Pa}\cdot\text{s}$ , density  $\rho = 1186\text{ kg/m}^3$ , and surface tension  $\gamma = 0.063\text{ N/m}$ ) and air as the dispersed gas phase. The glycerol used in the experiments was kept in sealed containers to minimize the effect of humidification and the viscosity was measured before and after the tests to ensure no water absorption. The glass capillary, which was fixed to the sides of the refractive index matching box, was connected to a syringe pump using a long flexible tube at the entrance, whilst at the exit another flexible tube emptied the outlet fluid at atmospheric pressure (Fig. 10.2). The entire volume of all connection tubes was filled with glycerol. At the beginning of each experiment, a long air finger was created at the inlet of the flexible tube by slightly elevating the tube inlet relative to the outlet. The air-filled inlet was then connected to the syringe pump needle that was filled with liquid to create a confined bubble of length  $L \sim 20a$ . The bubble was carried into the ROI as glycerol was pumped at a constant flow rate. This procedure ensured no acceleration or deformation of the bubble caused by the injection geometry.

### 10.2.3 Visualization and image processing

Experimental measurements were obtained by processing the digital shadow-graphy images. The refractive index matching box was placed between a green collimated light source and a home-made tube microscope equipped with long working distance objectives of 5X and 10X magnification (with spatial resolution, respectively,  $2.44 \mu\text{m}$  and  $1.22 \mu\text{m}$  per pixel). Bright-field microscopy allowed visualization and consequently detection of a sharp interface between the gas and the liquid phases using a Canny edge detection algorithm (Khodaparast *et al.* (2014)). Images of the ROI were recorded by a Nikon D5100 camera at 30 frames per second. Film thickness measurements were performed using the bright-field images captured at the front and the back of the bubble. Prior to each measurement, the horizontality of the camera was ensured using a digital level. To measure the film thickness at the top of the channel, acquired images at the front and back of the bubble were cropped starting from the top wall towards the middle plane of the channel. The bubble edge was detected on the cropped image with a Canny edge detection algorithm. The film thickness was inferred as  $h_{\infty}^{+} = y$ , where  $y$  is the coordinate of the detected edge in the direction perpendicular to the flow. To measure the film thickness on the bottom wall, acquired images at the front and back of the bubble were cropped starting from the bottom wall towards the middle plane of the channel and the procedure described above was repeated. The maximum relative error in the film thickness measurements reported for the smallest  $Ca$  is 14%, while the rest of the measurements have a maximum experimental error of 5%.

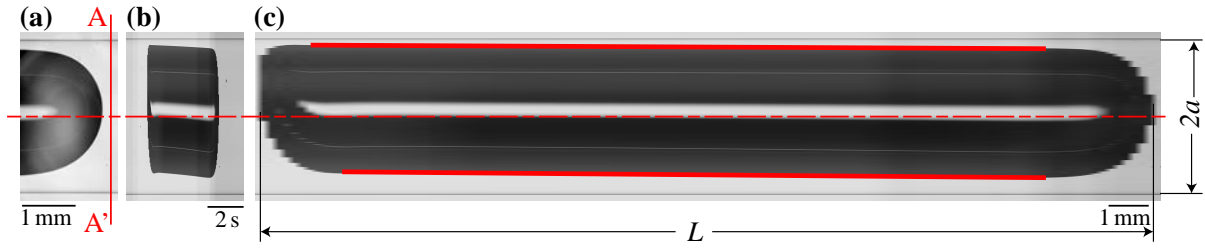


Figure 10.3: Sample visualization results for an elongated bubble of length  $L = 22 \text{ mm}$  in a horizontal tube of radius  $a = 1.51 \text{ mm}$  at  $Ca = 0.076$  and  $Bo = 0.42$ . The dashed horizontal line shows the centerline of the tube. (a) A sample image of the grey-scale bright-field microscopy. Bubble translates from the left to the right. Time-strip analysis is performed along a sample line such as section AA'. The field of view in a typical image covers less than 2 mm length of the tube. (b) Time-strip analysis result showing evolution of section AA' in time. Note that the horizontal axis represents time. (c) The horizontal time axis in (b) is converted to the length axis using the bubble velocity. The inclination angle is measured by fitting a straight line to the bubble interface as shown by the red lines. Note that images similar to the one presented in (c) are only used to measure the length and the inclination angle of the bubble.

Obtaining high spatial resolution in the images requires high magnification in the optical setup, which consequently leads to a relatively small field of view (FOV). For example, using the 5X objective in our experiments, we could visualize only about 2 mm of the tube length in the images, which is obviously not adequate to capture the axial evolution of the shape of the long bubbles (Fig. 10.3a). In order to construct an image of the full length of the bubble that does not fit in the FOV, we applied the post-processing time-strip method to the sequence of shadow-graphy images (Borhani *et al.* (2010)). In this approach, we followed the evolution of a specified vertical line of pixels along the tube diameter (Fig. 10.3a) for a long period of time starting before the arrival of the bubble front until after departure of the back of the bubble (Fig. 10.3b). Knowing the bubble velocity, time is then converted to the displacement of the bubble and the shape of the bubble is constructed (Fig. 10.3c). The final image was then processed to obtain the length and the inclination angle of the bubble. The difference between the thickness of the liquid film at the top and at the bottom as well as the inclination of the bubbles are clearly noticeable in Fig. 10.3b and Fig. 10.3c. In order to obtain the inclination angle, a straight line was fitted to the

detected air-glycerol interface. The maximum experimental error in identifying the inclination angle at the lowest  $Bo$  and  $Ca$  is 30%, while the rest of the measurements contain a maximum experimental error of 10%. The capillary number  $Ca = \frac{\mu U}{\gamma}$  was calculated based on the bubble velocity measured by tracking the nose of the bubble. The high optical resolution used in the present study allowed determination of  $Ca$  down to values on the order of  $Ca = 10^{-6}$ . The spatial resolution of the time-strip image perpendicular to the flow is fixed by the physical pixel size, the objective magnification and the numerical aperture of the objective. On the other hand, the axial resolution of the time-strip image along the flow depends on the image acquisition frequency and on the speed of the bubble. The minimum and maximum axial resolutions of the time-strip images in the experiments reported here were respectively of  $256 \mu\text{m}$  and  $1.3 \mu\text{m}$ . Note that the low optical resolution observed at the nose and the back of the bubble in Fig. 10.3c is due to the large velocity of the bubble at larger  $Ca$ . This effect, however, does not influence measurement of the bubble length or the inclination angle.

The camera and the tube were levelled horizontally prior to the start of the experiments. Furthermore, in order to ensure that the tube is horizontal, the refractive index matching box is mounted on a stage that is translated in the axial  $x$ -direction. Two images were captured as the box is moved between two points that were axially 5 cm apart. Comparison between these two images ensured no inclination in the ROI.

#### 10.2.4 First experimental observation

Examples of the shape of the nose, the central region and the back of the bubbles at different  $Ca$  and  $Bo$  are shown in Fig. 10.4. Two major differences are observed when comparing the present side-view visualizations at finite  $Bo$  numbers with the classic predictions of bubble shape with negligible buoyancy effects: (1) Due to non-negligible buoyancy effects, the liquid film at the front of the bubble is not uniformly distributed but instead is thinner at the top than at the bottom of the tube. (2) Furthermore, the back of the bubble is elevated relative to the nose. This feature was shown by Leung *et al.* (2012) to be caused by the drainage of the liquid in the film from the top to the bottom of the tube.

### 10.3 Theoretical predictions

In this section, we provide theoretical considerations to predict quantitatively both the film thickness and the inclination angle as a function of  $Ca$  and  $Bo$ . The model presented here for the film thickness at the front of the bubble is mainly based on the two-dimensional analysis proposed by Jensen *et al.* (1987) at low  $Ca$  and finite  $Bo$  in Hele-Shaw geometries. This model is extended here to account for the effect of finite  $Ca$  using the correction that was originally suggested by Aussillous and Quéré (2000), and a physical argument is provided to show that the lateral curvature of the tube does not affect the thin film thickness. The basic steps of Jensen *et al.* (1987) are included in this section, wherever necessary, to ensure the self-sufficiency of the arguments. Moreover, we utilize the mass balance analysis proposed by Leung *et al.* (2012) to obtain an estimate for the average inclination angle of the bubble. In the next section, these theoretical models are compared to our experimental measurements of the film thickness at the front and the inclination angle of the bubble, for a range of  $Ca$  and  $Bo$  ( $< 1$ ).

#### 10.3.1 Thickness of the liquid film at the front of the bubble

Following the classical approach of Bretherton, we divide the front of the bubble into three distinct regions, as discussed in Chapter 8 (Fig. 10.5). The description of these regions is similar to that of Chapter 8 with few

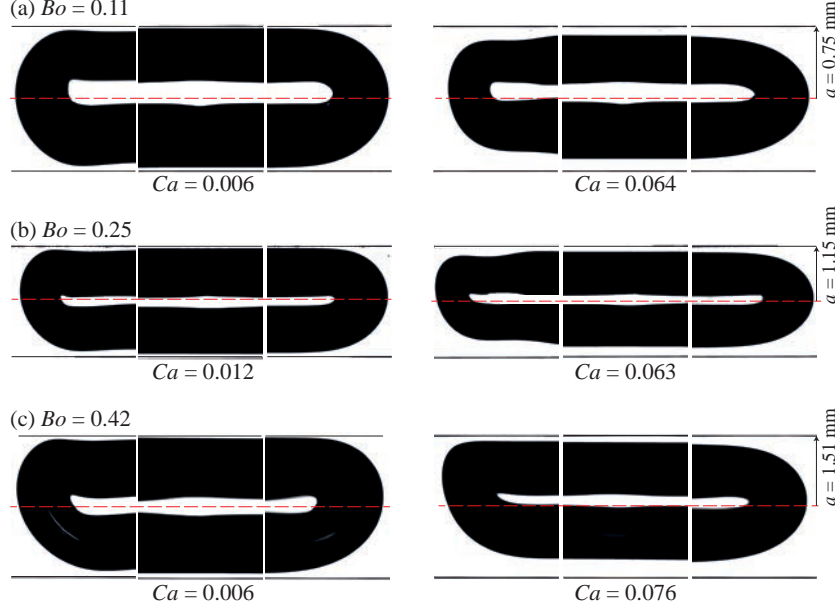


Figure 10.4: Examples of bubble shapes at different  $Ca$  and  $Bo$ . (a)  $Bo = 0.11$ , (b)  $Bo = 0.25$ , and (c)  $Bo = 0.42$ . Bubbles move from the left to the right. Images contain experimental visualization of the nose, the central part and the back of the bubble. The central region demonstrates a typical zone between the bubble nose and back, where the liquid film at the top/bottom acquires a linearly decreasing/increasing thickness towards the back. The back of the bubble exhibits a capillary wave, meaning a region of negative curvature (Giavedoni and Saita (1999)). The red dashed lines indicate the centerline of the tube. Note that the optical magnifications used in visualization of flows at different Bond numbers are not identical.

differences:

1. In region I, entitled the capillary static region (CS), the pressure is hydrostatic, in contrast to the case presented in Chapter 8 where buoyancy was neglected and, consequently, the pressure was considered as constant (see Eq. (8.8)).
2. In region II, entitled the transition region, the surface tension force is balanced by the viscous forces.
3. In region III entitled the thin film region, the axial flux (in the reference frame translating with the bubble) is balanced by the lateral drainage induced by buoyancy.

### Capillary static region (CS)

In this region, our approach follows closely that of Jensen *et al.* (1987). However, we extend the original formulation by adding the condition that at higher  $Ca$  the thickness of the film is not negligible compared to the radius of the front nose of the bubble (Aussillous and Quéré (2000)). Moreover, we consider the top to bottom asymmetry in the interface height with respect to the tube centerline (Fig. 10.5).

The dimensionless film thickness at the front of the bubble  $\bar{h}_{\infty}^{\pm}$  in a two-dimensional geometry and at very low capillary numbers  $Ca \rightarrow 0$  was determined by Jensen *et al.* (1987) to be

$$\bar{h}_{\infty}^{\pm} = \frac{\bar{h}_{Br}}{1 \pm Bo}, \quad (10.3)$$

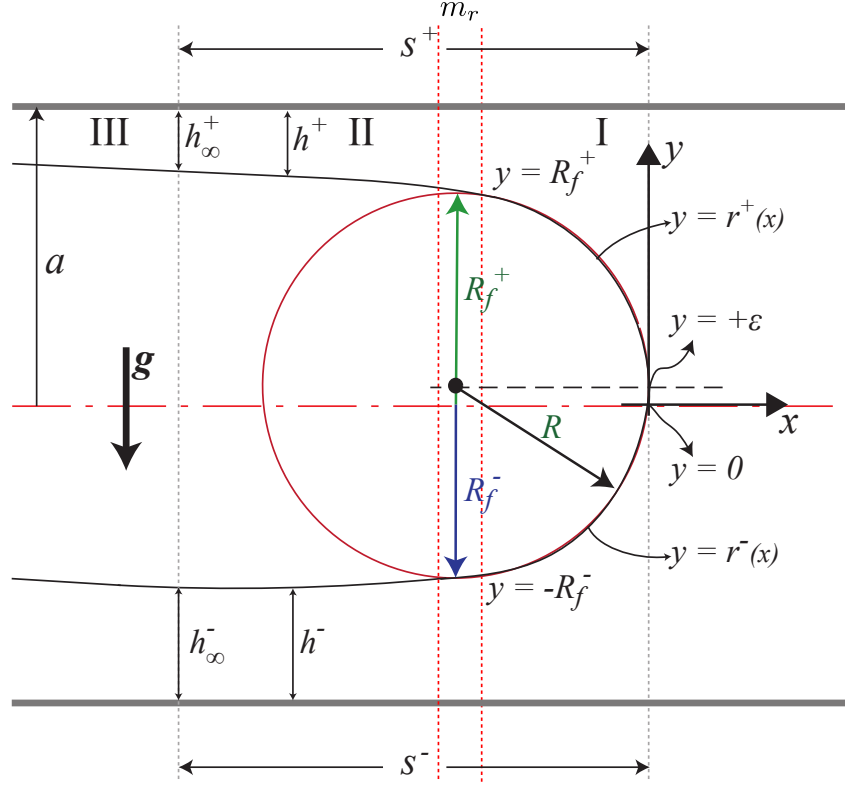


Figure 10.5: Side-view schematic of the front of a bubble in a horizontal tube of radius  $a$ . The bubble moves from left to right and is inclined with respect to the centerline of the tube. The + and – superscripts stand for the quantities at the top and the bottom, respectively. The bubble is divided in three regions: (I) indicates the capillary static region, where the tip of the bubble forms a sphere of radius  $R$ . The tip of the bubble is off-center with respect to the tube and is located at  $(x, y) = (0, \epsilon)$ . (II) indicates the transition region in which the viscous forces are balanced by the capillary forces due to the variation of the curvature along the interface. Between (I) and (II), a matching region  $m_r$  is present where the interface shape of (I) and (II) match. The position of the interface in the matching region with respect to the tube centerline is at  $y = \pm R_f^\pm$ . (III) indicates the thin film region, where the axial flux (in the reference frame of the bubble) is balanced by the lateral drainage flux of the liquid in the film.

where  $\bar{h}_{Br} = 1.337\text{Ca}^{\frac{2}{3}}$  is the classic prediction of the film thickness by Bretherton (1961) at very low  $\text{Ca}$  and negligible buoyancy effects and  $\pm$  indicates the top (+) or the bottom (–) relative to the axis of symmetry. Both of these analyses were conducted by neglecting the azimuthal curvature of the bubble. For a two-dimensional configuration, in a Hele-Shaw cell, the pressure difference caused by capillary forces between the liquid and the gas in the thin film region is  $\delta p_f \approx 0$ , while in the  $CS$  region  $\delta p_{CS} \approx -\frac{\gamma}{a}$  leading to a pressure difference between the thin film and the  $CS$  region of  $\delta p_f - \delta p_{CS} \approx \frac{\gamma}{a}$ . In a tube of circular cross-section and for thin liquid films, the pressure difference caused by capillary forces between the liquid and the gas in the thin film region is  $\delta p_f \approx -\frac{\gamma}{a}$  due to the azimuthal curvature and in the  $CS$  region is  $\delta p_{CS} \approx -\frac{2\gamma}{a}$ , which leads to a pressure difference between the thin film and the  $CS$  region of  $\delta p_f - \delta p_{CS} \approx \frac{\gamma}{a}$ . Thus, the azimuthal curvature of the interface does not change the pressure difference between the thin film region and the  $CS$  region in a tube when compared to the two-dimensional case. We will, therefore, conduct this first part of our analysis by not considering the azimuthal curvature.

In the  $CS$  region, where the pressure is hydrostatic, the coordinate system  $(x, y)$  has its  $y$  origin at the center of the channel and its  $x$  origin at the tip of the bubble (Fig. 10.5). Due to buoyancy, the tip of the bubble is elevated with respect to the center plane of the geometry and is located at  $y = \epsilon \ll a$ . In the liquid phase, the pressure

gradient is given by

$$\frac{\partial p}{\partial y} = -\rho g \quad (10.4)$$

where  $\rho$  is the density and  $g$  the gravitational acceleration. We emphasize on the fact that the present equation is different from Eq. (8.8) presented in Section 8. In fact, due to gravity, the pressure in the capillary static region is hydrostatic. This has an influence on the curvature of the front meniscus of the bubble as shown in what follows. In fact, integrating the pressure gradient with the Laplace pressure jump condition at the interface, i.e. at  $y = r^\pm(x)$ :  $p_g - p = \mp \gamma \kappa^\pm$ , where  $p_g$  is the pressure inside the bubble,  $\gamma$  the surface tension, and  $\kappa$  the curvature of the interface, yields:

$$p + \rho g y - p_g = \rho g r^\pm \pm \gamma \kappa^\pm. \quad (10.5)$$

Using the Cartesian coordinate system  $(x, y)$  shown on Fig. 10.5, the curvature of a two-dimensional interface in a Hele-Shaw configuration is given by:

$$\kappa^\pm = \frac{\partial_{xx} r^\pm}{\left(1 + (\partial_x r^\pm)^2\right)^{\frac{3}{2}}} \quad (10.6)$$

Since the gas pressure is constant, we can set  $p_g = 0$  without loss of generality. Furthermore, we can express the pressure in terms of the reduced pressure  $p_r = p + \rho g y$  such that  $p_r$  is independent of  $y$  and use the scales  $a$  for  $r$  and  $\frac{\gamma}{a}$  for  $p_r$  to finally obtain

$$\bar{p}_r = \text{Bo} \bar{r}^\pm \pm \frac{\partial_{\bar{x}\bar{x}} \bar{r}^\pm}{\left(1 + (\partial_{\bar{x}} \bar{r}^\pm)^2\right)^{\frac{3}{2}}}, \quad (10.7)$$

where  $\text{Bo} = \frac{\rho g a^2}{\gamma}$  is the Bond number and an overbar denotes dimensionless variables. Next, we multiply Eq. (10.7) by  $\partial_{\bar{x}} \bar{r}^\pm$  and integrate assuming  $\bar{p}_r$  constant to find

$$\bar{p}_r \bar{r}^\pm = \frac{\text{Bo}}{2} \bar{r}^{\pm 2} \mp \frac{1}{\left(1 + (\partial_{\bar{x}} \bar{r}^\pm)^2\right)^{\frac{1}{2}}} + c^\pm, \quad (10.8)$$

where  $c^\pm$  is the integration constant. The hypothesis of constant reduced pressure in the CS region will be verified subsequently. We evaluate this equation in the matching region, where we assume viscous effects become significant. In the matching region  $|\partial_{\bar{x}} \bar{r}^\pm| \ll 1$  and  $\bar{r}^\pm = \pm \frac{R_f^\pm}{a}$ , where  $R_f^\pm$  is the distance between the interface and the cell centerline (+) top and (-) bottom. Substituting these expressions in Eq. (10.8), we obtain

$$\pm \bar{p}_r \frac{R_f^\pm}{a} = \frac{\text{Bo}}{2} \left(\frac{R_f^\pm}{a}\right)^2 \mp 1 + c^\pm. \quad (10.9)$$

Setting  $R_f^\pm = a$  in Eq. (10.9), we recover the formulation proposed by Jensen *et al.* (1987) for  $p_r$  in the limit of vanishing  $\text{Ca}$  and  $R_f^\pm \approx a$ . We can evaluate Eq. (10.8) at the tip of the bubble, where  $\partial_{\bar{x}} \bar{r}^\pm \rightarrow \mp \infty$  and  $\bar{r}^\pm = \frac{\epsilon}{a}$ , in which  $\frac{\epsilon}{a} \ll 1$  and subtract the equation corresponding to the bottom from the top to find  $c^+ = c^-$  as Jensen *et al.* (1987). We then evaluate Eq. (10.9) at the top and at the bottom and do the subtraction top minus bottom to obtain  $p_r$ :

$$\bar{p}_r \left( \frac{R_f^+}{a} + \frac{R_f^-}{a} \right) = -2 + \frac{\text{Bo}}{2} \left( \left( \frac{R_f^+}{a} \right)^2 - \left( \frac{R_f^-}{a} \right)^2 \right) \quad (10.10)$$

For  $\text{Bo} \ll 1$  Eq. (10.10) can be approximated as:

$$\bar{p}_r \approx -\frac{2a}{R_f^+ + R_f^-} \quad (10.11)$$

Note that  $p_r$  does not depend on the axial coordinate as assumed before when integrating Eq. (10.7). Equation 10.11 says that the pressure in the liquid in the CS region is less than in the gas by the amount  $-4\gamma/(R_f^+ + R_f^-)$ . If  $\text{Bo} = 0$ ,  $R_f^+ = R_f^-$ , the Laplace pressure jump condition is recovered, in dimensional form it gives  $p = -\gamma\frac{2}{R_f}$ . Having the expression of  $\bar{p}_r$ , we substitute it in Eq. (10.7) and evaluate this equation in the matching region, i.e. for  $|\partial_{\bar{x}}\bar{r}^\pm| \ll 1$ , to find:

$$\partial_{\bar{x}\bar{x}}\bar{r}^\pm = \mp \frac{2a}{R_f^+ + R_f^-} - \frac{\text{Bo}R_f^\pm}{a}, \quad (10.12)$$

Note that the choice of coordinate system gives that  $\partial_{\bar{x}\bar{x}}\bar{r}^+ < 0$  and  $\partial_{\bar{x}\bar{x}}\bar{r}^- > 0$  (Fig. 10.5). Equation (10.12) shows that buoyancy affects the curvature of the front meniscus of the bubble, through the Bond number. As it will be shown, this has an influence on the thickness of the lubrication film.

### Transition region

In the transition region, we start by considering the lubrication approximation and the balance between the pressure gradient and the viscous forces (per volume) along the  $x$ -direction. The steps are standard, as first developed by Bretherton (1961), and summarized in Chapter 8 of this thesis. With the coordinate system introduced earlier, in dimensionless variables, we have:

$$\frac{\partial \bar{p}}{\partial \tilde{x}^\pm} = \text{Ca} \frac{\partial^2 \bar{u}}{\partial \tilde{y}^{\pm 2}} \quad (10.13)$$

where  $\bar{u} = \frac{u}{U_b}$  with  $U_b$  the bubble velocity,  $\tilde{y}^\pm = \mp \bar{y} + 1$  and  $\tilde{x}^\pm = \bar{x} + \bar{s}^\pm$ , with  $s$  being a shift in the axial coordinate, as defined in Fig. (10.5) and  $\bar{s} = \frac{s}{a}$ . We integrate Eq. (10.13) twice with  $\bar{u} = -1$  at  $\tilde{y}^\pm = 0$  and the no shear stress condition at the interface, i.e.  $\frac{\partial \bar{u}}{\partial \tilde{y}^\pm} = 0$  at  $y = h^\pm$ , where  $h^\pm = 1 \mp r^\pm$ . The pressure gradient along  $\tilde{x}^\pm$  is given by the curvature gradient  $\frac{\partial \bar{p}}{\partial \tilde{x}^\pm} = -\partial_{\tilde{x}^\pm \tilde{x}^\pm} \tilde{h}^\pm$ . Integrating the velocity field along  $\tilde{y}^\pm$  yields the classical third-order differential equation (also presented in Chapter 8), where the variables have been rescaled as  $\bar{h}^\pm = \frac{\tilde{h}^\pm}{\text{Ca}^{\frac{2}{3}}}$  and  $\bar{x}^\pm = \frac{\tilde{x}^\pm}{\text{Ca}^{\frac{1}{3}}}$ ,

$$\bar{h}^{\pm 3} \frac{d^3 \bar{h}^\pm}{d\bar{x}^{\pm 3}} = 3 \left( \bar{h}^\pm - \bar{h}_\infty^\pm \right), \quad (10.14)$$

where  $\bar{h}_\infty^\pm = \frac{h_\infty^\pm}{a\text{Ca}^{\frac{2}{3}}}$ . We obtain the classical form by defining  $H = \frac{\bar{h}^\pm}{\bar{h}_\infty^\pm}$  and  $X = \frac{\bar{x}^\pm}{\bar{h}_\infty^\pm}$

$$H^3 \frac{d^3 H}{dX^3} = 3(H - 1). \quad (10.15)$$

We now express the second derivative  $\partial_{xx}r^\pm$ , with the variables from the transition region:

$$\partial_{xx}r^\pm = \mp \frac{1}{a\bar{h}_\infty^\pm} \partial_{XX}H. \quad (10.16)$$

The curvature expressed with the variables from the transition region and from the CS region should match in a common overlap region, in which one can rewrite Eq. (10.12) in the form

$$\mp \frac{1}{\bar{h}_\infty^\pm} \lim_{X \rightarrow \infty} \partial_{XX}H = \mp \frac{2a}{R_f^+ + R_f^-} - \frac{\text{Bo}R_f^\pm}{a}, \quad (10.17)$$

where a numerical solution of Eq. (10.15) shows that  $\lim_{X \rightarrow \infty} \partial_{XX}H = 1.337$  (Bretherton (1961)), which finally leads to

$$\frac{h_\infty^\pm}{a} = \frac{1.337\text{Ca}^{\frac{2}{3}}}{\frac{2a}{R_f^+ + R_f^-} \pm \frac{\text{Bo}R_f^\pm}{a}}. \quad (10.18)$$

This result generalizes the development of Jensen *et al.* (1987) to the case of moderate values of Ca and the development of Klaseboer *et al.* (2014) to the case of finite Bo. From Eq. (10.18) we are able to recover the three limiting cases presented previously in the literature:

- At very low capillary numbers  $Ca \rightarrow 0$  and consequently very thin lubricating liquid films, the nose of the bubble approximately fits the entire gap between the top and bottom plane (or the tube diameter), thus  $R_f^\pm \approx a$ . In this limit and for  $Bo > 0$ , we recover

$$\frac{h_\infty^\pm}{a} = \frac{1.337Ca^{\frac{2}{3}}}{1 \pm Bo}, \quad (10.19)$$

which was originally obtained by Jensen *et al.* (1987).

- For negligible buoyancy effects  $Bo \rightarrow 0$ , no asymmetry is present at the nose of the bubble, thus  $R_f^\pm = R_f$ . In this limit, if we consider moderate Ca the radius of the spherical cap of the bubble no longer fits the radius of the tube, i.e.  $a \neq R_f$ , and Eq. (10.18) is reduced to the form presented by Aussillous and Quéré (2000) and discussed further by Klaseboer *et al.* (2014):

$$\frac{h_\infty^\pm}{R_f} = 1.337Ca^{\frac{2}{3}}. \quad (10.20)$$

- Finally, for  $Ca \rightarrow 0$  and  $Bo \rightarrow 0$ ,  $R_f^\pm \approx a$ , we recover the expression of Bretherton (1961):

$$\frac{h_\infty^\pm}{a} = 1.337Ca^{\frac{2}{3}}. \quad (10.21)$$

The distance between the cell/tube centerline and the interface in the matching region  $R_f^\pm$  and the liquid thickness  $C_N h_\infty^\pm$  should fit the radius of the tube. This gives an additional equation as proposed by Klaseboer *et al.* (2014)

$$a = C_N h_\infty^\pm + R_f^\pm, \quad (10.22)$$

where  $C_N$  is a constant and  $h_\infty^\pm$  is given by Eq. (10.18). Notice that combining Eq. (10.18) and Eq. (10.22) in the limiting case when  $Bo = 0$  and  $R_f^+ = R_f^-$ , we recover an equation similar to Aussillous and Quéré (2000) and Klaseboer *et al.* (2014),

$$\frac{h_\infty^\pm}{a} = \frac{1.337Ca^{\frac{2}{3}}}{1 + 1.337 C_N Ca^{\frac{2}{3}}}, \quad (10.23)$$

where  $C_N = 2.5$  by fitting Eq. (10.23) to the experimental measurements of Taylor (Taylor (1961); Aussillous and Quéré (2000)), and  $C_N = 2.79$  following a theoretical analysis proposed by Klaseboer *et al.*. However, Klaseboer *et al.* (2014) pointed out that the exact value of  $C_N$  depends on where  $R_f^\pm$  is evaluated in the matching region and can take a value up to 2.9 if  $R_f^\pm$  is evaluated for  $H > 10^6$ , i.e.  $X > 10000$ , and 2.34 if it is evaluated for  $H = 6 \times 10^2$ , i.e.  $X = 50$ . We choose  $C_N = 2.5$  in this work since it has been shown to fit the experimental measurements. It should be noted that as the film gets thicker with increasing Ca, for a given value of the tube radius  $a$ ,  $C_N$  could decrease since the liquid plus the bubble should fit in the tube radius. However, experimental results of Taylor (Taylor (1961); Aussillous and Quéré (2000)) show no such effect for Ca up to 2. On the other hand, the influence of Bo on  $C_N$  needs further investigation. Eq. (10.18) and (10.22) form a system of 4 equations with 4 unknowns  $R_f^+$ ,  $R_f^-$ ,  $h_\infty^+$ ,  $h_\infty^-$ , which is solved numerically using the Nsolve function of Wolfram Mathematica. Note that much above a critical Bond number, i.e.,  $Bo \gg Bo_c$ , the pressure in the bottom film becomes hydrostatic:

$$\rho g R_f \gg \frac{U \mu l}{(h_\infty^-)^2} \quad (10.24)$$



where  $l$  is the length of the transition region and scales with  $l \sim \text{Ca}^{1/3}$ ,  $h_\infty^- \sim \text{Ca}^{2/3}$  and  $R_f \sim 1 - \text{Ca}^{2/3}$ , thus:

$$\text{Bo}_c \sim \frac{1}{1 - \text{Ca}^{2/3}} \quad (10.25)$$

The critical value for the Bond number is  $\text{Bo}_c = 1$  for vanishing  $\text{Ca}$ , i.e.,  $R_f^\pm \approx a$ , however, for moderate  $\text{Ca}$ , i.e.,  $R_f^\pm < a$ , the value of  $\text{Bo}_c$  increases with  $\text{Ca}$ . Equation (10.18) is valid for  $\text{Bo} \ll \text{Bo}_c$ .

As first discussed by Jensen *et al.* (1987) and extended in this work, in a Taylor flow, buoyancy mainly affects the lubrication film thickness through affecting the front meniscus of the bubble. This give rise to Eq. (10.18) that predicts a thinner film at the top of the bubble when compared to the bottom. However, as it is discussed in the next section, buoyancy also affects the thin film region through the drainage of liquid it causes in this region.

### 10.3.2 Inclination angle in the thin film region

Leung *et al.* (2012) directly visualised the drainage flow from the top to the bottom of the channel in the thin film region. Using a mass balance analysis in the central region of the bubble, and assuming the thin film limit, they demonstrated that the drainage was causing the thin film to be inclined at an angle. Their main point was that, in the reference frame translating with the bubble velocity, liquid flows in the film. The volume of liquid in the film that is drained from the top to the bottom of the channel increases as one proceeds towards the back of the bubble, leading to less liquid flowing in the film as the back of the bubble is reached at the top of the channel; this description rationalizes the thinning of the film at the top. From their mass balance (Eq. (14) from ref. Leung *et al.* (2012)) we can obtain

$$\tan \alpha^\pm = \mp \frac{h_\infty \left(\theta = \frac{\pi}{2}\right)^3}{3\text{Ca}} \text{Bo}, \quad (10.26)$$

where  $h_\infty \left(\theta = \frac{\pi}{2}\right)$  is the film thickness at the center plane of the channel and is approximately given by  $h_\infty \left(\theta = \frac{\pi}{2}\right) \approx \frac{(h_\infty^+ + h_\infty^-)}{2}$ . It should be noted that possible deformation of bubble in the cross-sectional plane is assumed to be negligible in order to obtain Eq. (10.26).

## 10.4 Experimental results and discussions

In this section, we present results of our experimental measurements as a function of capillary  $\text{Ca}$  and Bond  $\text{Bo}$  numbers for the range of  $5 \times 10^{-4} < \text{Ca} < 0.12$  and  $0.05 < \text{Bo} < 0.42$ . The largest value of the Reynolds number in our experiments was  $\text{Re} = 0.023$ , therefore, inertial effects are negligible. We distinguish features of the thin film at the top and bottom of the front of the bubble as well as quantifying the inclination of the bubble due to buoyancy effects. Moreover, we present measurements of the film thickness at the back of the bubbles, which are different from those obtained at the front due to the inclination of the bubble. Our main goal in this section is to report experimental results, organized systematically using  $\text{Ca}$  and  $\text{Bo}$ , and to compare with the theory presented in the previous section.

### 10.4.1 Thickness of the liquid film at the front of the bubble

Experimental measurements of the film thickness at the front of the bubble are performed at both top and bottom of the tube. Results of these measurements are presented in Fig. 10.6 for four different values of the Bond number. Note that these experimental data points may correspond to bubbles of different lengths. Nevertheless,

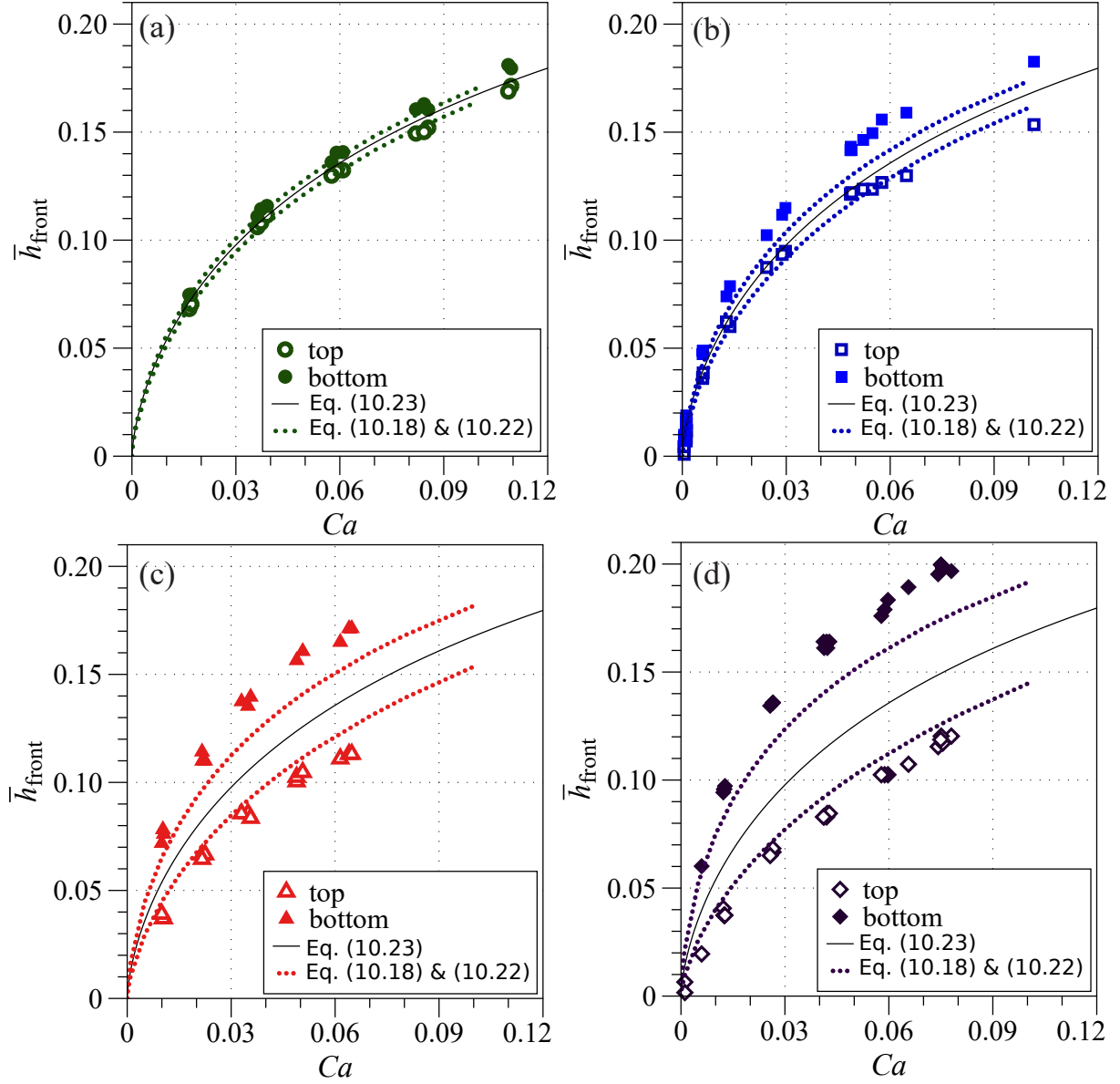


Figure 10.6: Top (open symbols) and bottom (full symbols) film thickness measurements at the front of the bubble for different Bond numbers: (a)  $Bo = 0.056$ , (b)  $Bo = 0.11$ , (c)  $Bo = 0.25$ , (d)  $Bo = 0.42$ . The thin black solid line is the prediction given by Eq. (10.23) with the empirical constant  $C_N = 2.5$ . The dotted lines are the predictions obtained by solving the system of Eqs (10.18) and (10.22) numerically. The results computed with Eq. (10.18) are in good agreement with the experiments. As  $Bo$  increases the agreement becomes less satisfactory due to the non-negligible drainage of liquid in the transition region. For the smallest  $Bo$ , the dashed and the dotted lines converge toward the solid line.

the dispersion of the experimental points are within the experimental error and the film thicknesses at the front of the bubble  $h_{\text{front}}^{\pm}$  do not depend significantly on the length of the bubble. Consistent with the theoretical prediction, the film thickness at the front of the bubble is thicker at the bottom than the top, whilst the difference between the values of the top and bottom film thicknesses at the front become larger as the  $Bo$  increases.

The data in Fig. 10.6 is compared with two models presented in section 10.3, one being the extended Bretherton without buoyancy effect as presented in Eq. (10.23), and a second model derived here, which was inspired by Jensen *et al.* accounting for buoyancy effects. The extended Bretherton formulation (solid line in Fig. 10.6) always lies in between the experimental measurements at the top and bottom of the tube. The theoretical prediction obtained by solving the system of Eq. (10.18) and Eq. (10.22) (dotted lines in Fig. 10.6) follows the

experimental measurements well. However, we note that an under-prediction of the film thickness at the bottom and an over-prediction of that at the top is present for all cases, which can be due to non-negligible lateral drainage from the top to the bottom of the channel in the transition region.

A scaling argument supporting this idea is the following: the time taken for liquid to be convected in the transition region is  $t_c \approx \frac{l}{U_b}$ , where  $l$  is the length of the transition region. The drainage time of the liquid from top to bottom is  $t_d \approx \frac{\pi a}{U_d}$ , where  $U_d$  is the drainage velocity. One can estimate the drainage velocity by balancing gravity and viscous shear along the vertical direction  $\frac{U_d \mu}{h_\infty (\theta \approx \frac{\pi}{2})^2} \approx \rho g$  which yields:

$$U_d \approx \frac{\rho g h_\infty (\theta = \frac{\pi}{2})^2}{\mu} \quad (10.27)$$

Using the scales  $l \sim Ca^{\frac{1}{3}}$  and  $h_\infty (\theta = \frac{\pi}{2}) \sim Ca^{\frac{2}{3}}$  we obtain the ratio between the two time scales:

$$\frac{t_d}{t_c} \sim \frac{1}{Bo Ca^{\frac{2}{3}}} \quad (10.28)$$

For sufficiently small values of  $Bo$  and  $Ca$ , the ratio of time scales is large enough to ensure no influence of the lateral drainage, but for the upper bounds of these parameters in our experiments the ratio decreases towards 3, meaning that drainage in the transition region begins to be significant. It should be noted that the larger difference between the experiments and the proposed model for the film thickness at the bottom compared to that at the top, especially at higher Bond numbers ( $Bo = 0.25$  and  $Bo = 0.42$ ), may also be a consequence of enhanced drainage for thicker films.

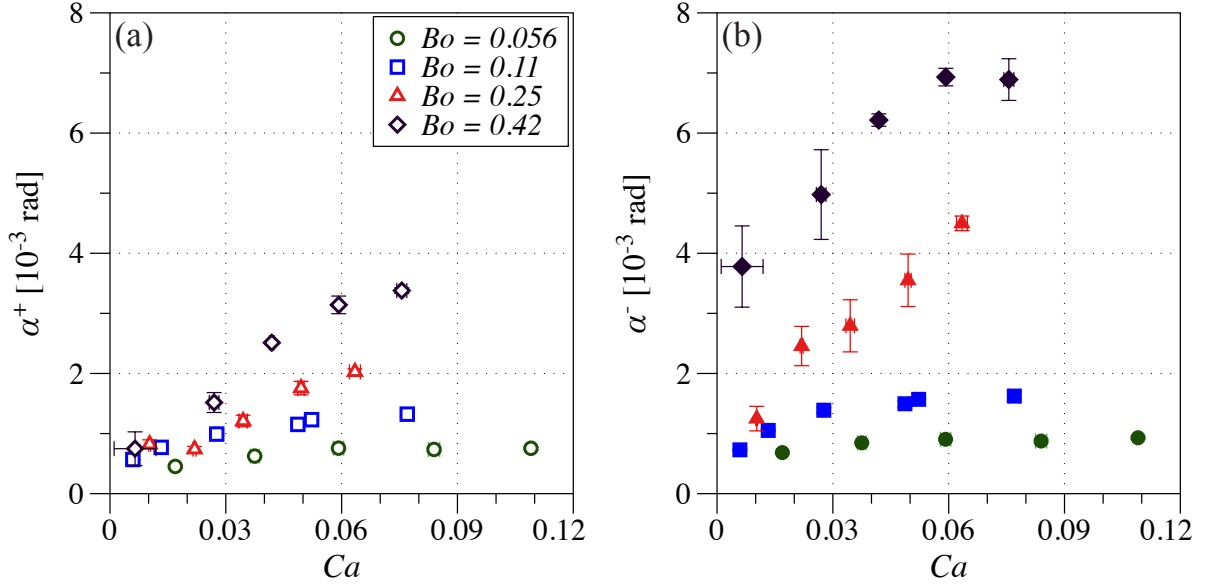


Figure 10.7: Inclination angle of the bubble at the (a) top and (b) bottom as a function of capillary number  $Ca$  for different Bond numbers  $Bo$ . The error bars (visible when larger than the symbol size) correspond to the standard deviation of the measurements obtained in three independent experimental tests.

#### 10.4.2 Inclination of the bubble

Measurements of the inclination angle  $\alpha$  of the bubble at the top  $\alpha^+$  and bottom  $\alpha^-$  of the tube are presented in Fig. 10.7. The inclination angle increases at higher  $Bo$  due to the enhanced drainage from the top to the bottom of the tube. We observe that the inclination angle at the top of the bubble is smaller than that at bottom of the tube.

This feature is believed to be due to the slight deformation of the circular cross-section of the bubble due to the buoyancy, which is not included in the theoretical analysis provided here. Such deformations due to gravity have been reported by de Lózar *et al.* (2008).

Since the scaling analysis discussed in Eq. (10.26) is performed considering a circular cross-section all along the bubble, we compare the theoretical prediction with the average inclination angle calculated for the top and bottom  $\alpha_{ave} = \frac{\alpha^+ + \alpha^-}{2}$ . The result of this comparison is presented in Fig. 10.8, where excellent agreement is obtained between the experimental measurements and the prediction of the mass balance analysis, Eq. (10.26). Note that according to both theory and the present experiments, buoyancy effects are observable even at the lowest Bond number  $Bo = 0.056$ . Moreover, the dependency of the inclination angle on the capillary number diminishes at higher  $Ca$ . Fig. 10.8 shows that the mass balance argument provided by Leung *et al.* (2012) can provide a reliable prediction method for the average inclination angle of the bubble in the presence of non-negligible buoyancy.

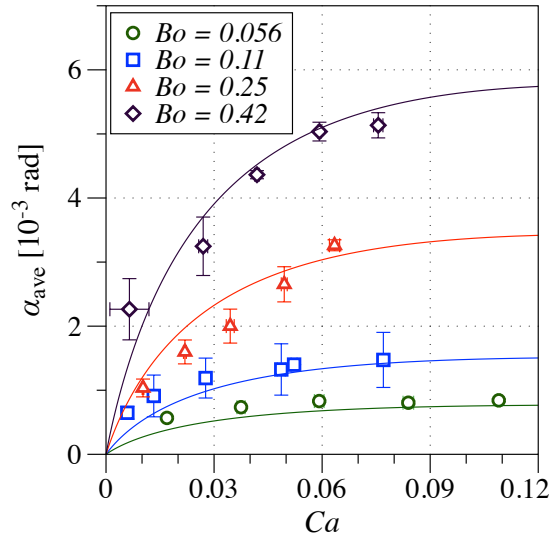


Figure 10.8: Mean inclination angle of bubbles computed by averaging the measurements at the top and the bottom  $\alpha_{ave} = (\alpha^+ + \alpha^-)/2$ . Solid lines present the prediction of Eq.(10.26).

### 10.4.3 Liquid film at the back of the bubble

Unlike the film thickness at the front of the bubble, the film thickness varies with the length of the bubble at the back due to the drainage of the liquid film and the consequent inclination of the bubble. This effect is observed in our experimental measurements of the film thickness at the back of the bubble  $h_{back}^\pm$ . Fig. 10.9 presents the ratio of the film thickness at the back of the bubble to that at the front  $\bar{h}_{back}^\pm/\bar{h}_{front}^\pm$  versus the dimensionless length of the bubble  $\bar{L} = L/a$  obtained in the experiments. Three main features are clearly observed in Fig. 10.9: (1)  $\bar{h}_{back}^\pm/\bar{h}_{front}^\pm$  is linearly correlated to the dimensionless length of the bubble  $\bar{L} = L/a$ . (2) The magnitude of the slopes of the best linear fits to experimental data are slightly larger at the bottom compared to the top of the tube. This finding once again shows that the cross-section of the bubble loses its circular shape towards the back of the bubble. (3) For the limit of  $\bar{L} \rightarrow 0$  all the linear trends at both the top and the bottom of the tube reach unity (Fig. 10.9).

At low  $Ca$  and finite  $Bo$ , the film thickness at the top of the tube and at the nose of the bubble is less than  $10 \mu\text{m}$ . As this thickness decreases towards the back of the bubble, it can eventually reach values smaller than  $1 \mu\text{m}$  for long bubbles of  $L \sim 10 \text{ mm}$ . Thin films of partially wetting liquids with thicknesses below  $1 \mu\text{m}$  are

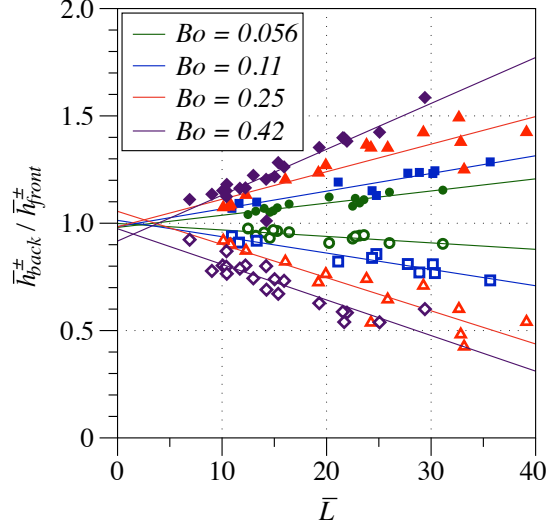


Figure 10.9: Ratio of the back to front film thicknesses  $\bar{h}_{back}^{\pm} / \bar{h}_{front}^{\pm}$  obtained in the experiments versus the dimensionless length of the bubble  $\bar{L} = L/a$ . Open and closed symbols correspond to the measurements at the top and bottom of the channel, respectively. Solid lines represent the best linear fit to the experimental data.  $\bar{h}_{back}^{\pm} / \bar{h}_{front}^{\pm}$  shows a linear trend with  $\bar{L}$  and approaches unity in the limit  $\bar{L} \rightarrow 0$ .

known to be metastable and thus may dewet the wall of the channel (Callegari *et al.* (2005); Huerre *et al.* (2015b); Khodaparast *et al.* (2018)). This effect causes dewetting on the top wall of the channel, which was observed in our experiments at low capillary numbers  $Ca < 10^{-3}$ . Therefore, not only the mean liquid film thickness but also the minimum film thickness caused by the effect of the buoyancy at the top rear of the bubble must be considered in studies where the film thickness has a critical effect on the final results, e.g. critical heat transfer determination for a heated pipe.

## 10.5 Conclusion

In this chapter we investigated the effect of buoyancy on the thickness of the liquid film formed around elongated confined bubbles, which translate in a horizontal tube of circular cross-section. We performed systematic experiments, in which the dimensionless parameters, namely capillary  $Ca$  and Bond  $Bo$  numbers were studied. In general, buoyancy effects were observed even at very low Bond numbers  $Bo$  and were amplified at higher  $Bo$ .

At finite  $Bo$ , the film thickness at the front of the bubble is thinner at the top than the bottom. We extended the theory originally proposed by Jensen *et al.* in a two-dimensional configuration for low capillary numbers  $Ca < 10^{-3}$  and finite  $Bo$  (Jensen *et al.* (1987)), to account for the film thickening effect observed at moderate capillary numbers (Aussillous and Qu  r   (2000); Klaseboer *et al.* (2014)). The resulting theoretical correlation quantitatively predicts the present experimental measurements with less than 12% relative error. In general, the theory underpredicts the effect of buoyancy on the film thickness especially at higher  $Bo$  and  $Ca$ , which may be a consequence of the lateral drainage in the transition region.

Due to buoyancy, a lateral drainage of liquid exists from the top to the bottom, which leads to the thinning of the liquid film towards the back of the bubble at the top. Therefore, the body of the bubble is inclined relative the centerline of the tube so that the back of the bubble is elevated. We quantified this inclination angle at the top and the bottom of the bubble. Whilst the angle of inclination remains constant along the bubble, it is slightly

larger at the bottom of the bubble. We believe that this effect is a consequence of the deformation of the bubble in the cross-sectional plane as compared to a circular shape. If the cross-sectional deformation of the bubble is neglected, a mass balance analysis for the liquid around the bubble in the central region by Leung *et al.* provides a theoretical prediction for the inclination angle (Leung *et al.* (2012)). We showed that this prediction can well predict the mean value of our experimental measurements of the inclination angles at the top and bottom of the bubble. Additionally, our findings suggest that the role of the drainage of the liquid in the transition region at the nose of the bubble and deformation of the bubble in the cross-sectional plane is an avenue for future theoretical analysis.

# CHAPTER 11

## Conclusions and perspectives

### 11.1 Conclusion

This work has focused on obtaining fundamental knowledge of gas-liquid dispersed flows in microfluidics using experimental and numerical approaches together with analytical modelling.

The first part of this work focused on characterizing the effect of soluble surfactants and deformability on the dynamics of bubbly flow inside a horizontal microchannel. A numerical study has been performed for this purpose. A numerical method allowing to solve the transport equation of surfactants on a moving and deforming surface has been implemented to JADIM. This equation has been coupled to the transport equation inside the bulk phase. The Marangoni stresses induced by an inhomogeneous distribution of surfactants on an interface has been discretized using the continuum surface force model. The simulations results obtained regarding the dynamics of bubbly flow in microfluidics in the presence of surfactants give insights into the complexity of the coupling of the different phenomena controlling the dynamics of the studied system. To begin with, it rationalized the “rigidification” process of bubble interfaces in microchannels due to the presence of surfactants for the first time. In particular, accounting for surfactants in the numerical method allowed to cover the entire range of possible speeds for centered spherical bubble in microchannels, namely from the stress-free to the rigid limit. In addition it unveiled the coupled effect of surfactants and deformability on the dynamics of the single bubble. More precisely, we showed that the speed and drag coefficient of deformable bubble is less affected by surfactants than spherical bubble. However, at a certain point, increasing the bubble deformability and the surfactants in the system may lead to the bubble bursting, a mechanism that we rationalized within this thesis.

The development of the numerical method allowing to simulate dispersed two phase flows with soluble surfactants gave rise to a collaboration with Prof. Roberto Zenit. In this collaboration, an ancient technique to asses the amount of alcohol in Mezcal, an alcoholic beverage produced in Mexico was studied. In this technique, bubbles are produced in a vessel filled with Mezcal, and the lifetime of the bubbles under the free surface are monitored. The lifetime of these bubbles are extended when the Mezcal contains the correct concentration of alcohol, i.e., 50% volume content. Using JADIM and the numerical method implemented in this thesis to account for surfactants, insight was gain into the mechanisms controlling the lifetime of these bubbles under the free surface. We elucidated by numerical inspection the two mechanism responsible for longer lifetime of the bubbles in the ancestral process. There are the viscosity effect and the size effect. In fact, a dynamic balance between viscous shear created by the presence of Marangoni stresses and gravitational drainage, taking place inside the thin film separating the bubble surface and the free surface was identified to play a role in determining the lifetime of these bubbles. In addition, a static balance that takes place in a larger scale, between capillary forces and gravitational forces, the outcome of which determines the shape of the bubble and of the free surface, was shown to play a role in determining the lifetime of these bubbles. However, work still remains in order to identify and model the key phenomena creating the Marangoni stresses on both surfaces(i.e., the evaporation of alcohol inside the thin film).

The second part of this work aimed at characterizing the dynamics of Taylor flow.

In the first section of this second part, a new method was developed to measure the thickness of the lubrication film forming between a pancake-like bubble and the walls of a microchannel. The method requires only a single

snapshot of the bubble and the knowledge of the refractive index of the liquid surrounding the bubble. In addition to the snapshot, if the bubble velocity is measured, then the surface tension or the viscosity can be measured. In addition to measuring the lubrication film thickness and the surface tension, the technique also allows to measure the depth of a microchannel with a single snapshot of a quiescent bubble. We believe that the simplicity of use of this technique and the few amount of equipment it requires makes it of wide interest to the scientific community.

In the second section of the second part, we performed experiments and theoretical analysis for a long bubble in a horizontal microchannel of circular cross section, to investigate the effect of  $Bo$  on the thickness of the liquid film and the bubble orientation at different  $Ca$ . In particular, we provide prediction, derived from available theoretical considerations, that gives the evolution of the film thickness from the front to the back of the bubble. Moreover, we provided systematic experimental measurements for  $10^{-3} < Ca < 10^{-1}$  and  $0.05 < Bo < 0.5$ , which allow verification of the proposed theory. Specifically, we investigated several features of the lubricating film around the bubble: (1) Due to the gravitational effects, the film deposited on the upper wall of the channel is thinner than the film at the bottom wall. We extended the available theory for the film thickness at the front of the bubble in a two-dimensional geometry at low capillary numbers  $Ca < 10^{-3}$  and finite  $Bo$  to account for the effect of larger  $Ca$ . The resulting model shows good agreement with the experimental measurements. (2) Due to the asymmetry in the liquid film thickness and the consequent drainage of the liquid from the top to the bottom of the tube, the bubble is inclined relative to the channel centerline and our side-view visualizations allowed direct quantification of the inclination angle, which increases with both  $Bo$  and  $Ca$ . While the inclination angle at the top is smaller than that at the bottom of the tube, the average of these two values follows the predictions of a mass balance analysis in the central region of the bubble. (3) The inclination of the bubble causes the thickness of the thin film at the back of the bubble to depend on the length of the bubble. This feature can have important consequences in applications where the thickness of the film is an important parameter for the design and functioning of microfluidic devices, e.g. heating/cooling of pipes, microreaction engineering. In fact, at low  $Ca$  and finite  $Bo$ , the film thickness at the top of the tube and at the nose of the bubble is less than  $10\text{ }\mu\text{m}$ . As this thickness decreases towards the back of the bubble, it can eventually reach values smaller than  $1\text{ }\mu\text{m}$  for long bubbles of  $L \sim 10\text{ mm}$ . Thin films of partially wetting liquids with thicknesses below  $1\text{ }\mu\text{m}$  are known to be metastable and thus may dewet the wall of the channel (Callegari *et al.* (2005); Huerre *et al.* (2015b); Khodaparast *et al.* (2018)). This can influence the heat transfer capabilities of the aforementioned applications.

The dynamics of dewetting of the lubrication film in a Taylor flow has been investigated in the frame of this thesis in collaboration with Sepideh Khodaparast and Professor Howard A. Stone (Khodaparast *et al.* (2018)). In particular in a microchannel of rectangular cross section, the liquid in the film leaks towards the low pressure corners of the geometry leading to local minima of the thickness of the film in the cross sectional plane of the microchannel. It was shown in this study that this feature induces dewetting of the thin film of partially wetting liquids at the location of those minima. Depending on the capillary number and on the wettability of the microchannel walls, it was shown that this feature can create either dry patches or wide dry zones on the microchannel wall, as depicted in Fig. 11.1. In this figure, an in-line bright-field image of a bubble translating at  $Ca \approx 10^{-3}$  inside a microchannel filled with water is shown. In (a), the microchannel wall is hydrophobic, and as can be seen, the lubrication film surrounds the bubble only on its front part and the rest of the bubble is directly in contact with the microchannel wall. The red arrow on this figure shows the 3 phase contact line between the walls of the microchannel, the air bubble and the lubrication film. In (b), the walls of the microchannel are hydrophilic. In this case, the whole bubble is surrounded with a lubrication film except at specific locations where dry patches form (highlighted in red in Fig. 11.1).

It can be seen that this work has contributed to several key aspects regarding the dynamics of bubbles in microchannels. It has contributed to give insight to the understanding of the complex coupling between the liquid flow inside a microchannel, the dynamics of surfactants, and the bubble dynamics. It has also contributed to the



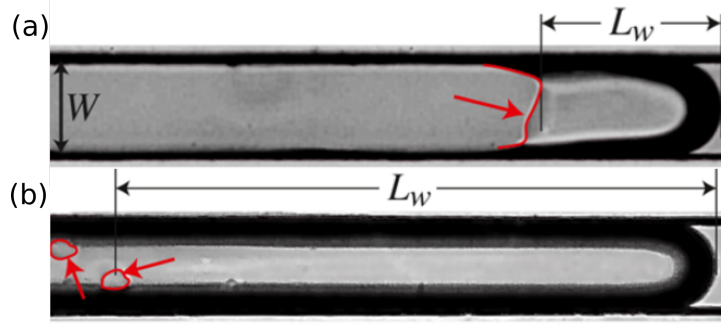


Figure 11.1: Taylor bubble translating from the left to the right inside a microchannel at  $Ca \approx 10^{-3}$ . (a): the channel wall has not received any surface treatment and is less wettable by the surrounding water. (b) the channel wall has received plasma treatment and is more wettable. Taken from Khodaparast *et al.* (2018).

characterization of the thickness of the lubrication film in Taylor flows. In fact, a new and simple technique to measure the thickness of the lubrication film in Taylor flows has been developed and tested. Finally, it has brought into light that, gravity, though often neglected in microfluidics, can have an impact on the dynamics of the Taylor flow. However, much work still remains and the outlooks for future work are various and promising.

## 11.2 Perspectives

The direct outlooks of this work concerning the study of the bubbly flow regime in the presence of surfactants, is to extend the parametric study performed in this work to other non dimensional numbers characterizing the surfactants, in an attempt to construct a multidimensional map depicting regions where the bubbles are stable, or regions where the bubbles burst. In parallel, an experimental work can be conducted to test if these regimes, observed in the simulations, can also be observed in the experiments for a bubble. The invagination and bursting of a viscous drop has been observed by Olbricht and Kung (1992), as presented in Fig. (11.2). However, to our knowledge, the bursting of bubbles and the role of surfactants on this behaviour has not been studied experimentally. In addition, the numerical method that accounts for surfactants that was implemented in this thesis needs to be extended to 3D in order to consider the combined effect of surfactants, bubble deformability and bubble eccentricity on the dynamics of the bubble translating along the microchannel.

Concerning the characterization of the thickness of the lubrication film in Taylor flows, the experimental method developed in this work for bubbles can be extended to drops of non vanishing viscosity ratio. As it was observed in Chapter 9, the sensitivity of the method increase as the ratio of the refractive index of the outer phase to the refractive index of the droplet increases. Furthermore, the method is only applicable if this ratio is larger than one. For these reasons, first, the list of the refractive index of usual liquids needs to be done, and if there is sufficient couple of liquids for which the refractive index ratio of the inner phase is larger than the one of the outer phase, then a generalized correlation, valid for bubble and drops of non vanishing viscosity ratio can be built using the methodology developed in this thesis.

In recent years experimental work have shown that the lubrication film around a pancake-like bubble has a complex 3D topography (Huerre *et al.* (2015a); Reichert *et al.* (2018)). Thus, the methodology we developed in this thesis to measure the thickness of the lubrication film near the middle plane of the pancake bubble should be extended to the whole bubble. For this purpose, experiments need to be performed to test if the method is sufficiently sensitive to the variation of the thickness of the lubrication film around the bubble perimeter. If yes, the raytracing algorithm needs to be applied on a appropriate shape function that takes into account the azimuthal

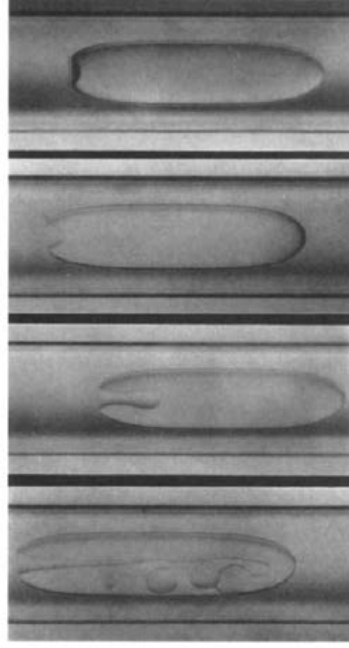


Figure 11.2: Sequence of photography depicting a droplet with  $Ca = 1$  and  $\mu_d/\mu_c = 0.1$  (from Olbricht and Kung (1992))

variations of the bubble shape. The raytracing algorithm needs to be applied on this model and a generalized correlation that predicts the film thickness as a function of the position of the glare circle at a given azimuthal angle needs to be built.

In addition, it might be interesting to study the effect of soluble surfactants on the shape and dynamics of a pancake like bubble. A recent work conducted by Reichert *et al.* (2018) study this subject experimentally, and few studies exists on this subject. Fig. 11.3 show the 3D topography of the lubrication film around a pancake drop translating inside a microchannel filled with a liquid that contains surfactants. The drop translates from the left to the right. As can be seen, the lubrication film exhibits a complex topography. In particular, it is thicker at the back than at the front of the drop, because of surfactant accumulation at the back and consequent Marangoni stress inducing a local thickening of the lubrication film. The 3D topography of the lubrication film surrounding

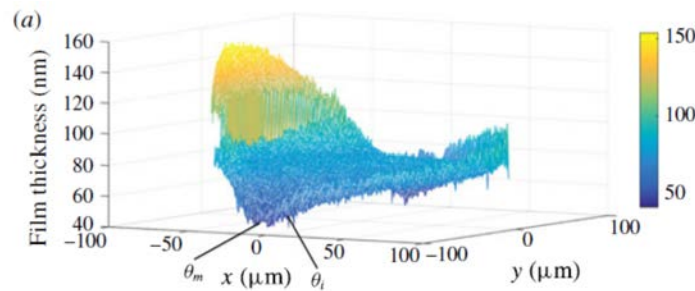


Figure 11.3: Three dimensional topography of the lubrication film around a pancake-like bubble translating at  $Ca = 7 \cdot 10^{-4}$ . This figure was taken from Reichert *et al.* (2018)

a pancake drop needs to be better characterized and the effect of the surfactants on this topography as well. For this purpose, the Level-set modulus of JADIM where the method allowing to simulate surfactant transport and Marangoni stress was implemented can be used. For this purpose, the equation implemented in the frame of this thesis needs to be extended to 3D.

# CHAPTER 12

## Appendixes

### 12.1 Appendix A

In this appendix we present the fifth order, Weighed Essentially Non Oscillatory (WENO) scheme. This scheme uses 5 discrete point around the discrete location where the derivative of the scalar field is calculated. It then constructs 3 stencils with this 5 points around the point "i" where the derivative is calculated. The derivative at this point will then be calculated as a weighted sum of the derivatives calculated with each of the stencils. The weights are calculated such that derivatives calculated with the stencils where the function is the most regular are dominant in the sum. The stencils where the derivatives  $D_x^- \tilde{\Gamma}_{i,j}^n$  and  $D_x^+ \tilde{\Gamma}_{i,j}^n$  are calculated, are represented on figure 12.1. The derivatives  $D_x^\pm \tilde{\Gamma}_{i,j}^n$  are given by :

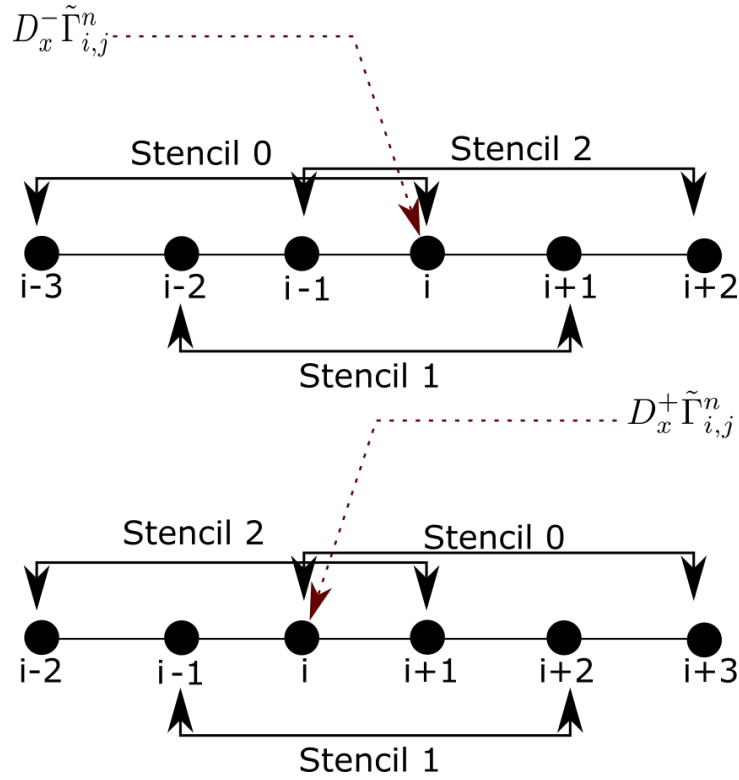


Figure 12.1: Stencils for the construction of the derivatives  $D_x^- \tilde{\Gamma}_{i,j}^n$  and  $D_x^+ \tilde{\Gamma}_{i,j}^n$ , with the 5th order WENO scheme

$$\begin{cases} D_x^\pm \tilde{\Gamma}_{i,j}^{n,0} = \frac{1}{3}q_1^\pm - \frac{7}{6}q_2^\pm + \frac{11}{6}q_3^\pm \\ D_x^\pm \tilde{\Gamma}_{i,j}^{n,1} = -\frac{1}{6}q_2^\pm + \frac{5}{6}q_3^\pm + \frac{1}{3}q_4^\pm \\ D_x^\pm \tilde{\Gamma}_{i,j}^{n,1} = +\frac{1}{3}q_3^\pm + \frac{5}{6}q_4^\pm - \frac{1}{6}q_5^\pm \end{cases} \quad (12.1)$$

where  $q^\pm$  are given by :

$$\left\{ \begin{array}{l} q_1^- = \frac{\tilde{\Gamma}_{i-2,j}^n - \tilde{\Gamma}_{i-3,j}^n}{\Delta x}, q_1^+ = \frac{\tilde{\Gamma}_{i+3,j}^n - \tilde{\Gamma}_{i+2,j}^n}{\Delta x} \\ q_2^- = \frac{\tilde{\Gamma}_{i-1,j}^n - \tilde{\Gamma}_{i-2,j}^n}{\Delta x}, q_2^+ = \frac{\tilde{\Gamma}_{i+2,j}^n - \tilde{\Gamma}_{i+1,j}^n}{\Delta x} \\ q_3^- = \frac{\tilde{\Gamma}_{i,j}^n - \tilde{\Gamma}_{i-1,j}^n}{\Delta x}, q_3^+ = \frac{\tilde{\Gamma}_{i+1,j}^n - \tilde{\Gamma}_{i,j}^n}{\Delta x} \\ q_4^- = \frac{\tilde{\Gamma}_{i+1,j}^n - \tilde{\Gamma}_{i,j}^n}{\Delta x}, q_4^+ = \frac{\tilde{\Gamma}_{i,j}^n - \tilde{\Gamma}_{i-1,j}^n}{\Delta x} \\ q_5^- = \frac{\tilde{\Gamma}_{i+2,j}^n - \tilde{\Gamma}_{i+1,j}^n}{\Delta x}, q_5^+ = \frac{\tilde{\Gamma}_{i-1,j}^n - \tilde{\Gamma}_{i-2,j}^n}{\Delta x} \end{array} \right. \quad (12.2)$$

The 5th order WENO scheme computes an approximation of the derivatives of a scalar field on  $(i, j)$ , by doing a weighted sum of  $D_x^\pm \tilde{\Gamma}_{i,j}^{n,0}$ ,  $D_x^\pm \tilde{\Gamma}_{i,j}^{n,1}$ ,  $D_x^\pm \tilde{\Gamma}_{i,j}^{n,2}$  :

$$D_x^\pm \tilde{\Gamma}_{i,j}^n = \omega_0^\pm D_x^\pm \tilde{\Gamma}_{i,j}^{n,0} + \omega_1^\pm D_x^\pm \tilde{\Gamma}_{i,j}^{n,1} + \omega_2^\pm D_x^\pm \tilde{\Gamma}_{i,j}^{n,2} \quad (12.3)$$

where the weights  $\omega_0^\pm, \omega_1^\pm, \omega_2^\pm$  are given by :

$$\left\{ \begin{array}{l} \omega_0^\pm = \frac{\alpha_0^\pm}{\alpha_0^\pm + \alpha_1^\pm + \alpha_2^\pm} \\ \omega_1^\pm = \frac{\alpha_1^\pm}{\alpha_0^\pm + \alpha_1^\pm + \alpha_2^\pm} \\ \omega_2^\pm = \frac{\alpha_2^\pm}{\alpha_0^\pm + \alpha_1^\pm + \alpha_2^\pm} \end{array} \right. \quad (12.4)$$

so that the weighting is consistent,  $\omega_0^\pm + \omega_1^\pm + \omega_2^\pm = 1$ , and with  $\alpha_0^\pm, \alpha_1^\pm, \alpha_2^\pm$  given by :

$$\left\{ \begin{array}{l} \alpha_0^\pm = \frac{1}{10} \left( \frac{1}{\epsilon + IS_0^\pm} \right)^2 \\ \alpha_1^\pm = \frac{6}{10} \left( \frac{1}{\epsilon + IS_1^\pm} \right)^2 \\ \alpha_2^\pm = \frac{3}{10} \left( \frac{1}{\epsilon + IS_2^\pm} \right)^2 \end{array} \right. \quad (12.5)$$

where  $\epsilon$  is generally fixed to  $10^{-6}$  to avoid the denominator to be null, and where the  $IS^\pm$  represent the regularity indicators :

$$\left\{ \begin{array}{l} IS_0^\pm = \frac{13}{12} (q_1^\pm - 2q_2^\pm + q_3^\pm)^2 + \frac{1}{4} (q_1^\pm - 4q_2^\pm + 3q_3^\pm)^2 \\ IS_1^\pm = \frac{13}{12} (q_2^\pm - 2q_3^\pm + q_4^\pm)^2 + \frac{1}{4} (q_2^\pm - 4q_3^\pm + 3q_4^\pm)^2 \\ IS_2^\pm = \frac{13}{12} (q_3^\pm - 2q_4^\pm + q_5^\pm)^2 + \frac{1}{4} (3q_3^\pm - 4q_4^\pm + q_5^\pm)^2 \end{array} \right. \quad (12.6)$$

The procedure is identical when computing the following non-centered derivatives :  $D_y^+ \tilde{\Gamma}_{i,j}^n$  et  $D_y^- \tilde{\Gamma}_{i,j}^n$ . The procedure is applied one direction at the time.

## 12.2 Appendix B

In this appendix, the calculation of the instantaneous surfactant mass on the surface of an axisymmetric bubble is detailed.

In the level set formulation, the surface integral of the surfactant concentration on the interface,  $\Gamma$ , can be written as (Xu and Zhao (2003)):

$$M(t) \equiv \int_{S(t)} \Gamma dS(t) = \int_{V(t)} \tilde{\Gamma} \delta(\phi) dV \quad (12.7)$$

where  $S$  is the surface on which the surfactant mass is calculated and  $V$  is the volume of the domain embedding the interface;  $\delta(\phi)$  is a Dirac distribution that accounts for the distribution of the surfactant mass along the numerical thickness of the interface. It is given by (Xu and Zhao (2003)):

$$\delta(\phi) = \begin{cases} 0 & \text{if } |\phi| > \epsilon \\ -\frac{1}{6\epsilon} \left( 1 + \cos \left( \frac{\pi\phi}{\epsilon} \right) \right) + \frac{4}{3\epsilon} \left( 1 + \cos \left( \frac{2\pi\phi}{\epsilon} \right) \right) & \text{if } |\phi| < 0.5\epsilon \\ -\frac{1}{6\epsilon} \left( 1 + \cos \left( \frac{\pi\phi}{\epsilon} \right) \right) & \text{if } 0.5\epsilon < |\phi| < \epsilon \end{cases} \quad (12.8)$$

Finally, in the axisymmetric configuration studied in the chapter 6, the surfactant mass is calculated as:

$$M(t) = 2\pi \int_0^{0.5d_h} \int_0^L r \tilde{\Gamma} \delta(\phi) dz dr \quad (12.9)$$

The evolution of the surfactant mass on the surface of a bubble translating inside a cylindrical microchannel with  $La = 0.1$ ,  $Ca = 10^{-2}$  and  $d/d_h = 0.15$  (see chapter 6) is shown in Fig. 12.2.

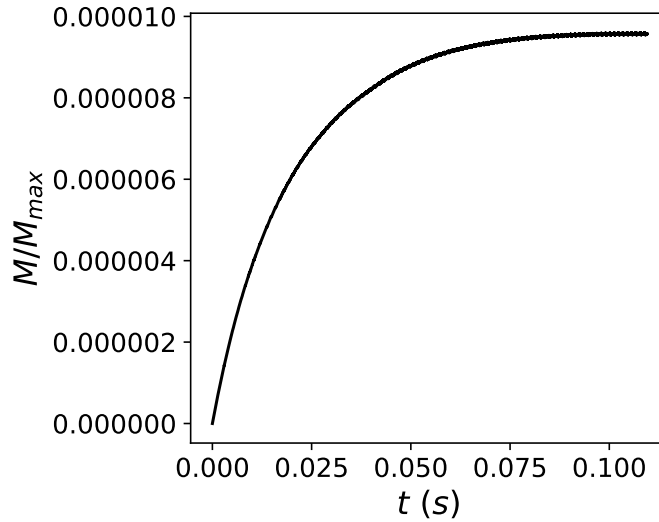


Figure 12.2: Surfactant mass on the bubble surface as a function of the time;  $M_{max} = \pi d^2 \Gamma_\infty$  is the maximum mass of surfactant that can be present on the bubble surface.

The bubble surface is initially clean of surfactants. At time  $t = 0$ , surfactant begin to adsorb to finally reach a constant mass on the surface at  $t \approx 0.1$  s. This constant mass on the bubble surface is the result of an equilibrium between the overall adsorption flux of surfactants towards the surface and the desorption flux. The

mass of surfactant on the bubble surface was monitored for all the simulations performed in chapter 6 in order to ensure that the studied system has reached its equilibrium condition regarding the bubble velocity and adsorbed surfactant mass.

## REFERENCES

1. **Abadie, T.** (2013). *Hydrodynamics of gas-liquid Taylor flow in microchannels*. Ph.D. thesis, Institut National Polytechnique de Toulouse, Toulouse, France.
2. **Abadie, T., J. Aubin, and D. Legendre** (2015). On the combined effects of surface tension force calculation and interface advection on spurious currents within Volume of Fluid and Level Set frameworks. *Journal of Computational Physics*, **297**, 611–636. ISSN 00219991.
3. **Abadie, T., J. Aubin, D. Legendre, and C. Xuereb** (2012). Hydrodynamics of gas-liquid Taylor flow in rectangular microchannels. *Microfluidics and Nanofluidics*, **12**(1-4), 355–369. ISSN 1613-4982, 1613-4990.
4. **Abadie, T., C. Xuereb, D. Legendre, and J. Aubin** (2013). Mixing and recirculation characteristics of gas-liquid Taylor flow in microreactors. *Chemical Engineering Research and Design*, **91**(11), 2225–2234. ISSN 02638762.
5. **Abiev, R.** (2013). Bubbles velocity, Taylor circulation rate and mass transfer model for slug flow in milli- and microchannels. *Chemical Engineering Journal*, **227**, 66–79. ISSN 13858947.
6. **Abiev, R., S. Svetlov, and S. Haase** (2017). Hydrodynamics and Mass Transfer of Gas-Liquid and Liquid-Liquid Taylor Flow in Microchannels. *Chemical Engineering & Technology*, **40**(11). ISSN 1521-4125.
7. **Allain, C., D. Ausserre, and F. Rondelez** (1985). A new method for contact-angle measurements of sessile drops. *Journal of Colloid and Interface Science*, **107**(1), 5–13. ISSN 0021-9797.
8. **Anna, S. L.** (2016). Droplets and Bubbles in Microfluidic Devices. *Annual Review of Fluid Mechanics*, **48**(1), 285–309.
9. **Atasi, O., B. Haut, S. Dehaeck, A. Dewandre, D. Legendre, and B. Scheid** (2018a). How to measure the thickness of a lubrication film in a pancake bubble with a single snapshot (editor’s pick). *Applied Physics Letter*.
10. **Atasi, O., B. Haut, A. Pedrono, B. Scheid, and D. Legendre** (2018b). Influence of soluble surfactants and deformation on the dynamics of centered bubbles in cylindrical microchannels. *Langmuir*. ISSN 0743-7463, 1520-5827.
11. **Atasi, O., S. Khodaparast, B. Scheid, and H. A. Stone** (2017). Effect of buoyancy on the motion of long bubbles in horizontal tubes. *Physical Review Fluids*, **2**(9). ISSN 2469-990X.
12. **Aussillous, P. and D. Quéré** (2000). Quick deposition of a fluid on the wall of a tube. *Phys. Fluids*, **12**(10), 2367–2371.
13. **Balestra, G., L. Zhu, and F. Gallaire** (2018). Viscous Taylor droplets in axisymmetric and planar tubes: from bretherton’s theory to empirical models. *Microfluidics and Nanofluidics*, **22**(6), 67.
14. **Baret, J.-C., F. Kleinschmidt, A. El Harrak, and A. D. Griffiths** (2009). Kinetic Aspects of Emulsion Stabilization by Surfactants: A Microfluidic Analysis. *Langmuir*, **25**(11), 6088–6093. ISSN 0743-7463.
15. **Baroud, C. N., F. Gallaire, and R. Dangla** (2010). Dynamics of microfluidic droplets. *Lab on a Chip*, **10**(16), 2032. ISSN 1473-0197, 1473-0189.
16. **Batchelor, G. K.**, *An Introduction to Fluid Dynamics*. 1967, cambridge university press edition.
17. **Bel Fdhila, R. and P. C. Duineveld** (1996). The effect of surfactant on the rise of a spherical bubble at high Reynolds and Peclet numbers. *Physics of Fluids*, **8**(2), 310–321. ISSN 1070-6631, 1089-7666.
18. **Benkenida, A.** (1999). *Développement et validation d’une méthode de simulation d’écoulements diphasiques sans reconstruction d’interfaces : application à la dynamique des bulles de Taylor*. Ph.D. thesis, Institut National Polytechnique de Toulouse, France.

19. **Bonometti, T. and J. Magnaudet** (2007). An interface-capturing method for incompressible two-phase flows. Validation and application to bubble dynamics. *International Journal of Multiphase Flow*, **33**(2), 109–133. ISSN 0301-9322.
20. **Borhani, N., B. Agostini, and J. R. Thome** (2010). A novel time strip flow visualisation technique for investigation of intermittent dewetting and dryout in elongated bubble flow in a microchannel evaporator. *Int. J. Multiphase flow*, **53**(21–22), 4809 – 4818.
21. **Brackbill, J. U., D. B. Kothe, and C. Zemach** (1992). A continuum method for modelling surface tension. *Journal of Computational Physics*, **100**, 335–354.
22. **Brener, E., M. Rabaud, and H. Thomé** (1993). Effect of gravity on stable Saffman-Taylor fingers. *Phys. Rev. E*, **48**, 1066–1072.
23. **Bretherton, F. P.** (1961). The motion of long bubbles in tubes. *J. Fluid Mech.*, **10**, 166–188.
24. **Budwig, R.** (1994). Refractive index matching methods for liquid flow investigations. *Exp. Fluids*, **17**(5), 350–355.
25. **Burgess, D. and M. R. Foster** (1990). Analysis of the boundary conditions for a Hele–Shaw bubble. *Physics of Fluids A: Fluid Dynamics*, **2**(7), 1105–1117. ISSN 0899-8213.
26. **Callegari, G., A. Calvo, and J. P. Hulin** (2005). Dewetting processes in a cylindrical geometry. *The European Physical Journal E*, **16**(3), 283–290.
27. **Campbell, J. M. and H. K. Christenson** (2018). Dynamic Measurement of Low Contact Angles by Optical Microscopy. *ACS Applied Materials & Interfaces*, **10**(19), 16893–16900. ISSN 1944-8244, 1944-8252.
28. **Carofiglio, T., P. Donnola, M. Maggini, M. Rossetto, and E. Rossi** (2008). Fullerene-Promoted Singlet-Oxygen Photochemical Oxygenations in Glass-Polymer Microstructured Reactors. *Advanced Synthesis & Catalysis*, **350**(17), 2815–2822. ISSN 16154150.
29. **Chang, C.-H. and E. I. Franses** (1995). Adsorption dynamics of surfactants at the air/water interface: a critical review of mathematical models, data, and mechanisms. *Colloids and Surfaces A: Physicochemical and Engineering Aspects*, **100**, 1–45.
30. **Chen, H., Q. Meng, and J. Li** (2015). Thin lubrication film around moving bubbles measured in square microchannels. *Applied Physics Letters*, **107**(14), 141608. ISSN 0003-6951, 1077-3118.
31. **Chen, J.-D.** (1986). Measuring the film thickness surrounding a bubble inside a capillary. *Journal of Colloid and Interface Science*, **109**(2), 341–349. ISSN 00219797.
32. **Clift, R., J. R. Grace, and M. E. Weber**, *Bubbles, drops, and particles*. Academic Press, New York, 1978. ISBN 978-0-12-176950-5.
33. **Couderc, F.** (2007). *Développement d'un code de calcul pour la simulation d'écoulements de fluides non miscibles. Application à la désintégration assistée d'un jet liquide par un courant gazeux.*. Ph.D. thesis, Institut National Polytechnique de Toulouse.
34. **Cubaud, T., M. Sauzade, and R. Sun** (2012). CO<sub>2</sub> dissolution in water using long serpentine microchannels. *Biomicrofluidics*, **6**(2), 022002.
35. **Cuenot, B., J. Magnaudet, and B. Spennato** (1997). The effects of slightly soluble surfactants on the flow around a spherical bubble. *Journal of Fluid Mechanics*, **339**, 25–53.
36. **Culick, F. E. C.** (1960). Comments on a Ruptured Soap Film. *Journal of Applied Physics*, **31**(6), 1128–1129. ISSN 0021-8979.
37. **de Lózar, A., A. Juel, and A. L. Hazel** (2008). The steady propagation of an air finger into a rectangular tube. *J. Fluid Mech.*, **614**, 173–195.
38. **Dehaeck, S. and J. van Beeck** (2007). Simultaneous determination of bubble diameter and relative refractive index using glare circles. *Applied optics*, **46**(23), 5957–5963.
39. **Dehaeck, S., J. P. A. J. Van Beeck, and M. L. Riethmuller** (2005). Extended glare point velocimetry and sizing for bubbly flows. *Experiments in Fluids*, **39**(2), 407–419. ISSN 0723-4864, 1432-1114.



40. **Driscoll, M. M. and S. R. Nagel** (2011). Ultrafast Interference Imaging of Air in Splashing Dynamics. *Physical Review Letters*, **107**(15). ISSN 0031-9007, 1079-7114.
41. **Dupont, J.-B. and D. Legendre** (2010). Numerical simulation of static and sliding drop with contact angle hysteresis. *Journal of Computational Physics*, **229**(7), 2453–2478. ISSN 00219991.
42. **Fairbrother, F. and A. E. Stubbs** (1935). Studies in electro-endosmosis. Part VI. The “bubble-tube” method of measurement. *J. Chem. Soc.*, 527–529.
43. **Feng, J. Q.** (2010). Steady axisymmetric motion of a small bubble in a tube with flowing liquid. *Proceedings: Mathematical, Physical and Engineering Sciences*, **466**(2114), 549–562. ISSN 1364-5021.
44. **Fukuta, M., S. Takagi, and Y. Matsumoto** (2008). Numerical study on the shear-induced lift force acting on a spherical bubble in aqueous surfactant solutions. *Physics of Fluids*, **20**(4), 040704. ISSN 1070-6631, 1089-7666.
45. **Garrett, W. D.**, Stabilization of air bubbles at the air-sea interface by surface-active material. *In Deep Sea Research and Oceanographic Abstracts*, volume 14. Elsevier, 1967.
46. **Garstecki, P., A. M. Ganan-Calvo, and G. M. Whitesides** (2005). Formation of bubbles and droplets in microfluidic systems. *Technical sciences*, **53**(4).
47. **Gavrilovic, M. R.** (2017). Impact of the cavitation bubble on a plasma emission following laser ablation in liquid. *Eur. Phys. J. D*, **71**(316).
48. **Giavedoni, M. D. and F. A. Saita** (1999). The rear meniscus of a long bubble steadily displacing a Newtonian liquid in a capillary tube. *Phys. Fluids*, **11**(4), 786–794.
49. **Giribabu, K. and P. Ghosh** (2007). Adsorption of nonionic surfactants at fluid–fluid interfaces: Importance in the coalescence of bubbles and drops. *Chemical Engineering Science*, **62**(11), 3057–3067. ISSN 00092509.
50. **Glover, A. R., S. M. Skippon, and R. D. Boyle** (1995). Interferometric laser imaging for droplet sizing: a method for droplet-size measurement in sparse spray systems. *Applied Optics*, **34**(36), 8409–8421. ISSN 2155-3165.
51. **Gupta, R., D. F. Fletcher, and B. S. Haynes** (2010a). CFD modelling of flow and heat transfer in the Taylor flow regime. *Chemical Engineering Science*, **65**(6), 2094–2107. ISSN 00092509.
52. **Gupta, R., H. Hagnefelt, D. F. Fletcher, and B. S. Haynes** (2010b). On the importance of buoyancy in Taylor flow in horizontal microchannels. *Proceedings of the Seventh International Conference on Multiphase Flow*.
53. **Han, Y., Y. Liu, M. Li, and J. Huang** (2012). A review of development of micro-channel heat exchanger applied in air-conditioning system. *Energy Procedia*, **14**, 148–153. ISSN 18766102.
54. **Han, Y. and N. Shikazono** (2009). Measurement of the liquid film thickness in micro tube slug flow. *Int. J. Heat Fluid Flow*, **30**, 842–853.
55. **Han, Y., N. Shikazono, and N. Kasagi** (2011). Measurement of liquid film thickness in a micro parallel channel with interferometer and laser focus displacement meter. *International Journal of Multiphase Flow*, **37**(1), 36–45. ISSN 0301-9322.
56. **Harlow, F. H. and J. E. Welch** (1965). Numerical Calculation of Time-Dependent Viscous Incompressible Flow of Fluid with Free Surface. *The Physics of Fluids*, **8**(12), 2182–2189. ISSN 0031-9171.
57. **Haroun, Y., D. Legendre, and L. Raynal** (2010). Volume of fluid method for interfacial reactive mass transfer: Application to stable liquid film. *Chemical Engineering Science*, **65**(10), 2896–2909. ISSN 00092509.
58. **Hassanvand, A. and S. H. Hashemabadi** (2012). Direct numerical simulation of mass transfer from Taylor bubble flow through a circular capillary. *International Journal of Heat and Mass Transfer*, **55**(21-22), 5959–5971. ISSN 00179310.
59. **Hayashi, K. and A. Tomiyama** (2012). Effects of surfactant on terminal velocity of a Taylor bubble in a vertical pipe. *International Journal of Multiphase Flow*, **39**, 78–87. ISSN 03019322.
60. **Hirt, C. W. and B. D. Nichols** (1981). Volume of fluid (VOF) method for the dynamics of free boundaries. *Journal of Computational Physics*, **39**(1), 201–225. ISSN 0021-9991.

61. **Hostache, G. and J. H. Mol** (1998). Reproductive biology of the neotropical armoured catfish *hoplosternum littorale* (siluriformes: callichthyidae): a synthesis stressing the role of the floating bubble nest. *Aquatic Living Resources*, **11**(3), 173–185.
62. **Howard, J., P. Walsh, and E. Walsh** (2011). Prandtl and capillary effects on heat transfer performance within laminar liquid-gas slug flows. *International Journal of Heat and Mass Transfer*, **54**, 4752–4761.
63. **Huerre, A., O. Theodoly, A. M. Leshansky, M.-P. Valignat, I. Cantat, and M.-C. Jullien** (2015a). Droplets in Microchannels: Dynamical Properties of the Lubrication Film. *Physical Review Letters*, **115**(6). ISSN 0031-9007, 1079-7114.
64. **Huerre, A., O. Theodore, A. Leshansky, M. P. Valignat, I. Cantat, and M. C. Julien** (2015b). Droplets in microchannels: Dynamical properties of the lubrication film. *Phys. Rev. Lett.*, **115**, 064501.
65. **Hulst, H. C. and R. T. Wang** (1991). Glare points. *Applied Optics*, **30**(33), 4755–4763. ISSN 2155-3165.
66. **Irlandoust, S., S. Ertlé, and B. Andersson** (2009). Gas-liquid mass transfer in taylor flow through a capillary. *The Canadian Journal of Chemical Engineering*, **70**(1), 115–119. ISSN 1939-019X.
67. **Jensen, M. H., A. Libchaber, P. Pelcé, and G. Zocchi** (1987). Effect of gravity on the Saffman-Taylor meniscus: Theory and experiment. *Phys. Rev. A*, **35**, 2221–2227.
68. **Kashid, M. N., A. Renken, and L. Kiwi-Minsker** (2011). Gas-liquid and liquid-liquid mass transfer in microstructured reactors. *Chemical Engineering Science*, **66**(17), 3876–3897. ISSN 0009-2509.
69. **Khodaparast, S., O. Atasi, A. Deblais, B. Scheid, and H. A. Stone** (2018). Dewetting of Thin Liquid Films Surrounding Air Bubbles in Microchannels. *Langmuir*, **34**(4), 1363–1370.
70. **Khodaparast, S., N. Borhani, G. Tagliabue, and J. R. Thome** (2013). A micro particle shadow velocimetry ( $\mu$ psv) technique to measure flows in microchannels. *Exp. Fluids*, **54**, 1474.
71. **Khodaparast, S., N. Borhani, and J. R. Thome** (2014). Application of micro particle shadow velocimetry  $\mu$ PSV to two-phase flows in microchannels. *Int. J. Multiphase flow*, **62**, 123–133.
72. **Khodaparast, S., M. Magnini, N. Borhani, and J. R. Thome** (2015). Dynamics of isolated confined air bubbles in liquid flows through circular microchannels: an experimental and numerical study. *Microfluidics and Nanofluidics*, **19**(1), 209–234. ISSN 1613-4982, 1613-4990.
73. **Klaseboer, E., R. Gupta, and R. Manica** (2014). An extended Bretherton model for long Taylor bubbles at moderate capillary numbers. *Phys. Fluids*, **26**, 032107.
74. **Kobayashi, J., Y. Mori, K. Okamoto, R. Akiyama, M. Ueno, T. Kitamori, and S. Kobayashi** (2004). A Microfluidic Device for Conducting Gas-Liquid-Solid Hydrogenation Reactions. *Science*, **304**(5675), 1305–1308. ISSN 0036-8075, 1095-9203.
75. **König, G., K. Anders, and A. Frohn** (1986). A new light-scattering technique to measure the diameter of periodically generated moving droplets. *Journal of Aerosol Science*, **17**(2), 157–167.
76. **Kosior, D., J. Zawala, R. Todorov, D. Exerowa, and K. Malysa** (2014). Bubble bouncing and stability of liquid films formed under dynamic and static conditions from n-octanol solutions. *Colloids and Surfaces A: Physicochemical and Engineering Aspects*, **460**, 391–400. ISSN 09277757.
77. **Kurimoto, R., K. Hayashi, and A. Tomiyama** (2013). Terminal velocities of clean and fully-contaminated drops in vertical pipes. *International Journal of Multiphase Flow*, **49**, 8–23. ISSN 03019322.
78. **Legendre, D.** (1996). *Quelques aspects des forces hydrodynamiques et des transferts de chaleur sur une bulle sphérique*. Ph.D. thesis, INP, Toulouse.
79. **Legendre, D. and M. Maglio** (2013). Numerical simulation of spreading drops. *Colloids and Surfaces A: Physicochemical and Engineering Aspects*, **432**, 29–37. ISSN 09277757.
80. **Legendre, D. and J. Magnaudet** (1998). The lift force on a spherical bubble in a viscous linear shear flow. *Journal of Fluid Mechanics*, **368**, 81–126. ISSN 1469-7645, 0022-1120.
81. **Legendre, D., J. Magnaudet, and G. Mougin** (2003). Hydrodynamic interactions between two spherical bubbles rising side by side in a viscous liquid. *Journal of Fluid Mechanics*, **497**, 133–166. ISSN 1469-7645, 0022-1120.

82. **Leung, S. Y., R. Gupta, D. F. Fletcher, and B. S. Haynes** (2012). Gravitational effect on Taylor flow in horizontal microchannels. *Chem. Eng. Sci.*, **69**(1), 553–564.
83. **Levich, V.**, *Physicochemical Hydrodynamics*. 1962, prentice hall edition.
84. **Liu, C.-Y., M. S. Carvalho, and S. Kumar** (2017). Mechanisms of dynamic wetting failure in the presence of soluble surfactants. *Journal of Fluid Mechanics*, **825**, 677–703. ISSN 0022-1120, 1469-7645.
85. **Liu, D. and S. Wang** (2011). Gas–liquid Mass Transfer in Taylor Flow through Circular Capillaries. *Industrial & Engineering Chemistry Research*, **50**(4), 2323–2330. ISSN 0888-5885.
86. **Liu, X.-D., S. Osher, and T. Chan** (1994). Weighted Essentially Non-oscillatory Schemes. *Journal of Computational Physics*, **115**(1), 200–212. ISSN 0021-9991.
87. **López, M. G.** (2010). Major and minor compounds in a Mexican spirit, young mezcal coming from two Agave Species. *Czech J. Food Sci. Vol.*, **28**(2), 127–132.
88. **Magnaudet, J., M. Rivero, and J. Fabre** (1995). Accelerated flows past a rigid sphere or a spherical bubble. Part 1. Steady straining flow. *Journal of Fluid Mechanics*, **284**(-1), 97. ISSN 0022-1120, 1469-7645.
89. **Magnini, M. and J. R. Thome** (2016). A CFD study of the parameters influencing heat transfer in microchannel slug flow boiling. *International Journal of Thermal Sciences*, **110**, 119–136. ISSN 1290-0729.
90. **Malysa, K., M. Krasowska, and M. Krzan** (2005). Influence of surface active substances on bubble motion and collision with various interfaces. *Advances in Colloid and Interface Science*, **114-115**, 205–225. ISSN 0001-8686.
91. **Mazutis, L. and A. D. Griffiths** (2012). Selective droplet coalescence using microfluidic systems. *Lab on a Chip*, **12**(10), 1800–1806. ISSN 1473-0189.
92. **Mei, R., J. F. Klausner, and C. J. Lawrence** (1994). A note on the history force on a spherical bubble at finite Reynolds number. *Physics of Fluids*, **6**(1), 418–420. ISSN 1070-6631.
93. **Mikaelian, D.** (). *Etude de la dynamique et de la morphologie de bulles confinées et non confinées et de leur transfert de matière vers le liquide environnant*. Ph.D. thesis, Université libre de Bruxelles.
94. **Mikaelian, D., B. Haut, and B. Scheid** (2015). Bubbly flow and gas-liquid mass transfer in square and circular microchannels for stress-free and rigid interfaces: dissolution model. *Microfluidics and Nanofluidics*, **19**(4), 899–911. ISSN 1613-4982, 1613-4990.
95. **Muradoglu, M. and G. Tryggvason** (2008). A front-tracking method for computation of interfacial flows with soluble surfactants. *Journal of Computational Physics*, **227**(4), 2238–2262. ISSN 00219991.
96. **Nath, B., G. Biswas, A. Dalal, and K. C. Sahu** (2017). Migration of a droplet in a cylindrical tube in the creeping flow regime. *Physical Review E*, **95**(3). ISSN 2470-0045, 2470-0053.
97. **Olbricht, W. L. and D. M. Kung** (1992). The deformation and breakup of liquid drops in low Reynolds number flow through a capillary. *Physics of Fluids A: Fluid Dynamics*, **4**(7), 1347–1354. ISSN 0899-8213.
98. **Osher, S. and J. A. Sethian** (1988). Fronts propagating with curvature-dependent speed: Algorithms based on Hamilton-Jacobi formulations. *Journal of Computational Physics*, **79**, 12.
99. **Patel, M. A., Sweta and A. Chandra** (2016). THE ROLE OF LAB-ON-A-CHIP DEVICE IN HEALTH CARE. *International Journal of Pharmaceutical Sciences and Research*, **7**, 5.
100. **Pereira, A. and S. Kalliadasis** (2008). On the transport equation for an interfacial quantity. *The European Physical Journal Applied Physics*, **44**(2), 211–214. ISSN 1286-0042, 1286-0050.
101. **Popinet, S. and S. Zaleski** (1999). A front-tracking algorithm for accurate representation of surface tension. *International Journal for Numerical Methods in fluids*, **6**, 775–793.
102. **Rage, G. R.** (2017). *Perlas de mezcal: Estudio del comportamiento de burbujas superficiales en mezclas agua-etanol*. Ph.D. thesis, Universidad Autonoma de Mexico, Mexico.
103. **Rage, G. R., O. Atasi, M. M. Wilhemus, J. F. Hernandez-Sanchez, B. Haut, B. Scheid, D. Legendre, and R. Zenit** (2018). Bubbles determine the amount of alcohol in mezcal. *Submitted to Proceedings of the National Academy of Science*.

104. **Reichert, B., A. Huerre, O. Theodoly, M.-P. Valignat, I. Cantat, and M.-C. Jullien** (2018). Topography of the lubrication film under a pancake droplet travelling in a Hele-Shaw cell. *Journal of Fluid Mechanics*, **850**, 708–732. ISSN 0022-1120, 1469-7645.
105. **Riaud, A., H. Zhang, X. Wang, K. Wang, and G. Luo** (2018). Numerical Study of Surfactant Dynamics during Emulsification in a T-Junction Microchannel. *Langmuir*, **34**(17), 4980–4990. ISSN 0743-7463.
106. **Rivero-Rodriguez, J. and B. Scheid** (2018). Bubbles dynamics in microchannels: inertial and capillary migration forces. *Journal of Fluid Mechanics*, **842**, 215–247. ISSN 0022-1120, 1469-7645. ArXiv: 1708.01114.
107. **Scardovelli, R. and S. Zaleski** (1999). Direct Numerical Simulation of Free-Surface and Interfacial Flow. *Annual Review of Fluid Mechanics*, **31**(1), 567–603.
108. **Scheid, B., S. Dorbolo, L. R. Arriaga, and E. Rio** (2012). Antibubble Dynamics: The Drainage of an Air Film with Viscous Interfaces. *Physical Review Letters*, **109**(26). ISSN 0031-9007, 1079-7114.
109. **Schiller, L. and Z. Naumann** (1935). A drag coefficient correlation. *Z. Ver. Deutsch. Ing.*, 77–308.
110. **Shim, S., J. Wan, S. Hilgenfeldt, P. D. Panchal, and H. A. Stone** (2014). Dissolution without disappearing: multicomponent gas exchange for CO<sub>2</sub> bubbles in a microfluidic channel. *Lab on a Chip*, **14**(14), 2428. ISSN 1473-0197, 1473-0189.
111. **Srinivas, A. and P. Ghosh** (2012). Coalescence of Bubbles in Aqueous Alcohol Solutions. *Industrial & Engineering Chemistry Research*, **51**(2), 795–806. ISSN 0888-5885, 1520-5045.
112. **Stan, C. A., L. Guglielmini, A. K. Ellerbee, D. Caviezel, H. A. Stone, and G. M. Whitesides** (2011). Sheathless hydrodynamic positioning of buoyant drops and bubbles inside microchannels. *Physical Review E*, **84**(3). ISSN 1539-3755, 1550-2376.
113. **Stone, H. A.** (1990). A simple derivation of the time dependent convective diffusion equation for surfactant transport along a deforming interface. *Physics of Fluids A: Fluid Dynamics*, **2**(1), 111–112. ISSN 0899-8213.
114. **Sunol, F. and R. González-Cinca** (2010). Rise, bouncing and coalescence of bubbles impacting at a free surface. *Colloids and Surfaces A: Physicochemical and Engineering Aspects*, **365**(1-3), 36–42. ISSN 09277757.
115. **Suresh, V. and J. B. Grotberg** (). The effect of gravity on liquid plug propagation in a two-dimensional channel. *Phys. Fluids*, **17**(3). ISSN 031507.
116. **Sussman, M., E. Fatemi, P. Smereka, and S. Osher** (1998). An improved level set method for incompressible two-phase flows. *Computers & Fluids*, **27**(5), 663–680. ISSN 0045-7930.
117. **Sussman, M., P. Smereka, and S. Osher** (1994). A Level Set Approach for Computing Solutions to Incompressible Two-Phase Flow. *Journal of Computational Physics*, **114**(1), 146–159. ISSN 0021-9991.
118. **Taha, T. and Z. Cui** (2006). CFD modelling of slug flow inside square capillaries. *Chemical Engineering Science*, **61**(2), 665–675. ISSN 00092509.
119. **Takagi, S., T. Ogasawara, M. Fukuta, and Y. Matsumoto** (2009). Surfactant effect on the bubble motions and bubbly flow structures in a vertical channel. *Fluid Dynamics Research*, **41**(6), 065003. ISSN 1873-7005.
120. **Takemura, F.** (2005). Adsorption of surfactants onto the surface of a spherical rising bubble and its effect on the terminal velocity of the bubble. *Physics of Fluids*, **17**(4), 048104. ISSN 1070-6631.
121. **Tasoglu, S., U. Demirci, and M. Muradoglu** (2008). The effect of soluble surfactant on the transient motion of a buoyancy-driven bubble. *Physics of Fluids*, **20**(4), 040805. ISSN 1070-6631, 1089-7666.
122. **Taylor, G. I.** (1961). Deposition of a viscous fluid on the wall of a tube. *J. Fluid Mech.*, **10**, 161–165.
123. **Teixeira, M. A. C., S. Arscott, S. J. Cox, and P. I. C. Teixeira** (2015). What is the Shape of an Air Bubble on a Liquid Surface? *Langmuir*, **31**(51), 13708–13717. ISSN 0743-7463.
124. **Thulasidas, T. C., M. A. Abraham, and R. L. Cerro** (1997). Flow patterns in liquid slugs during bubble-train flow inside capillaries. *Chemical Engineering Science*, **52**(17), 2947–2962. ISSN 0009-2509.
125. **Tran, T., H. J. J. Staat, A. Prosperetti, C. Sun, and D. Lohse** (2012). Drop Impact on Superheated Surfaces. *Physical Review Letters*, **108**(3), 1079–7114. ISSN 0031-9007.

126. **Triplett, K. A., S. M. Ghiaasiaan, S. I. Abdel-Khalik, and D. L. Sadowski** (1999). Gas-liquid two-phase flow in microchannels Part I: two-phase flow patterns. *International Journal of Multiphase Flow*, **25**(3), 377–394. ISSN 0301-9322.
127. **Unverdi, S. O. and G. Tryggvason** (1992). A front-tracking method for viscous, incompressible, multi-fluid flows. *Journal of Computational Physics*, **100**(1), 25–37. ISSN 0021-9991.
128. **van Baten, J. M. and R. Krishna** (2004). CFD simulations of mass transfer from Taylor bubbles rising in circular capillaries. *Chemical Engineering Science*, **59**(12), 2535–2545. ISSN 0009-2509.
129. **van der Net, A., L. Blondel, A. Saugey, and W. Drenckhan** (2007). Simulating and interpreting images of foams with computational ray-tracing techniques. *Colloids and Surfaces A: Physicochemical and Engineering Aspects*, **309**(1-3), 159–176. ISSN 09277757.
130. **Van Dyke, M.**, *Perturbation methods in fluid mechanics*. Academic Press, 1964.
131. **Wang, S., T. Guo, S. Dabiri, P. P. Vlachos, and A. M. Ardekani** (2017). Effect of surfactant on bubble collisions on a free surface. *Physical Review Fluids*, **2**(4), 043601.
132. **Warnier, M. J. F., E. V. Rebrov, M. H. J. M. de Croon, V. Hessel, and J. C. Schouten** (2008). Gas hold-up and liquid film thickness in Taylor flow in rectangular microchannels. *Chemical Engineering Journal*, **135**, S153–S158.
133. **Xu, J.-J. and H.-K. Zhao** (2003). An Eulerian formulation for solving partial differential equations along a moving interface. *Journal of Scientific Computing*, **19**(1-3), 573–594.
134. **Young, N. O., J. S. Goldstein, and M. J. Block** (1959). The motion of bubbles in a vertical temperature gradient. *Journal of Fluid Mechanics*, **6**(03), 350–356.
135. **Yu, Z., O. Hemminger, and L.-S. Fan** (2007). Experiment and lattice Boltzmann simulation of two-phase gas-liquid flows in microchannels. *Chemical Engineering Science*, **62**(24), 7172–7183. ISSN 0009-2509.
136. **Zawala, J., M. Krasowska, T. Dabros, and K. Malysa** (2007). Influence of Bubble Kinetic Energy on its Bouncing During Collisions with Various Interfaces. *The Canadian Journal of Chemical Engineering*, **85**(5), 669–678. ISSN 1939-019X.
137. **Zhang, N. and D. F. Chao** (2002). A new laser shadowgraphy method for measurements of dynamic contact angle and simultaneous flow visualization in a sessile drop. *Optics & Laser Technology*, **34**(3), 243–248. ISSN 0030-3992.
138. **Zhang, N. and D. F. Chao** (2003). Caustics and caustic-diffraction in laser shadowgraphy of a sessile drop and identification of profile near contact line. *Optics & Laser Technology*, **35**(3), 155–161. ISSN 0030-3992.
139. **Zheng, Y., H. Fujioka, and J. B. Grotberg** (2007). Effects of gravity, inertia, and surfactant on steady plug propagation in a two-dimensional channel. *Phys. Fluids*, **19**(8), 082107.
140. **Ziemecka, I., B. Haut, and B. Scheid** (2015). Hydrogen peroxide concentration by pervaporation of a ternary liquid solution in microfluidics. *Lab on a Chip*, **15**(2), 504–511. ISSN 1473-0197, 1473-0189.